Improved Industrial Robot Positional Accuracy for Machining with Bias Correction

Ian Jeavons

A Thesis submitted to the University of Sheffield for the degree of

Doctor of Engineering

The University of Sheffield

Faculty of Engineering

Department of Mechanical Engineering

Submission Date

September 2020

Acknowledgements

First and foremost I would like to thank my academic supervisor Dr. Robert Barthorpe for his persistence, perspective and guidance throughout, and without whom this work would not have been possible. I would also like to thank my AMRC supervisor Dr. Tom McLeay for his focus and support early in the process that has lead to me completing my research. Special thanks to Dr. Chao Sun and Dr. David Curtis who at crucial times, stepped in with the guidance that I needed.

I would like to thank all of those at my sponsoring company, Hexagon Manufacturing Intelligence for this opportunity, their equipment and training, and the open armed welcome that they offered me and my family. A special thanks must go to Mick Walters, Tim Gears, Kieran McLoughlin and Les Randle whose generosity sustained me throughout.

I would like to thank the IDC in Machining Science and the EPSRC (grant reference EP/I01800X/1) for providing me with this opportunity and funding my research, along with the AMRC. A special thanks to Ben Morgan and Tom Smith at the AMRC for their guidance and enthusiasm for all robotics matters. I'd like to extend my gratitude to the AMRC Training Centre for providing me with a career outlet and also being patient while I took time to write my thesis.

Finally, thank you to my family for their faith in me and their support. To my wife and children especially whom I have relied on entirely for motivation, perspective and a belief that it will all be worthwhile.

Abstract

Robotic machining has the potential to provide advantages as a substitute for conventional CNC machine tool operations. However, conventional industrial robots are restricted to low accuracy tasks due to their poor positional accuracy. This creates challenges in achieving the tolerances required for machining tasks. Data-based modelling of the positional error data is a potential solution which learns the positional errors in order to compensate and minimise them.

There has been some success in improving industrial robot accuracy in research literature, by first calibrating the kinematic model and then using machine learning (ML)-based bias correction to learn the positional errors. However, the limitations of ML-based bias correction applied to the industrial robot positional accuracy problem have not been fully explored with the accuracies required to achieve tight machining tolerances. Mapping the positional errors with a greater resolution of training data, and reducing the burden on bias correction by calibrating the kinematic model with a higher level of calibration, are two examples which have the potential to improve accuracy. This thesis focusses on both training data resolution and bias reduction to maximise outcomes whilst informing trade-offs when using ML-based bias correction in this application.

The key finding of this thesis is that substantial gains in accuracy can be achieved using ML-based bias correction and that the accuracy limit can be achieved with practicable amounts of data gathering and processing. Also that calibration prior to bias correction did not significantly improve overall accuracy for the cases investigated. This suggests that data may be better utilised in training the bias corrector rather than for calibration of the physical model. In conclusion, ML-based bias correction methods can provide a solution that provides substantial gains in positional accuracy for conventional industrial robots, bringing them to a level that may facilitate broader adoption in machining applications.

Contents

List of Figures

Chapter 1

Introduction to Industrial Robot Machining

1.1 Introduction

The manufacturing sector has increasingly turned to industrial robots as a flexible solution to meet the demands for greater product variation in smaller volumes. An integral part of a flexible manufacturing system is the machining process. Machining is the process of removing material to achieve size tolerances, such as part length and hole locations relative to a datum; geometric tolerances, including flatness and concentricity; and surface finish tolerances, such as roughness. Machining tasks such as drilling, milling and turning have traditionally been undertaken on CNC machine tools which are designed to produce parts that meet machining tolerances. To achieve this, CNC machine tools are designed to have independent axes, a highly rigid structure, and they are available in a range of configurations (typically 3 to 7 axes). However, they are also expensive and inflexible, in a manufacturing sense. On the other hand, finishing tasks that have very small material removal rates, such as polishing, are usually completed manually as they require high dexterity to keep the tool normal to the surface. However this can be an unhealthy environment for the operator. Robotic machining can offer an alternative to both.

Industrial robots are typically used in manufacturing for part handling, welding and paint spraying, and have a high working volume to footprint ratio compared to CNCs. However, only 10% of industrial robots are used in metal industries and it is estimated that less than 2% are used for machining tasks [2]. Conventional 6-axis articulated robots have poor positional accuracy and low rigidity, which means that it is very challenging for industrial robots to achieve machining tolerances. As a result, they are limited to low accuracy tasks and are rarely used for conventional machining applications such as drilling and milling metals.

Industrial robots have found their use in niche machining applications where machining process forces are low, which include deburring and milling of non-metals [3][4][5], milling [6][7][8][9], drilling large parts [10][11][12] and finishing processes [13][14][15][16].

When implemented successfully for machining applications, industrial robots have the potential to increase manufacturing capability and capacity by offering integration with larger automation systems. They are kinematically flexible and dexterous so can approach complex tasks from multiple paths and configurations [17][18][19]. For example, Figure 1.1a shows an articulated robot which is mounted to a mobile platform to increase the workspace capacity for machining large aerospace structures [20]. Figure 1.1b shows an articulated robot with the capability of drilling holes in the circumference of a wind turbine without repositioning for access to the face [17].

(a)

(b)

Figure 1.1: Industrial robot machining examples:(a) aerospace structure edge trimming, (b) wind turbine drilling.

There is considerable motivation and potential to increase the use of industrial robots for machining applications. For the advantages of robotic machining to be accessed in wider machining applications, there are a number of challenges that must first be overcome.

1.1.1 Challenges in industrial robotic machining

The challenges that currently prohibit the use of industrial robots for the majority of machining tasks are associated with all three of the machining tolerance types i.e.

size, geometric and surface finish. A summary of robotic machining focused review papers [2][17][18][21] identified the following barriers to widespread application:

1. **Achieving acceptable positional accuracy**: In this context, positional accuracy is a measure of how close the robot tool-centre-point (TCP) position is to a desired position. Accuracy determines whether part size tolerances can be achieved. To respond quickly to manufacturing changes, and in order to machine free-form surfaces, offline programming is used to generate the robot programs. Poor positional accuracy is usually attributed to a difference in the kinematic model of the robot, used by the program to predict TCP positions, and the physical robot. To improve its positional accuracy, an industrial robot can be calibrated. *Calibration* is broadly defined here as the identification and updating of model parameters, specifically, updating the kinematic model, which is used to determine the robot end effector position from given joint angles. Calibration is defined in further detail in Section 2.2. Industrial robot calibration is an active field of research which has focussed on improving robot positional accuracy in general, but has not focussed on achieving the accuracies required for machining applications.

2. **Structural stiffness modelling and process force monitoring**: Structural stiffness, or rigidity, is the resistance to deflection when the end effector of the robot is subjected to a *wrench* (load or torque). Deflection due to payload determines not only the capability to achieve a required positional accuracy, but also achieve a required path accuracy and thus achieve geometric tolerances, for example, flat, parallel part surfaces. The problem has been extensively researched and approaches include stiffness modelling and prediction of path offsets [22], optimisation of stiffness by careful selection of configuration [23][24] and online force feedback control of machining parameters [10][11][25], or all three [26], as well as ‘look ahead’ path adaptation [4][27].

3. **Programming robot trajectories with task-base planning software**: the planned trajectory of the robot TCP during a machining process also determines the accuracy of the path and the ability to achieve geometric tolerances. Integrated robot programming languages are ’robot-centric’, unlike machine tool G-codes which are ’task-centric’. By this it means that robot programs focus on trajectories that best suit the robot by avoiding excessive joint rotations and singularities, whereas machine tool G-codes generate paths that closely match the part geometry. There are CAM based software solutions from OEMs, such

as ABB RobotWare Machining FC, Mastercam and Robotworx that map between the two, however there is still work to be done to integrate the discussed optimisation strategies such as stiffness.

4. **Vibration and chatter**: excitation of the modal responses from machining process forces is more likely to result in excessive vibration and chatter, which determine whether surface finish tolerances can be achieved. The first natural frequency of an industrial robot structure is considerably lower than that of a CNC machine tool, in the order of 10Hz compared to 1000Hz. Industrial robots may therefore be more likely to be excited at conventional machining speeds. Approaches to mitigate this effect in existing research include tool selection, optimised location and posture selection [28], path and feed selection [29][30] and suppression [15][31].

The focus of this thesis is to explore novel solutions for the first of the challenges, improving robot positional accuracy for machining tasks, through improved modelling of the robot kinematics.

1.2 Industrial robot positional accuracy for machining applications

Accuracy (robot accuracy or model accuracy) is defined in the context of this thesis as the closeness of the robot end effector position (in Cartesian coordinates), or model predictions of the end effector position, to the measured position. This is expressed in terms of error in mm, so that a large error is attributed to a low accuracy i.e. the robot is not near to its desired target position. The positional accuracy required to enable robotic machining to be accessible to wider machining application is difficult to quantify. Certainly, the positional accuracy of conventional industrial robots is prohibitively low for the majority of machining tasks. However, OEMs rarely publish positional accuracy capability on data sheets in favour of repeatability. *Repeatability* is the ability of the robot to return to a pose consistently when conducting the same task, repeated n times in the same conditions [32].

The accuracy required for industrial robots to achieve machining tasks is dependent on the task and therefore high and low accuracies, in relation to accessing wider machining tasks, are arbitrary concepts at this point. A comparison of the positional accuracies reported in current industrial robot research literature and current CNCs may provide an upper an lower bound to a desirable accuracy region.

1.2.1 CNC machine tool accuracy

To determine the wider machining capability that robots must achieve to displace CNCs from some machining tasks, it is useful to understand the capability of CNC machine tools and the differences by which the performance of the two systems are measured. A direct comparison of accuracy between industrial robots and CNC machine tools is difficult to make as machine tool manufacturers use a different set of accuracy test standards to robotics manufacturers, and both are available in a range of structural configurations. CNC machine tool accuracy is often quantified by its *volumetric accuracy*, which is broadly defined as the root-mean square (rms) of the displacement along three axes, for example, positional error in x, y and z. Besides, volumetric accuracy has multiple definitions and is calculated differently, depending on the configuration of the machine axes [33][34]. In [35] the volumetric accuracy of ten conventional machine tools was compared and the results ranged between 42μm and 78μm using a body diagonal test, which can be used as an approximate performance measure. The Taniguchi curve in Figure 1.2 approximates the accuracy capability of different machining processes over time. The chart indicates that modern, conventional CNC machine tools are capable of achieving a positional accuracy of 0.1mm and below, which will be used in this thesis as a lower bound to the desired accuracy for an industrial robot.

The accuracy of an industrial articulated robots is wide ranging but can be expected to be in the order of approximately ±1mm. Values approaching 0.3mm have only been achieved with calibration or compensation [36].

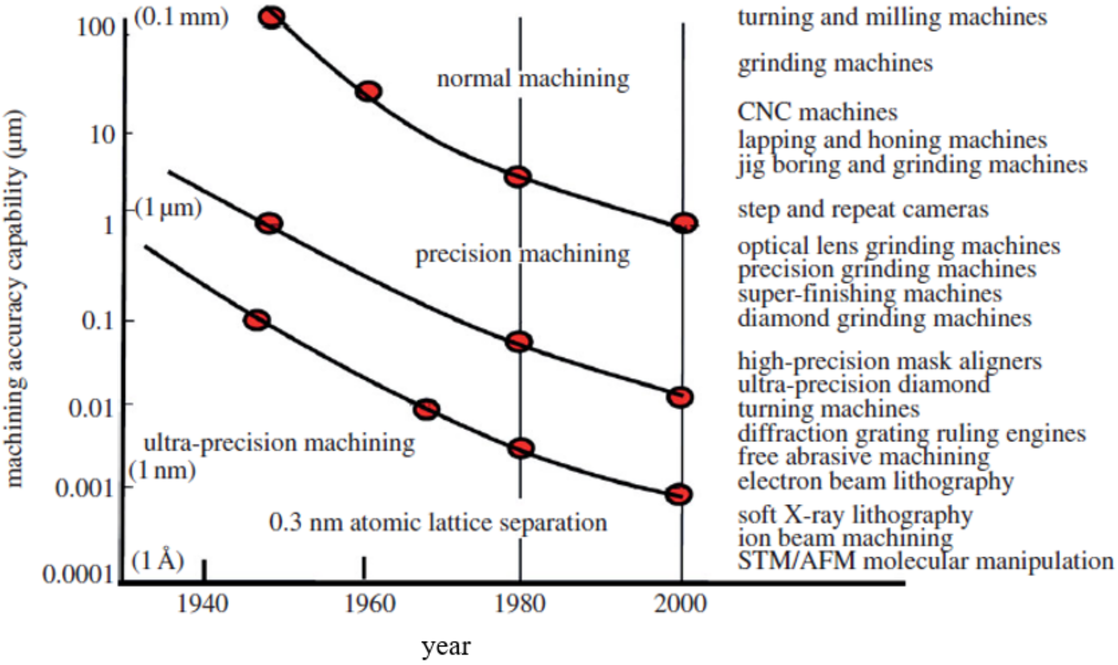

Figure 1.2: Taniguchi machining capability chart [1]

1.2.2 Industrial robot positional accuracy

Industrial robot accuracy is commonly reported as a volumetric error, either as a mean or rms Euclidean distance error (square-root of errors in x, y and z) although never tested in the same way in the research literature. In an investigation as to whether conventional industrial robots can achieve the accuracy required for an aerospace drilling application, the accuracy of four robots from ABB, Staubli and Kuka were evaluated [37]. A positional accuracy of 0.2mm was set as a desired accuracy, presumably a position tolerance which is maximum error in workspace volume, and the author concluded that none of the robots were capable of achieving it. In fact, the accuracy of an industrial articulated robot is expected to be approximately ±1mm, and values approaching 0.3mm have only been achieved with calibration or compensation [36]. A region of accuracy between 0.3mm, as the current capability of industrial robots, and 0.1mm, the lower capability of current CNCs provides a desirable range for this thesis. An accuracy of 0.2mm for a drilling task is set as a target. Questions remain as to what causes robot positional errors and what the solution is?

Inaccurate kinematic modelling of a robot is typically the result of geometric errors (manufacturing tolerances result in inaccurate robot geometry parameters in the kinetic model) and non-geometric errors (unmodelled errors, for example, joint stiffness and gearbox misalignment)[38]. As a result of a sequence of model errors along the robot serial chain, the positional errors can be considerable and highly non-linear making them challenging to model parametrically. The terms *linear* and *non-linear* are defined in the context of this thesis as: A *linear equation* is one which satisfies the principle of superposition (the output of variables and functions are added) and whose output changes in direct proportion to the input. A simple linear equation is typically expressed as a straight line function $y = ax + b$. A *linear system* is a collection of two or more linear equations that are solved simultaneously. The robot error model is later expressed as a linear system and solved using *linear least-squares estimation*. Some system error factors are described in this thesis as highly non-linear. A *non-linear* equation is one which does not satisfy the principle of superposition (for example, variables may be multiplied) and whose output does not change in direct proportion to the input. A *non-linear system* may contain some but not all linear equations. *Highly non-linear*, in the context of this thesis, means that very large output changes may occur from small input changes and that a non-linear system is the combination of two or more equations, one or more is non-linear, and is therefore very challenging to model.

The current industrial solution for improving robot positional accuracy is to conduct a calibration procedure in order to update the kinematic model parameters. However, this procedure is only offered by some manufacturers and typically results in an update on only the parameters that describe the robot geometry. As a result, some model form errors may still remain. The subject of robot calibration has been extensively researched, with seminal works conducted in the 1980's [39][40]. In subsequent decades, research on robot model calibration appears to have fragmented into calibration themes focussing on (1) modelling, (2) measurement (metrology and measurement strategies) and (3) identification (parameter estimation). Despite extensive research efforts into calibrating the parametric model of the robot kinematics, the positional error of a conventional, industrial robot remains prohibitively high for the majority of machining applications. The use of existing calibration tools will be a starting point for the solution investigated in this thesis, and the question is asked as to what extent can the positional errors be modelled non-parametrically?

Early successes have been made using data-based model compensation as a solution to robot positional error modelling, but it will require rigorous exploration to become a robotic machining solution. In this thesis, regression tools developed within the machine learning field are investigated and applied to the problem of reducing robot positional errors.

1.3 Machine Learning (ML) based bias correction

ML is a set of methods that automatically learns patterns in data [41], and combines tools from the fields of artificial intelligence and statistics. In the context of this thesis, *bias* refers to the positional errors between the system model predictions and measured values i.e. pose error data. *Bias correction* is the post-processing of the model predictions, in this study by using machine learning, with the aim of minimising the bias and for the predictions to match the measured values. Also in the context of this thesis, *bias reduction* is the reduction in the magnitude of the positional errors, prior to bias correction. This is achieved by calibration of the kinematic model of the robot. ML tools are employed in a wide range of fields and commonplace systems, such as self-driving cars, image classification, structural health monitoring, biology and many more [42]. Broadly speaking, the problems that ML tools are tasked with solving can be categorised as *regression* and *classification.* Regression is the problem of learning the relationship between input and output data where the input variable is continuous. Classification is the problem of labelling discrete data such as ‘pass’ or ‘fail’.

Machine learning can be broadly separated into three groups: *supervised learning*, *unsupervised learning* and *reinforcement learning* [43].

- **Supervised learning** uses labelled input-output examples to predict the output of new inputs. Regression and classification problems may use supervised learning as a solution.
- **Unsupervised learning** is tasked with learning patterns in unlabelled output data. Classification problems may use unsupervised learning as a solution.
- **Reinforcement learning** finds an optimal or sufficiently good action when occasionally rewarded or punished.

In the context of this thesis, the problem to be solved is one of regression, and a solution may be approached via supervised learning. The tasks of the ML are to learn the relationships between the robot TCP positional error data-the output across a range of configurations (a configuration is the posture of the robot defined from an input of joint angles), and joint angles-the input.

In engineering, many machine learning tools have become familiar parlance, such as artificial neural networks (ANN), support vector machines (SVM); and some tools that have grown in prominence more recently, including Gaussian processes (GP) and deep learning (DL). There has been some recent success in research where ML has been applied as a bias correction tool to improve industrial robot positional accuracy [44][45], but none with a focus on achieving a level of accuracy for machining tasks. Significant gains in accuracy were made by using bias correction, compared to the level achieved by the calibrated model, however the limitations were not explored and a desirable accuracy for machining has not been achieved.

The most common approach to date has been the application of an ANN, preceded by calibration to reduce the burden of bias correction. The full use of existing calibration tools and models to reduce the bias level has not been utilised, and the potential to achieve greater accuracy with more extensive calibration, or no calibration, has not been explored.

GPR can be defined as a Bayesian approach to non-parametric modelling, which fits a probability distribution to functions that fit data, rather than distributions to the data themselves [46]. GPR has been applied to related problems with some success, namely improving the positional accuracy of surgical robots and robot dynamics problems. However, GPR has been applied to the industrial robot positional accuracy problem by only one author [45], and has been shown to be a viable alternative to ANN bias correction.

Research literature related to the use of ML tools in this application is discussed further in Chapter 2.

A question remains as to what extent can ML-based bias correction improve the accuracy of an industrial robot? Specifically, the question is directed at achieving the desired accuracy for machining applications.

In this thesis, existing ML tools will be used for bias correction, extending the work presented in literature, but with a particular focus of whether ML tools are capable of improving robot positional error accuracy to the extent required for machining applications.

1.4 Aim and scope

The aim of this thesis is to explore the use of ML-based bias correction to improve the positional accuracy of industrial robots for machining applications. The focus of the research will be the use of ML as a solution, with the principal novelty arising from tailoring these tools to the robotic machining task. Existing parameter estimation and ML tools will be used throughout. This thesis seeks to answer the following research questions:

- Research question 1: What are the limitations of the positional accuracy of an industrial robot, given sufficient training data quantities, when using bias correction to reduce positional errors?
- Research question 2: To what extent does bias reduction, by robot model calibration prior to bias correction, increase the positional accuracy of an industrial robot?

To answer the research questions, a sequence of studies will be conducted to meet the following objectives:

1. Investigate the error sources on a conventional industrial robot and develop a numerical model to simulate robot positional errors.
2. Test the proposed bias correction method on simulated models with increasing complexity.
3. Validate the results of the bias correction method with an empirical study of an industrial robot for the general positional accuracy case.
4. Validate the bias correction method for a robotic machining task.

1.5 Thesis overview

This thesis consists of 8 chapters within three main parts.

In PART I (Chapters 2 and 3), the research is situated in relation to industrial robot literature and established methods, providing the reader with the background knowledge required to understand the experimental work ahead. Chapter provides a discussion of the challenges and accepted norms in robotics along with a critical review of literature and current practice. While both parameter estimation and bias correction are extensively researched fields, the review focusses on applications to robots. In Chapter 3, the research methodology is presented along with necessary underpinning parameter estimation and machine learning theory.

In PART II (Chapters 4,5,6 and 7), a series of numerical and experimental studies are presented which investigate the application of bias correction to robot models with increasing complexity. In Chapter 4, the error sources present in a conventional industrial robot are investigated, and the associated effect on kinematic behaviour is analysed by measuring errors in isolation. In Chapter 5, the proposed calibration and bias correction method is tested on a simulation of a conventional industrial robot. In Chapter 6, the results in Chapter 5 are validated by testing the method on an industrial robot. In Chapter 7, the method is validated on a robot machining focussed study.

In PART III (Chapter 8) the discussion, conclusions and recommendations of future work of the study are presented.

Chapter 2

Literature Review

This chapter provides an overview of the literature on the topics of industrial robot calibration and the application of bias correction to robot positional errors. The chapter is separated into three sections, however, many researchers present research that contributes to multiple topics and will appear multiple times in the chapter. For example, it is common to present research for a novel application of a parameter estimation technique and a novel metrology solution combined.

Section 2.1 presents an overview of the sources of positional error in industrial robots. Section 2.2 presents a critical review of related work on industrial robot calibration methods. Finally, section 2.3 presents a critical review of research literature where bias correction and ML tools have been applied in related works. Particular attention is paid to the use of Gaussian Process Regression (GPR) in related works. It is commonplace in the industrial robot accuracy research field for research literature to overlap multiple themes and so some works will be referred to in multiple or all sections.

2.1 Robot kinematic error sources

In this section, the robot positional error problem is described by reviewing existing research literature, with particular attention to error classification and ranking. To understand the challenges associated with robot positional accuracy, one must first understand the sources of error in the kinematics of the robot and the inaccuracies in the kinematic model. The kinematic model of a robot is a mathematical description of the geometry of its structure. The structure consists of a serial or parallel chain of joints, which has a motor and gearbox transmission, and links that separate them to create an arm.

The error between the desired pose of the end-effector and actual pose is the result of incorrect kinematic model parameters and/or unmodelled kinematics. Consider incorrect link length parameters in the model or flexible links as examples. Error sources, modelled or unmodelled, can be categorised as *geometric* or *non-geometric* [47] and the distinction between them often leads to separate research themes.

- *Geometric* errors are the deviations from the geometric parameters in the kinematic model, such as link lengths, offset distances along joint axes and joint axis orientation. Geometric errors may arise due to manufacturing tolerances and alignment errors during assembly.
- *Non-geometric* errors include joint gearbox and link elasticity, gearbox transmission errors e.g. backlash, gear runout and orientation, and thermal effects. Some of the error sources may be negated by moving the gearbox encoder from the motor side to the gearbox transmission output side and by improving manufacturing tolerances. Given that repeatability is the main driver of industrial robot design, which is not affected by geometric errors, there is little motivation to increase manufacturing costs to reduce tolerances. Instead, software solutions (i.e. calibration) are used.

The geometric and non-geometric error sources above have been described fully in research [40] but it remains difficult to concentrate research efforts when a consensus on the ranking of relative positional error attributed to the different error sources has not been reached.

Early research demonstrated that non-geometric errors accounted for less than 10% of the total error [38]. Judd and Knasinski [48] investigated many error sources individually on a single robot for comparison and concluded that joint encoder errors contributed to 90% of the error, link length tolerances contributed an additional 5% percent while gear transmission errors contributed just 1%. Most of the gear error was reportedly the result of a misalignment in the joint 1 due to payload torque when the arm is outstretched. Gearbox backlash has been reported to contribute to 0.5% to 1% of the error whilst thermal effects contributed to 0.1% [47]. Few researchers have concentrated on modelling the gearbox transmission, backlash and thermal effects parametrically. In modern, temperature controlled factories, thermal effects are typically assumed to be negligible.

Contrary to this, Whitney [49] demonstrated experimentally that non-geometric errors rival geometric errors on a different robot. To add to the debate, more recently, Young and Pickin [50] and Nubiola and Bonev [51] argued that improvements in manufacturing techniques and measurement accuracy mean that the previous statements, regarding the ranking of error sources, are no longer valid for modern industrial robots. The accuracy results for three similar, modern robots from different manufacturers were compared (Croos, ABB and Kuka). The authors evaluated the robots using the ISO 9283 accuracy test which is insufficient for determining accuracy [50] and not widely used in related works.

In summary, the consensus amongst researchers is that the rank and relative proportion of positional error associated with each source is unique to each robot, which makes targeting sources for calibration difficult to achieve. Undoubtedly, manufacturing tolerances are the largest error source in a conventional industrial robot, and updating the geometric parameters in the kinematic model is a convenient starting point. Non-geometric errors may be relatively small in comparison, but also may be sufficiently large to make the robot positional errors prohibitively high for some machining applications. The complexity and coupling of the sources produces a highly non-linear positional error, hence the motivation for both parametric models and non-parametric bias correction.

2.2 Robot calibration

In this section, a critical review of industrial robot calibration research literature is presented. The section is organised in the order of calibration stages: *modelling*, *measurement*, *identification* and *compensation* [39]. Industrial robot calibration is a subject that has received considerable interest in the past four decades and many metrology solutions and mathematical tools exist. Several are described in this section to provide a view of the breadth of the subject.

The focus of calibration efforts can been classified by level in the order of expected reduction, positional error and increase in calibration effort. *Level 1* calibration determines the relationship between joint encoder reading and actual joint angle. *Level 2* calibration is the identification and updating of geometric model parameters. *Level 3* calibration is the modelling of non-geometric errors [39].

2.2.1 Modelling

Section 2.1 concluded that many error sources exist and that there is no consensus on the rank in terms of contribution to the positional error. The majority of research in this field has focussed on parametrically modelling the geometry of the robot as a kinematic model, modelling deflection due to payload and gearbox transmission errors. The latter are discussed in separate subsections.

2.2.1.1 Geometric model conventions

The *Denavit-Hartenburg* (DH) convention is the most popular model used to describe the robot kinematics, and is the standard adopted by the industrial robotics industry. Its success stems from its generality i.e. it can be used to describe many different robot structures and joint types. Most geometric models consist of the sequential multiplication of homogeneous transformation matrices (HTM) between coordinate systems placed on each link. The DH convention simplifies each transformation by describing it with only four parameters instead of the six required for full transformation. Calibration of the DH parameters however, suffers from issues of *completeness* and *proportionality* [40] when consecutive joint axes are parallel, which is a common structure in articulated robots. This leads to issues of singularity when calibrating.

- *Completeness* refers to the problem when some axis rotations and translations are not parametrised. The ideal robot, in DH convention terms, has joint axes that are parallel or perpendicular to each other. Small deviations in these cannot be modelled with existing parameters.
- *Proportionality* is a parameter estimation problem when the consecutive axes are parallel and the common normal used to establish the reference frame is non-unique. Then the model positional errors are not a continuous function of the DH parameters. In the case of a small misalignment between axes, a common normal may exist but it will be far away from the structure.

Numerous geometric models have been proposed to solve the completeness and proportionality problem. The most common solution is the *modified DH* (mDH) model proposed by Hayati et al. [52] which replaces a redundant joint offset length parameter with a link twist. The *S-model* [53], a form of screw-axis measurement method, describes each joint with 6 parameters, from which later, the DH parameters can be extracted. The *S-model* method was later adapted to identify the DH parameters directly [54]. The *zero-reference model* [40] describes the joint axes separately with six parameters, relative to a fixed reference point, rather than from link to link. The *product-of-exponentials* (POE) model, based on zero-reference, uses matrix exponentials that vary smoothly with joint axes variations for improved parameter estimation [55][56][57]. Li et al. [58] proposed a Dual Quaternion (DQ) alternative to the common HTM representation of link transformation and demonstrated that it is a more compact and efficient model for calibrating DH parameters. The reader is guided to [39] and [38] for a comparison of some of these.

2.2.1.2 Elasticity modelling

Elasticity in the robot kinematic chain refers to a combination of elasticity in the joint gearbox (parameterised by stiffness values) and elasticity in the links, which can be considered as bending beams. Elasticity models determine the deflection at the TCP when the end effector is subjected to a force and/or torque such as a static payload, machining process forces or collision. Industrial robot elasticity modelling is a subject that has received a great deal of attention from the field of robot machining research [59]. Reportedly, a 500N force on the end effector may cause a 1mm deflection [25] which far exceeds most machining tolerances. Given that a machining spindle is a static payload, which may weigh considerably more than 50kg, elasticity deflection modelling has become significant in this application. At the foundation, elasticity modelling is the conventional virtual joint model (VJM) which represents all elasticity effects (joint and link) as a torsional spring for each joint [60].

Calibration of the elasticity model is tasked with identifying the stiffness parameters in the model represented in a stiffness matrix K_x. However, the stiffness of the structure is dependent on the joint configuration of the robot [61]. This means that, if a machining task requires the robot to move to substantially different configurations, then the stiffness matrix must be determined for each new joint configuration in order to predict the deflections and the TCP accurately, which is an arduous task.

An evolution of the stiffness model is the joint compliance model, which utilises joint compliance parameters C[rad/Nmm] which are the inverse of the stiffness parameters K[Nmm/rad] [25][51]. The joint compliance parameters are constant and independent of joint configuration, which is more convenient to identify and model. Also, in a robot with n joints, the stiffness matrix has $n \times n$ parameters to estimate, compared to the n compliance parameters, hence the compliance model is preferable for parameter estimation.

It is argued that the joint compliance model is only valid in the unloaded case. To conserve properties of conservation of energy, the conventional VJM can be updated with an additional complimentary matrix which represents the stiffness due to a change in geometry [62][63]. This updated model is referred to as the *Conservative Congruence Transformation* (CCT) and has been demonstrated to be a more complete model. However, its foundation comes from research into highly compliant finger-like grips rather than relatively stiff industrial robots. The additional complexity of the model and marginal gain in accuracy may not be applicable to large, articulated industrial robots.

More recently, the inclusion of a linear spring to represent link elasticity, and passive joints was included in the VJM. This research has been extended to include analysis of parallel robots, structural buckling analysis (joint buckling rather than column buckling) and gravity compensation [64][65]. The motivation again comes, in part, from the development of lighter, low-inertia industrial robots use in fast pick and place tasks such as electrical component assembly. This approach may not be applicable to machining robots.

2.2.1.3 Gearbox transmission error modelling

Gearbox transmission errors, such as bearing misalignment, are observed as periodic errors at the TCP. An investigation of the gearbox errors demonstrated an amplitude of 0.20mm in joint 6 alone [51]. A TCP that is 100mm from the end flange would result in a 0.35mm deviation, which is large compared to machining tolerances. The author reported that this was only noticeable when isolated and was modelled as a Fourier function, but was later neglected in the final evaluation due to its negligible contribution to model accuracy. In the same study backlash was reported to produce errors of 0.055mm in joints 1 to 3 and 0.084mm in joints 4 to 6. Ma et al. [66] used a comprehensive, high-order polynomial to make predictions of joint gearbox transmission errors. The authors tested a range of orders (1st – 10th) and data size (150 – 350 measurements) and determined that a 6th order Chebychev polynomial with 250 measurements was optimal, but that it would be robot dependent. Investigation of gearbox transmission errors is therefore an arduous task, which requires a search for both an appropriate function and parameters.

2.2.2 Measurement

In this subsection, a wider view of research approaches and measurement strategies is taken, whilst the *identification* subsection will focus on the parameter estimation tools used. Calibration strategies can largely be separated into three approaches: *circle point analysis* (CPA), *relative pose* and *absolute pose* calibration. CPA involves isolating each parameter and measuring it indirectly. Relative pose calibration involves measuring the poses relative to each other or a common artefact. Absolute pose calibration involves measuring the pose of the end effector relative to a world co-ordinate system.

Circle point analysis, is a logical approach to identifying the geometry of a serial arm robot, from which the DH parameters can be obtained naturally. CPA takes measurements along an arc as the robot joints are rotated one at a time, with all other joints fixed and then identifies joint axes from fitted planes, circles and normal vectors. Conventionally identification of joint axis relationships follow the approaches of either Sklar or Stone in [40][67]. These are referred to as *screw-axis measurement*. This method identifies the geometry without the influence of non-geometric errors, plus it avoids iterative searching, convergence issues and local minima associated with parameter estimation techniques [68]. However, without fitting to positional error data (which includes all error factors), the accuracy of the model is often poor in comparison. Relatively few researchers [69][70] continue to use this approach. Recently Hayat et al. [71] used a monocular vision camera to take measurements and used computer-aided design (CAD) to determine DH parameters with this approach. The author also uses singular value decomposition (SVD) to determine the quality of the measurements and to select the data used to construct the geometry form in CAD. The parameters were similar to those determined using a laser tracker but with considerably worst results, exposing the sensitivity of this method.

Relative pose calibration avoids the transformation from world measurement system to base frame, which is notoriously difficult to obtain, making it a popular choice in industrial robot research literature [72][73][74][75][76]. However, relative error models are limited by ignoring non-linear effects [74]. Motivated by a low-cost and low skill, factory environment solution, Ha [77] used a laser height gauge and grid plate with 0.1mm spacing to minimise relative position error. The author measured the distance between actual and model positions, relative to the grid, in two configurations. The positional error was reduced to approximately 0.3mm in x, y, and z which is relatively high. He et al. [78] used the robot's IK model positional errors when aligning an end effector spike to a fixed spike artefact in different postures. Chen et al. [79] moved the end effector along a laser line and also used the robot IK model predictions to determine positional errors and calibrated joint offsets only. Joubiar and Bonev [80] used a high precision Renishaw touch probe as an end effector to measure the centres of three spherical artefacts with known distances apart. The error in the prediction of the distance between the spheres was reduced from a mean of 0.698mm to 0.086mm. Xie et al. [81] used a structured light source end effector to measure the radius and centre of a spherical artefact to calibrate kinematic parameters. As an alternative, Driels [82] demonstrated the use of a ball-bar to create a closed loop, whereby the end effector is set at a fixed distance from a location on the base but is allowed to rotate via the ball bar. The advantage of a closed loop approach is that no external pose measurements are required and measurements are fast, however the restricted poses mean that not all parameters can be identified.

In most of the relative pose calibration (RPC) research literature, the calibrated model accuracy is not validated in absolute positions throughout the workspace and cannot be fully compared to absolute pose calibration methods. While RPC is attractive as a low-cost and low skill solution, the results are subject to the tolerance of the artefact as well as accuracy of the metrology equipment, which is often less than the absolute pose calibration solutions. Also the calibration is highly localised in both workspace and joint-space which means that the model may not generalise well across the full workspace.

Wang [74] demonstrated that absolute pose calibration is more accurate than relative pose or relative position calibration. The relative calibrations were not able to identify all of the wrist parameters, which partially explains the results.

Absolute pose calibration (APC) is a well-established approach that measures the end effector pose relative to the world coordinate system (often the robot base frame), in a large workspace and typically requires more expensive equipment to retain accuracy for longer distances than for relative pose calibration. Much of the APC research is motivated by novel parameter estimation tools, which are discussed in the following subsection. Other APC research themes include *metrology*, *sampling strategies* and *measurement optimisation*.

When evaluating the pose errors in a large workspace or subspace, the results are more comparable to machine tools and are more general. If calibrated within a large workspace, or joint-space, it is easier to determine the capability of the robot for a range of different tasks. Typically, more expensive metrology equipment is required to attain a high level of accuracy within a large workspace.

2.2.2.1 Metrology

Nubiola and Bonev [83] used a single telescopic ball-bar with novel planar fixtures attached to the robot base and an end effector to calibrate a small articulated robot. Slamani et al. [84] argue that the telescopic ball-bar is more accurate than a laser tracker and less expensive but is limited to a small workspace. Validation of the calibrated model, by measuring the end effector position with a laser tracker in a robust 9905 configurations, showed an improvement in accuracy from 1.355mm to just 0.796mm. The authors evaluated the performance of three small robots, using a laser interferometer for position errors along a linear path, a laser tracker for contouring errors at speed, and a telescopic ballbar to measure dynamic errors such as overshoot. Nubiola et al. [85] compared the performance of an optical CMM (C-track camera-based tracking system) and laser tracker to measure and calibrate a small articulated robot. The laser tracker measured the position of three reflective targets on a planar artefact and the C-track measured multiple passive reflective stickers on the same artefact. The results were inconclusive due to contradictory results reported between tests in the lab and outside of the lab. Interestingly, the results demonstrated that the C-track did not perform better with a novel special artefact built to have a large number of reflective targets. Most of these required some form of novel device or fixture, which is outside of the scope of this thesis.

In practice, the selection of metrology technology is motivated either by cost or by accuracy and so the discussion will move on to measurement strategies.

2.2.2.2 Measurement sampling strategy

The identification of parameters, training configurations or poses are typically selected by the needs of the algorithm or capability of the metrology technology. The common approaches can be categorised as: (1) random sampling [45][51], [85][86] and (2) heuristic [87][88], [89][90]. These approaches were combined by Aoyagi et al. [91] by supplementing chosen observations with randomly generated and optimised observations. Interestingly, in the heuristic approach taken, the authors separated the workspace into a 3D Cartesian grid system. This ensured full coverage of the Cartesian workspace, but it is accepted that in any pose, the configuration, and therefore error is non-unique. Therefore, the ability to calibrate accurately with this approach is variable and most likely application driven.

Seminal work by Mooring et al. [40] addressed the issue of observation strategy, having recognised that not all observations yield the same results, and drew conclusions from a simulation study. The work was not extensive and did not cover a broad range of strategies but more recent works have confirmed some of the conclusions [87][92]. Recommendations of good practice are:

1. Simultaneous joint inputs (i.e. all joints rotate to a new configuration, and a wide joint angle range.
2. Random selection of observations outperformed heuristic joint displacements.
3. The calibration parameter estimations and model accuracy improves as the training configuration quantity increases, but with diminishing returns, and is less influential than the choice of observations.

2.2.2.3 Measurement optimisation

Alternative methods for generating observations appears to have been bypassed in favour of optimisation of the training observations. It is accepted that the number of measurements is less important than the selection of the joint configurations [93]. Minimising the condition number of the regressor matrix in a LLSE calibration approach, or maximising an *observability index* (OI) are options used by some researchers [51][92][87][91]. The OI is the root of the product of singular values from the SVD of the regressor matrix. The OI value represents the hyper-ellipsoid area created by the axes and is a maximum when the relative scales are similar and the hyper-ellipsoid approaches the optimal hyper-sphere where parameters are equally observable. These and other indices have been compared [67][94][95] and can be chosen depending on the desired goal (e.g. minimised parameter variance, minimised position uncertainty) although the most commonly used, for optimisation of observations, is the OI. Though the use of an observation metric as an optimisation strategy is questionable. The experimental data presented in literature [92][95] showed that a wide range of residual position errors (in $rms|\Delta p_{xyz}|$ terms) may be achieved at any observation metric value, but it is the upper limit of the error that decays exponentially with a more desirable metric value. It is entirely possible that an input with a highly desirable metric value will result in a worse accuracy than that achieved from an input with a less desirable metric score. Furthermore, it was shown that the upper bound is reduced by higher sample sizes but with diminished returns. The observation metrics can then only be used as a check for general observability, seeking large step changes indicating close to singularity and convergence issues. Contrary to other researchers, in 2019 Chen et al. [96] argued that previous OI's are typically based on SVD of the identification Jacobian which maximised parameter observability but may not in fact result in accurate estimations. The author proposed a self-adaptive particle swarm (SAPSO) method (similar to a Genetic Algorithm (GA) to find optimal observations by combining previous OIs with an identification indice) while including sensor visibility limitations.

Most researchers adopt a non-standard accuracy test, and as such it is difficult to make direct comparisons between robots, error sources and calibration methods. ISO 9283:1998 [97] describes standard tests for the performance of an industrial robot. The tests can be summarised as the combinations of *path* and *pose*, *accuracy* and *repeatability* (along with additional multi-direction, overshoot and stabilisation metrics). While repeatability is often reported by manufacturers, accuracy is not. Rarely in industry or research is the ISO accuracy test used to evaluate the performance of an industrial robot. The ISO pose accuracy test requires the accuracy of only five poses to be measured on a plane within a workspace cube. This was shown to be insufficient as a metric compared to a point cloud, tested robustly with 1000 validation poses within a large workspace [51].

2.2.3 Identification

The identification phase is the use of optimisation tools to estimate the model parameters that minimise the positional or pose errors in the training data. The specific parameter estimation method used by researchers is largely dependent on the formulation of the problem (i.e. how positional error relates to model parameters). The RPC approach and polynomial models, present a non-linear least squares estimate (NLLSE) problem, whilst the APC approach is presented as either a linear least-squares estimate (LLSE) or NLLSE problem. A range of NLLSE tools have been used, including Levenberg-Marquardt (LM) [88][96] and the maximum likelihood estimate (MLE)[47]. However, most of the NLLSE tools used to estimate the model parameters are undisclosed by the authors. LLSE calibration is a common solution [51][89][94] that must be solved iteratively, but can suffer from singularity issues without careful selection of training data. Kalman filters have been used as an alternative by some researchers [44][49][98][99].

Omodei et al. [100] compared LLSE, NLLSE and extended Kalman filter (EKF) for calibrating a SCARA robot and concluded that all methods converged to almost identical solutions. EKF was the fastest in computational terms. In 2018 Jiang [98] used an EKF as a first calibration prior to using a particle filter (PF) to complete the estimation of parameters. The author argued that EKF does not work well with significantly non-linear data that has non-Gaussian noise(which is common in real systems). The results showed an improvement over EKF alone. In 2016 Messay et al. [101] used a probing approach to parameter estimation first by using Simulated Annealing to determine the most fruitful starting estimates, then by Trust region (TR) optimisation. TR is a Levenberg-Marquardt (LM) based optimiser that takes larger steps in poor estimate regions. A cable-base 'Compu-gauge' measurement system (cables attached to a spool with a rotary encoder) was used which only had an accuracy of ±0.150mm and so results were not comparable to related works.

In summary, motivation to improve the accuracy of industrial robots for offline programming has been widely researched over recent decades. This has resulted in many research themes and an increase in the availability of mature metrology solutions and mathematical tools. Furthermore, a range of kinematic models have been proposed for mathematical simplicity or singularity avoidance. The calibration approach is motivated by error isolation, workspace generality, or the cost and convenience of metrology equipment. Absolute pose measurement in a large work subspace (with a laser tracker or camera) remains the most widely used, which provides a model that is calibrated and evaluated in a large input-space to determine its suitability for a range of tasks.

Numerous parameter estimation techniques have been used, primarily driven by the problem formulation (i.e. linear or non-linear) and best practice has only been established in terms of computation efficiency. Performance can be improved by optimising training data observations, but these may not account for sensor limitations. In this thesis, existing parameter estimation tools will be used, based on the problem formulation presented in chapter 3. Without a standard test, it is impossible to say with confidence that there is a limit to the positional accuracy that can be achieved by calibration of the robot kinematic model. However, a hypothesis can be formed that there is an industrial robot calibration accuracy floor of approximately 0.3mm, in rms Euclidean error terms (point to point distance error). The results in this thesis may contribute to proving or disproving the hypothesis. The error floor still remains prohibitively large for many machining tasks. The calibrated robot model accuracy is typically at least an order of magnitude worse than the repeatability (positional errors are high due to model inaccuracies compared to repeatability), and therefore there is potential (beyond calibration) to achieve higher levels of accuracy i.e. smaller positional errors. Bias correction methods that do not rely on parametric models, offer a possible solution.

2.3 A machine learning (ML) approach to bias correction in robots

In this section, a critical review of ML tools used to improve the positional accuracy of industrial robots is presented. The section is separated into general interpolation methods; artificial neural network (ANN), which is the most common tool used for this application; and Gaussian Process Regression (GPR), which is novel to this application.

With or without calibration, a robot will retain some residual positional error within the workspace. Alici et al. [102] used Fourier and ordinary polynomials to model the residual positional error. They argue that it is virtually impossible to consider all error factors and that developing higher fidelity parametric models is fruitless. ML-based bias correction is an intuitive approach, that allows the data to speak more clearly. The problem can be considered to be one of bias correction (where the aim is to learn the positional error as bias, and then correct the position), typically by providing the controller with false pose targets.

2.3.0.1 Interpolation

In a typical interpolation approach in this application, the Cartesian workspace is separated into subspaces (e.g. 2D grid or 3D cube) and the vertices are used to provide reference bias data for any position within the cube. This is generally achieved offline via a look-up table. The interpolation algorithm creates a bias surface within the space to determine the bias value at any location within the space, so compensation can be applied. Interpolation such as this assumes that the positional error is an attribute of the position, which is usually not the case. Positional error is a function of joint variables and a single position can be obtained in multiple joint configurations (i.e. the bias is a continuous function of joint angles and not position). Consequently, similar positions may have dissimilar joint configurations and therefore dissimilar errors, which is challenging to model. This is typified by the 'elbow up-elbow down' conundrum (the same end effector pose can be achieved by a joint configuration where the elbow is pointing up or down, which is an inverse kinematic model decision to make).

Bai and Menq [103] compared *bilinear*, *cubic spline* and *dynamic fuzzy interpolation* methods on a 2D grid and demonstrated that the dynamic fuzzy interpolation outperformed the others, however, none were accurate enough for machining tasks. Bai [104] also demonstrated that the same dynamic fuzzy interpolation can marginally outperform calibrated models in the 3D case but cube sizes needed to be 10mm×10mm×10mm or smaller which requires extensive training and may be too time-consuming for workshop applications. Zeng et al. [105] constrained the 'elbow' decision in the robot programme and minimised the wrist rotations in order to assume that positional error is an attribute of position and that errors in nearby positions have spatial similarity (i.e. joint angles change very little for small changes in pose). The authors used a *semivariogram* curve to quantify similarity of nearby positions and *Kriging* to interpolate and predict errors. Wei et al. [106] exploited the same spatial similarity and predicted the positional error with a simple *inverse distance weighting* algorithm on a rail mounted drilling robot and improved the accuracy by an order of magnitude. Interpolation methods are not accurate enough for many machining tasks and require large data sets or online measurement and updating.

2.3.0.2 Neural Networks

The most common ML approach to bias correction of robot positional errors has been the use of an ANN [44][90][91][107][108][109]. Aoyagi et al. [91] used a NLLSE calibration and then ANN bias correction to reduce the positional error of a 7-DOF (i.e. 7 joints) industrial robot. The primary objective was to demonstrate the use of a Genetic Algorithm (GA) to minimise the number of calibration poses. However (after calibration of the geometric parameters) the author compared the additional calibration of gearbox errors with a periodic function and bias correction using an ANN. The additional non-geometric model showed only marginal improvement, suggesting a complex and time consuming task to model errors parametrically (now requiring 68 parameters to be estimated) whilst the ANN approximately halved the positional error. The results indicate that the use of ML tools is a more general tool, and a more efficient and more effective solution. The author used an unusual approach of training using 100 targets from a grid and then validating with 100 targets on a circular path. The joint angle inputs were determined from the grid targets using an imperfect, inverse kinematic model, which raises concerns about the accuracy of the input data to the ANN.

Nguyen et al. [44] used a novel combination of geometric model calibration using an EKF, followed by an artificial neural network (ANN) bias correction to reduce the positional error of a 6-DOF articulated industrial robot. 300 poses over the full joint range were measured with a laser tracker and separated into 200 training and 100 validation data sets. The results showed a reduction in mean positional error (standard deviation in brackets) from 4.1mm (6.3) for the nominal model, to 0.81mm (3.18) by EKF calibration, and to 0.33mm (0.84) with bias correction, which is the lowest positional error reported in research literature to date. 200 training data points in a large space is sparse and the use of more data or just NN alone was not explored, but the potential of bias reduction compared to calibration was demonstrated.

Tao and Yang [86] also demonstrated the improvement in accuracy of an industrial robot by calibrating a POE geometric model using LLSE and then using ANN bias correction to reduce the residual positional error further. The authors used 300 pose measurements (separated into 150 measurements for training and 150 for validation subsets) with a laser tracker. The results showed a reduction in mean positional error from approximately 1mm (with just base and tool calibration) to 0.50mm with geometric model calibration and to 0.36mm with bias correction. The mean positional error alone is not sufficient information to evaluate the robot for machining applications but does confirm that bias correction, using an ANN, will substantially reduce the positional error of a robot compared to calibration.

Yuan et al. [108] modelled positional error as a function of position, using an extreme learning machine (ELM) to correct the positional errors in an aviation drilling task. The author stated that ELM offers improved generalisation and simplified training compared to an ANN and demonstrated improved accuracy and speed over the approach used by Nguyen. The author was the first to explore the limitations of ML, demonstrating experimentally that the mean error was stable with 300 training data values and above, whilst the maximum error stabilised after 1000 training data values. However, the input range was not disclosed and some joints had very little movement for planar drilling applications.

The use of an ANN for bias correction was the first approach that demonstrated a significant reduction in position error over the calibrated robot. ANNs, however, typically require large training data sets so this has only been partially explored in research literature.

2.3.0.3 Gaussian Process Regression

GPR is a probabilistic ML tool that is highly flexible and works with much smaller training data sets compared to ANNs. Furthermore, the output includes an estimate of prediction uncertainty. GPR has been more commonly used to model industrial robot dynamics rather than kinematics, with very few examples of the latter. Dynamic system modelling using GPR is discussed briefly in this subsection. The main focus is the use of GPR to model industrial and medical robot kinematics and related works.

The *inverse dynamic* model of an industrial robot has been used extensively as a testbed for sparse GPR approximation methods that are designed to address the issue of modelling non-linear systems with high dimensional data and/or large data sets. Typically the joint torques are modelled as a function on joint angles, velocities and accelerations $(q, \dot{q}, \ddot{q})$. So a 6-DOF robot dynamic model has a minimum of 18 input dimensions. Kocijan et al. [110] present an early discussion on GPR used for dynamical system modelling. The author promotes the use of GPR for its flexibility, automatic relevance detection (weighting of inputs provides an indication of sensitivity) plus the use of the variance output to identify low accuracy regions. A summary of industrial robot dynamic response modelling (using GPR) is presented by Duy and Peters [111] who also demonstrated the use of a novel local-GPR method to reduce computational load enough to enable the real-time dynamical system modelling and correction of a SARCOS robot. Chalupka et al. [112] presents a comparison of GPR approximation methods and proposes a set of comparison metrics. The testbed used was inverse dynamic data from a SARCOS robot, which is also used by Rasmussen and Williams [113].

Wang [114], Seeger et al. [115], Snelson and Ghahramani [116] proposed GPR approximation methods and evaluated them on two known artificial datasets; the *pumadyn-32nm* inverse dynamic data set, and the *kin-40K* 8-DOF kinematic data set. The data provides 40,000 positional error measurements associated with inputs of joint angles. In all studies, the results demonstrate some success in modelling the data with GPR.

Bias correction of robot positional error, using GPR bias correction, has been recently applied by a few researchers. Mahler et al. [117] used GPR to improve the accuracy of a Raven II robotics surgical assistant (RSA). The Raven II is a 7-DOF, cable driven robot with a small workspace. The non-linear effects of cable stretch and spring counter-weights were modelled, which are not present in industrial robots. A novel approach of data localisation using SVD was used to reduce the bias level (and minimise the burden on the GPR), which modelled the pose error from an input of joint angles and velocity. Starting from a very high nominal model error of 25.5mm, the results demonstrated a reduction from 10.1mm using SVD alone, to 4.4mm using SVD calibration and then GPR bias correction and to 2.4mm using velocity in addition to joint angles as an input. No comparison was made against applying GPR alone to determine the importance of the initial localisation. In addition, the results show that the path accuracy improves by a factor of 10 by having a more accurate start and finish position.

Likewise, Pastor et al. [118] used data localisation and then GPR bias correction to improve the positional accuracy of a vision based DARPA ARM-S robot, which has two cable driven 4-DOF arms for gripping and assembly tasks. Like the previous Raven II case, the modelling was highly task-based and modelled from an input of joint angles only. The results demonstrated a reduction in pose error by a factor of two by localisation alone and then a further factor of three by using GPR. No comparison was made to bias correction alone, and the effect of a simple localisation to reduce the burden on the GPR has not been fully explored.

Fan Zhang et al. [119] also used GPR to model a RSA for the purpose of optimising surgical metrics as part of pre-op planning. The simulation testbed was a robot with three arms, each with 6-DOF, attached to a central prismatic joint. GPR was used to model the dexterity of the robot, quantified by the Global Isotropy Index (GII) and surgical capability, quantified by a Cooperation Capability Index (CCI) in order to select optimal configurations based on a balance of robotics and surgical best practice. GII and CCI were modelled from an input of Cartesian positional data, which is usually unwise practice.

The work of Tao et al. was extended during the writing of this thesis by Jing et al. [45]. The authors used GPR after calibration of the POE model of an industrial robot. Using a quadratic kernel for the GPR covariance function, the results showed a reduction in positional error from 0.8mm, with just calibration to 0.4mm with additional GPR bias correction. However, the workspace size was unclear and the results were measured from the cross-validation of 300 training data values and not separate validation set. Nonetheless, this further demonstrated the superiority of bias correction and GPR as an effective alternative to ANN. The experiments were also repeated with five different payloads which confirmed the requirement of payload as a training input.

In summary, ML-based bias correction has been shown to reduce positional error by a (numerically) small, but significant amount (in machining practice) and are typically applied as a post-calibration process. ANNs have been the most common ML tool used in research literature for this application, but the limitations of achievable accuracy have not been fully explored. GPR is relatively novel to this application. However, in a few related works, it has been shown to demonstrate the potential to reduce positional error.

It is difficult to compare the results and conclusions of the related research presented in literature due to the many differences in approach. Some of these include: input choice (e.g. joint angle, position and velocity), robot kinematic structure, data quantity, calibration model, and evaluation metric (e.g. rms, mean, standard deviation of positional errors).

We can say in general that a typical approach would be:

- ⇒ Geometric model calibration using absolute pose data, using a laser tracker.
- ⇒ Bias correction of positional errors, modelled using joint angles as input variables.
- ⇒ Trained with 100 to 300 data values and validated with a similar quantity of test values.

2.4 Chapter summary

In this chapter, a review of literature in the field of industrial robotics was conducted to provide the reader with an overview of the error sources in industrial robots, and complexity of the problem. A critical review of robot calibration methods provides a broad view of existing tools and approaches, and a critical review of current progress made using ML tools as bias correction for positional errors. The following conclusions are drawn from the literature in this chapter:

1. Industrial robot positional errors are highly non-linear and challenging to model. Error sources are categorised as geometric and non-geometric and the ranking

of their contribution to positional error is unique to each robot, which makes it challenging to focus research efforts.

2. Calibration of geometric parameter errors is the most common calibration level in research literature and industry, with joint compliance modelling included as an additional calibration level.
3. Robot calibration is a mature subject with a range of established tools, both mathematical and experimental. There is no consensus on best practice. The choice of model, measurement and identification is largely dependent on the problem formation (e.g. absolute pose and linear model), and should follow good practice guidance.
4. The positional accuracy of robots (using existing calibration methods) have reached an approximate floor of 0.3mm (mainly due to unmodelled, non-geometric errors) and this prohibits their use for many machining tasks (e.g. the ±0.2mm tolerance often required for aerospace drilling).
5. Bias correction, using ML tools, can reduce robot positional errors to below the level achieved by calibration alone. However, the use of ML tools for this application has not been fully explored and there remains potential to improve robot positional accuracy further.

2.4.1 Gap analysis

We can consider that further research into industrial robot calibration may provide only marginal gains in positional accuracy, and that bias correction has greater potential but has not been fully explored. The following gaps in the use of ML tools for bias correction in this application have been identified as:

- The limit of robot positional accuracy by using bias correction, with regards to training data quantities has not been explored and a question remains concerning the achievable accuracy within pragmatic measurement quantities.
- The contribution made by calibrating the kinematic model prior to bias correction has not been explored in research literature. A question remains as to whether bias reduction by calibration is necessary or whether a high level of calibration should be conducted to maximise bias correction accuracy.
- GPR is a relatively novel ML tool for this application but has demonstrated potential in a few studies in research literature. Demonstrating its use on more

case studies in this application would contribute to a relatively small body of knowledge.

Existing tools and approaches have been identified from research literature, along with gaps that will contribute to understanding the limitations of industrial robot accuracy by using bias correction. In Chapter 3, the research methodology is presented which provides details of how the gaps will be explored.

Chapter 3

Methodology

The aim of this chapter is to present a description of the case studies used in the experimental chapters, the experimental design used for gathering data, and the theory relating to the calibration and bias correction tools used.

In Chapter 2 it was stated that there has been some recent success in related robot accuracy works by first calibrating the robot kinematic model, and then using ML-based bias correction to learn and compensate for the remaining positional errors. The proposed methodology used in this thesis uses the same approach to solving the problem, with GPR used as a novel bias correction tool.

A review of literature in Chapter 2 showed that there are gaps in this field of research, specifically (i) the novelty of GPR as a bias correction solution in this application, (ii) the limitations of bias correction in this application relating to training data quantity and (iii) the limitations of bias correction in this application by calibrating the kinematic model to reduce the burden to the proceeding bias correction. In this chapter, a range of case studies are described to explore the second of the gaps, and a range of calibration levels are presented to explore the third.

3.1 Approach

An absolute pose (measurement relative to a world reference frame) approach is taken in the experiments in this thesis, in part due to access to industry state-of-the-art external measurement equipment. Namely a Leica laser tracker provided by the sponsor. This is the preferred option in research where cost and availability is not a consideration.

The limitations of the proposed methodology relating to training data quantity and bias reduction are tested simultaneously in different short case studies and with bias data from competing calibration models. The details of both are presented in the following subsections.

3.1.1 Case studies

In both the simulation study in Chapter 5 and experimental study in Chapter 6, the proposed methodology will be evaluated on case studies in sequence of problem difficulty. It is a expected that the bias form (positional error data in an n dimensional space) produced by rotating one joint will be relatively simple to model and will have only one input dimension. In comparison, the coupling of errors in the serial chain when all six joints are rotated may result in a more challenging bias form to model and higher input dimensions may result in many solutions. The case studies used to build up the complexity of the problems are described in Table 3.1.

Also, in order to compare results to both general robot calibration literature and remain machining focussed, the performance will also be evaluated in a small workspace, representing a milling station, and a more general, large workspace, for comparison to related works. These case studies are referred to as 6 dim(s) and 6 dim(l) respectively.

All tests will be conducted with the robot moving in free-space and stopping at each pose.

Table 3.1: Experimental case studies.

Case study	Nomenclature	Input joint variables	Workspace description
1	1 dim	3	Vertical plane
2	3 dim	1,2,3	Semi-cylindrical
3	6 dim (s)	1,2,3,4,5,6	semi-spherical
4	6 dim (l)	1,2,3,4,5,6	semi-spherical

3.1.2 Competing models

To test the performance of bias correction on a range of bias levels, four kinematic models will be used to generate TCP predictions. Bias level is a relative term which refers to the both the value of the bias data and the complexity. For example, the positional error data, used as bias, generated by the nominal (uncalibrated) kinematic model will be higher than generated by a calibrated model, and the bias form will be more complex as none of the error sources will have been modelled.

The competing models represent different levels of calibration. Calibration level refers to the number of parameters that are estimated in the model, which are presented the subsets: base frame parameters, geometric parameter errors, joint compliance parameters. The four competing models, M_0 to M_3 , are presented as calibration levels in Table 5.2 and the tick marks indicate which parameter subsets are calibrated in each model.

Table 3.2: Competing models.

Model	Base	Geometric parameter errors	Joint compliance
M_0			
M_1	✓		
M_2	✓	✓	
M_3	✓	✓	✓

The parameters in physical terms are described section 3.3.2 after the robot kinematics and joint compliance models are explained.

3.2 Experimental setup

3.2.1 ABB IRB6640 Industrial robot cell

The testbed used for all experiments, including in simulation studies, was an ABB IRB 6640-205/2.75 (205kg maximum payload, 2.75m reach) shown in Figure 3.1a. The ABB IRB 6640 is a conventional articulated robot with six independent rotational joints, providing six degrees-of-freedom (6-DOF), which is typical of the robots tested in related works. Robots of this type have high dexterity i.e. able to approach the pose from multiple angles and manipulate the TCP around three axes, a long reach and can carry large payloads, making them suitable for machining applications.

The test robot has a machining spindle mounted to a fixture as an end effector (Figure 3.1b). While the spindle was not used for machining, and is unnecessary for positional measurements, it remained as an end effector to provide a realistic static payload for machining tasks. The payload and centre of gravity specifications are be presented in the experimental chapters.

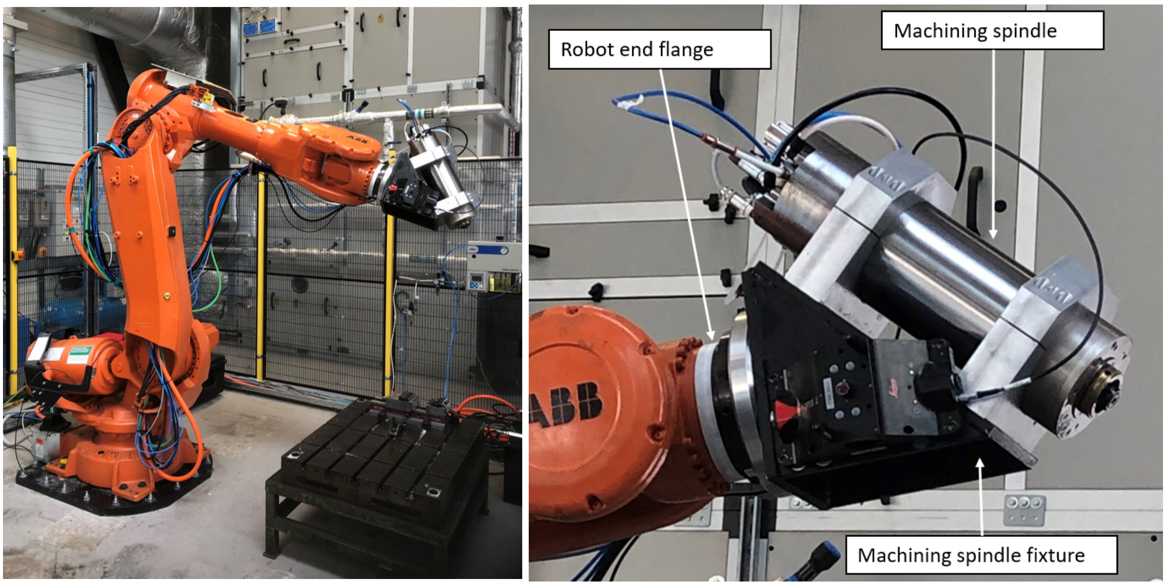

(a) (b)

Figure 3.1: (a) ABB IRB6640 robot, (b) Machining spindle and fixture static payload

A single static payload was used for the bias correction experiments which may be considered as a limitation in this study. However, the machining spindle is a system that requires cabling throughout the robot structure and integration with the robot controller, and therefore would remain as a permanent fixture in a production cell. It is assumed that tool changes provide negligible variations in payload.

3.2.2 Robot schematic

Most industrial robot structures consist of a chain of joints and links. Diagrams of the robot, with individual joints highlighted, are shown in Figure 3.2. The joint identification starts at the base, then joint 1 and works through the serial chain to the end effector flange (joint 6). Joint 1 has vertical axis and rotates the from side to side. Joints 2, 3 and 5 have axes that are perpendicular to the links and sweep the TCP through a plane whilst joints 4 and 6 are parallel to the links and can be considered as producing a twisting motion.

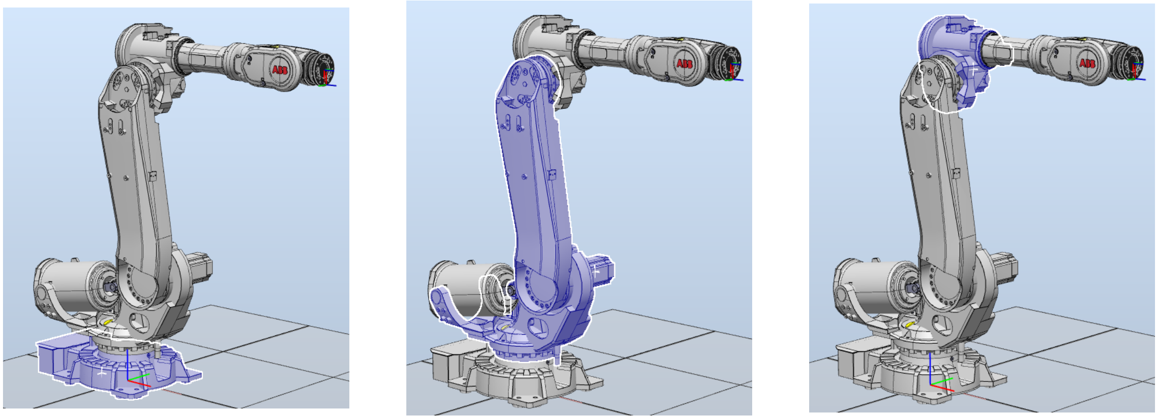

(a) Joint 1 (b) Joint 2 (c) Joint 3

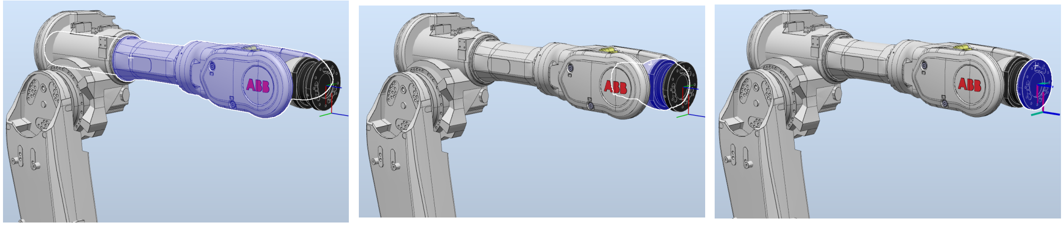

(d) Joint 4 (e) Joint 5 (f) Joint 6

Figure 3.2: Structural elements of an ABB IRB 6640 articulated robot.

3.2.3 Measurement

3.2.3.1 Pose definition

The pose of the TCP is the vector $p = [p_x, p_y, p_z, \phi_\alpha, \phi_\beta, \phi_\gamma]$, relative to a defined coordinate system e.g. the base frame. Pose is the combination of the position vector, $[p_x, p_y, p_z]$ and orientation vector $[\phi_\alpha, \phi_\beta, \phi_\gamma]$ which are a representation of the rotation matrix transformation in Euler angles in the order of ZYX or roll-pitch-yaw.

3.2.3.2 Leica laser tracker

A Leica AT-960 laser tracker, provided by the sponsoring company, was used to measure the absolute position of reflective targets secured either on the robot or around the cell. The AT-960 is an industry state-of-the-art system designed to operate in an industrial environment. A panel of the cell was removed for visibility and the laser tracker located just outside of the cell for safety. A laser tracker uses a line-of-sight distance measurement between the laser source (laser tracker) and target (reflective mirror), along with azimuth and elevation encoder readings to provide the laser direction, which are then used to determine the relative position of the target in polar and then Cartesian coordinates. The Leica laser tracker uses a combination of laser interferometer measurement (IFM) and absolute distance measurement (ADM) to measure distance. In principle, a laser interferometer splits the laser into two at source, one of which is reflected back internally, and the second is reflected back from the target. The two lasers are superimposed and the wave fringes created are counted as the target moves further from the source, and an accurate relative distance is measured. The ADM uses the time to travel from the source to the target and back to determine the distance. In addition to the position measurement, the Leica laser tracker uses a camera to identify LEDs mounted onto the T-Mac (described in 3.2.3.3), which also has a central reflector, to determine the relative orientation of the target. The data available from the Leica laser tracker is the target pose (relative position and orientation) if the T-mac is used.

The laser tracker was directly connected to a laptop with Spatial Analyzer (SA) software for recording and processing, also provided with training by the sponsor. SA is a portable metrology software solution that acts as an interface for data capture from metrology equipment, such as a laser tracker, and is a graphical interface to generate geometry from coordinate data, which can be compared to CAD model geometry. In the studies presented in this thesis, primarily, SA is used collate the measured data and export it in a format for comparison to model predictions.

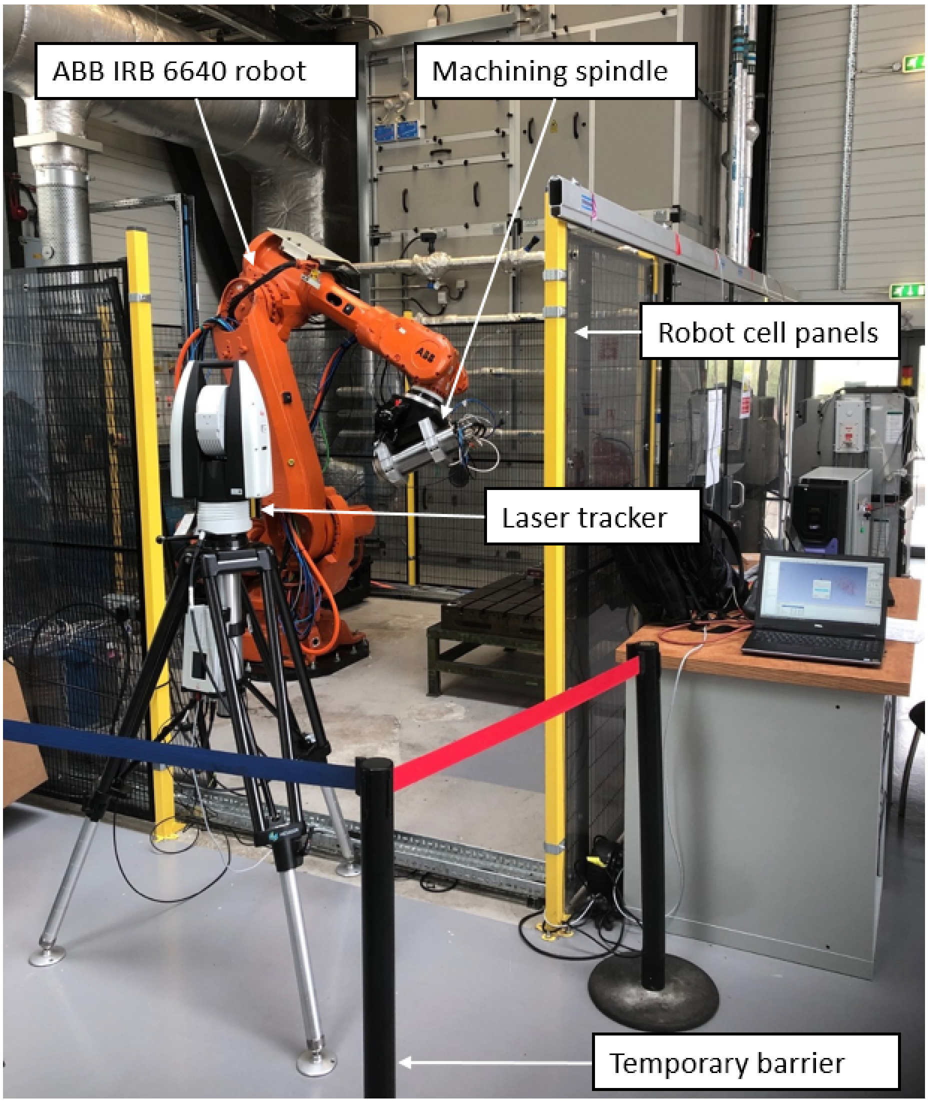

Figure 3.3: ABB IRB 6640 robot machining cell with panel removed for line of sight between Leica AT-960 Laser tracker and reflectors.

3.2.3.3 Reflective targets

The laser tracker measures the distance to the centre of a reflective target which the laser tracker is able to lock onto and track to new locations. A 1.5” SMR (spherically mounted retro-reflector - Figure 3.4a), which provides the laser tracker with a vertex of three mirrors, sits in a magnetic nest mounted at fixed locations around the cell. A T-Mac target (Figure 3.4b) provides a 0.5” central reflector for position measurement and LED’s to provide orientation measurement. The T-Mac was mounted to the spindle fixture and was defined as the TCP. It was possible to locate an actual milling tool TCP relative to the T-Mac, which would be necessary for machining trials, but was deemed unnecessary for free-space movement. The T-Mac is an expensive option, available only with Leica laser trackers and has not been used by in most other related works. Calibration can be completed with positional data only from a single SMR, referred to as *partial pose* measurement, however the T-Mac provides an additional 3 equations for LLSE calibration by providing orientation measurements. For machining tasks, it can be argued that orientation of the tool is equally as important as position when meeting tolerance demands and the T-Mac allows orientation to be quantified.

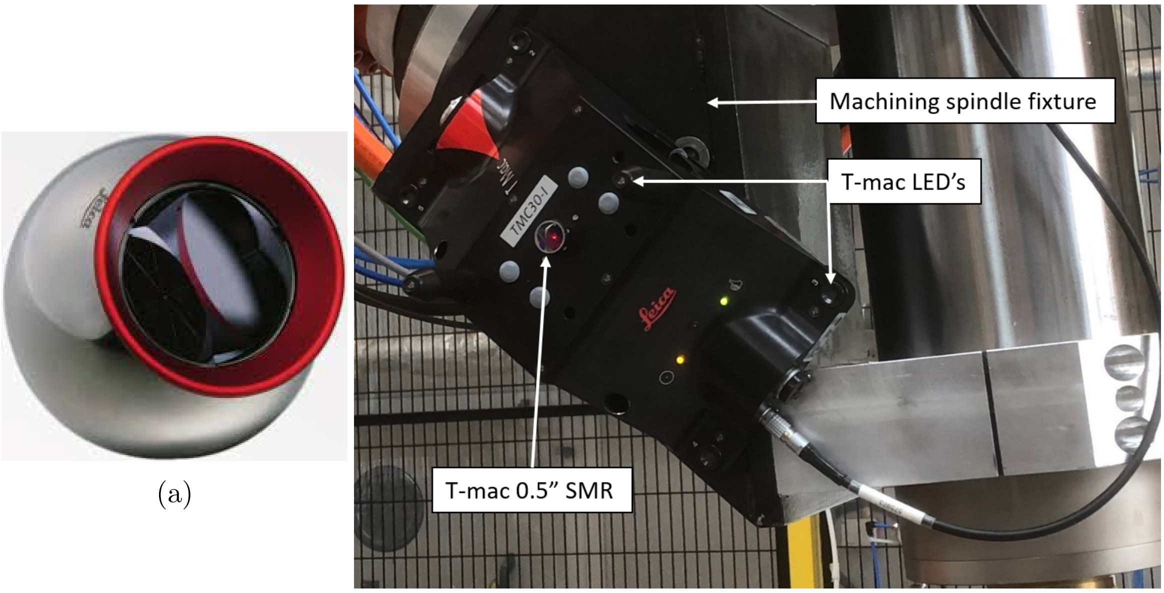

(a)

(b)

Figure 3.4: Laser tracker reflective targets: (a) example of a 1.5" SMR and (b) T-Mac.

The disadvantage of using a laser tracker over other forms of metrology is that line-of-sight must be maintained which limits the number of poses that can be measured.

3.2.3.4 Measurement uncertainty

Variability in laser tracker measurements are the result of laser tracker resolution, reflector tolerances and environmental factors e.g. air movement and direct sunlight. The manufacturer quotes a maximum permissible error (MPE) of 39μm ($\sigma_n = 13\mu$m) at distances within the cell. MPE refers to the maximum expected uncertainty in an industrial environment which is approximated to 3σ.

Volumetric accuracy is commonly used to evaluate and compare the accuracy of metrology equipment in a large volume. The procedure recommended by the sponsor to determine volumetric accuracy of the laser tracker was to complete a *USM* test which involves measuring the location of SMRs at locations throughout a volume and from multiple locations within and outside of the volume. The volumetric accuracy from the USM test in a similar volume next to the cell was calculated as $\sigma_n = 10\mu$m. There was a temptation to provide the calculated σ_n as a known GPR hyperparameter, instead σ_n was included as a parameter to be learned. This is consistent with standard practice in training GPR using noisy data.

3.2.4 World-to-base coordinates and localisation

Robot kinematic models determine the pose of the end effector relative to a base frame. The base frame is an arbitrary frame that cannot be located directly which is a common challenge in research. Some robots are supplied with a base plate that has specific features that can be used to locate the origin but this is an additional part and was not available on this robot. Common practice in related work, is to use the *circle point analysis* (CPA) approach which constructs the base frame from the axes of joints 1 and 2 and locate them on a common base plane (Figure 3.5).

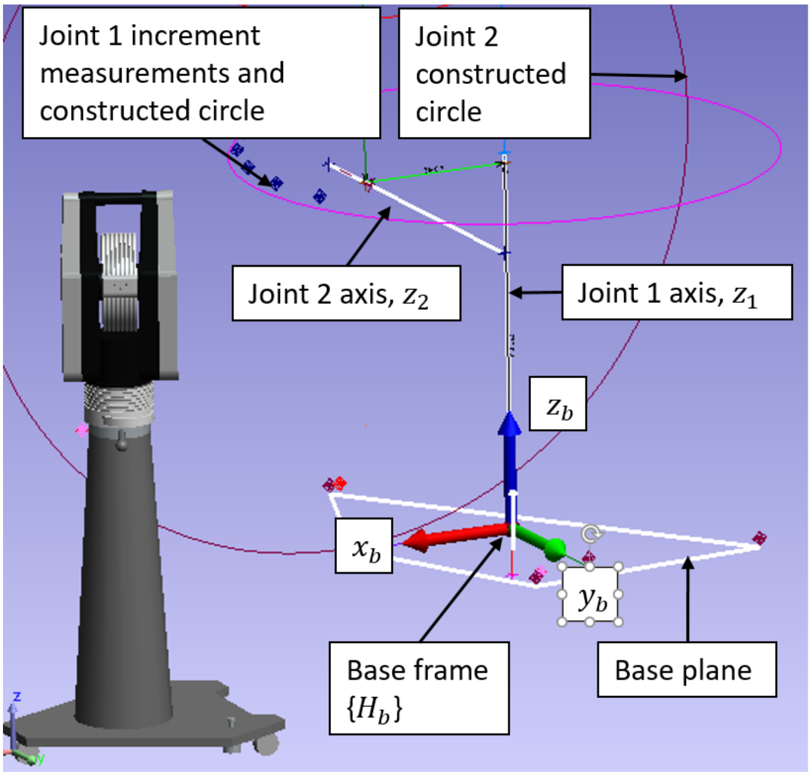

Figure 3.5: Base coordinate system constructed in SA from constructed geometry (highlighted in white).

As all measurements are made relative to the laser tracker world reference coordinates, any movement of the laser tracker location will result in corrupted data. To ensure that the experiment could continue after movement of the laser tracker, a simple transformation from the new world reference frame to the initial base frame was determined, and applied as a data localisation procedure. The transformation was determined by comparing the position data of five SMR sensors at fixed location in the cell, commonly referred to as an ERS system, which were measured when the base frame was created, and then at the new laser tracker location Along with localisation, the ERSs were used to detect sensor drift in between tests. By comparing the measurements after a test to the first set, SA reported an rms positional error value. For rms values above 20μm, the laser tracker was localised for the next test. For values above 100μm, the laser tracker was also localised and the test repeated.

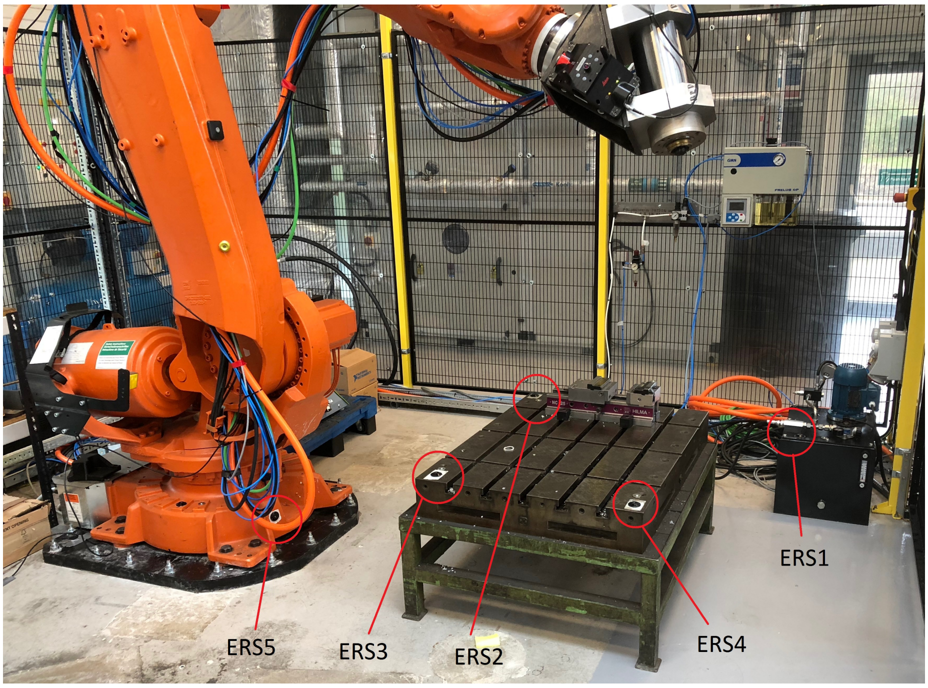

Figure 3.6: ERS sensor locations.

3.2.4.1 Tool identification

The position and orientation of the TCP i.e. T-Mac, relative to the end effector frame was determined using the CPA method. Some researchers include the tool parameters as calibration parameters but it was decided in this thesis to reduce the number of calibration parameters.

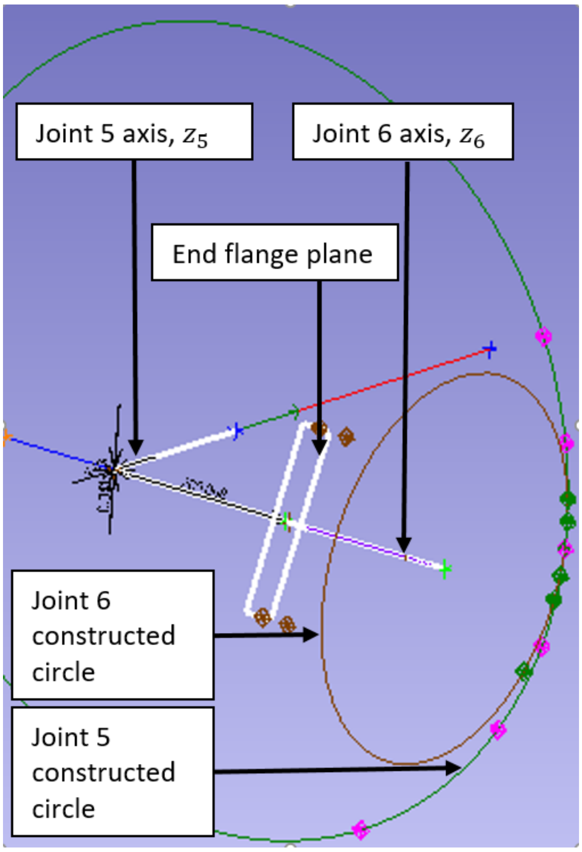

Figure 3.7: T-Mac reported relative to the robot end effector flange, identified using constructed geometry which are highlighted in white.

3.2.4.2 Automatic measurement and vibration suppression

For efficiency and repeatability, the robot was programmed to move to each target using the ‘MoveAbsJ’ command (robot moves to a target input described by joint angles instead of TCP pose), to avoid robot kinematic singularity problems which may occur with linear motion commands (linear interpolation between targets described by TCP poses may result in a mathematical singularity due to multiple solutions, when using the inverse kinematic model to determine required joint angles). The robot was instructed to wait while the laser tracker measured the end effector pose.

It was reported in literature that some robots suffer from significant errors due to gearbox backlash. The rotation of each joint is difficult to predict and gears may change direction suddenly during a seemingly simple, continuous movement. To avoid backlash errors, each joint vector q_i was approached from a nearby vector $q_i + 5^0$. This is commonly referred to as a ‘bump’.

It was noticed during the trial that the robot stopped abruptly at each target and visible transient vibrations occurred. As a counter-measure, the robot was programmed to approach quickly to the nearby 'bump' target and then proceed slowly to q_i. A 'WaitTime' operation of 5 seconds at each target was introduced and SA was programmed to measure the pose when the sensor was *stable*. A stability threshold of 25μm was set as a notification limit which was not reached.

3.3 Calibration

The process of calibration aims to minimise the difference Δp between the model pose p_m and measured, 'desired' pose p_d of the robot. Figure 3.8 shows the process of determining the positional error from the forward kinematic model $M(.)$ and true robot, represented by the system kinematic model $\zeta(q)$ and measurement variation ϵ. In this section, the theory relating to the modelling, measurement and identification of the model parameters θ is presented.

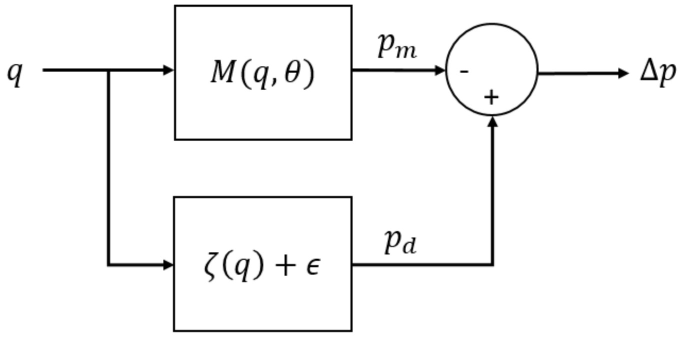

Figure 3.8: Modelling and measurement flowchart.

3.3.1 Modelling

3.3.1.1 Denavit-Hartenberg (DH) kinematic model

The kinematic model determines the pose p from an input of joint angles $q = [q_1, \ldots, q_n]$ for a robot with n joints. Numerous robot kinematic model solutions have been presented in research, largely focussed on removing the singularity problem during parameter estimation associated with consecutive parallel axes. However, to remain industry focussed, the mDH version of the industry adopted DH model will be used in this thesis. The DH model is constructed by attaching a coordinate frame to each joint/link pair (Figure 3.9).

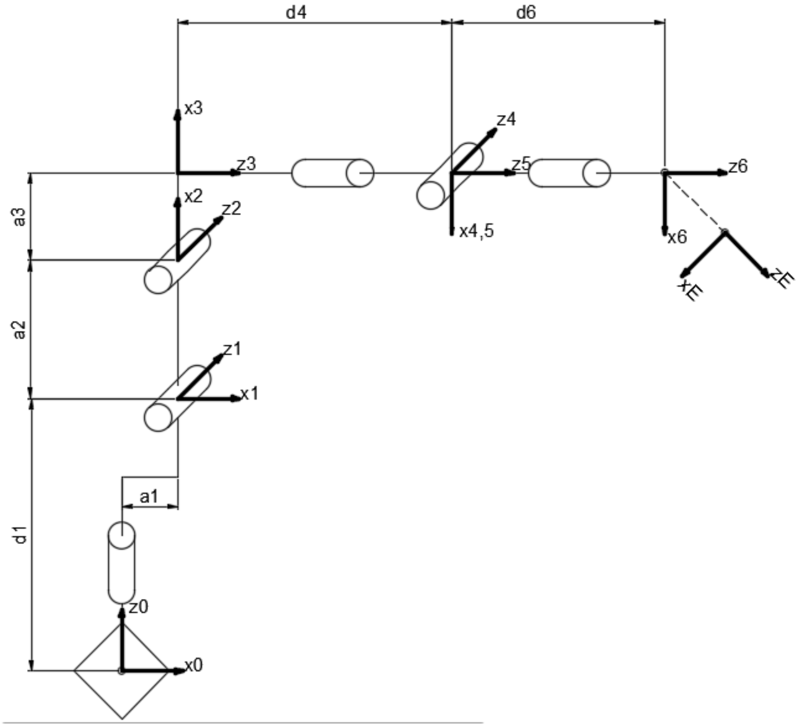

Figure 3.9: DH frame location on a 6-DOF articulated robot.

The transformation between consecutive frames $i-1$ to i is described by a homogeneous transformation matrix (HTM), H_{i-1}^{i}. The pose p can then be extracted from the 3x3 rotation submatrix R and 3x1 translation vector T

$$H_{i-1}^{i} = \begin{bmatrix} \begin{bmatrix} & R & \end{bmatrix} & \begin{bmatrix} T \end{bmatrix} \\ 0 \quad 0 \quad 0 & 1 \end{bmatrix} \tag{3.1}$$

The transformation from robot base, or world reference, to end effector (tool) is determined by multiplying successive HTM's. For an ABB IRB 6640 robot the transformation is

$$H_b^t = H_b^0 H_0^1 H_1^2 H_2^3 H_3^4 H_4^5 H_5^6 H_6^t \tag{3.2}$$

The DH convention is a convenient simplification of the transformation between frames, which is fully described by six parameters, by reducing this to four (rotation and translation in x and z axes only). With joints only able to rotate around a single axis, it is possible to fully describe any link to link transformation in this way, and has the advantage of reducing the number of model parameters. The procedure for describing the transformation parameters at joint i, which intersects links $i-1$ and i is as follows:

- first a common normal is established between any consecutive axes $i-1, i$. The common normal is often the link arm.
- translate along the joint axis z_{i-1} by the joint offset parameter d_i to the intersection with the common normal
- rotate the current reference frame by q_i around the current axis z_{i-1} to align the x axis with the common normal
- translate along the common normal (x_i) by a_i
- rotate around x_i by α_i to align z_{i-1} to the new joint axis z_i

For a visual reference, the two conventions are compared in Figure 3.10. The DH convention can be seen as translations in d and a, whilst the mDH absorbs the transformation d_i into $di + 1$, rotates through the misalignment α_i, creating a plane for link a_i to sweep through.

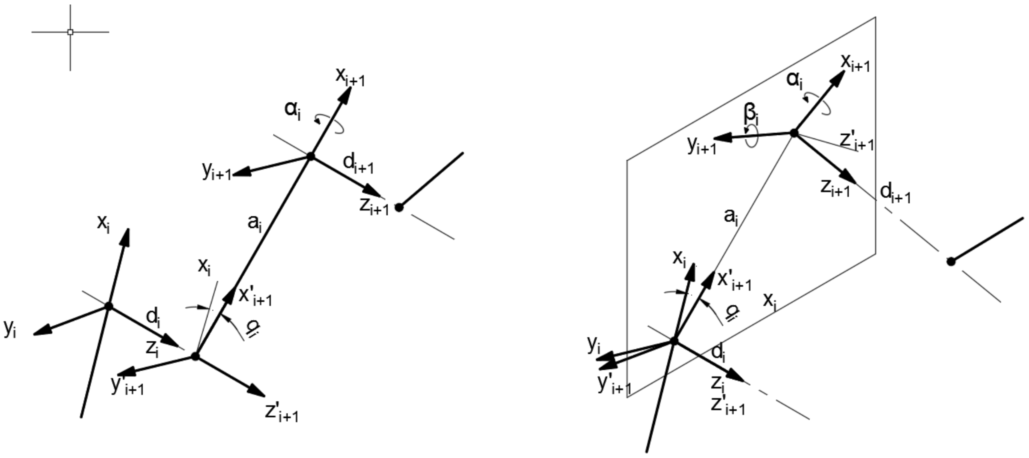

Figure 3.10: Consecutive parallel joint axes diagram with DH (left) and mDH (right) transformations.

More succinctly, the DH convention follows the following successive translations and rotations: In both models, for links 1 and 3, the standard DH sequence of transformations is used:

$$H_{i-1}^{i} = T_{z_{i-1}}(d_i) R_{z_{i-1}}(q_i) T_{x_i}(a_i) R_{x_i}(\alpha_i) \tag{3.3}$$

These parameters, which represent the geometry of the robot, are defined in a *DH table* used as a reference for the model. Stock robots are provided with nominal DH table parameters and it is the inaccuracies in these values that gives rise to *geometric errors.*

Table 3.3: Example mDH table.

Link i	q_i	d_i	a_i	α_i	β_i
1	q_1	d_1	a_1	α_1	β_1
n	q_n	d_n	a_n	α_n	β_n

While this reduced form is quicker to process and easier to calibrate, it also may result in a second geometric error. Where the axes are misaligned, a y axis rotation parameter does not exist to describe it and pose accuracies are incurred.

When consecutive joint axes are parallel, a problem occurs during calibration. The joint offset parameters d_{i-1} and d_i in this case, are both in the same direction and the common normal is non-unique. If the axes are misaligned by a small amount $R_{y_i}(\beta_i)$ then any parameter estimation solution becomes disproportionately large, with axes crossing at far away distances. Also, there is no parameter to describe the misalignment. Neither of these scenarios are desirable when calibrating.

The mDH is a commonly used alternative when two consecutive joint axis are parallel. In the mDH convention, d_i becomes redundant and is replaced with an axis misalignment term β_i which then makes the model complete and the parameters proportional. The sequence of transformation becomes:

$$H_{i-1}^{i} = R_{z_{i-1}}(q_i)T_{x_i}(a_i)R_{x_i}(\alpha_i)R_{y_i}(\beta_i) \tag{3.4}$$

The base transformation H_0^b, is fully defined in 3D space by a full 6 parameters (3 translation, 3 rotation).

$$H_b^0 = T_{x_b}(a_b)T_{y_b}(b_b)T_{z_b}(d_b)R_{z_b}(\gamma_b)R_{y_b}(\beta_b)R_{x_b}(\alpha_b) \tag{3.5}$$

3.3.1.2 The inverse kinematic model problem

The robot can be programmed to achieve its target either from an input of joint angles, referred to as the forward kinematic (FK) model $p = f(q)$, or from an input of desired target pose from which the inverse kinematic (IK) model $q = g(p)$, determines the appropriate joint angles to achieve it.

The FK model has the advantage of returning a unique pose for a given joint vector input. This case is the preferred choice to determine the accuracy of the kinematic model, by directly comparing the measured and predicted pose. The solution to the IK problem encounters a number of challenges. First, for complex geometry or higher degree of freedom robots, a closed-form solution may not exist. Secondly, multiple or infinite solutions may exist. The multiple solution case is often described by the 'elbow up' or 'elbow down' conundrum.

Most machining applications will require an input of the target pose in Cartesian space however, utilising the IK model. For example: defined hole centres, edge start and end are specified by location. To ensure that GPR, or any regression model, is able to interpolate accurately, the forward kinematic model must be used and the problem of inversion becomes a post-processing problem. In this thesis, the FK model will be used for model training and for validation generally in the workspace, whilst for the drilling validation case, the IK model must be used.

3.3.1.3 Joint stiffness model

In Chapter 2 it was stated that a large proportion of robot machining research has been devoted to elasticity modelling for both static and dynamic cases. For the static case, the elasticity model can be used to augment the forward kinematic model by adding a position correction value. It is assumed that the distortion of the links in a large articulated robot are small compared to the gearbox elasticity effects and that all elasticity effects can be captured by modelling each gearbox as a torsional spring. The simpler stiffness model based on early joint models is used in this thesis instead of the more complete *conservative congruence transformation* (CCT) model. This is in part to simplify the model, given that bias correction is the focus of the research and to reduce the number of parameters to estimate during calibration. Also, the CCT model was developed for highly compliant gripping fingers whose configuration changed considerably from gripping forces. While the TCP may move by a few millimeters, the posture of the robot is not expected to change significantly and the CCT model is likely to provide negligible gains in this context.

The end effector deflection $\Delta\mathbf{p}_c$, as a result of payload and the elasticity in the gearbox of each joint, is determined by

$$\Delta\mathbf{p}_c = J_q C J_q^T F \tag{3.6}$$

where $C = diag[C_1, ..., C_6]$ is a 6x6 joint compliance matrix, J_q is the system Jacobian matrix and the payload is defined by the *wrench* vector i.e. force and moment vector

$F = [F_x, F_y, F_z, M_x, M_y, M_z]^T$. The use of compliance terms instead of stiffness terms circumvents the problem associated with the stiffness matrix inversion.

The elements of J_q are the partial derivatives of pose change w.r.t. joint angle changes $\frac{\partial p}{\partial q}$:

$$J_q = \begin{bmatrix} \frac{\partial p_x}{\partial q_1} & \cdots & \frac{\partial p_x}{\partial q_n} \\ \vdots & \ddots & \vdots \\ \frac{\partial p_z}{\partial q_1} & \cdots & \frac{\partial p_z}{\partial q_n} \end{bmatrix} \tag{3.7}$$

3.3.2 Parameter estimation

In this section, the proposed parameter estimation techniques are presented in context to familiarise the reader with the problem formulation.

3.3.2.1 Competing model parameters

With the model parameters now described, the subsets of calibration parameters with reference to the competing models can now be presented. Table 3.4 shows the parameter subsets of base parameters(θ_b), DH table geometric parameters (θ_g) and joint compliance parameters (θ_c).

Table 3.4: Kinematic model parameter subsets for an example ABB 6640 robot using an DH model form. In the mDH convention, d_2 is substituted for β_2

Parameter Subset	No. of parameters	Parameters
θ_b	6	$\gamma_b, \beta_b, \alpha_b, x_b, y_b, z_b$
θ_g	24	$q_1, \ldots, q_6$ (Joint rotation) $d_1, d_3 \ldots d_6$ (Link translation) $a_1, \ldots, a_6$ (Axis translation) $\alpha_1, \ldots, \alpha_6$ (Axis twist) β_2 (Axis misalignment)
θ_c	6	$C_1, \ldots, C_6$

3.3.2.2 Base frame calibration

To measure the pose of the TCP, an arbitrary base must first be constructed and then estimated to minimise the pose error. It is not possible to isolate the base parameter errors from the geometric errors and so any estimation of the base is simply a best-fit of data.

Singular value decomposition (SVD) can be used as an efficient method to determine the best fit transformation between two point clouds of data in a least-squares sense. This method is referred to as localisation and has been applied to robot base calibration by [120]. *Data localisation* is the centring and rescaling of two or more sets of vector data to minimise the difference between data sets. The estimated transformation between predicted and measured data provides a HTM from which the six base parameters can be extracted.

The SVD process begins by centralising both the model and measured data sets by subtracting the centroid $(\bar{\mathbf{p_d}}, \bar{\mathbf{p_m}})$ from each set, and then combined as

$$A = (\mathbf{p_d} - \bar{\mathbf{p}}_\mathbf{d})(\mathbf{p_m} - \bar{\mathbf{p}}_\mathbf{m})^\mathbf{T} \tag{3.8}$$

A can then be represented as a left singular vector matrix V, a diagonal matrix S and right singular vector matrix V by decomposition

$$A = USV^T \tag{3.9}$$

The rotation matrix R and translation vector T between centralised data sets and the translation matrix between is determined by

$R = VU^T$ if $\det|R| \geq 0$ or $R = V'U^T$ if $\det|R| < 0$ where V' is matrix V but with the last column multiplied by -1. The translation is determined by

$$T = \bar{\mathbf{p_m}} - R\bar{\mathbf{p_m}} \tag{3.10}$$

The rotation matrix R is then converted to Euler angles $[\gamma_b, \beta_b, \alpha_b]$ and translations $[x_b, y_b, z_b]$ as an estimate of θ_b which are then combined into HTM H_b^0.

3.3.2.3 Linear least-squares parameter estimation

After calibration of the base parameters, the remaining parameters in models M_2 and M_3 can be estimated. The base parameters must also be estimated again, from a now improved initial estimate, to ensure a closer physical meaning to the parameters and an improved chance of locating the global minim.

Linear least-squares estimate (LLSE) is utilised as an existing calibration tool that has been used with some success used in this application.

The residual error pose error from a model prediction can be related to the model parameter deviation by

$$\Delta\mathbf{p} = \mathbf{J}_\theta \Delta\theta \tag{3.11}$$

where $\Delta\mathsf{p}$ is the column vector of pose error and $\Delta\theta$ is a column vector of parameters deviations. $\mathbf{J}_\theta$ is the Jacobian matrix (partial derivatives of the pose w.r.t. model parameter change $\frac{\partial p}{\partial \theta}$).

$$J_\theta = \begin{bmatrix} \frac{\partial p_x}{\partial \theta_1} & \cdots & \frac{\partial p_x}{\partial \theta_N} \\ \vdots & \ddots & \vdots \\ \frac{\partial p_z}{\partial \theta_1} & \cdots & \frac{\partial p_z}{\partial \theta_N} \end{bmatrix} \tag{3.12}$$

For n poses, the vectors and matrices are concatenated i.e. $\Delta\mathbf{p} = [\Delta\mathbf{p}_1, \Delta\mathbf{p}_2, ..., \Delta\mathbf{p}_n]^T$,

$$\begin{bmatrix} \Delta p_1 \\ \Delta p_2 \\ \vdots \\ \Delta p_n \end{bmatrix} = \begin{bmatrix} J_1 \\ J_2 \\ \vdots \\ J_n \end{bmatrix} \Delta\theta \tag{3.13}$$

The estimated solution $\Delta\theta$ that minimises $\Delta\mathbf{p}$ in the least-squares sense, is obtained by the matrix inversion $\Delta\theta = \mathbf{J}_\theta^{-1}\Delta\mathbf{p}$. But as $\mathbf{J}_\theta$ is not square, the pseudo-inverse Moore-Penrose alternative is used

$$\Delta\theta = (\mathbf{J}_\theta^T \mathbf{J}_\theta)^{-1} \mathbf{J}_\theta^T \Delta\mathbf{p} \tag{3.14}$$

The Jacobian matrix is also a function of the model parameters θ and therefore it too must be updated with the new parameter predictions $\theta' = \theta + \Delta\theta$. The LLSE process is therefore iterative (see Figure 3.11), updating the Jacobian in model $M(.)$ at each iteration and converging on a solution with a stopping condition of rms $|\Delta\mathbf{p}| \leq \mathbf{10^{-5}}$mm.

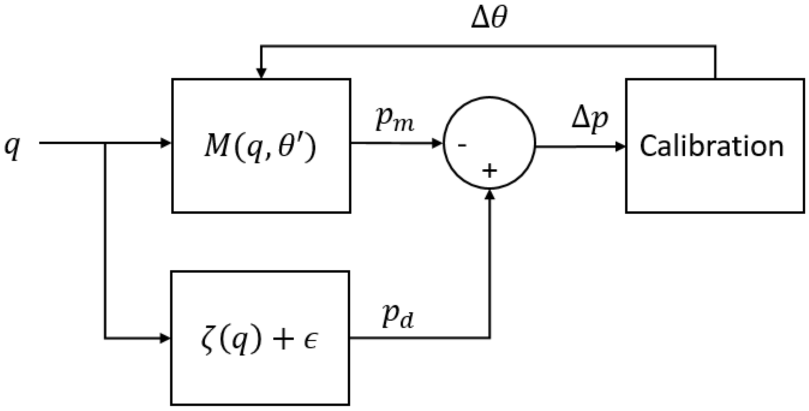

Figure 3.11: Calibration process flow chart.

3.4 Bias correction

It is not the intention in this thesis to extend the body of knowledge of GPR, only its application. To this end, a common relatively simple version of GPR, a general kernel choice in particular, is used unless the data dictates otherwise. This may be considered as a limitation in the research presented in this thesis.

After calibration of the kinematic model, the residual error $\Delta\mathbf{p}$ is the result of inaccurate model parameters and unmodelled errors. In this study, GPR is used to predict the residual errors $\Delta p_x, \Delta p_y$ and Δp_z separately for each model (referred to as $M_{0,GP}, M_{1,GP}, M_{2,GP}, M_{3,GP}$) from a joint vector input q. The motivation to learn the residual error as a function of joint-space relates to the uniqueness of the forward kinematic model previously discussed. For consistency with literature [113], GPR will be introduced using the generic terms (x, y). In this study x will comprise of the six dimensional input vector q, and y is the residual error $\Delta p_x, \Delta p_y$ or Δp_z.

The underlying expectation of GPR is that for similar inputs x and x', y' will be similar to y. This similarity extends to all other data pairs (x_i, y_i) to predict y' by a weighted *similarity*. The similarity weighting is captured by the covariance function $k(x, x')$.

From a regression perspective, GPR determines a function $f(x)$ with measurement variation $\epsilon \sim \mathcal{N}(0, \sigma_n^2)$

$$y = f(x) + \epsilon \tag{3.15}$$

As a non-parametric model, and thus no pre-selected model form, GPR considers all possible functions that describe the data. More accurately, with an infinite number of functions that pass through known data points, i.e. pass through training data points, GPR outputs a mean prediction $\bar{f}_*$ from the function distribution and in addition, provides a variance σ^2 as a measure of confidence.

From a probability perspective, we can start with the premise that a function can be perceived as an infinite number of points. A GP assumes that these points are jointly distributed so that a single sample from a multi-variate Gaussian of infinite dimensions outputs and infinite number of random variables which can be considered to be a function. To extend this, any subset such as the training data, are also jointly distributed with any other subset, such as the test data.

To learn from the training data in order to predict test data, the GP first defines the prior distribution for the functions $p(\mathbf{f}|\mathbf{x})$ and then marginalises to select only functions that describe the known data, to determine the posterior $p(\mathbf{f}|\mathbf{x}, \mathbf{y})$. For a set of inputs $\mathbf{x} = [x_1, \dots x_N]$, the random function variables from that sample $\mathbf{f} = [f(x_1), \dots, f(x_N)]$ are indexed by $\mathbf{x}$ to create input and output pairs. The GP prior for the marginalised training and test data, with zero mean, $p(\mathbf{f}|\mathbf{x}) \sim \mathcal{N}(0, \mathbf{K})$ is then

$$\begin{bmatrix} \mathbf{y} \\ y_* \end{bmatrix} \sim \mathcal{N}\left(\mathbf{0}, \begin{bmatrix} K + \sigma_n^2 \mathbf{I} & K_*^T \\ K_* & K_{**} \end{bmatrix}\right) \tag{3.16}$$

where K is the covariance matrix between training data inputs, K_* is the covariance between training and test data inputs and K_{**} is the covariance between test data inputs. A zero mean is commonly chosen if the mean function is not known. The predictions do not suffer in this case unless the test data inputs are far from the test data inputs, in which case the GP will not extrapolate well and reduces to a prediction of zero. In the marginalised prior the $\mathbf{f}$ term has been substituted with the known training data output $\mathbf{y}$ given the inclusion of the measurement variation. The test data output remains a function prediction $\mathbf{f}_*$. To predict the output, the posterior can be found by conditioning the joint Gaussian, giving

$$p(\mathbf{f}_*|\mathbf{x}_*, \mathbf{x}, \mathbf{y}) \sim \mathcal{N}(K_* K^{-1}\mathbf{y}, K_{**} - K * K^{-1} K_*^T) \tag{3.17}$$

The prediction of y_* is taken as the mean of the conditional probability $\bar{\mathbf{f}}_* = K_* K^{-1}\mathbf{y}$ and we are provided a measure of uncertainty by $\sigma_{f*}^2 = K_{**} - K * K^{-1} K_*^T$:

3.4.0.1 Kernel selection

In GP terms, the kernel is the covariance function which, along with the mean (which can be zero), fully describes the GP.

$$f \sim GP(m(x), k(x, x')) \tag{3.18}$$

The kernel quantifies the similarity between input and output pairs of training and test data which is at the very core of the GP. Careful selection of the kernel then, can help the predictive performance.

Kernel selection includes selection of the model or models, method of combining models and the estimation of model hyperparameters. These are discussed separately and briefly with reference to simulated data for context.

The choice of kernel model expresses any assumptions about the data and the function that we intend to represent it, e.g. smooth, periodic, discontinuous. Generally, a GP will not perform well is cases where the data is discontinuous, but a step change in the bias can be modelled with careful combination of kernels. The case of gearbox backlash is an example and will be discussed in brief in this section.

To help with the choice of kernel, the form of the bias data can be separated into two parts. First, the base, geometric and joint elasticity bias data, which can be simulated by models M_0 to M_3 . Figure 3.12 is an example of the bias data from the numerical model of the ABB 6640 robot used in Chapter 5 for context. Second is the reportedly, highly non-linear, non-geometric errors for which no assumptions can be made.

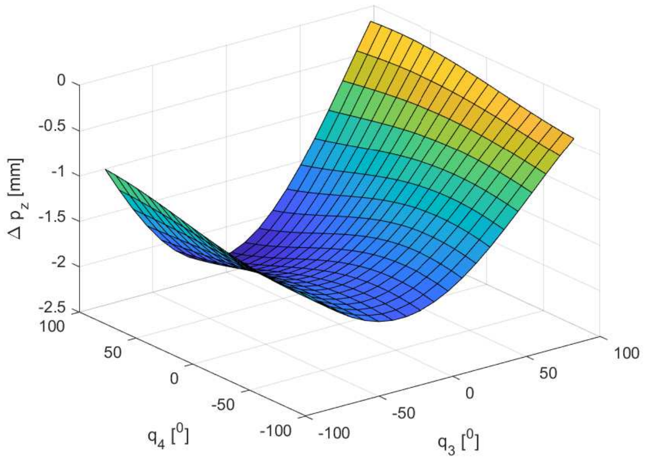

Figure 3.12: Surface plot of the residual error for in the direction of Δp_z for an input of joint 3 and joint 4 only from a simulated model with errors in the base, geometry and joint elasticity i.e. M_0 .

The residual error surface plot is smooth in just the two dimensional case i.e. only joints 2 and 3 were rotated. Extrapolating to the six dimensional input case case, the expectation is that the hyper-plane is more complex, but will remain relatively smooth which my be informative when selecting the appropriate GP kernel.

There are many kernels available, each with different qualities and which represent different assumptions about the data. It is equally important to avoid constraining the GPR model with a poor choice, and in fact it would be better to select a more general kernel in this case. The *squared-exponential* kernel and *Matern* kernel are described below as examples of general purpose kernels which are commonly used to model smooth data trends. A *periodic kernel* is also described as an appropriate example that allows the user to infer expectations about the function form. The examples are described with reference to [41][46].

The *squared-exponential* (SE) kernel in Equation 3.19 (also known as an RBF kernel) is the most common kernel choice for similar problems in literature.

$$k(x, x') = \sigma_f^2 exp\left[\frac{-(x_i - x_i')^2}{2l^2}\right] \tag{3.19}$$

The SE kernel assumes a smooth function, which is appropriate for the simulated bias data in Figure 3.12. The kernel is tuned by estimating the two hyperparameter types; σ_f the output scaling factor, and l the characteristic length scale which captures the input similarity i.e. distance between two points before the effect on each others output values is negligible.

The *Matern kernel* in Equation 3.20 is a generalisation of the radial basis function (RBF) where the additional ν parameter controls the smoothness of the resulting function. In the Matern kernel, K_ν is a modified Bessel function and $\Gamma(\nu)$ is the Gamma function.

$$k(x, x') = \frac{2^{1-\nu}}{\Gamma(\nu)} \left(\frac{\sqrt{2\nu r}}{l} \right)^{\nu} K_\nu \left(\frac{\sqrt{2\nu r}}{l} \right) \tag{3.20}$$

By careful selection of ν, the Matern kernel can be identical to the SE kernel, assuming a 'very smooth' function, or 'spiky' function to model a particle undergoing Brownian motion.

The *periodic* (PER) kernel in Equation 3.21 imposes one of the strongest assumptions about the data by constraining the function to a periodic wave.

$$k(x, x') = exp \left[-\lambda \frac{sin^2(x_i - x'_i)}{4l_2^2} \right] \tag{3.21}$$

Marginalisation of the GP prior is based on functions that pass through the known training data. Further flexibility can be built into the kernel with the addition of a noise term expressed as $\sigma_n^2 \delta(x, x')$, where σ_n is a noise hyperparameter and $\delta(x, x')$ is the Kronecker delta function. The additional term allows the acceptance of functions that pass near to the data, accepting that measurements have some uncertainty. As an example, the noise term is added to the SE kernel as

$$k(x, x') = \sigma_f^2 exp \left[\frac{-(x_i - x'_i)^2}{2l^2} \right] + \sigma_n^2 \delta(x, x') \tag{3.22}$$

3.4.0.2 Combining kernels

Combining kernels with different features or assumptions creates a new composite kernel. The full explanation and derivation can be found in Rasmussen and Williams [113], but for brevity, the options are discussed only in the context of this research. The two main options used in this research were to combine kernels as *product* models and *additive* models. The product model has already been employed in this research by expanding the SE kernel to multiple inputs. The product of SE kernels allows for a length scale for each input dimension. This option can be expanded to create a new kernel as a product of two different kernel types, such as the squared-exponential and periodic kernels, which when combined as a product results in a periodic function with an amplitude that may increase and decrease.

$$k(x, x') = k_{SE}(x, x') * k_{PER}(x, x') \tag{3.23}$$

The more interesting option is the additive model where the SE kernel can be used to describe the expected smooth function, whilst the periodic kernel models the wave on top of the SE function. The two kernels are not completely independent as they are trained simultaneously.

$$k(x, x') = k_{SE}(x, x') + k_{PER}(x, x') \tag{3.24}$$

This approach is demonstrated in [121] with an arbitrary example of a long-term smooth function with an added short-term periodic fluctuation. Rasmussen and Williams used both options to model CO_2 changes over 6 decades. The authors used added kernels to model specific features in the data. An SE kernel was used to model the long-term trend, a QR kernel for medium-term fluctuations and a periodic-SE product kernel for the season fluctuations. The product allowed the period to vary.

3.4.0.3 Hyperparameter estimation

Once the kernel has been selected the final stage is to tune the model to allow the data to speak clearly, by optimising the model hyperparameters. If not chosen carefully, the predictive performance will be poor. For example, in the SE case, a small length scale results in a function that nearly ignores data that is not near to it and models the data locally. Too small and the function over-fits. For a large length scale, the function is influenced by data that is far from any prediction and the result is a function of the underlying trend which fails to model local variations.

The best estimate of θ is when the maximum posterior $p(\theta \mid y, x)$ occurs (MAP). By referring to Bayes theorem and assuming that we have little or no prior knowledge of theta ($p(\theta)$), then this also occurs at the maximum likelihood $p(y \mid x, \theta)$.

$$p(\theta \mid y, x) = \frac{p(y \mid x, \theta)p(\theta)}{p(y)} \tag{3.25}$$

The landscape of the output plotted against each parameter is very steep owing the exponential form. The log likelihood can then be optimised using any gradient-based optimiser. The optimisation algorithm chosen is of little interest, but for repeatability, a Nelder-Meads optimiser was used to search for the kernel hyperparameters θ that minimises $-logp(y \mid x, \theta)$ where

$$logp(y \mid x, \theta) = -\frac{1}{2}\mathbf{y}^T K^{-1}\mathbf{y} - \frac{1}{2}log \mid K \mid - \frac{n}{2}log2\pi \tag{3.26}$$

The separate terms combined ensure that the function is balanced between simplicity and accuracy to the training data by rewarding the data fit but penalising complexity.

3.4.1 Target correction

Some robot control systems do not allow model or model parameter updating. The solution to improving the accuracy of a robot given this restriction must therefore be a general solution implemented offline. With this assumption comes the freedom to create any model form i.e. parametric and non-parametric. The use of a joint elasticity model and bias correction exploits this assumption in this thesis. The actual general offline solution is not the focus of this thesis but is described briefly below to support the premise that bias correction can be used in real industrial applications.

For a visual reference, the pose correction process is shown in Figure 3.13. The desired pose p is first converted to joint space q using the nominal inverse kinematic (IK) model, $q = M_0^{-1}(p)$. A presumed, accurate prediction of the actual pose p_m is determined by the calibrated model, $p_m = M_i(q)$. A pose correction value Δp exists between the target pose p and the true pose p_m. The assumption is that if a joint angle vector correction $\Delta q = J_q^{-1}\Delta p$ can be determined then the system can be provided the phantom input $p'_m = p_m^{(0)} + \Delta p$. However, the correction value relies on the Jacobian matrix from an input of q and not q'. An assumption must be made that $\Delta p' \approx \Delta p$.

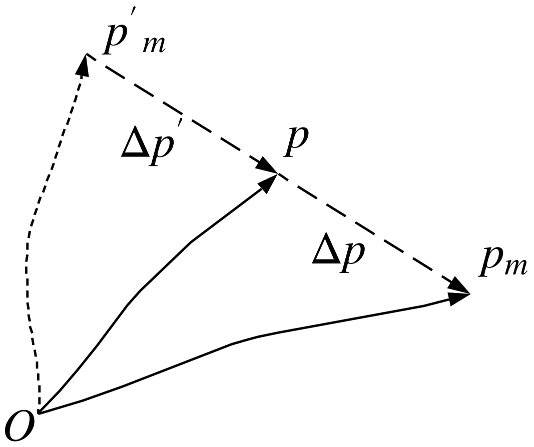

Figure 3.13: Vector diagram of target correction.

The process converts a problem involving the inverse kinematic nominal model, M_0^{-1},which has poor accuracy, to a forward kinematic problem using a more accurate model M_i. Figure 3.14 shows the iterative solution to the assumption that $\Delta p' \approx \Delta p$. A stopping function can be included but the solution converges in less than 10 iterations and is very quick.

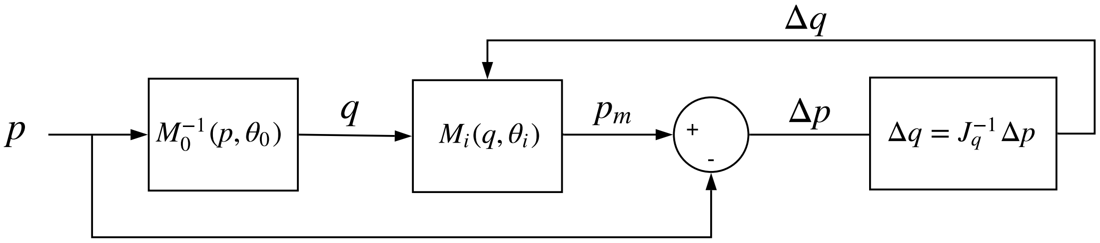

Figure 3.14: Target correction process flow chart.

As an example, this is demonstrated in Figure 3.15 on a simple three link planar arm simulation with a 5mm error in the link lengths. The process is very efficient having converged to sub-micron level after the first iteration.

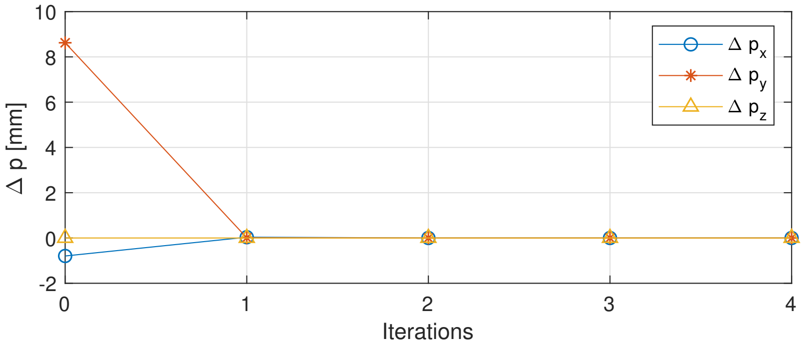

Figure 3.15: Example target correction results.

3.5 Chapter summary

A research methodology has been proposed in this chapter to answer the research question and address the three gaps identified in literature, namely the use of GPR and exploration of the limitations of bias correction relating to data size and calibration level. The method presented acknowledges the approaches and practices in literature whilst exploiting the state-of-the-art metrology equipment and software provided by the sponsor. The use of bias correction, GPR in this case, is the focus of the research and so where possible, the technology and models used have are widely available and/or commercial solutions.

To limit the scope and reduce the number of dimensions to the problem, a number of limitations to the research are imposed:

1. A single payload has been used on the assumption that a machining spindle will be fixed and tool changes will have a negligible effect on the deflection of the joints. This assumption means that the number of input variables to the GPR is reduced and the number of test combinations is manageable.

2. A long-standing LLSE tool is used for calibration in favour of more advanced parameter estimation techniques. The focus remains on the bias correction phase and research has demonstrated that only marginal gains, particularly in measurement and computational efficiency rather than accuracy are made with alternative tools. In the method proposed, a LLSE allows simplicity and close control over performance and parameter selection.

3. The GPR tool is used in an acknowledged, simple form with a general SE kernel. The SE kernel is a common kernel used when there is no prior knowledge of

the data. Other kernels are available but which will not be evaluated unless the data dictates it.

Looking forward, in Chapter 4 the geometry of the robot is measured using the CPA method, which was discussed in section 2.2.3. The joint compliance and link elasticity effects were measured in order to be able to test the rigid body assumptions made in the joint compliance model in section 3.3.1. The results will be used to create numerical model of the ABB IRB 6640 robot.

In Chapter 5, the proposed methodology is tested on a simulated data from the numerical model created in Chapter 4. The competing models are calibrated using the SVD and LLSE tools presented in section 3.3.2. Bias correction using GPR with an SE kernel is tested on the competing model bias data for each case study.

In each chapter, specific methods are described with the following design considerations:

I Data target generation should be generated with space-filling properties and parameter redundancy considered

II Laser tracker location and sensor visibility must be considered as practical considerations when generating training and validation targets whilst retaining (i)

III GPR and calibration tools have different needs and it may be appropriate to generate separate data.

Chapter 4

Error Investigation and Numerical Modelling of an Industrial Robot

The aim of this chapter is to meet thesis objective 1 by presenting an investigation into the error sources on an industrial robot and to develop a numerical model.

While it would be entirely permissible to choose arbitrary values for the numerical model and move on to the simulation trial in Chapter 4, the review of literature in Chapter 2 concluded that the size and rank of errors associated with each source was unique to each robot. The outcome of this chapter is a numerical model that provides a realistic bias correction challenge, the results of which can then be validated with empirical data.

The chapter is presented as two separated studies. Section 4.1 is focussed on isolating and measuring the geometric components of the structure, to determine DH geometric parameter errors.

Section 4.2 is focussed on measuring the deformation of isolated structural elements (i.e. joints and links), when subjected to a static payload to identify link elasticity and joint compliance parameters. The aim is to determine if a rigid body assumption used in the joint stiffness model (in section 3.3.1) produces an accurate model, and to identify the model parameters.

4.1 Geometry identification by circle-point-analysis (CPA)

In this study, the geometry of the robot is isolated and measured using the CPA method to identify geometric parameter errors in the mDH table.

4.1.1 CPA method and geometric construction

The CPA method uses the position data from sensors mounted on link i, measured as joint i rotates incrementally through an arc. The data is used to construct a plane and circle associated with joint i. The joint axis is identified from a vector, normal to the plane and passes through the circle centre. Once the joint axes have been identified, the mDH convention is followed to construct the joint axis origins and measure the mDH parameters.

An example of the construction and parameter identification is illustrated in Figure 4.1. Each axis is constructed from the measured position data (3 dots) that form a circle. The DH parameters a_1 and d_1 are identified from the lines that intersect along z_0 an x_1.

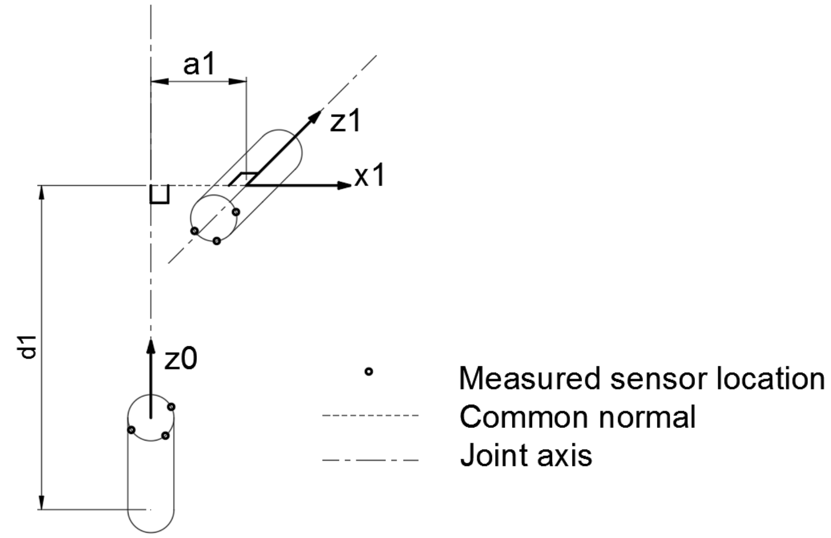

Figure 4.1: Example of geometry construction following the DH procedure in SA.

4.1.2 Experimental design

The experimental procedure was conducted as follows to create a geometric model. The procedure was repeated to created six models from the separate measurement data, the results of which are referred to as Test 1 to Test 6.

I Identify the base frame using the CPA method described in section 3.2.4.

II Measure the position of an SMR sensor at a fixed location on the link, at joint angle increments. During the data gathering for an element, all other joints are fixed.

III Construct planes, circles an then joint axes from position data for each element using the SA software.

IV Construct and measure mDH parameters from joint axes using SA.

V Validate the measured mDH model by measuring the positional error of the TCP in 10 randomly generated configurations.

4.1.2.1 Sensor placement and data gathering

A Leica AT960 laser tracker was used to measure the position of a 1.5" SMR secured to an arbitrary location on each link. A panel of the cell was removed for visibility and the laser tracker was located just outside of the cell for safety. The SMR was mounted to magnetic nests, which was glued to the link structure so that the SMR could be manually rotated in the nest to ensure visibility by the tracker and moved from link to link. The rotation of joint 6 (J6) was measured with a T-mac mounted on a fixture instead of a 1.5" SMR. Figure 4.2 shows nested SMR locations circled in white along the structure and T-mac at the end effector.

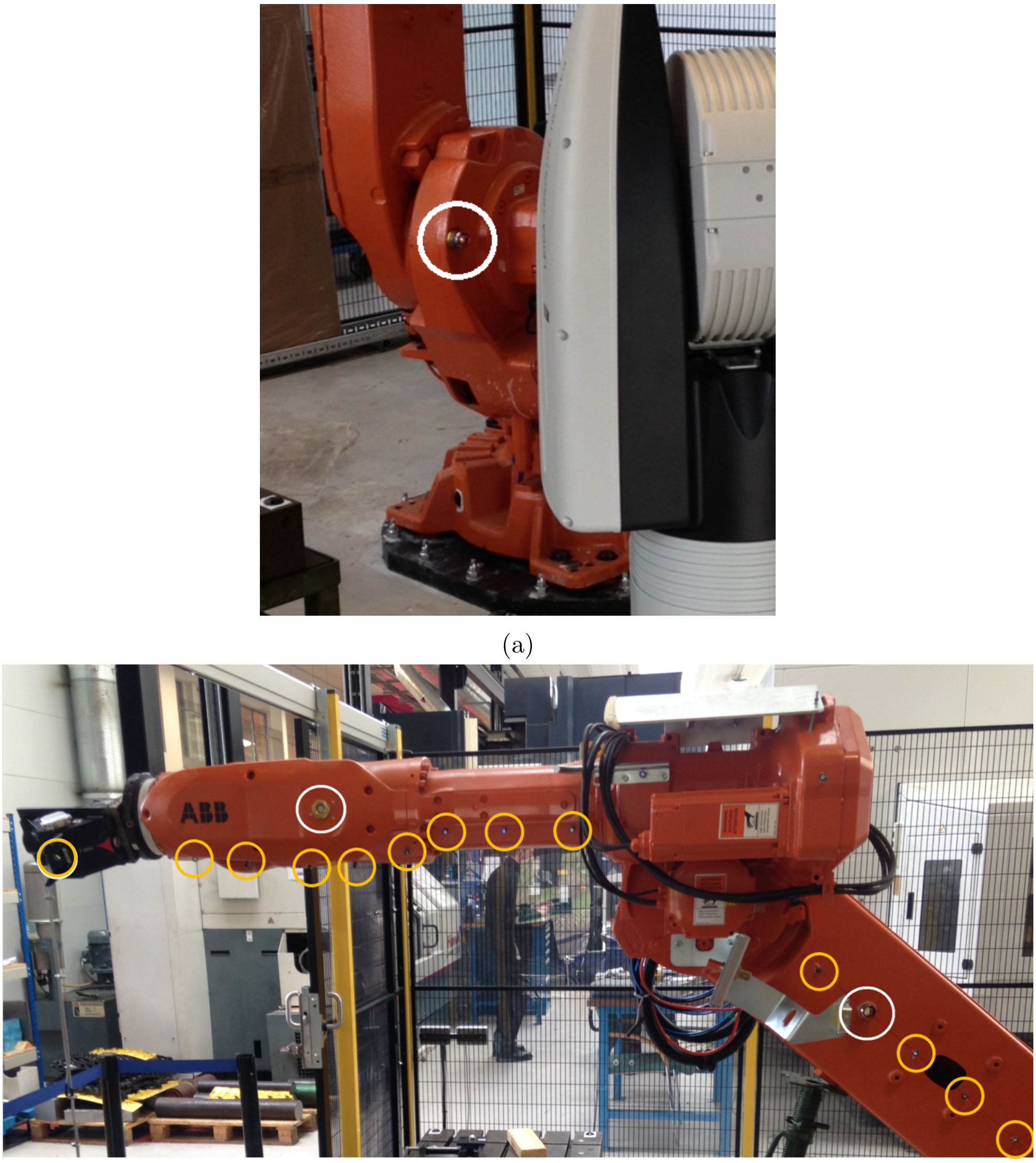

(a)

(b)

Figure 4.2: SMR laser tracker sensor locations on (a) link 1 and (b) links 2 to 6. 1.5” SMR locations circled in white, 0.5” SMR’s in circled in yellow.

Table 4.1 shows the number of targets data points and increments rotated by each joint.

Table 4.1: Geometric parameter rotation increments.

Feature	**Targets**
Base plane	T1 - T5
Joint 1 ($q1$)	15^0,0^0,-15^0,-30^0,-45^0
Joint 2 ($q2$)	-45^0,-30^0,-15^0,0^0,15^0,30^0,40^0
Joint 3 ($q3$)	-60^0,-30^0,-15^0,0^0,15^0,30^0,60^0
Joint 4 ($q4$)	-90^0,-60^0,-30^0,0^0,30^0,60^0,90^0
Joint 5 ($q5$)	-60^0,-30^0,-15^0,0^0,15^0,30^0,60^0
Joint 6 ($q6$)	-15^0,-8^0,0^0,8^0,-15^0
End flange plane	T6 - T9

The accuracy of the six models, determined from each test repetition, was validated in 10 joint configurations, generated using LHS and shown in shown in Table 4.2.

Table 4.2: CPA model validation configurations.

Configuration	Joint	Joint 2	Joint 3	Joint 4	Joint 5	Joint 6
p_1 [deg]	-9.73	26.08	-24.75	12.84	31.98	-5.50
p_2 [deg]	-19.68	4.25	-4.96	27.10	50.13	-20.31
p_3 [deg]	9.52	6.51	19.31	-31.79	-28.17	28.02
p_4 [deg]	21.82	24.35	-13.14	-44.33	22.01	19.70
p_5 [deg]	-4.68	15.27	3.42	27.90	-36.33	-38.70
p_6 [deg]	5.18	-4.43	-18.08	-22.9	-11.46	-27.66
p_7 [deg]	-15.70	32.42	16.04	-17.11	3.83	20.09
p_8 [deg]	28.26	-8.39	11.19	26.53	-58.32	-43.00
p_9 [deg]	-14.99	10.11	-8.70	-7.27	-23.26	-6.55
p_{10} [deg]	-29.3	15.5	-8.70	77.2	61.5	-89.00

4.1.2.2 Data processing

The end effector pose was measured by the Leica laser tracker and processed using the SA software, which also reported the accuracy of the fit (plane and circle geometries fitted to measurement data) and allowed for subsets of data to be used to improve the fit accuracy, in a least-squares sense.

The tools within SA were used to determine lines normal to planes, which in turn was used to determine axes and intersections and to define link length start and end points. SA then provided length and orientation measurements of lines between origins and intersections. The geometry of the robot was then constructed in sequence from base to end effector by following the DH convention. In the example shown in Figure 4.3 the base and the constructed axes and links are highlighted in white.

Interestingly, this approach confirmed in a practical way, the problem associated with used the DH convention for robots with consecutive parallel axes. In brief, the common normal origin (i') can be arbitrarily chosen between consecutive parallel joints with an infinite possible locations. One solution is to assume no joint offset and fix $i' = i$. A second problem occurs when there is a small misalignment between these axes assumed to be parallel. For a small misalignment, the location of the common normal will be disproportionately large and no longer representing the true geometry of the system. The preferred mDH form was adopted which fixed the origin of the common normal as previously mentioned, and instead provided an additional axis rotation term β, a rotation around y, as an axis of misalignment.

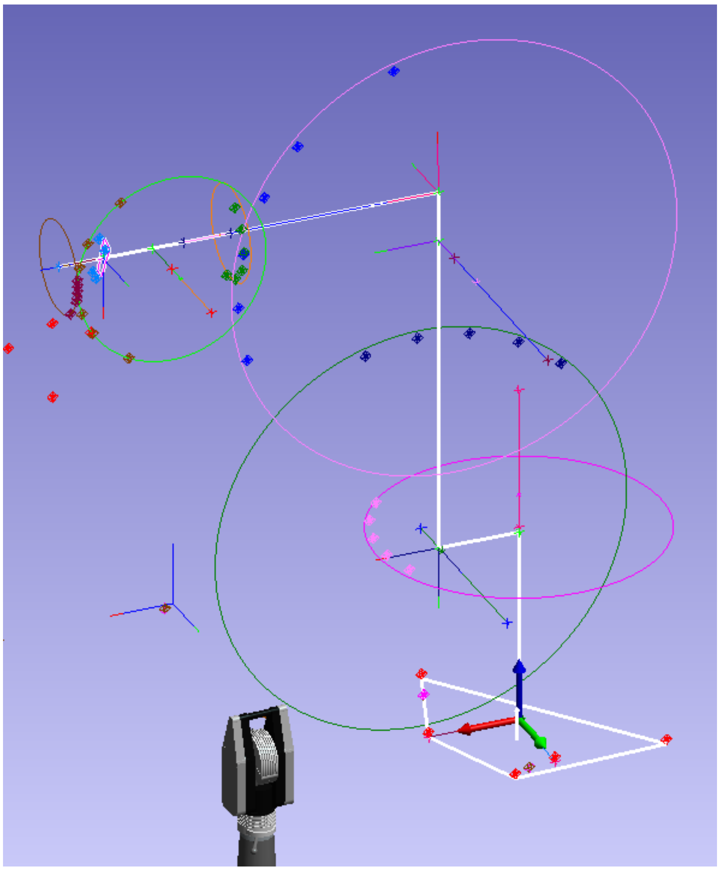

Figure 4.3: Robot geometry constructed in SA using the CPA method.

4.1.3 Results

The accuracy of the geometry values in each model is evaluated by determining the mean and standard deviations (std) of the geometric parameters and by the accuracy of the model predictions. The accuracy of the model in a given configuration is calculated as the Euclidean distance (Equation 4.1) between the predicted and measured position.

$$|\Delta p| = \sqrt{\Delta p_x^2 + \Delta p_y^2 + \Delta p_z^2} \tag{4.1}$$

The fit of the plane and circle geometries in test 1 is reported in Table 4.3 as an indication of confidence in the results. Joints 1 to 6 are abbreviated to J1, J2 etc. Most of the constructed geometry has a small mean rms ($<10\mu m$) compared to the expected robot accuracy and measurement uncertainty. However, the base plane and joint 3 geometries are an order higher which may result in inaccurate measurements or poor repeatability.

The range of model accuracy values is expected to be high due to a wide variation in base plane orientation. The base plate unfortunately has no machined features which in retrospect should be designed in prior to installation.

Many more parameters are affected by an uncertain construction of Origin 2 and z_2 from the joint 3 rotation data. Distances a_2, a_3 and d_3, and frame rotations α_2 and α_3 are directly affected by either the location of the circle centre or the orientation of the normal vector used to construct axis z_2. The impact of these uncertainties is less confidence in this method and potentially less accurate results when tested globally and lower repeatability.

Table 4.3: Constructed geometry uncertainty.

	Base plane	**J1**	**J2**	**J3**	**J4**	**J5**	**J6**	**End flange plane**
$\overline{rms}$[μm]	50	3.25	6.75	36.75	8	9.75	2.25	4.25

The measured geometry in each of the six test repetitions is separated into length geometry in Table 4.4 and frame rotations in Table 4.5 and is presented as a deviation from nominal.

Errors in the length parameters, both link lengths and joint offsets, are significantly high, in the order of -0.200 to -0.500 mm, with the exception of parameters that could not be measured (d_2 and a_6) and lengths near to the wrist (a_4, a_5 and d_6). The deviation in link length d_1 is particularly high, approaching 1mm. While to results seem high in comparison to the manufacturing tolerances of the machines that made them, it is likely to confirm the expectations from literature that geometric parameter errors are the main cause of positional errors in the order of 3-5mm.

A wide range in the length parameters however means that there will be low confidence in the accuracy of the model. For example, deviations in a_2, a_3, d_4, d_5 each have a standard deviation that is within the 0.1mm to 0.3mm range. The choice of parameter for the numerical model may in fact be arbitrary within realistic limits.

Table 4.4: Nominal model length *DH* parameters and measured deviations.

θ	Nominal	Test 1	Test 2	Test 3	Test 4	Test 5	Test 6	Mean (std)
a_1 [mm]	320	0.228	0.240	0.170	0.170	0.150	0.211	0.195 (0.036)
a_2 [mm]	1280	-0.326	-0.331	-0.609	-0.498	-0.439	-0.585	-0.465 (0.122)
a_3 [mm]	200	-0.344	-0.306	-0.072	-0.220	-0.316	-0.063	-0.220 (0.125)
a_4 [mm]	0	-0.052	-0.004	-0.033	0.000	-0.009	-0.032	0.022 (0.020)
a_5 [mm]	0	-0.002	-0.064	-0.025	-0.011	-0.038	-0.007	-0.025 (0.023)
a_6 [mm]	0	0.000	0.000	0.000	0.000	0.000	0.000	-
d_1 [mm]	780	0.932	0.847	0.870	0.878	0.920	0.883	0.888 (0.032)
d_3 [mm]	0	-0.037	-0.094	-0.063	-0.779	-0.189	-0.052	-0.202 (0.288)
d_4 [mm]	1142	-0.169	-0.228	-0.005	-0.226	-0.402	-0.054	-0.191 (0.148)
d_5 [mm]	0	-0.228	-0.610	-0.346	-0.422	-0.230	-0.211	-0.341 (0.156)
d_6 [mm]	200	na	0.019	0.006	-0.008	-0.004	0.010	0.005 (0.11)

The frame rotation errors show similar findings with significantly large errors in most parameters, particularly in Δq_1 which could be considered as the base frame calibration. For context, a 0.015^0 rotation will result in a 0.393 mm error at the end of a 1.5m arm and the majority of joints have a joint offset and twist greater than this. The parameter errors are large enough to contribute to a significantly large positional error at the end effector and one which will vary considerably with configuration.

There are notable outliers in test 3 and 4 which have a Δq_1 approximately three times larger than the other tests. The base frame data was shared between these two tests rather than all points repeated which would explain why if one test showed an anomaly in the base frame, then so would the other. The parameters will still be validated for the tests 3 and 4.

Table 4.5: Nominal model axis rotation *DH* parameters and measured deviations.

θ	Nominal	Test 1	Test 2	Test 3	Test 4	Test 5	Test 6	Mean(std)
Δq_1 [deg]	0	0.088	0.098	0.268	0.357	0.092	0.092	0.166 (0.177)
Δq_2 [deg]	-90	-0.037	-0.030	-0.033	-0.025	-0.016	-0.035	-0.029 (0.008)
Δq_3 [deg]	0	-0.039	-0.022	-0.012	-0.021	-0.030	-0.010	-0.022 (0.011)
Δq_4 [deg]	180	-0.038	-0.043	-0.042	-0.045	-0.042	-0.043	-0.042 (0.002)
Δq_5 [deg]	0	-0.038	-0.012	-0.008	-0.003	-0.010	-0.007	-0.013 (0.013)
Δq_6* [deg]	0	0	0	0	0	0	0	-
α_1 [deg]	-90	-0.011	-0.010	-0.011	-0.010	-0.014	-0.007	-0.010 (0.002)
α_2 [deg]	0	-0.014	-0.017	-0.015	0.016	-0.010	-0.015	-0.014 (0.002)
α_3 [deg]	-90	-0.013	-0.010	-0.015	0.013	-0.014	-0.019	-0.010 (0.011)
α_4 [deg]	-90	-0.008	-0.002	-0.002	0.022	0.001	-0.006	-0.042 (0.002)
α_5 [deg]	90	0.001	0.058	0.035	0.003	0.012	0.004	-0.013 (0.013)
α_6* [deg]	0	0	0	0	0	0	0	-

The accuracy of the mDH models created from the measured parameters in Tests 1 to 6 (T1 to T6) are presented in Table 4.6. The nominal model error is in the order expected. Despite the uncertainty in the models, they do in fact show that they are an improved representation of the robot geometry by predicting approximately half of the positional error of the nominal model. In fact, although the geometry was highly variable, the accuracy appears to be relatively insensitive to this with predictions ranging between 1.161mm and 1.517mm. The predictions of each target pose are presented in Figure 4.4 for visual scrutiny, which confirm the conclusions. The predictions from models T1 to T6 predict approximately half of the nominal model error in the majority of poses. Interestingly, no single model consistently outperforms the others and so the accuracy is configuration dependent. It is reasonable to assume that in constructing the geometry, compromises were made i.e. some length deviations were traded for other lengths or twist parameters and each model traded differently.

Table 4.6: Calibrated model accuracy for repeated tests compared to the nominal model.

	Nominal	Test 1	Test 2	Test 3	Test 4	Test 5	Test 6
rms $|\Delta p|$ [mm]	2.973	1.412	1.161	1.380	1.304	1.517	1.369

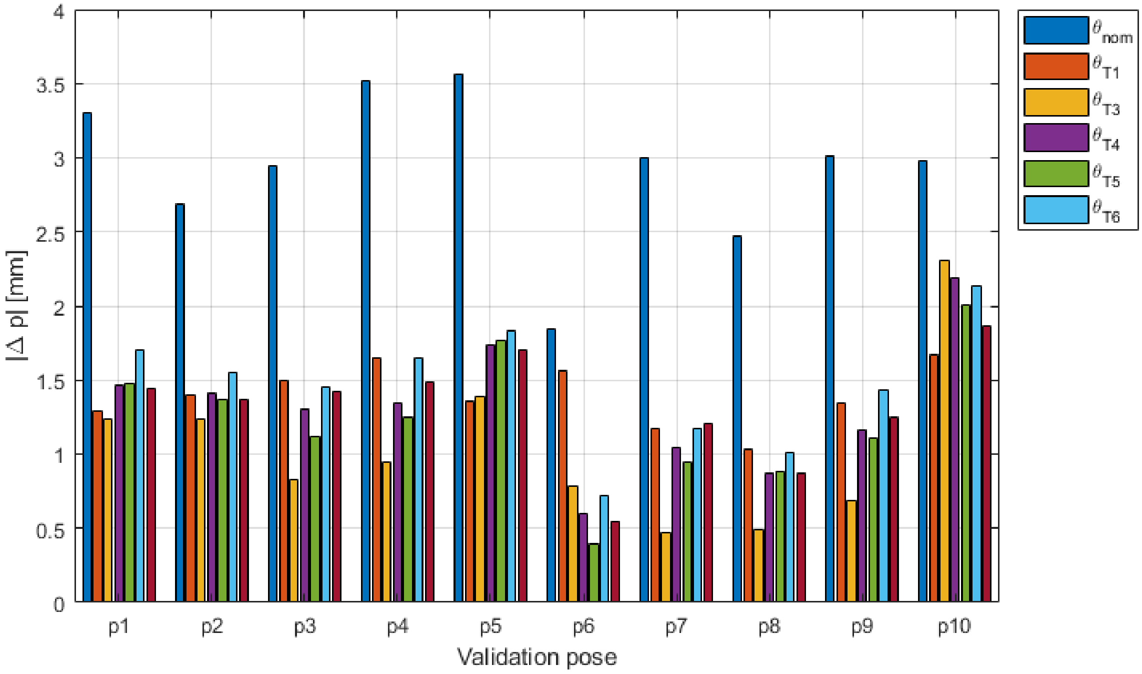

Figure 4.4: Geometric calibration accuracy with parameter in validation poses.

4.1.4 Discussion

In this study, the CPA method used was used with some success, to identify the geometry of the structure. Confidence in producing an accurate model however is low. Large variations in the initially constructed geometric features resulted in a large range in parameters across six tests. In future tests, the variation could be reduced by rotating each joint in smaller increments and a wider range. Alternatively, optimisation strategies could be used that explore the variation in planes and circles. However, CPA as a calibration method is not the focus of this research and approximate values will suffice. The accuracy of the six models was reasonably consistent even with very different parameters and no single model performed best in all configurations. The geometric errors for the numerical model can then be selected relatively arbitrarily within reasonable limits set by the range of values set in this study. The values chosen for the numerical model, with respect to values found in this study, are presented in the next chapter.

Assuming that the geometric parameters measured in this study are relatively close to the true geometry, and there is no way to directly test this, then the study has established that the non-geometric errors account for approximately half of the positional error. This remains dependent on the configuration. The challenge for the bias correction phase then remains significantly large and the research can continue on the ABB IRB 6640 as a testbed.

4.2 Stiffness identification by direct deflection measurement

This study is an investigation of the effects of joint and link elasticity when a robot is carries a payload, and the development of a representative numerical model for use as a simulation tool in the next chapter. The expectation from literature is that the joint elasticity contributes significantly to positional error at the end effector, in this case quantified as a compliance parameter. In order to simplify the elasticity model by reducing the number of calibration parameters whilst retaining the accuracy, the model presented in Chapter 3 assumes that the links are rigid and that the joint can be modelled as a torsional spring. That assumption is tested in this experiment by comparing results for competing models, one assuming a rigid link and one modelling the link as a beam.

4.2.1 Experimental design

The structure can be considered to be made from 6 structural elements where each element is a joint i and link i pair. Three of the six structural elements are studied in this experiment. The studied elements are listed below and shown in Figure 4.5.

- Element 2: joint 2 and link 2 (Figure 4.5a).
- Element 3: joint 3 and links 3 and 4 which are combined (Figure 4.5b). Joint 4 is parallel to the link and is included in the element as a part of the link.
- Element 5: joint 5 and link 5 (Figure 4.5c).

It was intended that the compliance of joints 2 to 6 were identified independently. Joint 1 is assumed to be non-compliant with respect to a vertical payload as the axis of joint 1 is also vertical. Joints 2,3 and 5 have joint axes that are perpendicular to the links and are identified from the rotation of the joint due to the torsion provided by the payload and outstretched arm. Joints 4 and 6 have axes that are parallel to the links and require a twist to rotate them. Unfortunately, the degree of twist measured was small compared to the larger structural deflection which is therefore difficult to model accurately, and positional deflection data was of the same order of magnitude as the measurement variation. Consequently, joints 4 and 6 were not able to be measured with confidence and the results are not reported in this study.

Reflective sensors were fixed along the length of the links in each element and the deviation from the unloaded case was measured for a six different payloads.

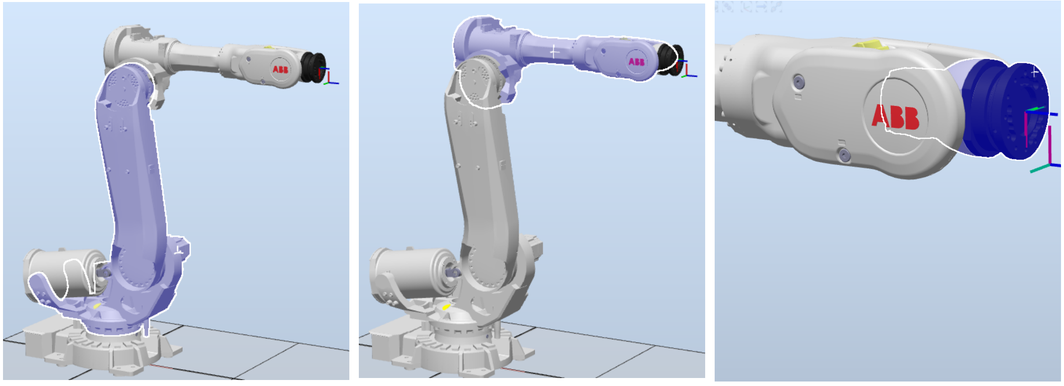

(a) Element 2

(b) Element 3

(c) Element 5

Figure 4.5: Illustration of elasticity study structural elements.

The elasticity deflections were measured when subjected to six payloads which were separated into four to provide training data and two for validation. The experiment was conducted twice. The parameters in each model were estimated using a Nelder-Meads optimisation.

The expectation was that the effects of link elasticity would be challenging to quantify accurately. The structure itself does not have a consistent cross-sectional profile along its length. The structural links between joints have hollow sections to maximise the strength and rigidity to weight ratio and to provide channels for cabling, but the wall thickness changes along each link. Link 2 is largely a rectangular section tube with thick walls and links 3 and 4 are a relatively simple circular tubes but with sections with complex profiles to house gearboxes. It was assumed that as deflections due to link elasticity would be relatively small, a simple model will suffice. The alternative would be to model the structure using finite-element-analysis which is beyond the scope of this research.

4.2.1.1 Sensor placement and data gathering

The position of 1.5” and 0.5” SMRs at fixed locations along the elements, and a T-mac, were measured with a Leica AT960 laser tracker. The 0.5” SMRs were glued directly to the links of the robot, whilst the 1.5” SMRs were located into magnetic nests that were also glued to the structure. A combination of sensors were used due to availability, and to maximise the amount of link deviation data. Sensors were placed at distances of approximately 20cm apart. Figure 4.6 shows the location of the sensors mounted along the structure in the test configuration. The 1.5” SMRs are circled in white and 0.5” SMRs are circled in yellow.

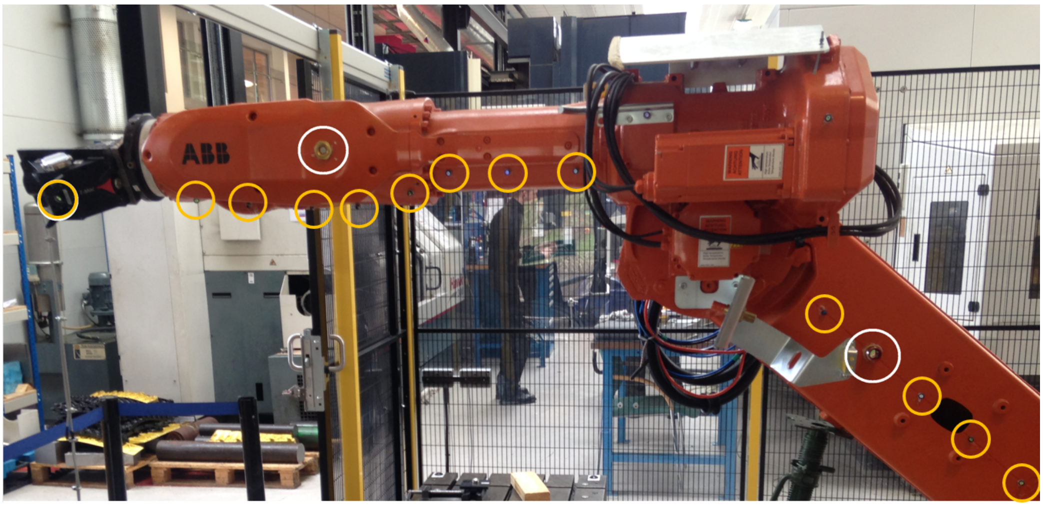

Figure 4.6: Elasticity study, SMR sensor locations.

4.2.1.2 Payload

The payloads were mounted to a fixture attached to the mounting flange as an end effector. The fixture is a simple L-shaped bracket, shown in Figure 4.7 with a machine tool lifting eye screwed into the face plate. Gym free-weights were attached to the eye via a cable to ensure that the location of the payload did not change, and the payload itself remained the only variable. The weights and cable were measured before testing and recorded in Table 4.7. The fixture and T-mac were not included in the payload calculation as they were taken as the reference zero load. Deviations were measured relative this.

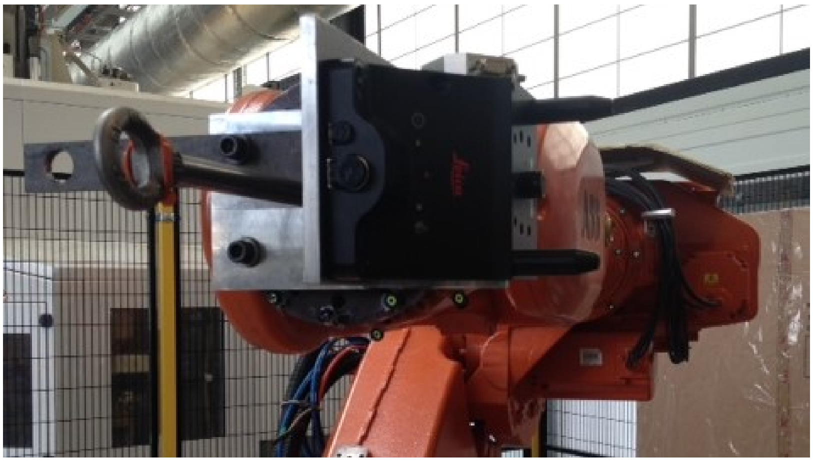

Figure 4.7: Elasticity study, payload fixture and T-mac sensor.

Table 4.7: Training and validation payloads.

	Load [N]
Training	[266.243, 798.338, 1064.974, 1596.283]
Local validation	[532.879, 1330.432]
Global validation	[532.879, 1064.974]

4.2.1.3 Elasticity models

Each element is modelled as a cantilever beam subjected to a moment M and static load w at the free end and a moment M_R (reaction) at the supported end as shown in Figure 4.8. The joint is modelled as a torsional spring.

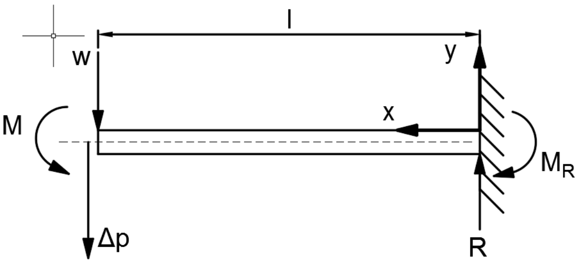

Figure 4.8: Conventional bending beam diagram for a single element.

Following conventional equations, the deflection at distance x along the beam is modelled in three parts: (a) beam deflection due to load w, $\frac{wx^2(3l-x)}{6EI}$; (b) beam deflection due to free end moment M, $\frac{Mx^2}{2EI}$; and deflection due to joint compliance, xM_RC. To test the assumption that the links are sufficiently rigid to neglect beam deflection terms, two competing models are presented.

Model 1:

$$\Delta p^{(1)} = \frac{wx^2(3l - x)}{6EI} + \frac{Mx^2}{2EI} + xM_RC \tag{4.2}$$

Model 2:

$$\Delta p^{(2)} = xM_RC \tag{4.3}$$

For simplicity, the link angle of each element is reported relative to the horizontal x_0 and deflections are reported in base frame coordinates x_0 and z_0 by multiplying Δp by the vector $[sin(\theta_2), -cos(\theta_2)]^T$.

Element 2

A free body diagram of Element 2 is shown in Figure 4.9.

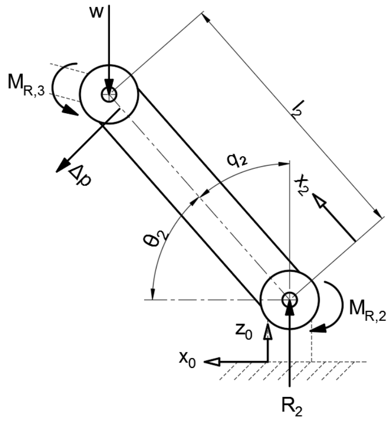

Figure 4.9: Element 2 free body diagram.

The Element 2 model is shown in Equation 4.4. Bias terms A and B were added retrospectively after it was observed that the bias was not constant but in fact load related which suggests that either the base or Joint 1 also deflected under load.

$$\begin{bmatrix}\Delta p_{x,2}\\ \Delta p_{z,2}\end{bmatrix} = \begin{bmatrix}sin(\theta_2)\\ -cos(\theta_2)\end{bmatrix} \Delta p_2 + \begin{bmatrix}B_{x,2}\\ B_{z,2}\end{bmatrix} M_{R2} + \begin{bmatrix}A_{x,2}\\ A_{z,2}\end{bmatrix} \tag{4.4}$$

Element 3

The free body diagram of Element 3 is shown in Figure 4.10. There are two perpendicular links (3 and 4) that make an L-shape. When adjusting for bias at the end of element 2, all data must be multiplied by $[cos(\theta_3), cos(\theta_3)]y_3$ to compensate, where y_3

is the location of the target sensor in the local y direction. Joint 4 is incorporated into element 3 but may have a significantly different elasticity characteristics to the rest of the link and therefore the deflection data along element 3 may be discontinuous.

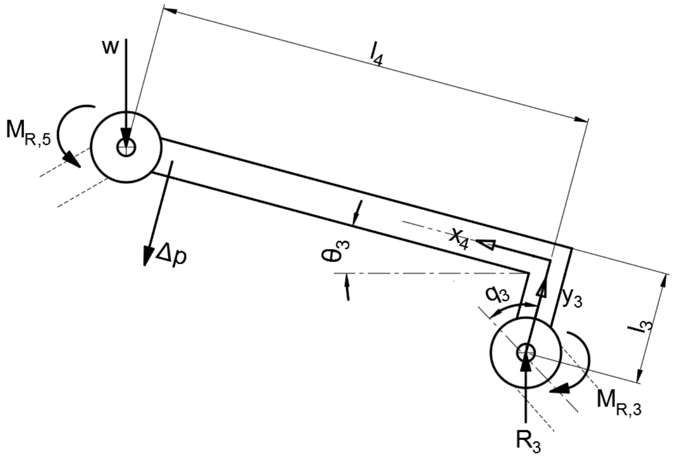

Figure 4.10: Element 3 free body diagram.

After bias correction from deflection and rotation from element 2, the model for of element 3 is

$$\begin{bmatrix} \Delta p_{x,3} \\ \Delta p_{z,3} \end{bmatrix} = \begin{bmatrix} sin(\theta_3) \\ -cos(\theta_3) \end{bmatrix} \Delta p_3 + \begin{bmatrix} A_{x,3} \\ A_{z,3} \end{bmatrix} \tag{4.5}$$

Element 5

The free body diagram of Element 5 is shown in Figure 4.11. The deflection Δp_6 is projected beyond Origin 6 to the TCP. Link 5 is short in relation to its diameter and wall thickness and has a complex profile. Also with little space to add sensors, element 5 is therefore assumed to be rigid and only model 2 will be used.

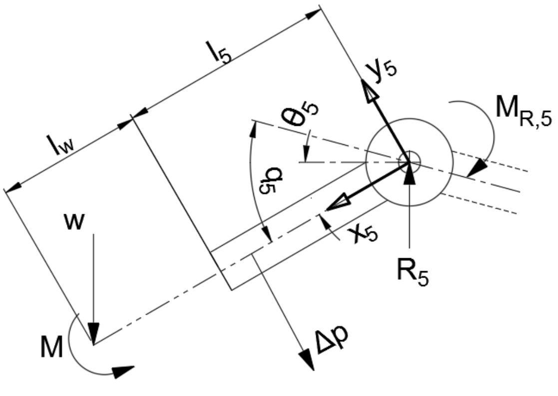

Figure 4.11: Element 5 diagram.

The model form of element 5 is

$$\begin{bmatrix}\Delta p_{x,5}\\ \Delta p_{z,5}\end{bmatrix} = \begin{bmatrix}sin(\theta_5)\\ -cos(\theta_5)\end{bmatrix} \Delta p_5 + \begin{bmatrix}A_{x,5}\\ A_{z,5}\end{bmatrix} \tag{4.6}$$

4.2.2 Results

The results of the robot structure deflection under different loads are first presented as a whole and then sequentially from Element 2 to Element 5 with model evaluations. The analysis of deflections in each element i will consist of an initial review of the training data, separated into $\Delta p_{x,i}$, $\Delta p_{y,i}$ and$\Delta p_{z,i}$ plotted against x_i, their distance along the link. A plot of the objective functions for pairs of model parameters will follow to identify local minima to avoid during parameter estimation, then parameter estimation and model performances.

Figure 4.12 shows the deflection of each target sensor along all elements, relative to the base origin. The joint origin locations are included to indicate where each element begins.

There is a clear separation of data between loads and a measurable deflection in each element is expected to improve the chances of an accurate model. The magnitude of the deflection, approaching 6mm in Δp_z under the maximum load, is very large compared to a machining tolerance which establishes elasticity as a major error factor and an important model. The deflection Δp_x, has an unusual pattern and unlike a standard beam. In retrospect, this is partly due to the location of the target sensor which has prompted the model of deflections in Element 3 to also be a function of y_3 as well as x_3. The deflection Δp_y was expected to be negligible, with all deflections expected in the x_0, z_0 plane, but is in fact in the order of 0.020 to 0.100 mm which is a significant portion of a manufacturing tolerance. However, the pattern in the Δp_y data, a deflection sideways, appears to follow that of the Δp_x data. This relationship is explored further in Figure 4.13 where Δp_x is plotted against Δp_y.

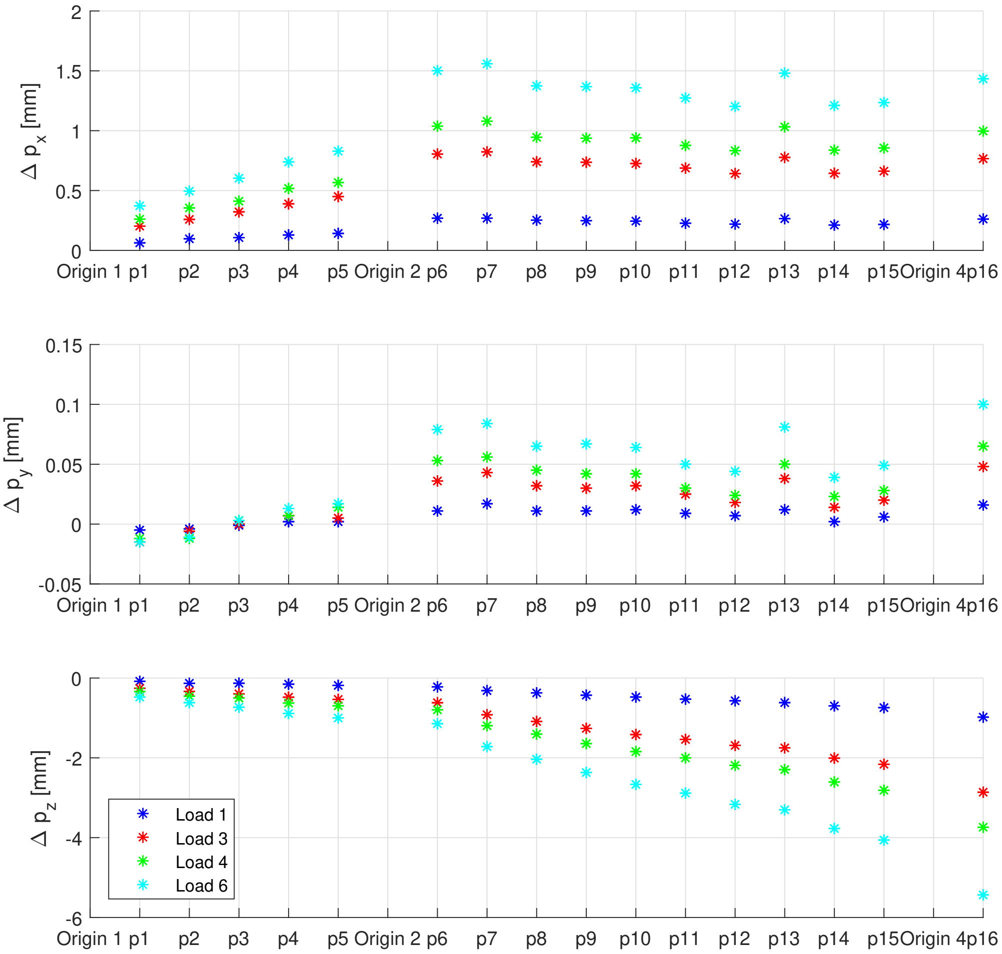

Figure 4.12: Complete system deflection data against payload.

The deflection in Δp_y may be explained by a number of plausible possibilities. Firstly, the complex profile of the links and the joint offset in Link 3 could cause a significant twist in the structure. Secondly, a misalignment in each joint could results in a deflection in p_y. Both of these would be observed as a proportional relationship between Δp_x and Δp_y and which would be different for each element. Finally, a misalignment in the calibrated base frame, would be observed as the proportional relationship for all element.

The relationship between Δp_x and Δp_y indicates that the deflection Δp_y is a result of a small misalignment in the base frame rather than a twist in the structure due to payload. The relationship can be modelled as a linear function with acceptable confidence ($R^2 = 0.838, rmse = 0.012mm$) resulting in equation 4.7.

$$\Delta p_y = 0.0634\Delta p_x – 0.015 \tag{4.7}$$

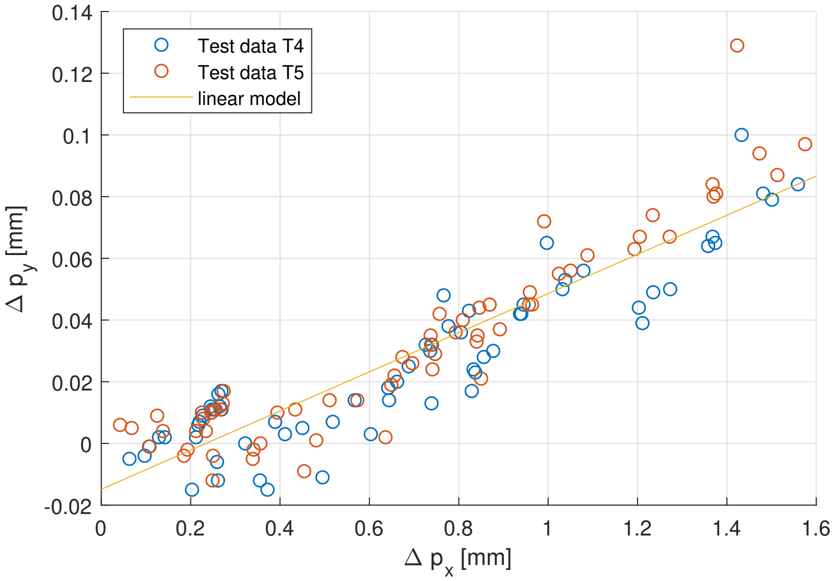

Figure 4.13: Elasticity deflection training data in the x_0, y_0 plane relative to the base Origin.

4.2.2.1 Element 2 results

Element 2 was expected to be one of the more rigid elements, however the additional distance from the load compared to other joints may still result in significant deflections from the increased leverage.

Figure 4.14 shows the measured deflections from tests T4 and T5 at positions along the element for the four training payloads. The deflections $\Delta p_{x,2}$ and $\Delta p_{z,2}$ are already large at the end of link 2 for the maximum load case, relative to the desired accuracy. The data is also clearly distinguishable by load which should improve the chance of an accurate model.

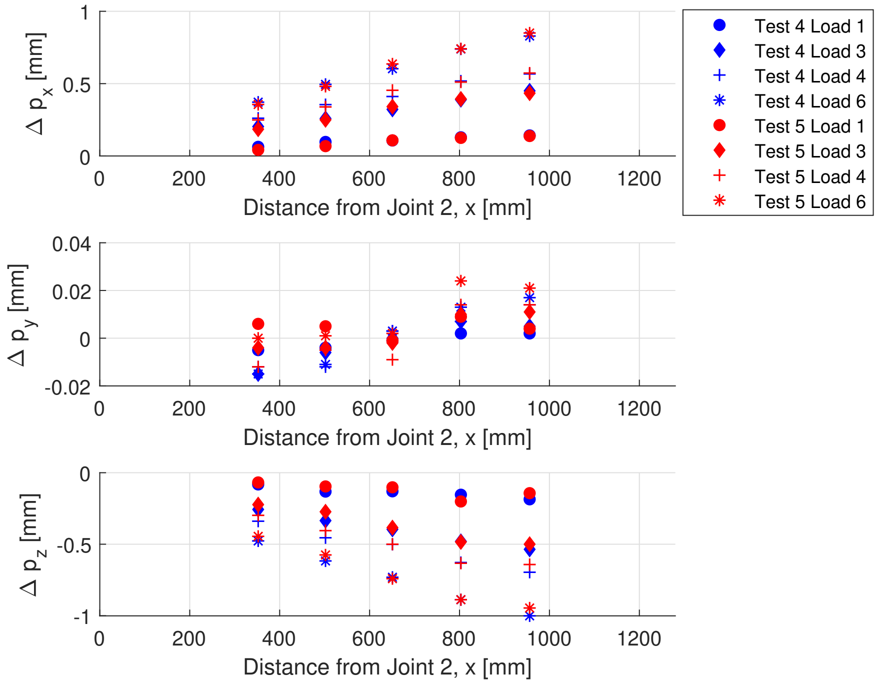

Figure 4.14: Joint 2, Link 2 deflection training data.

In Table 4.12 the estimated model parameters are presented, and in Table 4.9 their performance in predicting the training data and test data are shown.

It can be assumed that Element 2 has a rigid structure, evidenced by the identical compliance and bias parameters which indicates that beam elasticity parameters are negligible. This assumption can be further supported by the insensitivity of the beam elasticity parameters in model predictions.

More surprisingly, however, is the very large bias in the data as a result of deflection in the base and joint 1, modelled as a linear function of torque at joint 2 with parameters $B_x, 2$ and $B_z, 2$. For context, a deflection of $\Delta x = 0.163mm$ and $\Delta z = -0.084mm$ can be seen at joint 2 when subjected to the maximum load, in this configuration. The true source(s) of the bias will not be known without a further investigation of the effects of payload on the base plate and joint 1. For simplicity, the bias will remain as the simple function modelled here which will not be incorporated affect later trials. The bias from these parameters is not expected to be challenging for the bias correction phase.

Table 4.8: Element 2 estimated model parameters.

Model	EI_2	C_2	Bx_2	Bz_2	Ax_2	Az_2
model 1	2.2543x10^{25}	2.785x10^{-10}	3.748x10^{-8}	-1.959x10^{-8}	0.010	-0.180
model 2	n/a	2.785x10^{-10}	3.748x10^{-8}	-1.959x10^{-8}	0.010	-0.180

Table 4.9: Element 2 model performances.

Model	**Training data rms** $\lvert\Delta p\rvert$ [mm]	**Validation data rms** $\lvert\Delta p\rvert$ [mm]
model 1	0.039	0.034
model 2	0.039	0.034

4.2.2.2 Element 3 results

Element 3 contains the longest and least rigid structural elements and therefore link elasticity was expected to be more evident than in other elements. Figure 4.15 shows the training data deflections which have been corrected for the deflection of joint 3, predicted by the Element 2 model. The deflection at the end of the link, $\Delta p_{z,3}$ was greater than -2mm, which is considerably larger than the desired accuracy. The deflection $\Delta p_{x,3}$ is less easy to summarise as the sensor position in both x_3 and y_3 are variables. The deflection $\Delta p_{y,3}$ is measurable and is large enough at 0.1mm for it to be modelled.

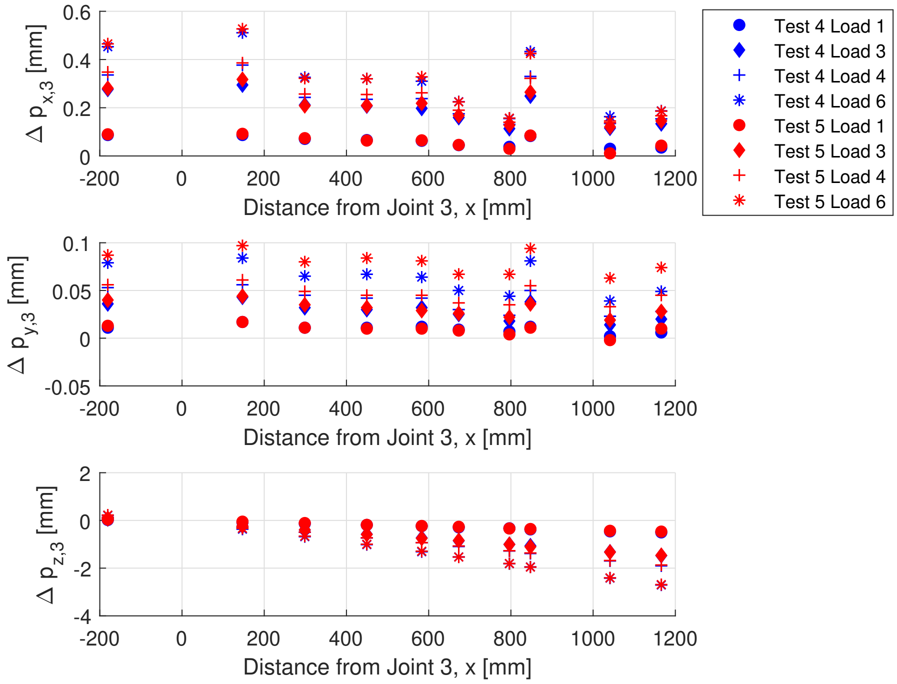

Figure 4.15: Joint 3, Link 3 and 4 deflection training data , adjusted for Joint 2 prediction.

Tables 4.10 and 4.11 show the estimated model parameters and their performance in predicting the training and validation data respectively. In element 3, the beam elasticity terms are not negligible and the link has distorted. The larger compliance term in model 2 suggests that the additional deflection due to beam elasticity is captured by the joint deflection term. Both models perform well in relation to a stated measurement variation, with a similar order of magnitude of approximately 0.050mm. The beam elasticity parameters make a considerable contribution in the order of an additional 0.016mm to the accuracy of the model. Naturally, this may reduce for lower loads or different configurations and so the assumption of a rigid body is no longer valid without context if accuracy is the primary goal.

Table 4.10: Element 3 estimated model parameters.

Model	EI_3	C_3	Ax_3	Az_3
model 1	3.4221x10^{12}	2.9710x10^{-10}	0.030	-0.071
model 2	n/a	4.0440x10^{-10}	0.005	-0.066

Table 4.11: Element 3 model performances.

Model	**Training data rms** $\lvert\Delta p\rvert$ [mm]	**Validation data rms** $\lvert\Delta p\rvert$ [mm]
model 1	0.034	0.046
model 2	0.050	0.057

4.2.2.3 Element 5 experimental results

With only a single sensor, the data for modelling Element 5 was very limited and consequentially, there was less confidence in the model. The length of the element is very short and so with only one sensor it is acceptable to model element 5 as a rigid beam. With models 1 and 2 providing different predictions from element 3, both will be used to correct the data in element 5. Models 1 and 2 in the element 5 analysis then use the same rigid model but from the two data sets from element 3 models corrections.

Figure 4.16 show the training data, corrected by the Element 3 models 1 and 2. Deflection $\Delta p_{z,5}$ is still large, in the order of 1mm, despite its close proximity to the load which was unexpected. This again confirms the significant contribution of joint compliance to the robot accuracy. However, $\Delta p_{x,5}$ and $\Delta p_{y,5}$ are relatively small, in the order of 0.010mm, which is smaller than the measurement uncertainty, resulting in no distinguishable load relationship. The negative deflection data observed is explained by a possible over-compensation by the models from element 3.

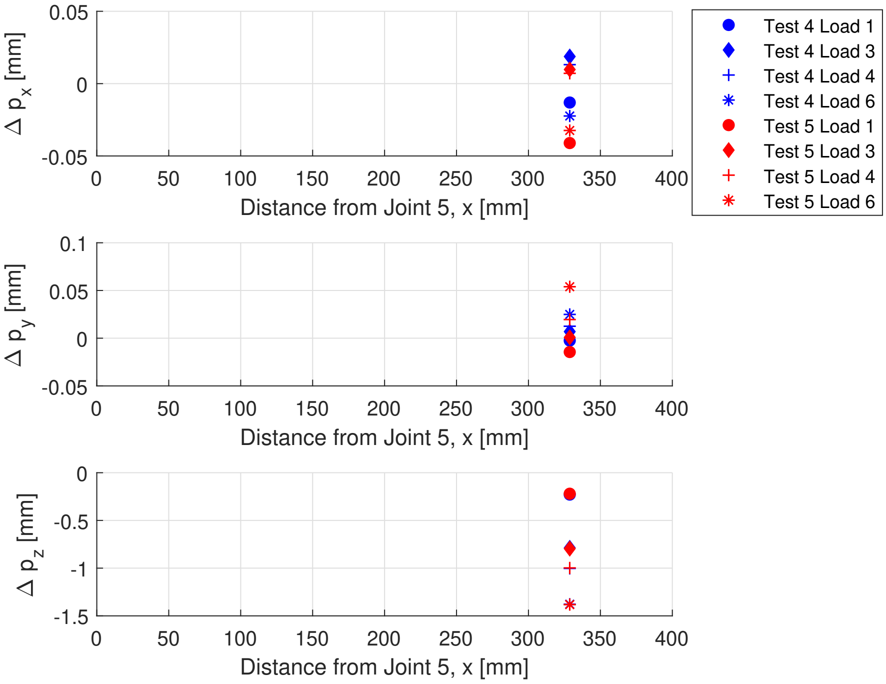

Figure 4.16: Joint 5, Link 5 deflection training data, adjusted for Joint 2 and Joint 3 prediction.

Tables 4.12 and 4.13 show the estimated model parameters and their performance in predicting the training and local validation data respectively. There is negligible difference in the final model predictions of the TCP when comparing rigid to non-rigid and a common Δp_y equation to separate $\Delta p_{y,i}$ equations for each element. This suggests initially that deflections due to link elasticity can be adequately compensated for by other parameters in the rigid body model. It also suggests that the deflection Δp_y was more observable in element 3 but could be the result of the base or joint misalignment. A comparison of the model predictions against the global validation data may provide a more conclusive insight.

Table 4.12: Element 5 estimated model parameters.

Model	C_5	Ax_5	Az_5
model1	2.8179x10^{-9}	0.005	-0.043
model2	2.7111x10^{-9}	-0.007	-0.048

Table 4.13: Element 5 model performance.

Model	**Training data rms** $\|\Delta p\|$ [mm]	**Local validation data rms** $\|\Delta p\|$ [mm]
model 1	0.058	0.046
model 2	0.059	0.049

4.2.2.4 Training data and local calibration results

For a visual analysis, the deviations of sensors along all elements and the predictions of models 1 and 2, for both training and test payloads, are presented in Figure 4.17. All models predict the target sensors similarly and relatively accurately for all element regardless of the rigid body assumptions and deflection in y models.

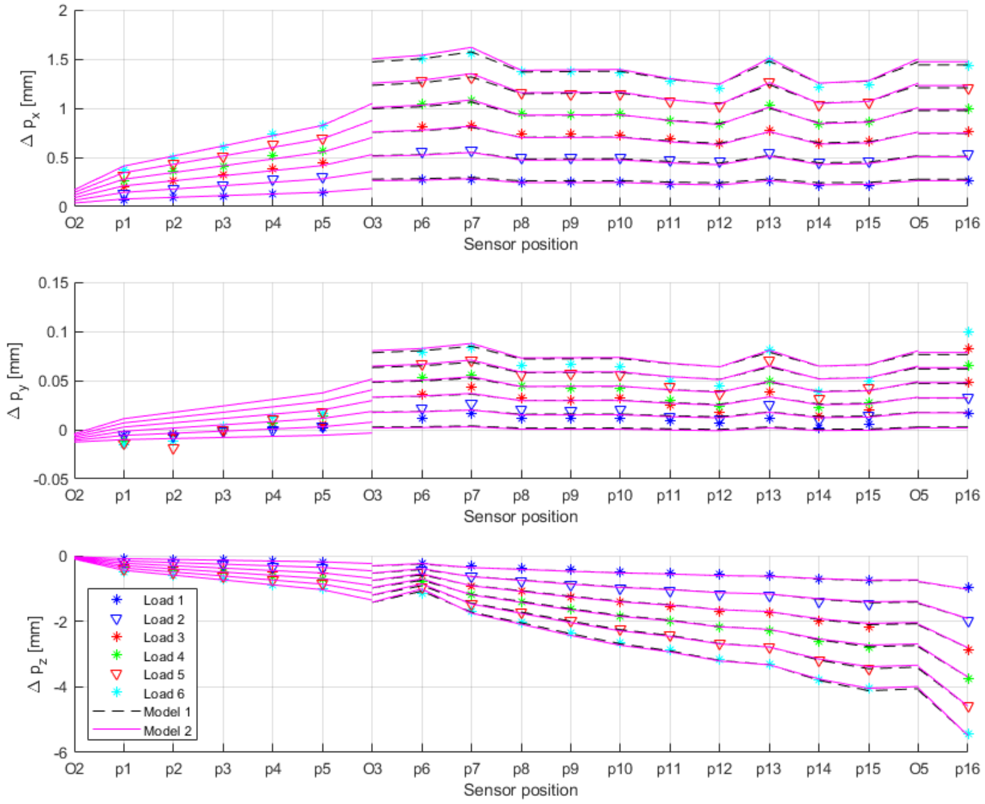

Figure 4.17: Elasticity model predictions.

4.2.2.5 Global validation results

The four competing models were evaluated in six different configurations, limited to the x_0, z_0 plane in front of the robot and visible by the laser tracker. In each configuration the robot was loaded with load 2 (532.879N) and load 4 (1064.974N).

For a visual analysis, Figure 4.18 shows the performance of the two models as an error in predicting the sensor deviations along all elements. Model 1 only marginally outperforms model 2 in nearly all configurations by up to 10μm which demonstrates that the link elasticity is observable but not significant. The accuracy of either model has a range of 50μm demonstrating that the effects of payload are greater in some configurations, which is expected.

The predictions are less accurate for higher loads which exposes the inadequacies of the models. In particular, a bias term was added to each element model which represented a bias between previous element predictions of the following element model origin. The bias term is a simple correction which represents additional distortion of the structure which will naturally increase with payload. Also, this is the likely effect of training across a wide range of payloads and the resulting model being an average. For high and relatively consistent payloads, training a model with data which closely represents the intended application should be considered.

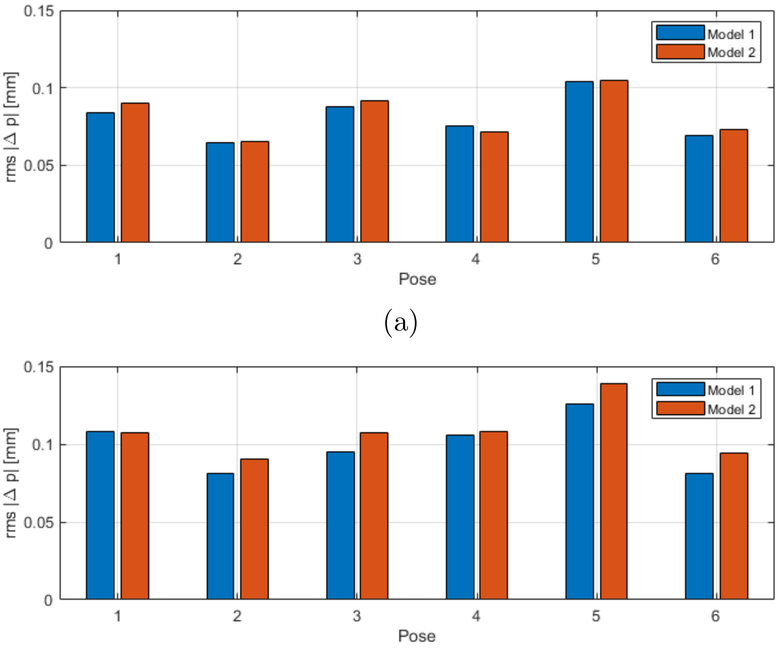

(a)

(b)

Figure 4.18: Elasticity model validation results for (a) load 2 and (b) load 4.

In Table 4.14 the results are summarised. Both models perform well in predicting deflections along the structure, with an improvement in accuracy by an order of magnitude over the nominal model. The additional link elasticity terms in model 1 provide little overall gain in accuracy with only approximately 20μm difference between models. For simplification, the model can be modelled as a rigid body with confidence.

Table 4.14: Elasticity model validation performance.

Model	**Load 2** rms $\|\Delta p\|$ [mm]	**Load 4** rms $\|\Delta p\|$ [mm]
Nominal	0.644	1.237
Model 1	0.082	0.101
Model 2	0.084	0.109

To summarise, the compliance values of joints 2, 3 and 5 can be approximated as $2.8 \times 10^{-10}, 4.0 \times 10^{-10}, 2.7 \times 10^{-9}$ rad/Nmm, respectively, to produce a representative model.

4.2.3 Discussion

In this study, the deflections in the robot structure due to joint stiffness and link elasticity were measured and a robot stiffness model was developed. The stiffness and elasticity of only some of the structural elements were identified and with only some success.

It was not possible to isolate each structural element, plus rotational displacement in parallel joints 4 and 6 were too small in comparison to the measurement uncertainty and therefore only three elements were tested. The numerical stiffness model developed in this study, has limited accuracy and the parameters can only be used as an approximate order of magnitude. In future work, a parameter estimation method that determines all compliance values simultaneously may be more successful.

The positional error at the TCP due to deflection, when the robot is carrying a 100kg payload can be as high as 3mm in p_z but also causes a significantly large positional error in p_x an p_y. In a machining application where a heavy machining spindle is used as an end effector, the joint stiffness errors may match the geometric parameter errors, in terms of resulting positional error. The joint stiffness model was therefore an important part of the numerical model.

In comparison to literature, the testbed robot deflects by approximately 60% of the 1mm per 500N, reported value which demonstrates that there is a large variation in industrial robot stiffness.

By comparing models with and without link elasticity terms, the experiment was successful in determining that the link elasticity of link 3 in particular has a measurable effect on model prediction but that a rigid body can be assumed for simplicity with marginal loss in accuracy. The residual effects of link deflection, in the order of 100μm, will be modelled as bias the GPR phase in the following studies.

4.3 Chapter summary

The aim of this chapter was to investigate error sources in an industrial robot and to develop a numerical model. The CPA and element isolation methods used in the two studies, respectively, were successful in identifying mDH parameters and a joint compliance model. The identified parameters can only be used as approximate orders of magnitude, but this is unlikely to result in a significantly different challenge compared to the true values.

Table 4.15 presents the values of the numerical model parameters (base misalignment, geometric parameter errors and joint compliance values) which are deviations from the nominal model parameters, and indicated by Δ, for example, d_1 is the geometry of link 1, whereas Δd_1 is to be estimated during calibration. Collectively, the calibration parameters are noted by θ. The parameters are separated into subsets which relate to the competing models i.e. in model M_2, the base (θ_b) and geometric parameters (θ_g) only are estimated.

The calibration, geometric parameters θ_g are added to the standard mDH table as shown in Table 4.16. Joints 2 and 3 have parallel axes and so $\Delta\beta_2$ is provided in place of Δd_2 by following the mDH convention.

Table 4.15: Numerical model (M_{actual}) parameter errors $\Delta\theta$.

Base (θ_b)	$\Delta x_0, \Delta y_0, \Delta z_0$[mm]	0.500
	$\Delta\alpha_0, \Delta\beta_0\Delta\gamma_0$[rad]	0.0017
Geom. (θ_g)	Δq_1[rad]	16x10^{-4}
	$\Delta q_{2,\ldots,6}$[rad]	-5.2x10^{-4}
	$\Delta b_1, \Delta b_{3,\ldots,6}$[mm]	-0.300
	$\Delta a_{1,\ldots,3}$[mm]	-0.300
	$\Delta a_{4,\ldots,6}$[mm]	-0.030
	$\Delta\alpha_{1,\ldots,3}3$[rad]	-2.6x10^{-4}
	$\Delta\alpha_{4,\ldots,6}$[rad]	-2.6x10^{-4}
	$\Delta\beta_2$[rad]	1x10^{-4}
Compl. (θ_c)	$C_{1,\ldots,6}$ [rad/Nmm]	$[0, 0.28, 4, 2, 2.8, 2.8, 2.8] \times 10^{-9}$

Table 4.16: Numerical model mDH table with geometric parameters for an ABB IRB 6640.

Link i	Δq_i [rad]	d_i [mm]	a_i [mm]	α_i [rad]	β_i [rad]
1	Δq_1	780 $+\Delta d_1$	320 + Δa_1	$-\pi/2 + \Delta\alpha_1$	-
2	$-\pi/2 + \Delta q_2$	0	1280 + Δa_2	$0 + \Delta\alpha_2$	$\Delta\beta_2$
3	Δq_3	0 $+\Delta d_3$	200 + Δa_3	$-\pi/2 + \Delta\alpha_3$	-
4	$\pi + \Delta q_4$	0 $+\Delta d_4$	0 + Δa_4	$-\pi/2 + \Delta\alpha_4$	-
5	Δq_5	0 $+\Delta d_5$	0 + Δa_5	$\pi/2 + \Delta\alpha_5$	-
6	Δq_6	0 $+\Delta d_6$	0 + Δa_6	$0 + \Delta\alpha_6$	-

Thesis objective 1 was met and a numerical model that can be used to simulate positional errors in the study in Chapter 5 was created from the data gathered. In addition, valuable experience was gained by following the mDH convention using the practical, CPA method.

Chapter 5

Bias Correction of Simulated Industrial Robot Positional Errors

The aim of this chapter is to meet thesis objective 2 by exploring the limitations of bias correction in predicting the positional error of a simulated robot. The calibration and GPR bias correction methodology proposed in Chapter 3 was tested on data generated by a numerical model as a controlled system, which allowed the limitations to be explored freely, whilst minimising time on the real robot. The focus was to explore limitations of bias correction in this application, with respect to training data quantity and bias reduction by calibration.

The chapter is divided into a number of case studies to meet the following objectives:

I Evaluate the positional accuracy of a simulated industrial robot. Use a numerical model to provide measured robot TCP pose data and determine pose errors compared to nominal model predictions.

II Calibrate the three competing models in addition to the nominal model, to provide a range of bias data levels in the bias correction case studies.

III Evaluate the performance of bias correction, using GPR to model and predict the robot positional error data for the case studies: 1 dim, 3 dim, 6 dim (s) and 6 dim (l).

IV In each case study, evaluate the GPR model for a range of training data quantities to determine the limitation of bias correction accuracy with consideration of practical limitations.

V In each case study, use GPR bias correction to model and predict the positional errors from each of the competing models to compare the effect of bias reduction on bias correction accuracy.

Each case study (along with results) is presented as an individual section in this chapter. The calibration study results are presented in section 5.2 along with the models used to generate data for all of the bias correction trials. The bias correction results are presented for the case studies in sections 5.3 to 5.6. In section 5.7, a final synthesis of all the case study results is presented.

5.1 Experimental design

The system model used for all case studies in this chapter is the numerical model of the ABB IRB 6640 industrial robot, shown as a simulation image from Robot Studio in Figure 5.1, which was described in Chapter 3 and modelled in Chapter 4.

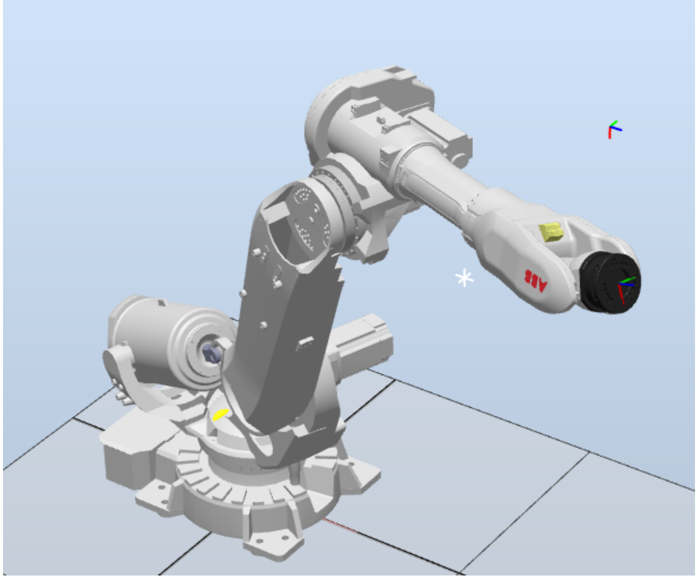

Figure 5.1: Image of an ABB IRB 6640 robot in Robot Studio.

5.1.1 TCP and Payload

On the real robot, the machining spindle is mounted at approximately -45^0 to the z_6 axis at the end of the robot. With the robot arm stretched out horizontally, the spindle will point downwards at 45^0. To continue to be representative, the TCP in the numerical study is also set at the same angle and with a tool offset of 100mm down and 150mm out relative to the end effector flange center (origin of joint 6).

The tool is expressed in the model as a H_6^t. The payload is an approximation of the spindle and fixture on the real robot in Table 5.1.

$$H_6^t = \begin{bmatrix} 0.707 & 0 & -0.707 & 100 \\ 0 & 1 & 0 & 0 \\ 0.707 & 0 & 0.707 & 150 \\ 0 & 0 & 0 & 1 \end{bmatrix} \tag{5.1}$$

Table 5.1: Numerical study payload and centre of gravity COG) location relative to the end effector.

Payload [kg]	100
COG (x, y, z)[mm]	0,0,100

5.1.2 Model parameters and calibration parameters

The range of models and calibration levels, which provide the bias data for GPR, are presented in Table 5.2 with a statement of what calibration tools were used. SVD was used as the primary parameter estimation tool for the base parameters. For the calibration of M_2 and M_3 , retrospectively, SVD was used to provide an improved initial estimate of the base parameters prior to LLSE calibration after early tests showed that the calibration was sensitive to the base parameters and an improved initial estimate avoided local minima.

Table 5.2: Description of competing model parameters and calibration tools used.

Model	Calibration parameters θ	Calibration tools
M_0	None	M_0 is the nominal model and is not calibrated
M_1	Base (θ_b)	SVD is used to calibrate the base which outputs a rotation and HTM
M_2	Base(θ_b) Geometric (θ_g)	Initial base estimate and localisation using SVD then base and geometric LLSE parameter estimation
M_3	Base (θ_b) Geometric (θ_g) Compliance (θ_c)	Initial base estimate and localisation using SVD then base, geometric and joint compliance LLSE parameter estimation

The complete model consists of 36 parameters: 6 base $[\gamma_b, \beta_b, \alpha_b, x_b, y_b, z_b]$, 24 geometric parameters $[\Delta q_1, \ldots, \Delta q_6]$,$[d_1, d_3, \ldots, d_6]$,$[a_1, \ldots a_6]$,$[\alpha_1, \ldots, \alpha_6]$,$[\beta_2]$ and 6 compliance parameters $[C_1, \ldots, C_6]$. This number is reduced for calibration with γ_b absorbed by Δq_1, and z_b absorbed by d_1 as they are not separable. In this study, the additional tool frame H_6^t is provided, assumed to be measured, as would be expected in industry, rather than estimated to reduce the number of calibration parameters.

5.1.3 Training and validation target generation

The training and validation targets for calibration and bias correction were generated as joint vectors using *Latin hypercube sampling* (LHS) between joint limits presented in Table 6.2. LHS was used to ensure maximum spacing in the joint-space whilst retaining pseudo-random generation. A wide range of joint angles were used for calibration to exploit the option in a simulation. In a machining cell, a real robot may not be able to utilise all possible joint angles as it may collide with the floor or machining bed.

Table 5.3: Numerical study joint angle limits by case study.

Joint	Calibration	Case study 1 1 dim	Case study 2 3 dim	Case study 3 6 dim (s)	Case study 4 6 dim (l)
q_1	$\pm 170^0$	5^0	$\pm 45^0$	$\pm 15^0$	$\pm 40^0$
q_2	$-65^0, 85^0$	0^0	$\pm 45^0$	$\pm 15^0$	$-15^0, 45^0$
q_3	$-180^0, 70^0$	$\pm 45^0$	$\pm 45^0$	$-15^0, 30^0$	$-15^0, 45^0$
q_4	$\pm 300^0$	0^0	0^0	$\pm 30^0$	$\pm 80^0$
q_5	$\pm 120^0$	0^0	0^0	$\pm 30^0$	$\pm 90^0$
q_6	$\pm 180^0$	0^0	0^0	$\pm 30^0$	$\pm 80^0$

5.1.4 Measurement Variation

In Chapter 3 the USM results of a preliminary, measurement uncertainty test on the Leica laser tracker was discussed. To present a similar problem to the empirical study, the same value of $\sigma_\epsilon = 13\mu$m was used in the numerical study in this chapter.

5.1.5 Euler and angle conversion

The parameter estimation method utilised full pose measurement data. That is, six equations are provided for each measurement (3 pose and 3 orientation values). The orientation of the tool was reported by the Spatial Analyzer (SA) software as ZYX Euler angles and the orientation error was reported as the error in the Euler angles $(\Delta\phi_\alpha, \Delta\phi_\beta, \Delta\phi_\gamma)$. However the functional relationship between the rotation matrix and ZYX Euler angles is discontinuous and degenerates at $\phi_\beta = \frac{\pi}{2}$. Moreover, there are different solutions for ϕ_β between $\frac{-\pi}{2}$ and $\frac{\pi}{2}$, and between $\frac{\pi}{2}$ and $\frac{3\pi}{2}$. This causes a problem when determining the linear relationship between pose error and parameter errors.

For example, in the robot home position $q_{home} = [0, 0, 0, 0, 0, 0]$, an ideal transformation with no errors between the base frame H_b and joint 6 frame H^6, is $0^0, 90^0, 0^0$ i.e. a 90^0 rotation around y_b. The transformation is shown in shown in Figure 5.2. If there is a small error in the orientation so that the actual transformation is $0^0, 90.5^0, 0^0$, the Euler angle conversion will return $-180^0, 90.5^0, -180^0$ and the orientation error will be $-180^0, 0.5^0, -180^0$. In this example the calibrated parameters will be poor, in terms of model accuracy.

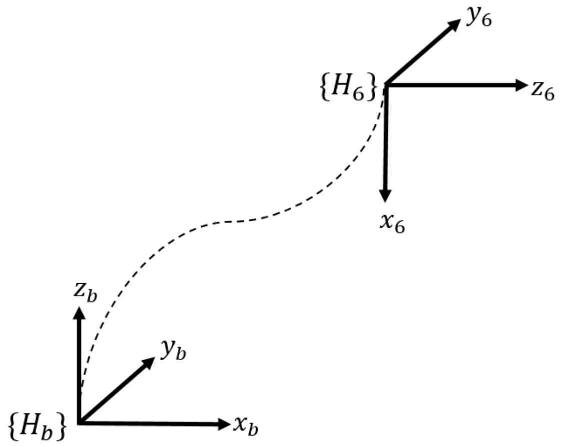

Figure 5.2: Diagram of the base frame H_b, to joint 6 frame H_6, transformation.

In this study, the simplest approach of filtering out configurations that returned orientation errors of greater than an arbitrarily chosen value of $\frac{\pi}{2}$, was used, prior to calibration.

5.2 Calibration results

In this section, the parameter estimation and accuracy results for the calibration of models M_0, M_1, M_2 and M_3 is presented. The 'true' model which includes the imposed parameter errors $\Delta\theta$, is referred to as M_{actual}. Model M_0 is the nominal model which was evaluated first to provide baseline data. Models M_1, M_2 and M_3 were then calibrated using data from 120 training poses. The prediction accuracy of all models was then compared for 998 validation poses. Two inputs were removed as outliers due to discontinuities with Euler angle conversions.

5.2.1 Nominal model accuracy

In Figure 5.3, the predictions of the training poses are presented as separate histograms in Δp_x, Δp_y and Δp_z to look for issues that may be a concern for the calibration phase. The performance of the nominal model, for both training and validation poses, is summarised as a mean and standard deviation in separate pose directions and orientations, and reported as an rms and maximum $|\Delta p|$ in Table 5.4.

The expectation was that the error Δp_z would be the largest, with a large mean ($\approx$ 3mm) due to the joint compliance. The overall positional error, in rms $|\Delta p|$ terms, was only expected to be in the order of 5mm. An initial observation is that the both the mean error in Δp_x and Δp_y, and distribution of errors in each direction was much greater than expected, which resulted in the larger rms $|\Delta p|$. Given that this model is a testbed for bias correction, discussions will revolve around whether the model is relevant and what challenges this data may provide for both calibration and bias correction. In a brief preliminary study, the error attributed to the base, geometric and joint compliance, showed that for the calibration input space, the different factors resulted in rms $|\Delta p|$ of approximately 7mm, 3mm and 6mm, respectively. The large mean error in Δp_x and Δp_y may be attributed in part to high base misalignment values. The large error from the base is a consequence of the sensitivity of the end effector position to any small misalignment at the base, scaled by a long arm length. However, although high, the bias resulting from the base misalignment is not expected to be challenging for either the parameter estimation during calibration or for the bias correction to learn in $M_{0,GP}$.

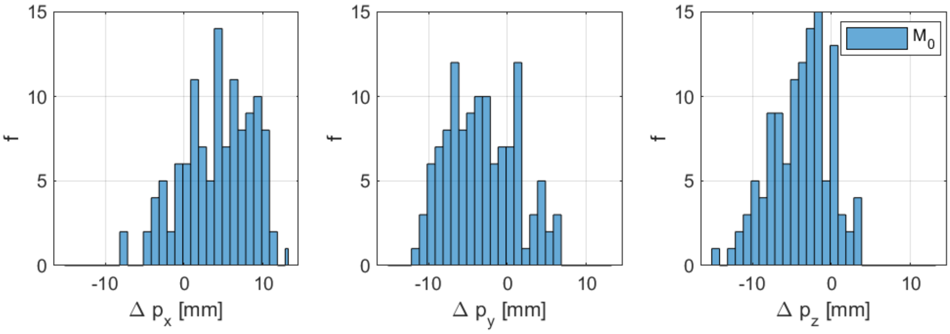

Figure 5.3: Numerical study, distribution of training bias data results for model M_0. f: frequency (number of measurements).

Table 5.4: Numerical study, summary of training bias data results for model M_0.

	M_0 Training	M_0 Validation
$\Delta\bar{p}_x$ (std) [mm]	4.191 (4.500)	3.912 (4.354)
$\Delta\bar{p}_y$ (std) [mm]	-3.206 (4.402)	-2.712 (4.311)
$\Delta\bar{p}_z$ (std) [mm]	-3.868 (3.742)	-4.118 (3.988)
$\Delta\bar{\phi}_\alpha$ (std) [deg]	0.210 (0.314)	0.165 (0.349)
$\Delta\bar{\phi}_\beta$ (std) [deg]	0.010 (0.155)	0.020 (0.153)
$\Delta\bar{\phi}_\gamma$ (std) [deg]	0.008 (0.295)	0.025 (0.331)
rms $\lvert\Delta p\rvert$ (max) [mm]	9.797 (17.528)	9.644 (20.319)

5.2.2 Estimated Parameters

The actual and estimated parameter errors from calibration are presented in Table 6.6.

The estimated parameters by calibration of the base only by M_1 , provides a useful insight into the error form. Four of the parameters remain similar to the actual parameters which suggests that the geometric and compliance errors produce relatively small errors in the $\Delta\beta_0, \Delta\alpha_0, \Delta x_0$ and Δy_0 directions. The estimations of $\Delta\gamma_0$ and Δz_0 are considerably larger than the actual parameters. $\Delta\gamma_0$ can be explained by the addition of the base rotation $\Delta\gamma_0$ and joint 1 error Δq_1 which were in the same direction and their sum is very close to the estimation of $\Delta\gamma_0$ alone.

Models M_2 and M_3 used the parameters from M_1 as an initial estimate to help avoid local minima. $\Delta\gamma_0$ and Δz_0 were fixed to avoid rank deficiency. The parameter changes were absorbed into Δq_1 and Δd_1 which were in the same directions as $\Delta\gamma_0$ and Δz_0 and the number of calibration parameters was reduced by two.

Model M_3 is a compete model with all error parameters estimated. The geometric and compliance parameters were accurately estimated which gives confidence in the method. Small errors in the base parameters may be explained by the measurement variation.

Table 5.5: Numerical study, calibrated parameters for competing models.

$\Delta\theta$	M_{actual}	M_1	M_2	M_3
$\Delta\gamma_0(10^{-3})$ [rad]	1.700	3.068	3.068	3.068
$\Delta\beta_0(10^{-3})$ [rad]	1.700	1.632	1.833	1.698
$\Delta\alpha_0(10^{-3})$ [rad]	1.700	1.828	1.499	1.702
Δx_0 [mm]	0.500	0.633	0.241	0.493
Δy_0 [mm]	0.500	0.648	0.051	0.507
Δz_0 [mm]	0.500	-3.806	-3.806	-3.806
Δd_1 [mm]	-0.300	-	-0.112	4.006
Δd_2 [mm]	-	-	-	-
Δd_3 [mm]	-0.300	-	-0.864	-0.300
Δd_4 [mm]	-0.300	-	0.954	-0.300
Δd_5 [mm]	-0.300	-	0.052	-0.300
Δd_6 [mm]	-0.300	-	-0.284	-0.300
Δa_1 [mm]	-0.300	-	0.573	-0.300
Δa_2 [mm]	-0.300	-	-0.493	-0.300
Δa_3 [mm]	-0.300	-	-0.959	-0.300
Δa_4 [mm]	-0.030	-	0.112	-0.030
Δa_5 [mm]	-0.030	-	-0.071	-0.030
Δa_6 [mm]	-0.030	-	-0.149	-0.030
$\Delta q_1(10^{-3})$ [rad]	1.600	-	0.509	0.232
$\Delta q_2(10^{-3})$ [rad]	-0.520	-	-1.551	-0.520
$\Delta q_3(10^{-3})$ [rad]	-0.520	-	0.698	-0.520
$\Delta q_4(10^{-3})$ [rad]	-0.260	-	-0.824	-0.260
$\Delta q_5(10^{-3})$ [rad]	-0.260	-	0.177	-0.260
$\Delta q_6(10^{-3})$ [rad]	0.100	-	0.549	0.100
$\Delta\alpha_1(10^{-3})$ [rad]	-0.260	-	-4.63E-02	-0.260
$\Delta\alpha_2(10^{-3})$ [rad]	-0.260	-	-4.12E-01	-0.260
$\Delta\alpha_3(10^{-3})$ [rad]	-0.260	-	4.20E-01	-0.260
$\Delta\alpha_4(10^{-3})$ [rad]	0.100	-	-5.17E-01	0.100
$\Delta\alpha_5(10^{-3})$ [rad]	0.100	-	8.77E-01	0.100
$\Delta\alpha_6(10^{-3})$ [rad]	0.100	-	8.92E-02	0.100
$\Delta\beta_2(10^{-3})$ [rad]	0.100	-	4.88E-01	0.100
C_1 [(10^{-9})rad/Nmm]	0.28]	-	-	0.28
C_2 [(10^{-9})rad/Nmm]	4.00	-	-	4.00
C_3 [(10^{-9})rad/Nmm]	2.80	-	-	2.80
C_4 [(10^{-9})rad/Nmm]	2.80	-	-	2.80
C_5 [(10^{-9})rad/Nmm]	2.80	-	-	2.80
C_6 [(10^{-9})rad/Nmm]	2.80	-	-	2.80

5.2.3 Results of calibrated model predictions

The prediction results of the competing models are summarised in Tables 6.7 and 6.8 for comparison, and then presented as histograms of errors in $\Delta p_x, \Delta p_y$ and Δp_z for visual analysis. As expected, the complete model M_3, produced results with a similar accuracy to the imposed measurement variation $\sigma_\epsilon = 13\mu$m. With no error due to unmodelled errors or incorrect parameter estimations, the accuracy of M_3 simply confirms LLSE as a suitable tool in this application, but the model does not provide a useful test bed from which to generate bias data for GPR.

The competing models M_1 and M_2 reduce the residual error to approximately a half that of M_0, but remain far in excess of what was expected. Anecdotally, after calibration, the accuracy of similar, real robots is approximately 0.3mm to 1mm, compared to the 4mm in this simulation. The mean errors in $\Delta p_x, \Delta p_y$ and Δp_z were reduced to almost zero as expected, which can be attributed almost entirely to the base calibration. The remaining, large rms $|\Delta p|$ of approximately 4mm is likely the result of the joint compliance errors. When measured over a wide range of configurations the joint compliance errors may produce a wide distribution of positional errors which cannot be effectively modelled with a simple base parameter or joint orientation parameter. This is an effect that may be seen in the real system in Chapter 6.

Table 5.6: Numerical study, summary of training bias data results for competing calibration models M_0, M_1, M_2 and M_3.

	M_0	M_1	M_2	M_3
$\Delta \bar{p}_x$ (std) [mm]	4.191 (4.500)	-0.001 (1.955)	-0.001 (1.706)	-0.001 (0.012)
$\Delta \bar{p}_y$ (std) [mm]	-3.206 (4.402)	0.002 (1.949)	0.002 (1.934)	0.002 (0.013)
$\Delta \bar{p}_z$ (std) [mm]	-3.868 (3.742)	0.000 (2.922)	0.000 (2.700)	0.000 (0.011)
$\Delta \bar{\phi}_\alpha$ (std) [deg]	0.210 (0.315)	0.037 (0.266)	0.031 (0.239)	0.000 (0.000)
$\Delta \bar{\phi}_\beta$ (std) [deg]	0.010 (0.155)	-0.003 (0.126)	0.010 (0.121)	0.000 (0.000)
$\Delta \bar{\phi}_\gamma$ (std) [deg]	0.008 (0.295)	0.019 (0.238)	0.000 (0.215)	0.000 (0.000)
rms $\lvert\Delta p\rvert$ (max) [mm]	9.797 (17.528)	4.003 (8.147)	3.718 (7.501)	0.021 (0.040)

Table 5.7: Numerical study, summary of validation bias data results for competing models M_0, M_1, M_2 and M_3.

	M_0	M_1	M_2	M_3
$\Delta\bar{p}_x$ (std) [mm]	3.912 (4.354)	0.103 (2.101)	0.149 (1.910)	0.000 (0.013)
$\Delta\bar{p}_y$ (std) [mm]	-2.712 (4.311)	0.096 (2.227)	0.044 (1.993)	0.000 (0.013)
$\Delta\bar{p}_z$ (std) [mm]	-4.118 (3.988)	-0.264 (2.966)	-0.189 (2.731)	0.000 (0.013)
$\Delta\bar{\phi}_\alpha$ (std) [deg]	0.165 (0.349)	-0.021 (0.294)	-0.026 (0.296)	0.000 (0.000)
$\Delta\bar{\phi}_\beta$ (std) [deg]	0.020 (0.153)	0.020 (0.126)	0.026 (0.126)	0.000 (0.000)
$\Delta\bar{\phi}_\gamma$ (std) [deg]	0.025 (0.331)	0.018 (0.261)	-0.001 (0.263)	0.000 (0.000)
rms $\lvert\Delta p\rvert$ (max) [mm]	9.644 (20.319)	4.272 (9.842)	3.889 (7.656)	0.023 (0.057)

The distribution of errors for models M_1 and M_2 shown in Figures 6.5 are similar suggests that much of the error due to geometric parameters can be modelled as a simple bias. Looking forward, the base calibration may provide a similar reduction in overall bias but it remains to be seen whether the additional complexity of the bias form resulting from the geometric parameters will affect the bias correction performance.

The skewed distribution in Δp_z for models M_1 and M_2 also suggests that a large portion of errors due to joint compliance are modelled relatively accurately, there remains configurations with poor predictions and large deflections.

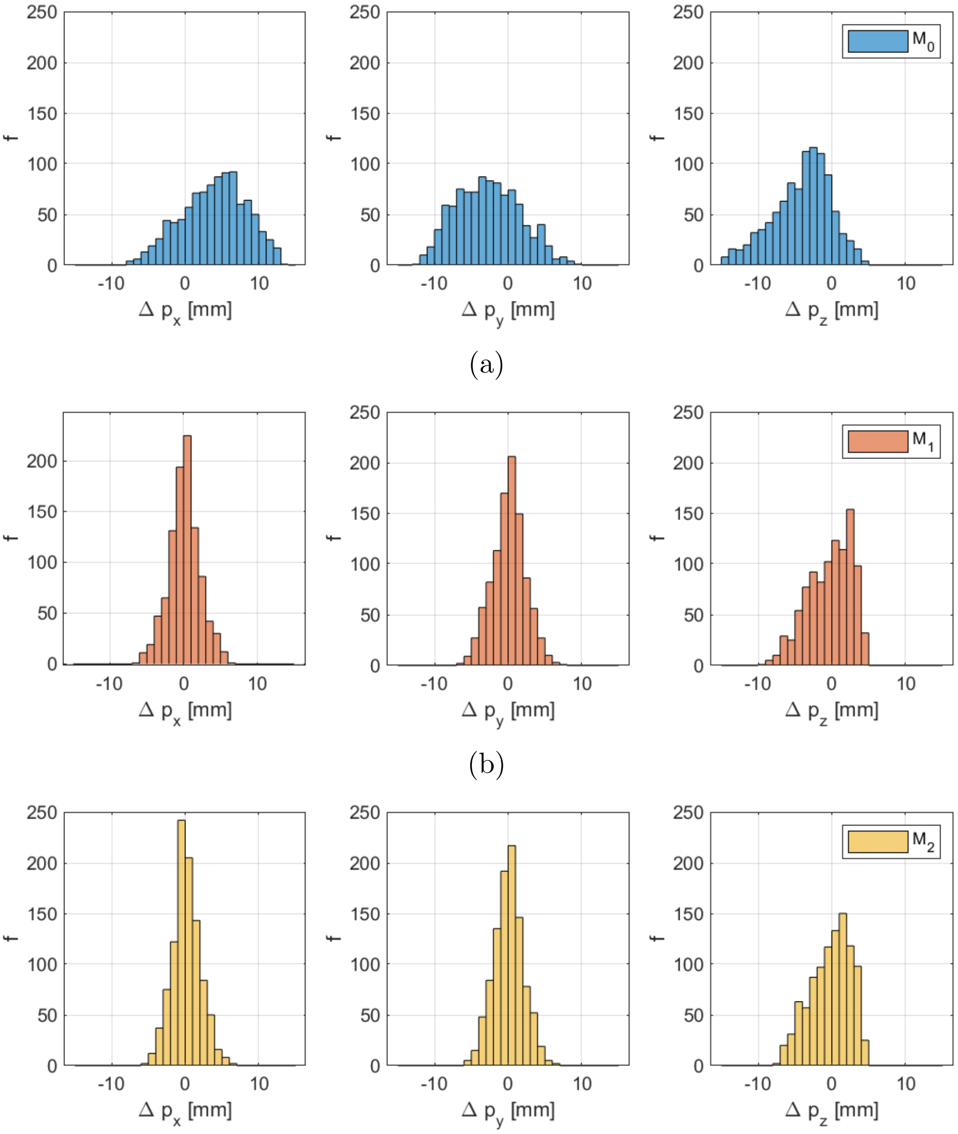

(a)

(b)

(c)

Figure 5.4: Numerical study, distribution of validation bias data results for competing models. f: frequency (number of measurements).

5.2.4 Summary

The aim of the calibration study was to evaluate the problem and create calibration models that would present the bias correction phase with a range of bias levels. The models were successfully calibrated with 120 training data poses and validated with 1000 poses with a wide range of joint angles. The nominal model (M_0) positional errors are higher than is expected in the real system (0.96mm compared to an expectation of approximately 3mm to 5mm), but the distribution of errors does not suggest that the problem is any more complex.

While M_0 was expected to produce the most challenging data set for bias correction, M_1 and M_2 have produced very similar data. However, it is still useful to explore whether the bias form will be smoother and therefore less changing for bias correction with the additional geometric parameters calibrated in M_2. Both M_1 and M_2 shall continue to provide data for the bias correction case studies. M_3 was a complete parameter model and successfully modelled the robot poses with an accuracy that matched the measurement variation. As such, there was no bias to be learned and M_3 was progressed to provide data for the proceeding case studies. This is not expected to be the case in the real system where other unmodelled errors may remain.

The challenge of finding a global minima when using LLSE as a parameter estimation tool was exposed when calibrating models M_2 and M_3. The solution was particularly sensitive to the initial estimate of the base parameters which is expected given that by simply arm length scaling. From an initial estimate of zero, as with all other parameters, local minima were found and the predictions were poor. By using the SVD base calibration as an initial estimate, a large step towards the global solution was made and the optimal solution found. An initial localisation of the data by base calibration is proposed as the approach in all studies in this thesis. SVD is described by Zhuang and Roth [120] and used by Yun et al. [76] as a simple calibration tool to obtain least squares parameter solutions. The sensitivity to parameter initial estimates, and thus the use of SVD, is not disclosed in related robot calibration research literature.

5.3 Bias correction of robot positional error with 1 joint angle input

The aim of this first case study is to test the proposed bias correction method in predicting robot positional error by presenting it with a 1 dimensional problem (referred to herein as 1 dim). Only the angle of joint 3 (q_3) was used as an input variable while other joint angles were fixed. The bias form is expected to be relatively simple and smooth, with many of the error parameter interactions being constant. For example, without rotation of joints 4 or 6, the twist in the structure is expected to be negligible. The identification of kernel hyperparameters is also expected also be the simplest case with only three hyperparameters required. In this case study, the effect of training data size on prediction accuracy will not be evaluated. The bias form is simple and only uncertainty between training data points is likely to change with data quantity. The results of this study are expected to be a starting point and motivation to test the methodology with more challenging cases.

The results will be presented in the following subsections: Analysis of nominal model M_0 data as a baseline; analysis of hyperparameter estimations; and prediction results for competing models using GPR.

5.3.1 Baseline data

The residual positional error between the actual robot model M_{actual} and competing model predictions in a range of configurations is presented as bias data for prediction using GPR. The bias data from M_0 is presented in Figure 5.5 as an example, with M_1 and M_2 showing similar forms.

The form of the bias data is a good example of the desirable *smooth* function that is ideally suited to GPR-based bias correction. It is expected that the data may be modelled accurately with bias correction, assuming sufficient training data. The largely sinusoidal form of the bias observed may be explained by an analysis of the robot kinematics as joint 3 is rotated, and torque characteristics from the payload during the rotation. As joint 3 (an elbow joint) rotates from 50^0 to outstretched and then to -50^0, the distance of the payload to joints 2 and 3 increases and then decreases again. The subsequent torques and deflections Δp_z (vertical deflection) and Δp_x (deflection outwards, away from the base) can be described as cosine and sine functions respectively. The error Δp_y would not be expected in the x, z planar motion but is present due to a misalignment in the base and joint 2 (β_2).

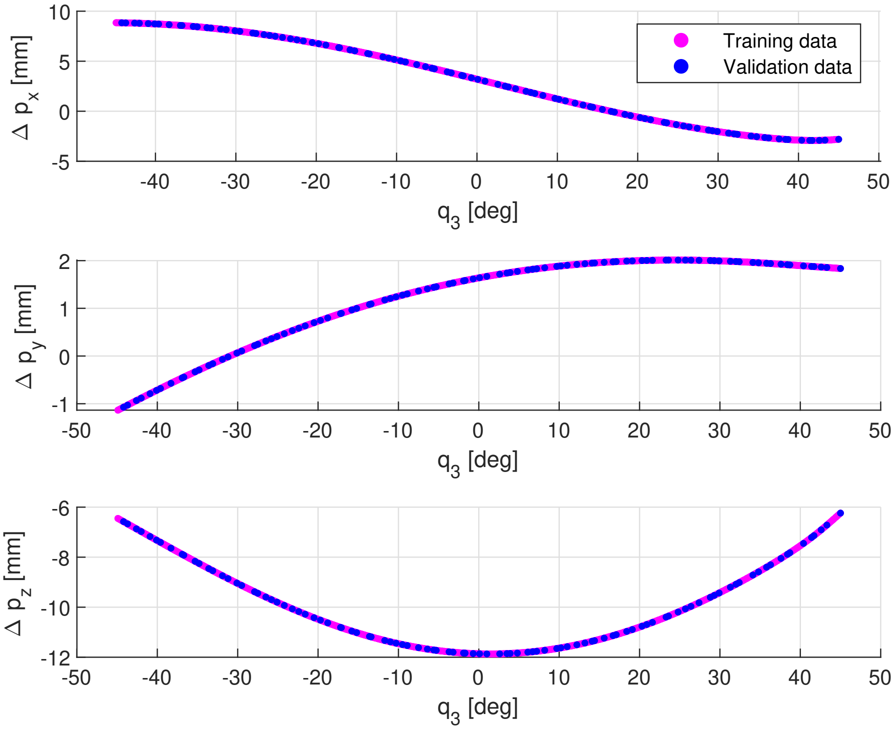

Figure 5.5: Numerical study, training and validation bias data from model M_0 in the 1 dim case study.

The results in predicting training and validation data by the competing models are summarised in Tables 5.8 and 5.9 respectively and provides an evaluation of the task provided to the GPR. The high bias levels and wide distribution are the result of substantially large, unmodelled joint compliance deflections. However, given the smooth form of the bias, it is still expected that the GPR will model the data accurately.

Table 5.8: Numerical study, summary of training bias data results for competing models M_0, M_1, M_2 and M_3 in the 1 dim case study.

	M_0	M_1	M_2
$\Delta\bar{p}_x$ (std) [mm]	3.077 (4.142)	-0.625 (3.089)	0.232 (3.087)
$\Delta\bar{p}_y$ (std) [mm]	1.191 (0.933)	-0.618 (0.454)	-0.608 (0.544)
$\Delta\bar{p}_z$ (std) [mm]	-9.927 (1.676)	-3.676 (1.480)	-3.016 (1.495)
rms $\|\Delta p\|$ (max) [mm]	11.405 (12.640)	5.109 (5.683)	4.632 (4.889)

Table 5.9: Numerical study, summary of validation bias data results for competing models M_0, M_1, M_2 and M_3 in a 1 dim case study.

	M_0	M_1	M_2
$\bar{\Delta p_x}$ (std) [mm]	3.071 (4.122)	-0.629 (3.074)	0.228 (3.072)
$\bar{\Delta p_y}$ (std) [mm]	1.190 (0.928)	-0.621 (0.452)	-0.612 (0.541)
$\bar{\Delta p_z}$ (std) [mm]	-9.930 (1.665)	-3.679 (1.470)	-3.018 (1.485)
rms $\lvert\Delta p\rvert$ (max) [mm]	11.404 (12.653)	5.109 (5.715)	4.632 (4.901)

5.3.2 Hyperparameter estimation

A squared-exponential (SE) kernel for a single input variable GP has 3 hyperparameters: σ_f is the signal variance (scaling in the y axis i.e. position prediction), l_1 is the characteristic length scale, (one per input variable) which scales the input, and σ_n is the noise term.

Searching for the hyperparameters which maximise the marginal likelihood may lead to local minima. While local minima are simply different interpretations of the data and not incorrect, a global minima is desirable. An initial investigation showed that there were no local minima in this case and an initial estimate of $h_0 = [1, 1, 1]$ as a vector of hyperparameters was used.

An initial analysis of the hyperparameter estimates is taken as a precautionary measure to identify modelling issues. Firstly, σ_n is approximately equal to the measurement variation σ_ϵ which is an indication that the data is modelled with high accuracy. An order of magnitude smaller suggests that the model was overfitting and confidence in predictions may deteriorate rapidly for inputs that are distant from training data. If σ_n is an order of magnitude larger than σ_ϵ, a portion or the bias would be described as noise and model predictions are less accurate. If the length scale $l_1 < 1$ then the model is more free to rise and fall quickly. For highly non-linear data this may allow the model to react quickly to bias changes and model more accurately, otherwise this may be an indication of overfitting. $l_1 >> 1$ suggests that the model is insensitive to the input variable and will react very little to changes in the bias.

For notation purposes, the GPR model associated with the competing model bias data is denoted by a subscript $_{GP}$. For example, $M_{1,GP}$ is the GPR model determined from the M_1 model bias data. The optimal hyperparameters selected for each of models i.e. $M_{0,GP}$, $M_{1,GP}$ and $M_{2,GP}$ are presented in Table 5.10. For each model, l_1

is close to 1 which again suggests that the model does not overfit or ignore the data. The expectation is that the training data are modelled accurately without overfitting.

Table 5.10: Numerical study, hyperparameter estimates for competing models in the 1 dim case study.

Model		σ_f	l_1	σ_n
$M_{0,GP}$	$h(\Delta p_x)$	4.34	0.92	0.013
	$h(\Delta p_y)$	2.58	1.83	0.013
	$h(\Delta p_z)$	9.10	1.00	0.011
$M_{1,GP}$	$h(\Delta p_x)$	3.29	0.86	0.013
	$h(\Delta p_y)$	0.48	1.30	0.013
	$h(\Delta p_z)$	8.14	0.99	0.011
$M_{2,GP}$	$h(\Delta p_x)$	3.37	0.86	0.013
	$h(\Delta p_y)$	0.62	1.48	0.014
	$h(\Delta p_z)$	88.39	0.99	0.011

5.3.3 Results of bias correction

Figure 5.6 shows an example of the training data and mean prediction of $M_{0,GP}$ for a visual analysis. A portion of the input range ($\pm 15^0$) and the training data only is presented for clarity.

As expected, model $M_{0,GP}$ follows the form of the bias and model predictions will be improved. Given the abundance of training data and accuracy of the predictions, the confidence is very high and the prediction variance (presented as $\pm 2\sigma$) is too small to display. The results are summarised in Table 5.11. Bias correction models $M_{0,GP}$, $M_{1,GP}$ and $M_{2,GP}$ perform equally and the results are presented together. As expected, the prediction accuracy was not affected by bias size, given the simplicity of the bias form, and the predictions were limited only to σ_n which is the ideal case.

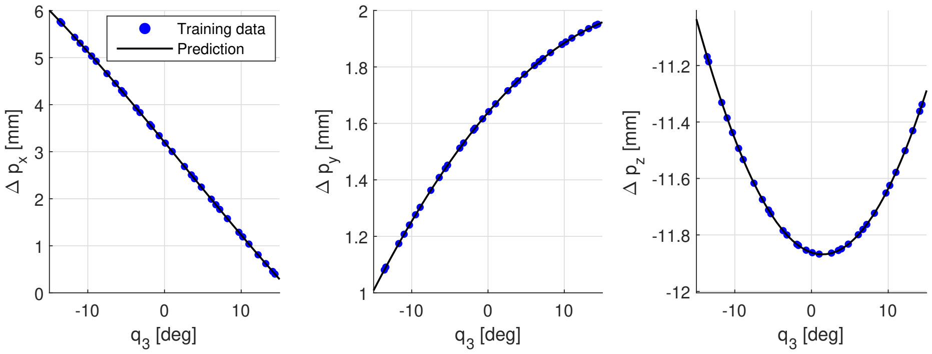

Figure 5.6: Numerical study, prediction results of training data bias correction for model $M_{0,GP}$ in the 1 dim case study.

Table 5.11: Numerical study, summary of training and validation data bias correction results for models $M_{0,GP}$, $M_{1,GP}$ and $M_{2,GP}$ in the 1 dim case study.

	Training	Validation
$\Delta\bar{p}_x$ (std) [mm]	0.000 (0.012)	-0.001 (0.014)
$\Delta\bar{p}_y$ (std) [mm]	0.000 (0.013)	0.003 (0.014)
$\Delta\bar{p}_z$ (std) [mm]	0.000 (0.011)	-0.001 (0.014)
rms $\lvert\Delta p\rvert$ (max) [mm]	0.021 (0.043)	0.024 (0.059)

5.3.4 Summary

The aim of the study in this section was to test the bias correction method on a simple 1 dim case study. The study was an example of an ideal case, exploiting an abundance of training data and estimating a small number of hyperparameters.

The effect of bias level, produced by the competing models, was negligible and the accuracy of all bias correction models were limited only by the measurement variation.

5.4 Bias correction of robot positional error with a 3 joint angle input

The aim of this study is to continue to investigate the limitations of bias correction by increasing the complexity of the problem to 3 input variables (referred to herein as 3 dim). In this study, only joints 1, 2 and 3 were rotated whilst all other joint angles were fixed. The challenge of prediction of bias data in relation to training data quantity and bias reduction from competing models are tested.

The effect of bias reduction may become more important in this study compared to the 1 dim case. A GP's penalises more complex functions and so if the bias form is too complex (i.e. highly non-linear), then reducing the complexity of the bias form may provide an easier challenge for bias correction and a more accurate model.

In addition, the number of hyperparameters to estimate is higher than the 1 dim case and a strategy to avoid local minima is a design consideration. Hyperparameter estimation and data quantity studies were run in parallel to determine optimal conditions.

5.4.1 Training data quantity

Bias correction accuracy is expected to improve by increasing the training data quantity as long as it is appropriately distributed and fills the same hypercube as the test data. While a numerical study can exploit this, the decisions made in this chapter will be mindful of the cost in terms of computation and also the practicality of measuring any proposed quantity of data in the experimental chapter. It may be more useful to retain some resemblance to the experimental study for comparison.

Figure 5.7 shows the residual error in predicting the validation set, after bias correction, in terms of rms $\Delta p_x, \Delta p_y$ and Δp_z separately, against increasing training data size. Given the approach of using a range of initial estimates, three initial estimates are presented and the optimal would typically be chosen. Firstly, it is evident by a spike in results for h_3 that the model is sensitive to the initial estimate even at high numbers of training data. The solution is therefore to continue to search for hyperparameters and select the optimal based on the minimum rms Δp. The results show that with the optimal hyperparameter selection there is only a marginal change of approximately 10μm between 200 and 1000 training data inputs. A reasonable compromise is 300 training data inputs which will form the basis for this study.

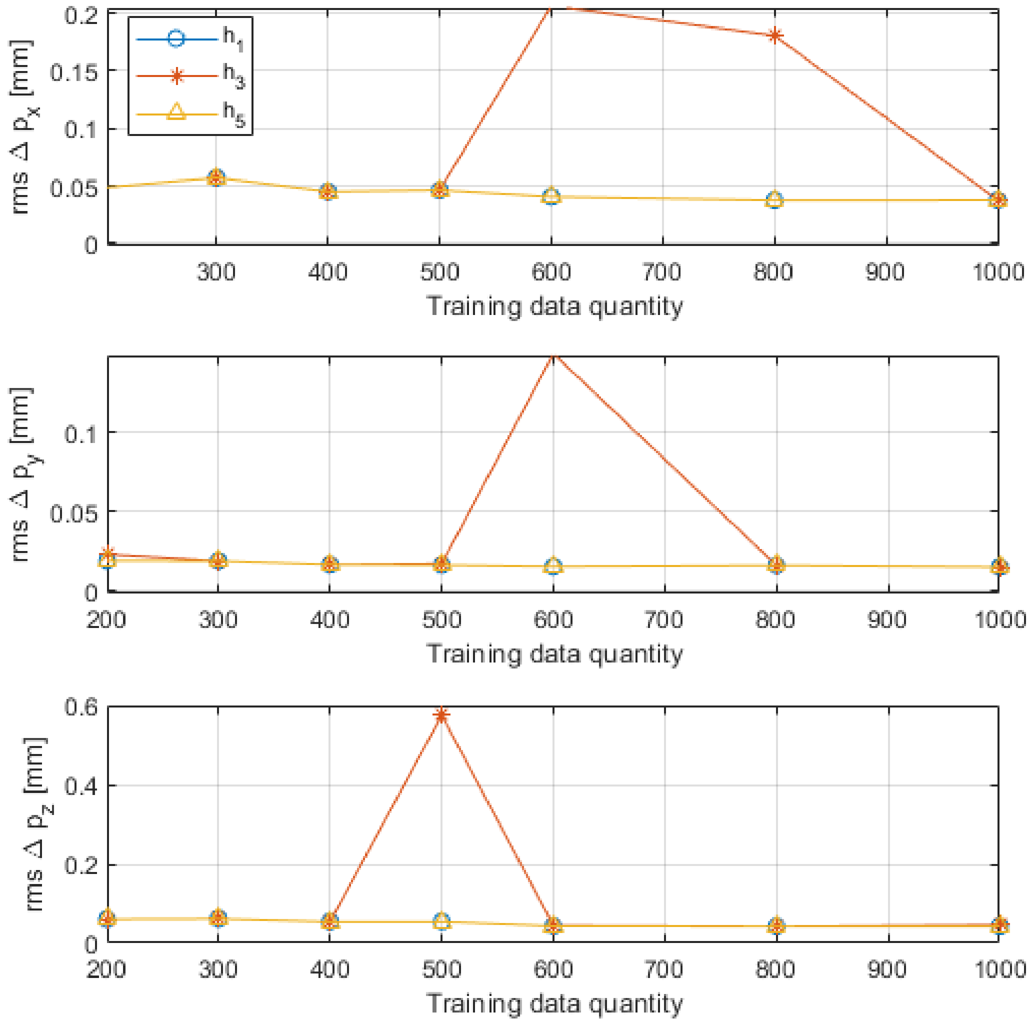

Figure 5.7: Convergence plot of bias correction prediction accuracy against training data quantity for model $M_{0,GP}$ in the 3 dim case study.

5.4.2 Baseline data

Figure 5.8 shows the distribution of validation bias data generated by the competing models for a visual analysis.

The bias data from M_1 and M_2 have very similar distributions and may present a similar challenge for bias correction. The similarity suggests that the majority of the positional error resulting from geometric error and joint compliance, or at least the complex form, can be modelled by base localisation. The payload will mostly produce a deflection downwards which can be modelled in part by an additional base or joint 1 rotation. The form of the joint compliance error does not produce a form that is as complex as expected. Base calibration alone however does present a significantly different challenge with a different and wider distribution of bias data in M_0 compared to M_1 and M_2.

A different challenge may be presented to bias correction of Δp_x, Δp_y and Δp_z with each showed different distributions.

The distribution of bias data in Δp_x indicates some bi-modality. Bi-modality indicates that the two modes are created by two data sets that could be separated. This could be by workspace regions or error sources. One probable cause would be the deflection in Δp_x resulting from joint compliance. While the deflection is always downwards in Δp_z, if the arm is raised above the horizontal, joint compliance will cause the TCP to deflect forward (positive error). If the arm is lowered below horizontal the deflection will be backwards (negative error). This possible explanation is partially supported by the smaller peaks in the data of M_1 and M_2. If this is the case, the separate data sets should not be a problem for GPR. The bias is modelled over a hyperplane of joint angles the bias form resulting from raised or lowered arms should will be modelled locally in separate regions. This would not be the case if the input variables were Cartesian co-ordinates.

The distribution of data in Δp_y is Gaussian which does not suggest any additional challenges.

The skewed distribution in the Δp_z bias data can again be explained by joint compliance deflections which will almost always be in the negative z direction. The distribution of bias data then does not necessarily indicate concerns for bias correction or the use of GPR.

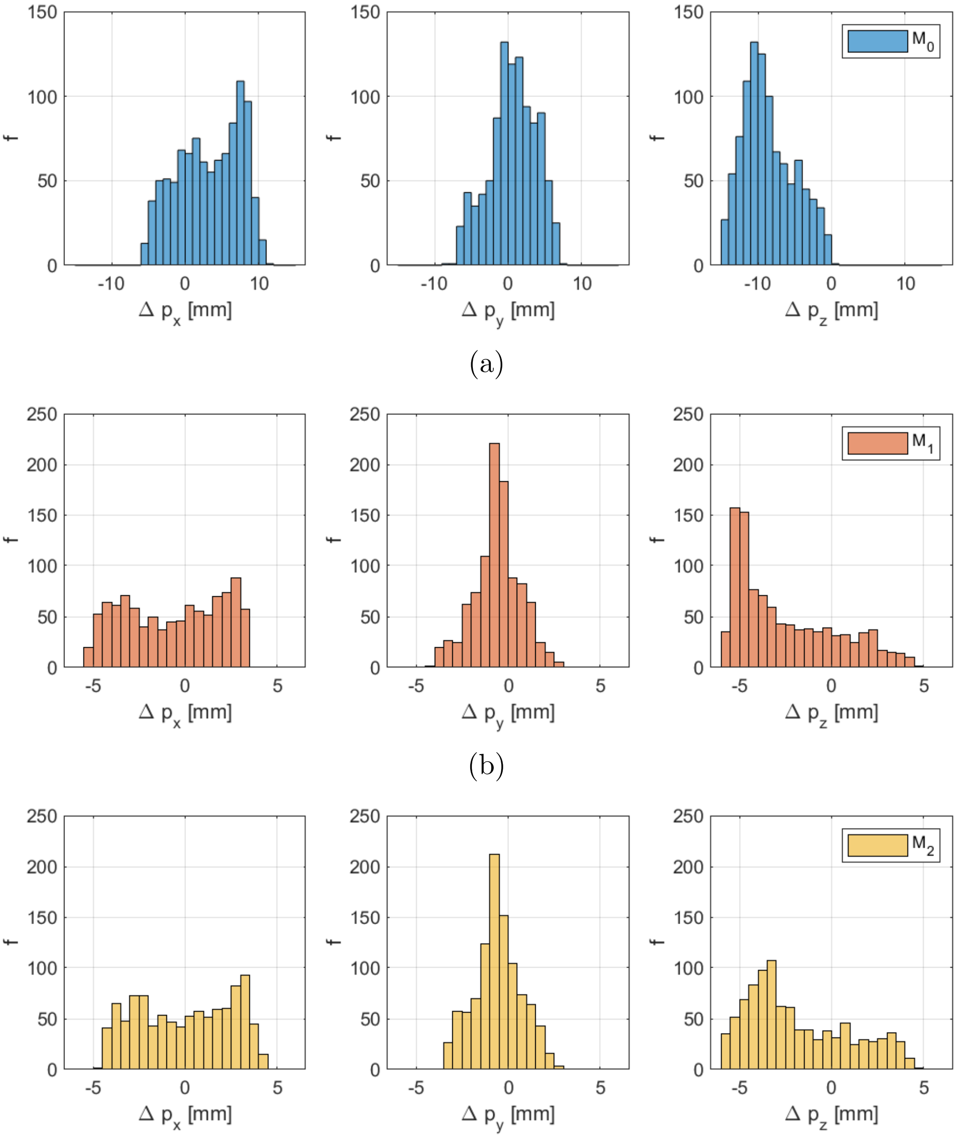

(a)

(b)

(c)

Figure 5.8: Numerical study, distribution of validation bias data results for competing models (a)M_0, (b)M_1 and (c)M_2 in the 3 dim case study. f: frequency (number of measurements).

The results in predicting training and validation data by the competing models are summarised in Tables 5.12 and 5.13 respectively and provides an evaluation of the task provided to the GPR.

Interestingly, the rms $|\Delta p|$ in the 3 dim case is of a similar magnitude to the 1 dim case. In fact, Δp_x and Δp_z standard deviations are similar to the 1 dim case which suggest that again, the results are dominated by the payload and joint compliance error.

The similarity in results between training and validation data is an indication that the training data provides good spatial coverage and that an accurate model of the training data should produce an accurate prediction of the validation data.

The bias data from M_1 and M_2 are again very similar in magnitude and distribution, and may not provide the GP with sufficiently different challenges. However, this can easily be confirmed in a numerical model.

Table 5.12: Numerical study, summary of training bias data for competing models in the 3 dim case study.

	M_0	M_1	M_2
$\Delta\bar{p}_x$ (std)[mm]	3.327 (4.321)	-0.585 (2.629)	0.080 (2.547)
$\Delta\bar{p}_y$ (std)[mm]	0.598 (3.066)	-0.592 (1.226)	-0.555 (1.240)
$\Delta\bar{p}_z$ (std)[mm]	-8.583 (3.388)	-2.537 (2.723)	-1.998 (2.751)
rms $\lvert\Delta p\rvert$ (max)[mm]	11.159 (17.295)	4.786 (6.001)	4.455 (6.470)

Table 5.13: Numerical study, summary of validation bias data for competing models in the 3 dim case study.

	M_0	M_1	M_2
$\Delta\bar{p}_x$ (std)[mm]	3.220 (4.288)	-0.690 (2.617)	-0.015 (2.529)
$\Delta\bar{p}_y$ (std)[mm]	0.598 (3.185)	-0.595 (1.260)	-0.557 (1.258)
$\Delta\bar{p}_z$ (std)[mm]	-8.533 (3.529)	-2.486 (2.732)	-1.944 (2.801)
rms $\lvert\Delta p\rvert$ (max)[mm]	11.157 (17.401)	4.785 (6.065)	4.461 (6.482)

5.4.3 Hyperparameter search

The SE kernel for a GP with three input variables has five hyperparameters, σ_f, σ_n and a length scale for each input variable (joint angle) l_1, l_2, l_3. The hyperparameter search was conducted from an initial estimate of $h_0 = [1, 1, 1, 1, 1]$ after an initial investigation showed that all searches converged to the same solution, indicating that there are no local minima near to the expected solutions. The hyperparameter search may still be sensitive to the initial estimate as the number of input dimensions increases.

The estimated hyperparameters for each set of bias data are presented in Table 5.14. $\sigma_n > \sigma_\epsilon$ in Δp_x and Δp_z which indicates that the model does not ideally fit the bias form and so a portion of the bias must be explained as 'noise' to prioritise a smooth fit. The expectation is that the accuracy of the predictions will be higher than the measurement variation.

The length scale parameters are all of a similar order and close to 1 which provides confidence that all the model is not attempting to overfit and the bias is a function of all parameters which is expected. The largest range of length scales can be seen in $h_1(\Delta p_z)$ for both models $M_{1,GP}$ and $M_{2,GP}$. l_1 which represents the angle of joint 1 is x4 larger than l_2 which represents joint 2. This demonstrates that the vertical deflection in z is relatively insensitive to the rotation of joint 1 which as a vertical axis, which is as expected. The ratio of length scales can be used as an indication of model sensitivity.

Table 5.14: Numerical study, hyperparameter estimates for competing models in the 3 dim case study.

Model		σ_f	l_1	l_2	l_3	σ_n
$M_{0,GP}$	$h_1(\Delta p_x)$	3.52	2.89	1.18	1.59	0.036
	$h_1(\Delta p_y)$	5.89	3.00	1.97	2.03	0.015
	$h_1(\Delta p_z)$	3.90	3.16	1.20	1.65	0.041
$M_{1,GP}$	$h_1(\Delta p_x)$	2.13	2.65	1.07	1.39	0.035
	$h_1(\Delta p_y)$	4.48	2.95	1.88	1.90	0.015
	$h_1(\Delta p_z)$	2.57	4.05	1.11	1.25	0.041
$M_{2,GP}$	$h_1(\Delta p_x)$	2.19	2.64	1.08	1.40	0.035
	$h_1(\Delta p_y)$	4.55	2.99	1.87	1.90	0.015
	$h_1(\Delta p_z)$	2.56	4.22	1.11	1.23	0.041

5.4.4 Results of bias correction

Figure 5.9 shows the distribution of residual positional errors after bias correction of the competing model validation data for a visual analysis.

Confidence can be gained that the GPR has modelled the bias form accurately by a zero mean Gaussian distribution of residual errors. The error sources that caused the skewed and possible bi-modality of bias data of models M_0, M_1 and M_2 have been modelled successfully.

Similar to the 1 dim case, reduction of bias from different levels of calibration has little or no effect on the bias correction accuracy, demonstrated by the near identical distributions for each model data.

The prediction of Δp_y is more accurate than the predictions of Δp_x and Δp_z, evidenced by a narrower distribution. The starting point for bias correction of Δp_y was already less challenging, having a Gaussian distribution and smaller standard deviation. The comparison suggests that the errors that caused the skewed and bi-modal distributions has only partially been modelled.

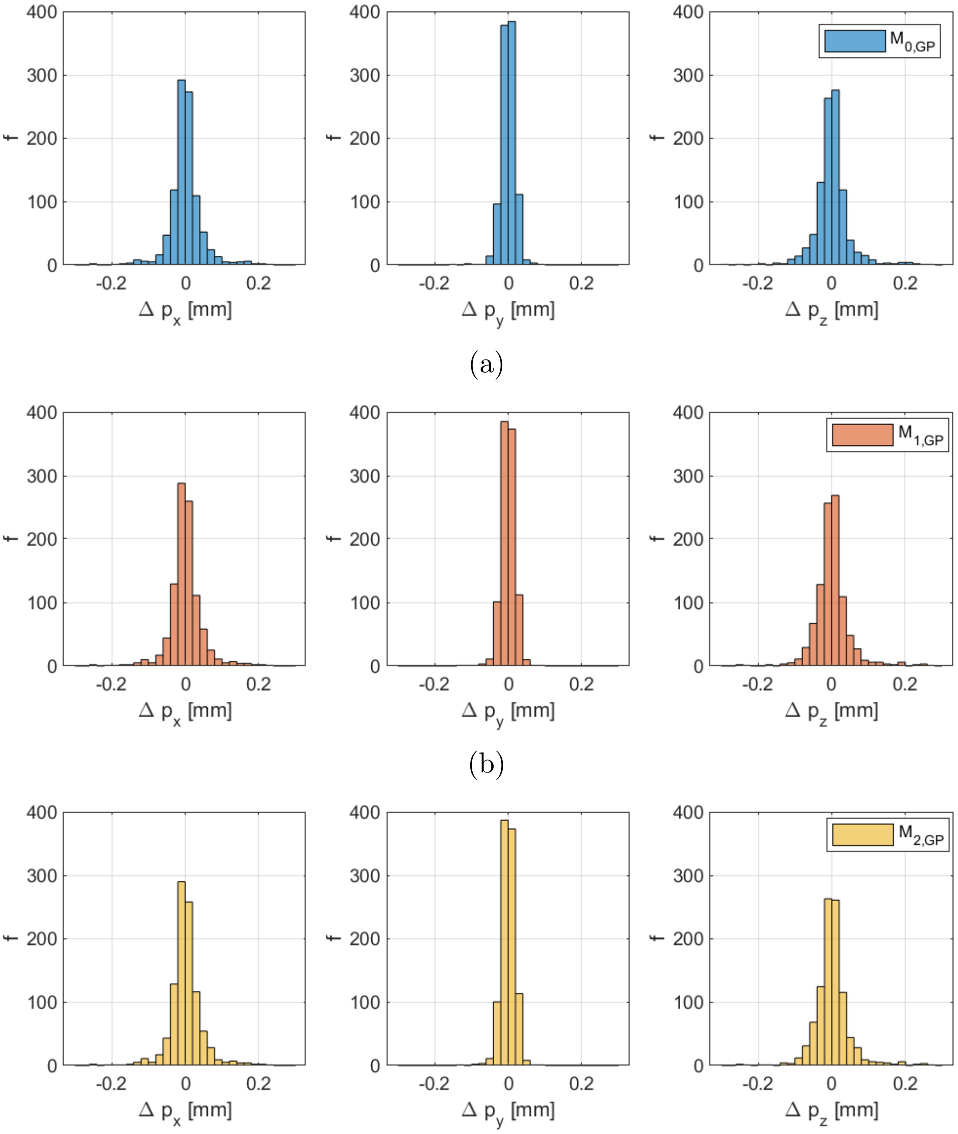

(a)

(b)

(c)

Figure 5.9: Numerical study, distribution of validation data bias correction results for models (a) $M_{0,GP}$, (b) $M_{1,GP}$ and (c) $M_{2,GP}$ in the 3 dim case study. f: frequency (number of measurements).

A summary of bias correction results for training and validation bias data is presented in Tables 5.15 and 5.16. The residual error in the bias data has been substantially reduced using bias correction. Bias correction reduced the positional error of the robot for the most challenging data, that of M_0, from a rms $|\Delta p|$ of 11mm to 48μm for the training data and 78μm for validation data. As in the 1 dim case, the accuracy of bias correction predictions is unaffected by the reduction of bias size and complexity, evidenced by near identical standard deviations and rms results for the competing models. It is still expected that as the number of input variables increases, the complexity of the bias form will change substantially between competing models and the bias correction results will begin to separate. However, it may also be the case that calibration is not necessary and that the bias correction results remain similar for all competing model bias data.

A completely accurate model of the training data has only been achieved for Δp_y, indicated by a standard deviation equal to the measurement variation σ_ϵ, which is the expected limit of bias correction accuracy. A small proportion of the complex bias form, indicated by the skewed and bi-modal distributions, has not been modelled accurately resulting in standard deviations of Δp_x and Δp_z two to three times higher than σ_ϵ. The bias form will become more complex for higher dimension cases studies and the prediction errors are expected to increase in the following case studies.

The accuracy of the validation data predictions is higher than that of the training data, which is expected. The space between training data inputs is sufficiently large and/or small changes in bias exist, so that the bias data is not accurately modelled for all inputs. In the higher dimension case studies, particularly with a wider input range, the more complex bias changes between training data points will not be modelled accurately and the difference between the training and validation data prediction accuracies after bias correction may increase.

Table 5.15: Numerical study, summary of training data bias correction results for competing models in the 3 dim case study.

	$M_{0,GP}$	$M_{1,GP}$	$M_{2,GP}$
$\bar{\Delta p}_x$ (std) [mm]	0.000 (0.030)	0.000 (0.029)	0.000 (0.029)
$\bar{\Delta p}_y$ (std) [mm]	0.000 (0.013)	0.000 (0.013)	0.000 (0.013)
$\bar{\Delta p}_z$ (std) [mm]	0.000 (0.035)	0.000 (0.035)	0.000 (0.035)
rms $|\Delta p|$ (max) [mm]	0.048 (0.340)	0.047 (0.324)	0.048 (0.322)

Table 5.16: Numerical study, summary of validation data bias correction results for competing models in the 3 dim case study.

	$M_{0,GP}$	$M_{1,GP}$	$M_{2,GP}$
$\bar{\Delta p}_x$ (std) [mm]	0.000 (0.051)	0.000 (0.051)	0.000 (0.051)
$\bar{\Delta p}_y$ (std) [mm]	0.000 (0.019)	0.000 (0.019)	0.000 (0.019)
$\bar{\Delta p}_z$ (std) [mm]	-0.001 (0.056)	-0.001 (0.055)	-0.001 (0.055)
rms $\lvert\Delta p\rvert$ (max) [mm]	0.078 (0.793)	0.077 (0.761)	0.077 (0.760)

5.4.5 Summary

The aim of this study was to investigate the limitations of bias correction in predicting robot positional error from an input of 3 joint variables, with respect to training data size and bias reduction. Bias correction in the 3 dim case was presented with more complex bias data than seen in the 1 dim case. Bi-modality and skewed distributions suggested more complex errors that were likely to be functions of joint angle, and as such able to be modelled by the GPR. This was confirmed by a substantial reduction in positional error. The accuracy of the prediction of training data did not reach the limit of σ_ϵ as seen in the 1 dim case and some of the bias form in Δp_x and Δp_z was modelled as noise by the GPR model. The increase in noise and reduction in accuracy are early indications that the bias form becomes more non-linear and challenging to model as the number of dimensions increases, confirming expectations.

Modelling accuracy above 200 training data values did not vary significantly, except for models with sub-optimal hyperparameter estimates. As the bias form becomes more non-linear with higher dimensional inputs, training data resolution may become a limitation and will continue to be investigated in the next case studies.

5.5 Bias correction of robot positional error with a 6 joint angle input and small joint angle range

The aim of this study is to continue to investigate the limitations of bias correction by increasing the complexity of the problem to 6 input variables, but with a relatively narrow input space (referred to herein as 6 dim (s)). The input space was narrowed by reducing the joint angle range to take a small step towards a more complex problem and to reflect the challenge of milling which is often in a smaller workspace, compared to panel drilling. In this study joints 1 to 6 were all be rotated to configurations that provide TCP poses. The challenge of prediction of bias data in relation to training data quantity and bias reduction from competing models were tested.

The expectation is that the bias form will be more complex in a 6 dimension space compared to 3 dimensions and be greater challenge to bias correction. In the previous cases, bias reduction had a negligible effect on bias correction accuracy, but the expectation is that bias reduction may still affect accuracy in higher dimension cases. The number of hyperparameters to estimate is higher than the previous cases and a strategy to avoid local minima is a design consideration. Hyperparameter estimation and data quantity studies will be run in parallel to determine optimal conditions.

5.5.1 Training data quantity

In the 3 dim study, 300 training data appoints were used. To retain the same resolution for a 6 dim case would require 90,000 data points which is not practical and may lead to computational challenges for GPR, which is slow with high training data quantities. The limitation of accuracy with respect to training data size is established again by testing. Figure 5.10 shows the residual error in predicting the validation set, after bias correction, in terms of rms Δp_x, Δp_y and Δp_z separately, against increasing training data size. Examples of the performance against training data quantity is presented for a sample of initial hyperparameter estimates. A spike in results for h_3 indicates that the model is sensitive to the initial estimate even at high numbers of training data. The solution is therefore to continue to search for hyperparameters and select the optimal based on the minimum rms Δp. While the accuracy of the predictions does not fully converge, with the optimal hyperparameters selected there is only a marginal gain in accuracy of less than 10μm beyond a training data quantity of 800. Training data will be generated by the competing models in 800 training data poses.

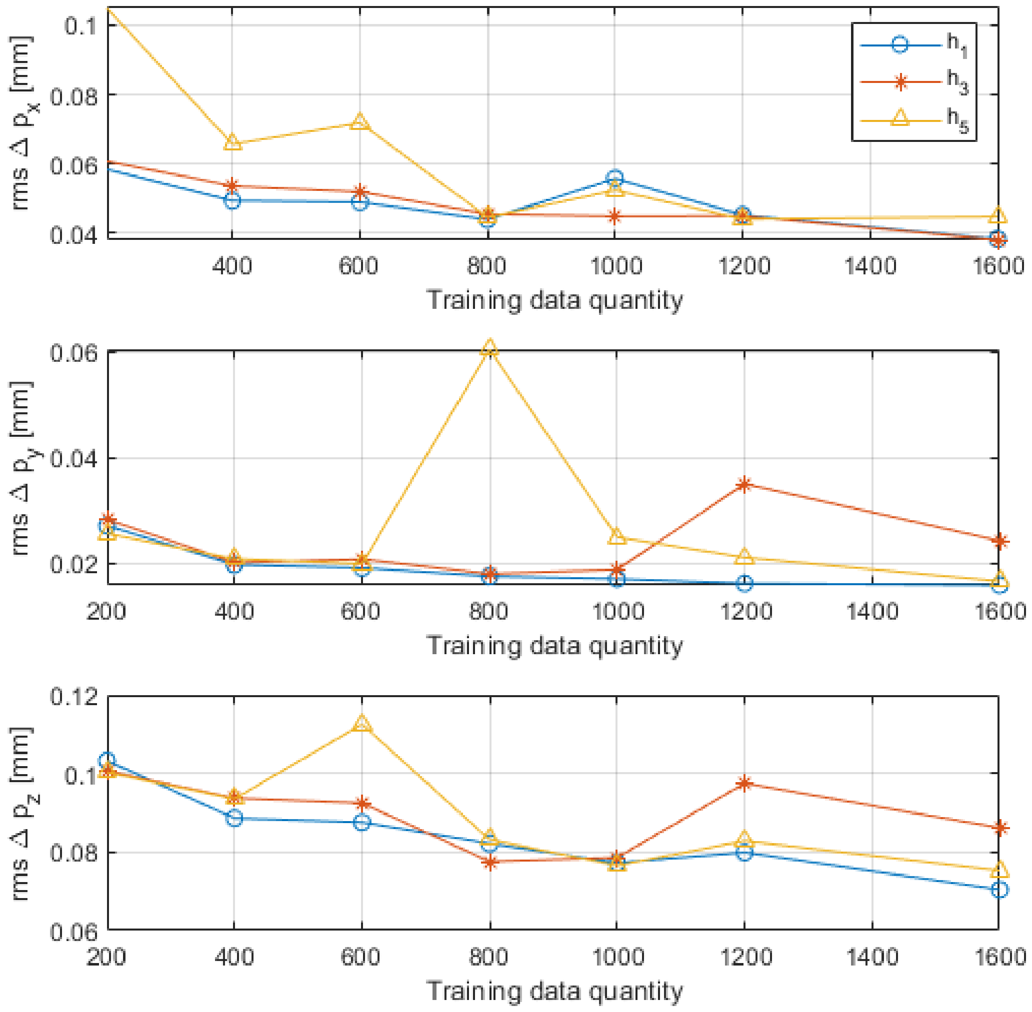

Figure 5.10: Convergence plot of bias correction prediction accuracy against training data quantity for model $M_{0,GP}$ in the 6 dim (s) case study.

5.5.2 Baseline data

Figure 5.11 shows the distribution of validation bias data generated by the competing models for a visual analysis.

The bias data from M_1 and M_2 have very similar distributions, as in the 3 dim case study, and may again present a similar challenge for bias correction. The same assumptions made in the 3 dim case can be made: that the large bias in Δp_z is the result of joint compliance deflection, whilst the bias in Δp_y may be mainly attributed to geometric errors which is largely unaffected by joint compliance.

A different challenge may be presented to bias correction of Δp_x, Δp_y and Δp_z with each showed different distributions.

The distribution of bias data in Δp_x no longer indicates some bi-modality and approaches a non-Gaussian distribution without a peak in the data of M_1 and M_2 . This could be the result of a multi-modal distribution with many peaks which suggests that the data may be separated into a number of subsets, each representing a joint subspace region for example, or a could be an indication of a challenging non-linear problem.

The distribution of data in Δp_y is Gaussian which does not suggest any additional challenges.

The skewed distribution in the Δp_z bias data can again be explained by joint compliance deflections which will almost always be in the negative z direction. The distribution of bias data in Δp_y and Δp_z then do not necessarily indicate concerns for bias correction or the use of GPR, but the distribution of Δp_x may be.

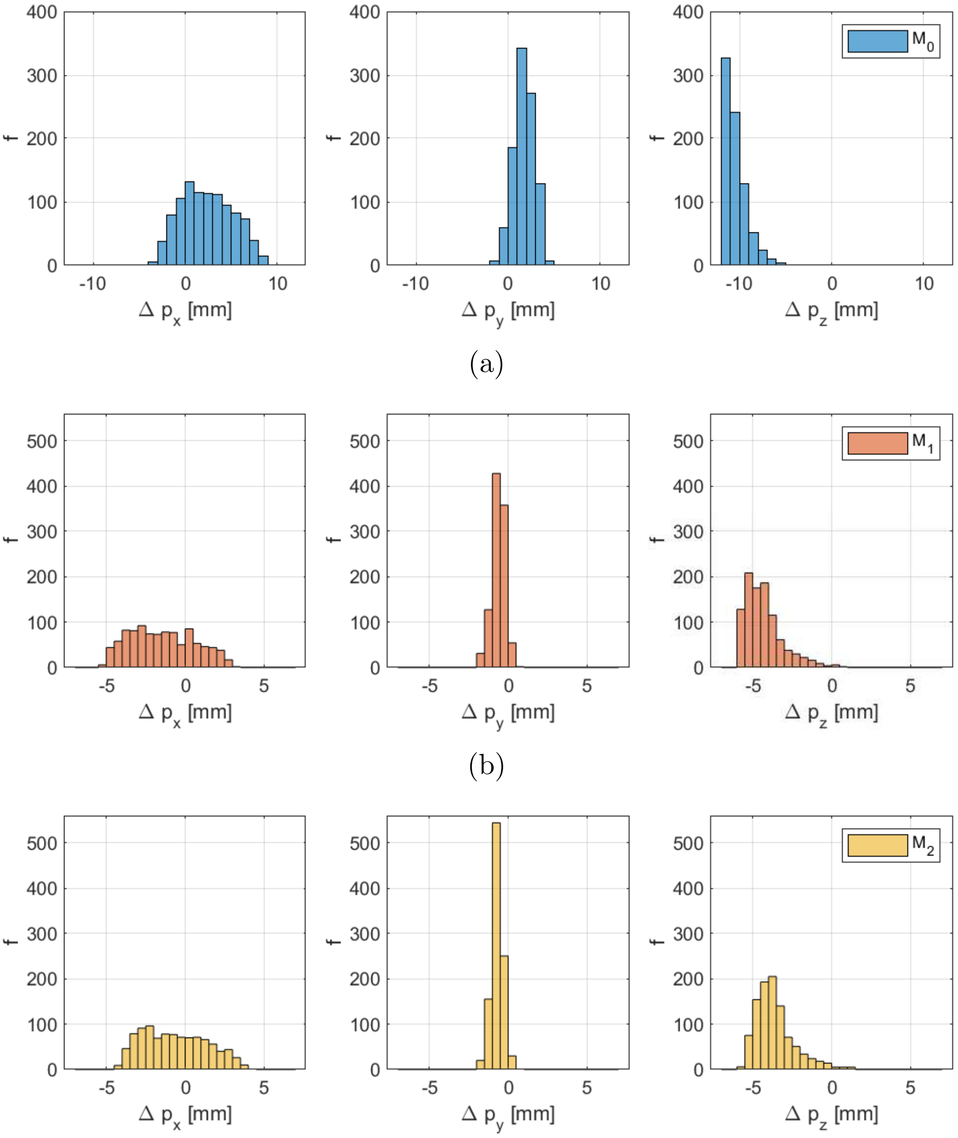

(a)

(b)

(c)

Figure 5.11: Numerical study, distribution of validation bias data results for competing models (a)M_0, (b)M_1 and (c)M_2 in the 6 dim (s) case study. f: frequency (number of measurements).

The results of training and validation data predictions by the competing models are summarised in Tables 5.17 and 5.18 respectively and provides an evaluation of the task provided to the GPR. While mean and standard deviations for Δp_x data may not be appropriate, they are presented for comparison. Interestingly, the rms $|\Delta p|$ in the 6 dim (s) case is of a similar magnitude to the 1 dim and 3 dim cases. This may be the result of the reduced joint space range but does still suggest that there are no additional extreme bias values.

The bias data of M_2 may in fact present a slightly different challenge for bias correction than the data from M_1. Whilst distributions are similar, M_2 has a mean bias Δp_x and Δp_z and rms $|\Delta p|$ of approximately 0.8mm smaller than that of M_1. The similarity in results between training and validation bias data is an indication that the training data provides good spatial coverage. Whilst this was also true in the 3 dim case, the predictions of the validation data were not as accurate as the training data which suggests the contrary.

Table 5.17: Numerical study, summary of training bias data results for competing models in the 6 dim (s) case study.

	M_0	M_1	M_2
$\bar{\Delta p}_x$ (std)[mm]	2.426 (2.795)	-1.416 (2.031)	-0.622 (2.016)
$\bar{\Delta p}_y$ (std)[mm]	1.743 (1.091)	-0.609 (0.393)	-0.690 (0.357)
$\bar{\Delta p}_z$ (std)[mm]	-10.927 (1.425)	-4.303 (1.248)	-3.601 (1.271)
rms $\|\Delta p\|$ (max)[mm]	11.804 (15.218)	5.169 (6.179)	4.430 (5.805)

Table 5.18: Numerical study, summary of validation bias data results for competing models in the 6 dim (s) case study.

	M_0	M_1	M_2
$\bar{\Delta p}_x$ (std)[mm]	2.418 (2.800)	-1.428 (2.044)	-0.636 (2.023)
$\bar{\Delta p}_y$ (std)[mm]	1.749 (1.091)	-0.605 (0.402)	-0.686 (0.361)
$\bar{\Delta p}_z$ (std)[mm]	-10.940 (1.397)	-4.312 (1.202)	-3.612 (1.225)
rms $\|\Delta p\|$ (max)[mm]	11.813 (15.114)	5.175 (6.189)	4.432 (5.730)

5.5.3 Hyperparameter search

The SE kernel for a GP with six input variables has eight hyperparameters, σ_f, σ_n and six length scales. The hyperparameter search was conducted with five randomly generated initial estimates. The optimal set for each model, in prediction accuracy terms, are presented in Table 6.22. The hyperparameter search may still be sensitive to the initial estimate as the number of input dimensions increases.

As in the 3 dim case, σ_n is approximately equal to σ_ϵ for all Δp_y models which suggests that all of the bias form is modelled by GPR function. The bias data in the models of Δp_x and Δp_z is partially explained as noise and therefore the model is not fully accurate. The majority of length scale parameters are all of a similar order in single units which provides confidence that all the model is not attempting to overfit and the bias is a function of all parameters which is expected. A relative insensitivity to joint 1 is expected and shown by large l_1 estimates for models $M_{1,GP}$ and $M_{2,GP}$. A relatively large l_6 estimation for the model of Δp_y in $M_{1,GP}$ is unexpected.

Table 5.19: Example of the estimated GPR SE kernel hyperparameters, representative of the majority of estimations from 20 initial estimates in the 6 dim (s) case study.

Model		σ_f	l_1	l_2	l_3	l_4	l_5	l_6	σ_n
$M_{0,GP}$	$h_3(\Delta p_x)$	3.24	7.89	4.95	3.38	7.28	3.08	8.86	0.036
	$h_1(\Delta p_y)$	2.03	7.20	3.66	3.34	8.13	5.20	5.66	0.014
	$h_5(\Delta p_z)$	3.09	17.94	2.66	1.71	7.76	3.23	5.30	0.066
$M_{1,GP}$	$h_3(\Delta p_x)$	1.97	13.42	2.15	3.32	9.88	3.12	5.62	0.037
	$h_4(\Delta p_y)$	6.34	7.02	6.79	4.40	7.59	6.27	35.17	0.014
	$h_3(\Delta p_z)$	1.79	7.75	2.43	1.87	9.64	1.92	4.91	0.061
$M_{2,GP}$	$h_1(\Delta p_x)$	1.69	7.45	3.94	2.65	5.48	3.15	7.92	0.036
	$h_1(\Delta p_y)$	1.92	5.00	3.71	3.80	11.44	5.19	11.02	0.015
	$h_1(\Delta p_z)$	1.68	8.92	2.91	1.84	6.94	1.96	4.98	0.063

5.5.4 Results of bias correction

Figure 5.12 shows the distribution of residual positional errors after bias correction of the competing model data for a visual analysis.

As seen in 3 dim case, a Gaussian distribution of residual bias predictions with a zero mean and narrow distribution provides confidence that the bias form has been modelled relatively accurately. The distribution of Δp_x bias data was initially wide spread and possibly multi-modal, which suggested that problem may exist in subsets which may be challenging to model from joint angle inputs. However, GPR successfully learnt the bias form as a function of joint angles.

Similar to the 1 dim and 3 dim cases, reduction of bias from different levels of calibration has little or no effect on the bias correction accuracy, demonstrated by the near identical distributions for each model data.

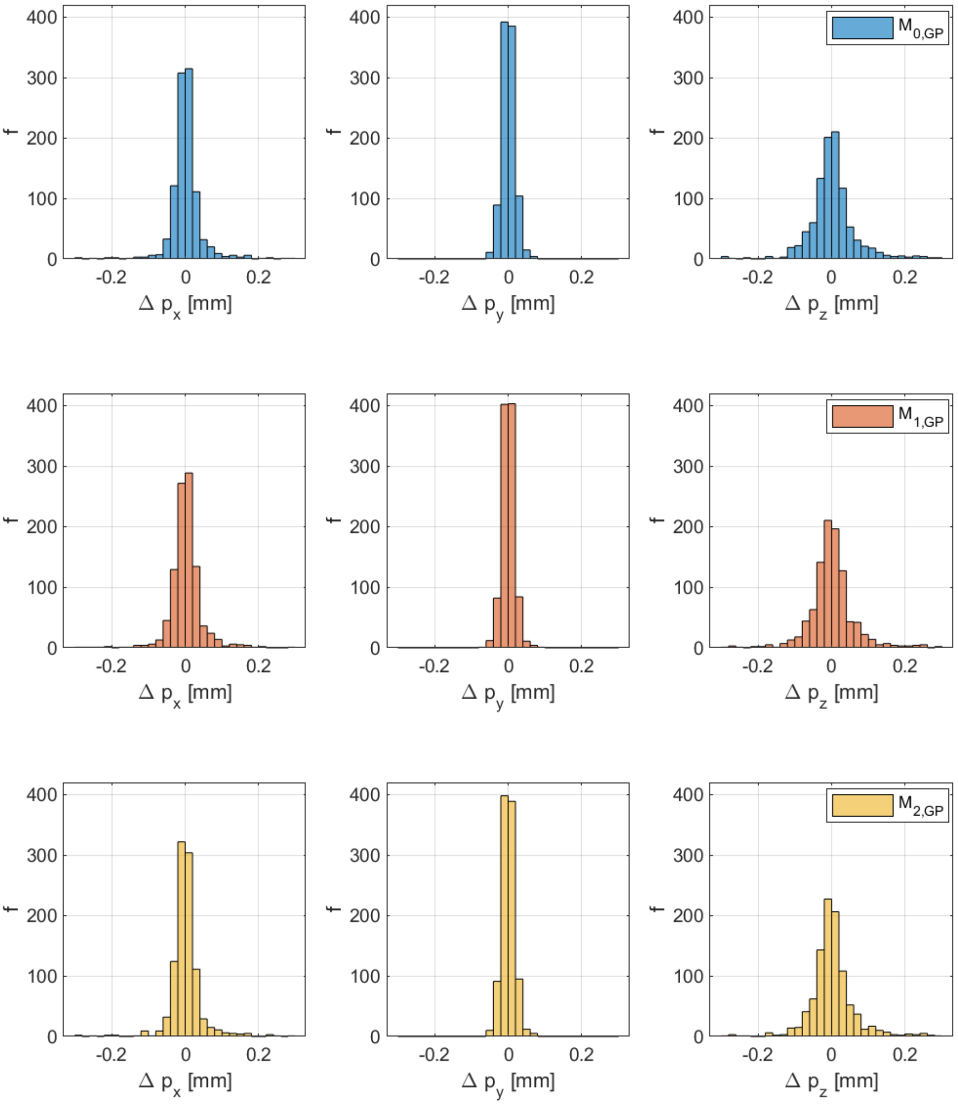

Figure 5.12: Numerical study, distribution of validation data bias correction results for models (a) $M_{0,GP}$, (b) $M_{1,GP}$ and (c) $M_{2,GP}$ in the 6 dim (s) case study. f: frequency (number of measurements).

A summary of bias correction results for training and validation bias data is presented in Tables 5.15 and 5.16. The residual error in the bias data has been substantially reduced using bias correction. Bias correction reduced the positional error of the robot for the most challenging data, that of M_0 , from a rms $|\Delta p|$ of 11mm to 67μm for the training data and 89μm for validation data. The doubling of input dimensions had little effect on the accuracy of the validation data predictions, with a standard deviation of just 12μm higher than in the 3 dim case.

The accuracy of the modelling of Δp_y training data, is unaffected by the additional degrees of freedom and is only limited by the measurement variation. The accuracy of the models of Δp_x training data are only marginally affected by the additional degrees of freedom with a standard deviation of only 3μm higher than in the 3 dim case. The higher rms $|\Delta p|$ in the 6 dim case compared to the 3 dim case is the due to the less accurate modelling of Δp_x. The standard deviation of the predictions of Δp_z is 20μm are higher in the 6 dim (s) case which indicates that the additional degrees of freedom present positional errors that are more challenging to model in the vertical direction.

The maximum $|\Delta p|$ is large, 0.571mm compared to the desirable accuracy range which indicates that within the machining workspace, there are regions of high accuracy but also regions of very poor accuracy.

The negligible effect on the accuracy of bias correction predictions by reducing the burden of bias is confirmed again by the near identical results for each model.

Table 5.20: Numerical study, summary of training data bias correction results for competing models in the 6 dim (s) case study.

	$M_{0,GP}$	$M_{1,GP}$	$M_{2,GP}$
$\overline{\Delta p}_x$ (std) [mm]	0.000 (0.032)	0.000 (0.033)	0.000 (0.032)
$\overline{\Delta p}_y$ (std) [mm]	0.000 (0.012)	0.000 (0.013)	0.000 (0.013)
$\overline{\Delta p}_z$ (std) [mm]	0.000 (0.058)	0.000 (0.053)	0.000 (0.055)
rms $|\Delta p|$ (max) [mm]	0.067 (0.427)	0.064 (0.429)	0.065 (0.420)

Table 5.21: Numerical study, summary of validation data bias correction results for competing models in the 6 dim (s) case study.

	$M_{0,GP}$	$M_{1,GP}$	$M_{2,GP}$
$\overline{\Delta p}_x$ (std) [mm]	0.002 (0.043)	0.002 (0.044)	0.002 (0.043)
$\overline{\Delta p}_y$ (std) [mm]	0.001 (0.017)	0.000 (0.017)	0.001 (0.017)
$\overline{\Delta p}_z$ (std) [mm]	0.001 (0.077)	0.000 (0.075)	0.001 (0.073)
rms $|\Delta p|$ (max) [mm]	0.089 (0.568)	0.088 (0.568)	0.086 (0.571)

5.5.5 Summary

The 6 dim (s) case study, presented a more challenging case for bias correction, compared to the 1 dim and 3 dim case studies. The challenge was in part, reduced by a relatively narrow joint angle range and a search for an appropriate training data size. Utilising considerably more training data inputs compared to the 3 dim case resulted in just a 10μm increase in rms $|\Delta p|$ and similar confidence in predictions. The GP was also able to reduce the positional error to the same level for each of the bias data, again suggesting that calibration may not be necessary. Unlike the 3 dim case, the hyperparameter search was sensitive to the initial estimate, with each estimate resulting in a different solution. While the accuracy of the predictions between the estimates was not large, there were some very poor solutions with large positional errors. In higher dimensions it becomes more important to refine the hyperparameter search and find the optimal results.

5.6 Bias correction of robot positional error with a 6 joint angle input and large joint angle range

The aim of this study is to continue to investigate the limitations of bias correction by increasing the complexity of the problem to 6 input variables with a large joint range (referred to herein as 6 dim (l)). The range of joint angles for joints 1, 2 and 3 were the same as the 3 dim case study in order to directly compare results and evaluate how increasing input dimensions affects the complexity of the problem and the accuracy of bias correction predictions. The joint ranges of joints 4, 5 and 6 were wider than in the 6 dim (s) workspace case in order to evaluate the method in a larger workspace, as is typical in robot calibration research literature, and compare to the smaller workspace case study.

The accuracy of bias data predictions in relation to training data quantity and bias reduction from competing models is tested. In all previous case studies in this chapter, bias reduction had a negligible effect of bias correction accuracy leading to a working hypothesis that calibration is an unnecessary precursory step to bias correction, to improve positional accuracy of a robot, in this simulation. Although it is expected that the bias form will be more complex, the results of this study will test the hypothesis. The same approach to hyperparameter estimation, used in the 6 dim (s) case study is used to identify the global minima is parallel with training data quantity tests.

5.6.1 Training data quantity

In the 3 dim study, 300 training data appoints were used, whilst in the 6 dim (s) case study, 800 training data points were used, which is a reduction in training data resolution. Figure 5.10 shows the residual error in predicting a test set, after bias correction, against increasing training data size. Examples of the performance against training data quantity is presented for a sample of initial hyperparameter estimates. A spike in results for h_5 confirms that the model is sensitive to the initial estimate as observed in the previous case studies. The solution is therefore to continue to search for hyperparameters and select the optimal based on the minimum rms Δp. While the accuracy of the predictions does not fully converge, with the optimal hyperparameters selected there is only a marginal gain in accuracy beyond a training data quantity of 800, which will be used in this study. This quantity of training data points is far in excess of those used in research literature but does confirm that the limitations of bias correction for industrial robots has not been fully explored.

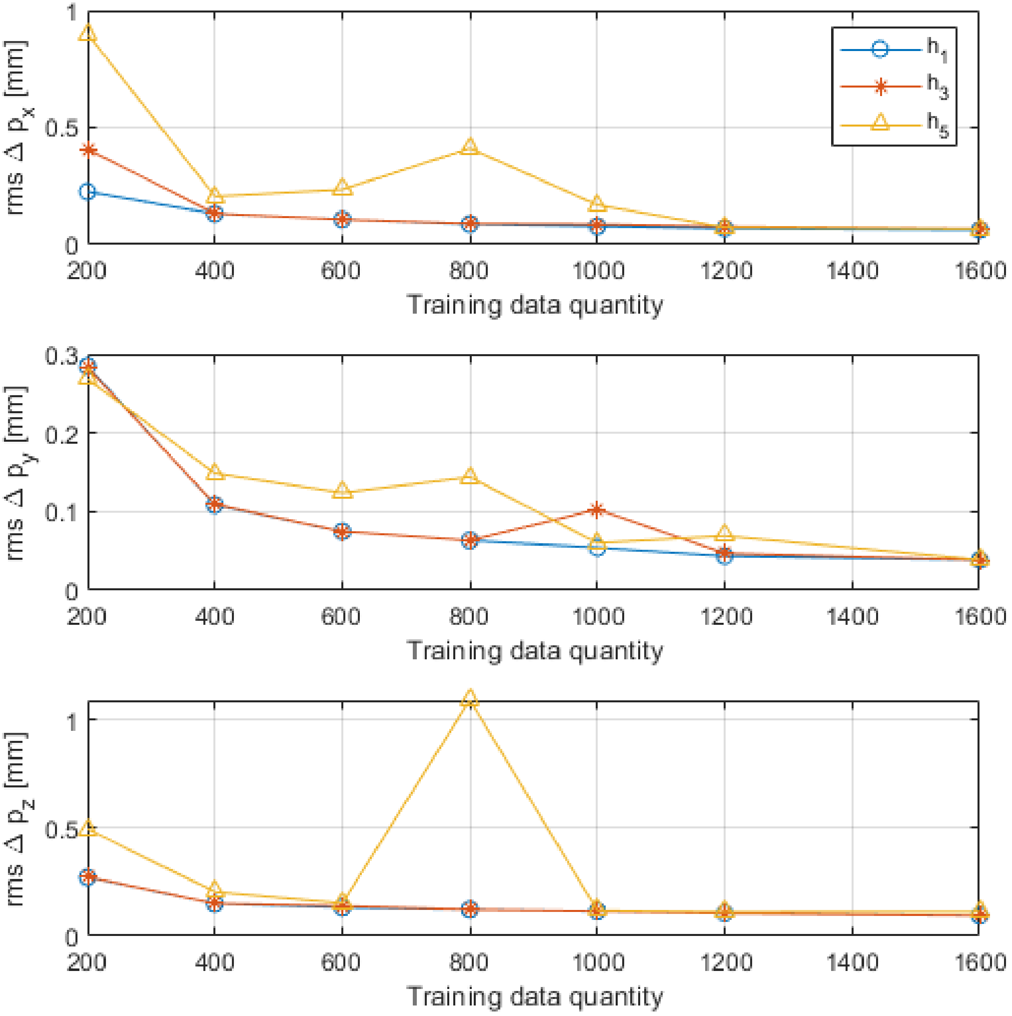

Figure 5.13: Convergence plot of bias correction prediction accuracy against training data quantity for model $M_{0,GP}$ in the 6 dim (l) case study.

5.6.2 Baseline data

Figure 5.14 shows the distribution of validation bias data generated by the competing models for a visual analysis.

As expected bias data from M_1 and M_2 have very similar distributions, and the results are expected to be nearly identical. Although a second, similar bias data set provides no additional value in the evaluation of bias reduction, all data sets will remain for continuity with the previous case studies. Interestingly, the distribution of Δp_x bias data no longer shows bi-modality or a flat, possible multi-modality as seen in the 3 dim and 6 dim (s) studies. The reason is unclear without further analysis which is assumed to be unnecessary given that both distributions demonstrated no significant challenge for bias correction. Both distributions of Δp_x and Δp_y are skewed which also have not indicated any significant problems for the bias correction.

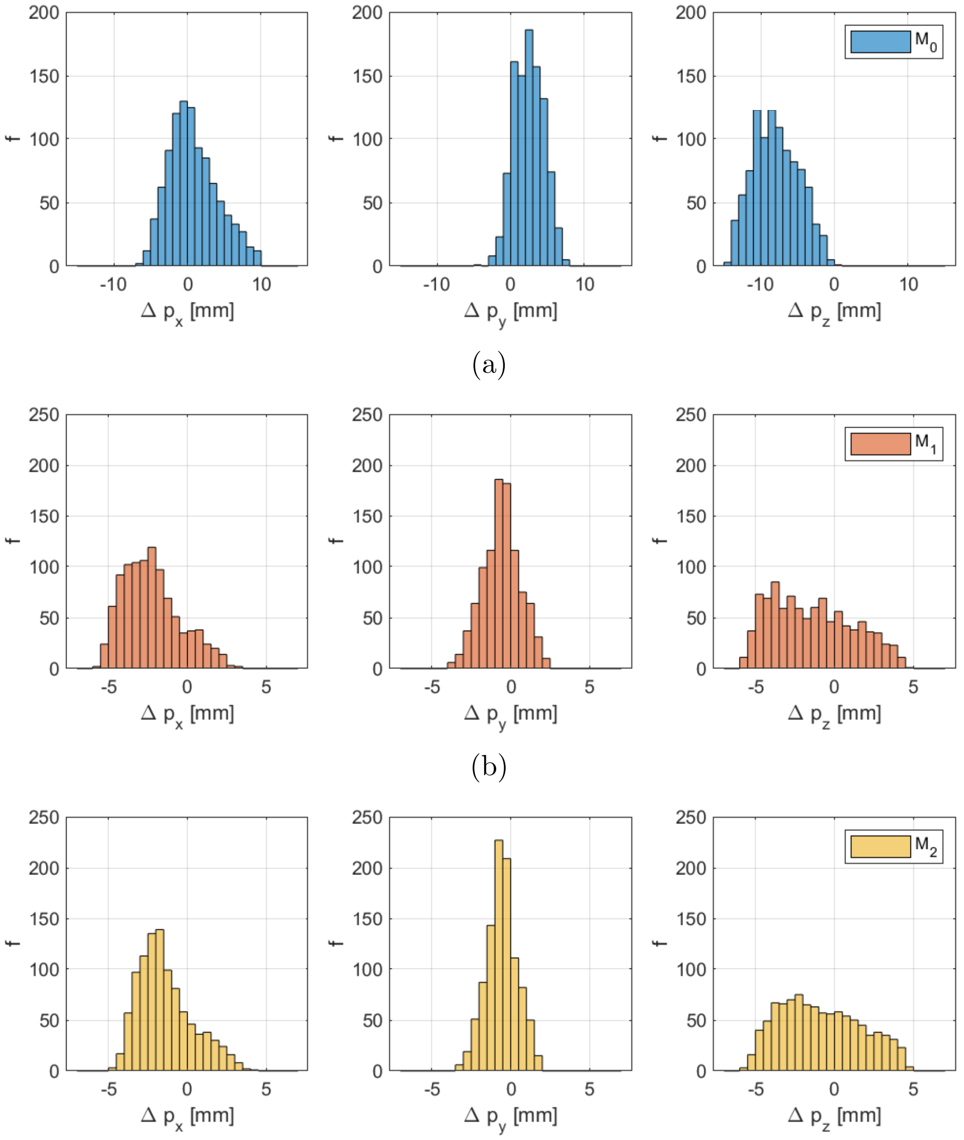

(a)

(b)

(c)

Figure 5.14: Numerical study, distribution of validation bias data results for competing models (a)M_0, (b)M_1 and (c)M_2 in the 6 dim (l) case study. f: frequency (number of measurements).

The results in predicting training and validation data by the competing models are summarised in Tables 5.22 and 5.23. Interestingly, rms $|\Delta p|$ of both training and validation data is smaller than in the 6 dim (s) case study, mainly as a result of a considerably lower mean Δp_z . The lower Δp_z may be explained by the wider joint range. In the smaller joint range, the problem was constrained to a region where the arm was largely outstretched and deflections of the TCP due to payload were all large. In the wider joint range case, a rotation of joint 4 results in an L-shaped configuration in which the payload twists the structure and the arm length is reduced. Also, in configurations where the robot reaches upwards, the payload produces a much smaller torque and deflection.

The difference in bias data distributions and bias size between competing models again provides a suitable challenge for bias correction to test the working hypothesis on parameters reduction.

Table 5.22: Numerical study, summary of training bias data results for competing models in the 6 dim (l) case study.

	M_0	M_1	M_2
$\Delta \bar{p}_x$ (std)[mm]	0.723 (3.274)	-2.286 (1.777)	-1.439 (1.708)
$\Delta \bar{p}_y$ (std)[mm]	2.474 (1.911)	-0.578 (1.243)	-0.552 (0.996)
$\Delta \bar{p}_z$ (std)[mm]	-7.962 (3.065)	-1.461 (2.546)	-0.908 (2.512)
rms $\lvert\Delta p\rvert$ (max)[mm]	9.683 (16.557)	4.343 (6.400)	3.661 (5.848)

Table 5.23: Numerical study, summary of validation bias data results for competing models in the 6 dim (l) case study.

	M_0	M_1	M_2
$\Delta \bar{p}_x$ (std)[mm]	0.818 (3.317)	-2.249 (1.803)	-1.402 (1.716)
$\Delta \bar{p}_y$ (std)[mm]	2.462 (1.977)	-0.572 (1.183)	-0.562 (0.967)
$\Delta \bar{p}_z$ (std)[mm]	-7.918 (3.076)	-1.392 (2.597)	-0.848 (2.550)
rms $\lvert\Delta p\rvert$ (max)[mm]	9.684 (16.365)	4.325 (6.183)	3.657 (5.820)

5.6.3 Hyperparameter search

The SE kernel for a GP with six input variables has eight hyperparameters, σ_f, σ_n and six length scales. The hyperparameter search was conducted with five randomly generated initial estimates. The optimal set for each model, in prediction accuracy terms, are presented in Table 5.24.

The estimated value of σ_n is higher than in all of the previous chapter case studies and has increased with higher input dimensions. The higher σ_n is an initial indication that the bias correction model is less able to model all of the bias form and the accuracy of the predictions will decrease. σ_n hyperparameter in the Δp_y models is lower than in the Δp_x and Δp_z models and is expected to remain as the most accurate model. However, the value of σ_n in the Δp_y models is also significantly higher than the limit of σ_ϵ unlike in the previous chapter cases studies, and a portion of the bias form is modelled as noise, which will reduce the accuracy of the predictions.

Interestingly, the scale of the length parameters has become more uniform, compared to the 6 dim (s) case study, which showed length scales in the orders of 0.1, 1 and 10. The uniform length scales provides confidence that the data has been modelled as a function of all joint angle input without favouring a simple model with a dominant input. The length scale of l_1 for the $M_{1,GP}$ model of Δp_z is the exception which is ten times higher than the other length scales in the model. The scale difference is not excessive or concerning but more interesting is that it is considerably larger than in the $M_{2,GP}$ model which is expected to have very similar bias data to model. An analysis of the results will indicate if the higher value is a concern.

Table 5.24: Example of the estimated kernel hyperparameters, representative of the majority of estimations from five initial estimates in the 6 dim (l) case study.

Model		σ_f	l_1	l_2	l_3	l_4	l_5	l_6	σ_n
$M_{0,GP}$	$h_4(\Delta p_x)$	2.95	3.75	2.54	2.66	2.43	1.46	3.49	0.054
	$h_3(\Delta p_y)$	2.53	2.64	2.68	2.73	2.40	1.59	4.39	-0.023
	$h_3(\Delta p_z)$	3.35	5.53	2.55	2.73	2.46	1.55	4.03	-0.081
$M_{1,GP}$	$h_1(\Delta p_x)$	1.63	3.41	2.08	2.17	2.23	1.29	3.15	-0.051
	$h_4(\Delta p_y)$	1.41	2.41	2.31	2.32	2.10	1.43	3.96	-0.022
	$h_3(\Delta p_z)$	2.37	20.41	2.28	2.30	2.37	1.43	3.63	-0.086
$M_{2,GP}$	$h_4(\Delta p_x)$	1.62	3.48	2.22	2.03	2.13	1.33	3.07	-0.049
	$h_4(\Delta p_y)$	1.40	2.39	2.30	2.27	2.09	1.42	3.80	-0.021
	$h_4(\Delta p_z)$	1.89	7.44	2.17	2.18	2.27	1.34	3.24	-0.081

5.6.4 Results of bias correction

Figure 5.15 shows the distribution of residual positional errors after bias correction of the competing model data for a visual analysis. The same observations made in all of the previous chapter case studies can be drawn again from the results in this study. Namely (i) challenging bias forms indicated by skewed distributions has been confidently modelled, resulting in an expected symmetric Gaussian distribution; (ii) the distributions of each model is very similar which again confirms the hypothesis that bias reduction has a negligible effect of bias correction; and (iii) the models were all able to predict Δp_y with higher accuracy than Δp_x or Δp_z which was expected by lower σ_n.

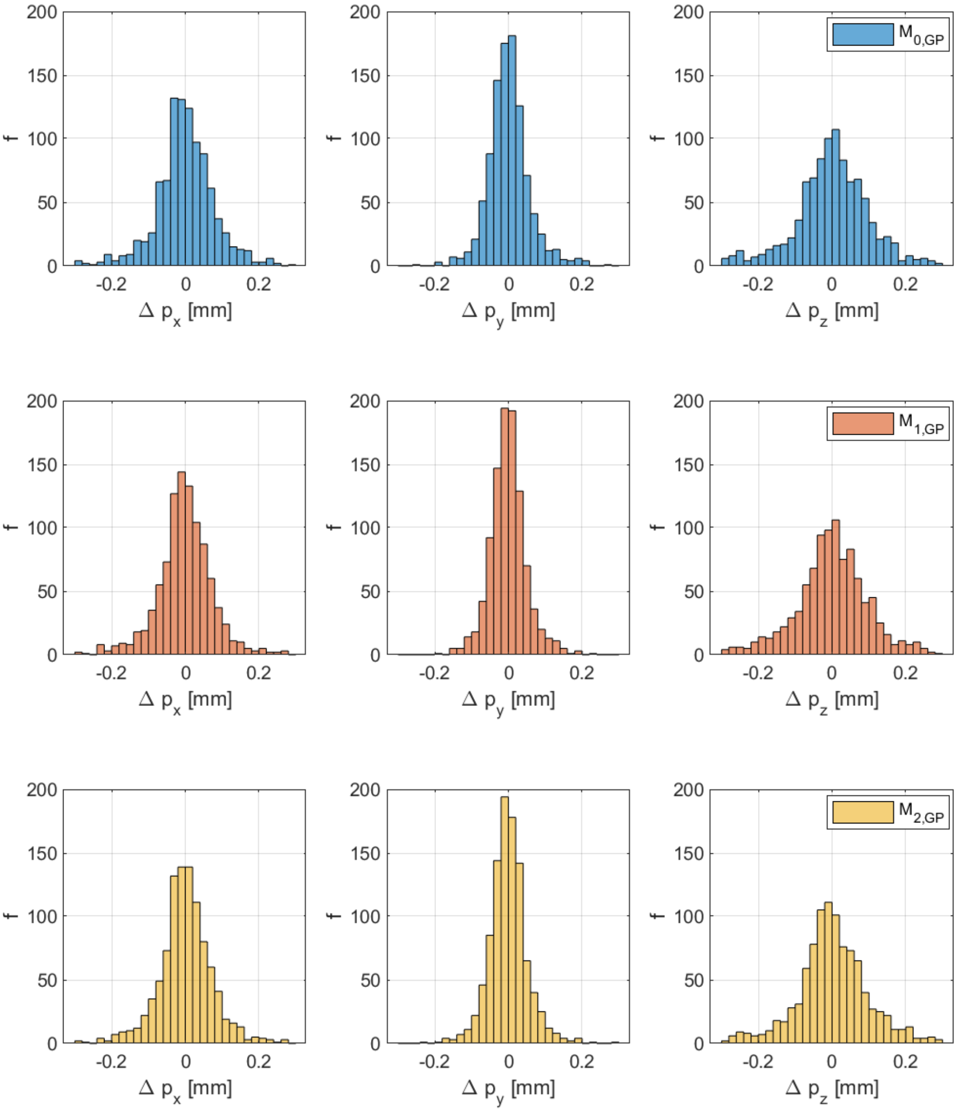

Figure 5.15: Numerical study, summary of validation data bias correction results for competing models in the 6 dim (l) case study. f: frequency (number of measurements).

A summary of bias correction results for training and validation bias data is presented in Tables 5.25 and 5.26.

As a broad analysis of the results, the residual error was substantially reduced using bias correction, as observed in all previous chapter studies. The prediction of validation data was considerably less accurate than the prediction of the training data which was not evident in the previous chapter studies. In this study, the rms $|\Delta p|$ for the validation predictions was larger than in the training poses by a factor of two. Given that the training data was modelled with relatively high accuracy, it is likely that the reduced training data resolution, compared to the other chapter studies, has resulted in unmodelled bias form between training data inputs. Referring back to the training data quantity test, a compromise was made between model accuracy and data quantity a data set with lower input resolution compared to the previous case studies was selected on practical grounds. Although it was evident that gains in accuracy were still made up to and beyond a training data quantity of 1600, the data quantity would be excessive with respect to a real experiment to have a significant improvement in model accuracy. The difference between validation and training prediction accuracy however is larger than expected and a larger training data quantity is recommended.

The working hypothesis that bias reduction has a negligible effect of bias correction accuracy is not confirmed by the results in this study. There is a small but possibly significant difference between the accuracy of $M_{0,GP}$ and $M_{1,GP}$. The residual error, in rms $|\Delta p|$ terms, of $M_{0,GP}$ in the prediction of the validation bias data is larger than that of $M_{1,GP}$ and $M_{2,GP}$. The rms $|\Delta p|$ difference is only 20μm which is not significant enough to prove or disprove the hypothesis. The reduction in training data resolution may have exposed the complexities of the bias form which are minimised by calibration. The hypothesis may be expanded to include two options:

I Bias reduction, by calibration, has negligible effect on bias correction accuracy for sufficiently large training data quantities. This meets general subject expectations but with regards to the former discussion on realistic data quantity, substantially larger training data sets will not be tested.

II Bias reduction, by calibration will significantly improve the bias correction accuracy for practical training data quantities. Practical training data quantity is a relatively arbitrary value which is dependent on the measurement system, application and bias correction tool. In this case 1600 training data points is considered large.

The maximum $|\Delta p|$ by all models is substantially larger, by an order of magnitude, than the desirable 0.1mm. Without being able to visualise the 6 dimensional input space it is not possible to confirm whether large positional errors exist in a subspace that can be avoided for machining applications.

Table 5.25: Numerical study, summary of training data bias correction results for competing models in the 6 dim (l) case study.

	$M_{0,GP}$	$M_{1,GP}$	$M_{2,GP}$
$\bar{\Delta p}_x$ (std) [mm]	0.000 (0.036)	0.000 (0.033)	0.000 (0.033)
$\bar{\Delta p}_y$ (std) [mm]	0.000 (0.013)	0.000 (0.012)	0.000 (0.012)
$\bar{\Delta p}_z$ (std) [mm]	0.000 (0.063)	0.000 (0.069)	0.000 (0.062)
rms $\|\Delta p\|$ (max)[mm]	0.073 (0.421)	0.078 (0.430)	0.071 (0.426)

Table 5.26: Numerical study, summary of validation data bias correction results for competing models in the 6 dim (l) case study.

	$M_{0,GP}$	$M_{1,GP}$	$M_{2,GP}$
$\bar{\Delta p}_x$ (std) [mm]	-0.002 (0.087)	-0.002 (0.080)	0.000 (0.078)
$\bar{\Delta p}_y$ (std) [mm]	0.002 (0.061)	0.000 (0.051)	-0.001 (0.051)
$\bar{\Delta p}_z$ (std) [mm]	-0.004 (0.122)	-0.004 (0.115)	-0.003 (0.112)
rms $\|\Delta p\|$ (max)[mm]	0.162 (1.185)	0.149 (0.764)	0.146 (0.699)

5.6.5 Discussion

In this study, the effect of a wider range of joint inputs, leading to more sparsely distributed training data was tested for comparison to the previous 'narrow joint angle range' study. As expected, the predictions were less confident but substantial reductions in positional error were made. Unlike the previous studies however, the results indicated that there may be small improvements ($\approx 20\mu$m) in accuracy made by calibrating the model before bias correction. This may specific to this data but should be pursued in the experimental study in Chapter 6, where additional unmodelled error factors are expected and the joint compliance model will be employed.

5.7 Synthesis of case study results

Figure 5.16 shows the bias correction results of all case studies in this chapter, as standard deviations for the predictions of validation bias data in Δp_x , Δp_y and Δp_z and the rms $|\Delta p|$ for comparison. The standard deviation is presented to indicate accuracy as all models have a near zero mean. The results are compared to analyse the limitations of bias correction with respect to input dimensions and input range.

Firstly, the 1 dim case study results present the ideal case of high resolution training data with minimal input dimensions and as such is a benchmark, having achieved an accuracy limited by measurement variation. Secondly, in all case studies, the prediction of Δp_y was a lesser challenge than that of Δp_x and Δp_z , largely expected due to the payload deflections being predominantly in the$x$ and z directions. The substantially higher residual error in Δp_y for the 6 dim (l) case study confirms this reasoning with large rotation in joints 4 and 6 leading to and L-shaped structure and consequently larger deflections in y.

In all case studies, Δp_z has been the least accurately modelled and has contributed the most to the $|\Delta p|$. The positional error is shown to increase as the number of input dimensions to the problem increases and that the increase can be lessened by reducing the joint range. This is true for the residual errors in Δp_x which shows an increase from 3 dimensional to 6 dimensional inputs and an increase from the small to large joint ranges. This is not true however for predictions of Δp_x and Δp_y where predictions in the 6 dim (s) case study are more accurate than in the 3 dim case study. It can only be presumed that the 6 dim (s) case study was in a subspace with a relatively simpler bias form to model. If this is true then an argument exists to identify subspaces that are more accurate for machining applications.

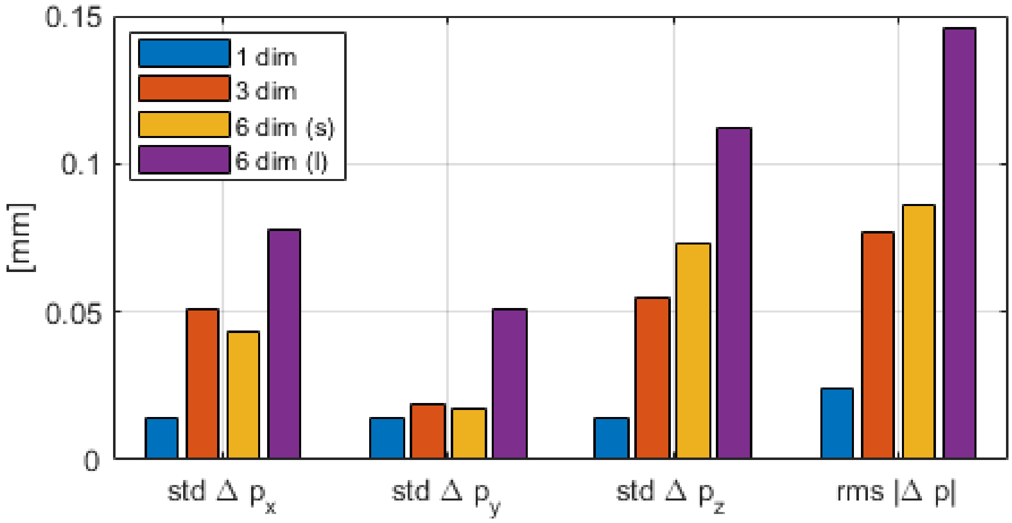

Figure 5.16: Numerical study, comparison of validation data bias correction results of each case study for model $M_{2,GP}$.

5.8 Chapter summary

The aim of this chapter was to explore the limitations of bias correction, using GPR, to reduce robot positional error of a simulated robot. Specifically, the effect of training data quantity and bias reduction on bias correction performance were tested.

In the calibration study, four competing models were successfully developed. Base calibration, using SVD is a simple method that requires small quantities of data to train, can produce a substantial gain in robot model accuracy. Additional gains in accuracy can be made by calibrating the geometric and joint compliance parameters but an initial base calibration is necessary to improve the initial parameter estimate.

The bias correction accuracy results reach an approximate limit for training data quantities that were two to three times larger than used in related works in literature. Practical quantities were successfully identified for each case study which will be used as recommendations in Chapter 6. The bias correction accuracy declined and the training data quantity increased as the number of input dimensions and input range increased. The bias form in the different case studies may not be more challenging, rather then, research question 1 becomes that of limitations with respect to training data resolution. This observation will be tested in Chapter 6.

A working hypothesis, that bias reduction has a negligible effect on bias correction accuracy, was developed as the case studies progressed. The hypothesis was only disproved in the 6 dim (l) case study, however the different in prediction accuracy was less that 20μm between the uncalibrated and calibrated models and the analysis was inconclusive. The hypothesis will be tested in Chapter 6.

Gaussian process regression was used successfully as a relatively novel tool in this application. One of the advantages of GPR is that it can be trained with relatively small training data quantities, compared to the quantity required by NN for example. However, computer processing time increases by $O(N^3)$ and can be high for large data quantities. In the 6 dim (s) and (l) case studies, relatively large training data quantities were required to approach the limit of model accuracy and the advantage of small data quantities was not exploited. Also, the GPR model is sensitive to the hyperparameter and many solutions exists. Searching for hyperparameters from many initial estimates, and with a high training quantity, required considerable processing time. The efficiency and accuracy of hyperparameter searching could be a design consideration in future work.

The case studies in this chapter presented a number of challenges that were not fully explored:

I The first is the discovery that Euler angle conversions are discontinuous in some configurations which results in inaccurate calibrations. A practical solution is to identify outliers by orientation error.

II Other non-linear effects such as gearbox misalignment were not modelled. The real robot is expected to present a more challenging bias form.

III The reasons for bi-modal and skewed symmetric bias data were not explored. The distributions did were not problematic for bias correction and so exploration was not considered to be within scope.

IV After bias correction, there remained some large bias data which were simulations of positional errors in the order of 1mm. Further analysis would be required to identify if there is a region of joint subspace that has poor accuracy. This is deemed to be beyond the scope of this study although would have a potentially useful outcome.

In summary, thesis objective 2 was met and GPR was used successfully to reduce the positional error of a robot in this study. The case study structure and methodology was informative and the limitations in bias correction have been identified. The same method and case studies will be used in Chapter 7 on the testbed robot with the expectation that the bias will be a greater challenge as a result of unmodelled errors.

Chapter 6

Bias Correction of Industrial Robot Positional Errors

The aim of this chapter is to meet thesis objective 3 by exploring the limitations of bias correction in predicting the positional error of an industrial robot. The calibration and bias correction methodology, proposed in this thesis, is tested on a range of case studies to validate the conclusions made in Chapter 4 with empirical evidence. The focus of this chapter is to explore limitations of bias correction with respect to (1) training data resolution and (2) bias reduction by calibration. A bias reduction hypothesis was proposed in Chapter 4 which stated that bias reduction was expected to have a negligible effect on bias correction accuracy. This hypothesis will be tested here. Substantial gains in bias correction accuracy are predicted, however, it is expected to be lower than the accuracy achieved in the simulation study in chapter 5. The real robot is expected to exhibit non-linear errors arising from gearbox transmission errors that were not presented in the numerical model in Chapter 5, and they are expected to be more challenging to model.

The case studies in this chapter will achieve the same individual objectives as Chapter 5 with the exclusion of testing bias correction accuracy for a range of training data quantities. Instead, the quantities recommended in Chapter 4 are used.

I Measure the pose of an industrial robot in a range or joint configurations, using a laser tracker, and compare to the nominal model pose predictions and evaluate the positional accuracy.

II Calibrate the three competing models in addition to the nominal model, to provide a range of bias data levels in the bias correction case studies.

III Evaluate the performance of bias correction, GPR, to model and predict the robot positional error data (bias) for the case studies: 1 dim, 3 dim, 6 dim (s) and 6 dim (l) which increase in order of complexity.

In this chapter, the following experimental design considerations will be made:

- Sensor visibility will reduce the number of achievable poses. Only a subspace of joint configurations will be tested.
- The hyperparameter search will be conducted with multiple initial estimates to find the global minima.

This chapter is organised into a number of sections. The calibration study results are presented in section 6.2. The bias correction results are presented as separate case studies in sections 6.3 to 6.6. In section 6.7, a synthesis of all the case study results is presented.

6.1 Experimental design

This section describes the robot, the measurement equipment and sensor placement, and the training and validation joint configuration generation for the study.

The robot cell and measurement equipment used by the studies in this chapter are presented in detail in Chapter 3 and are described briefly in this section. The cell layout is shown in Figure 6.1.

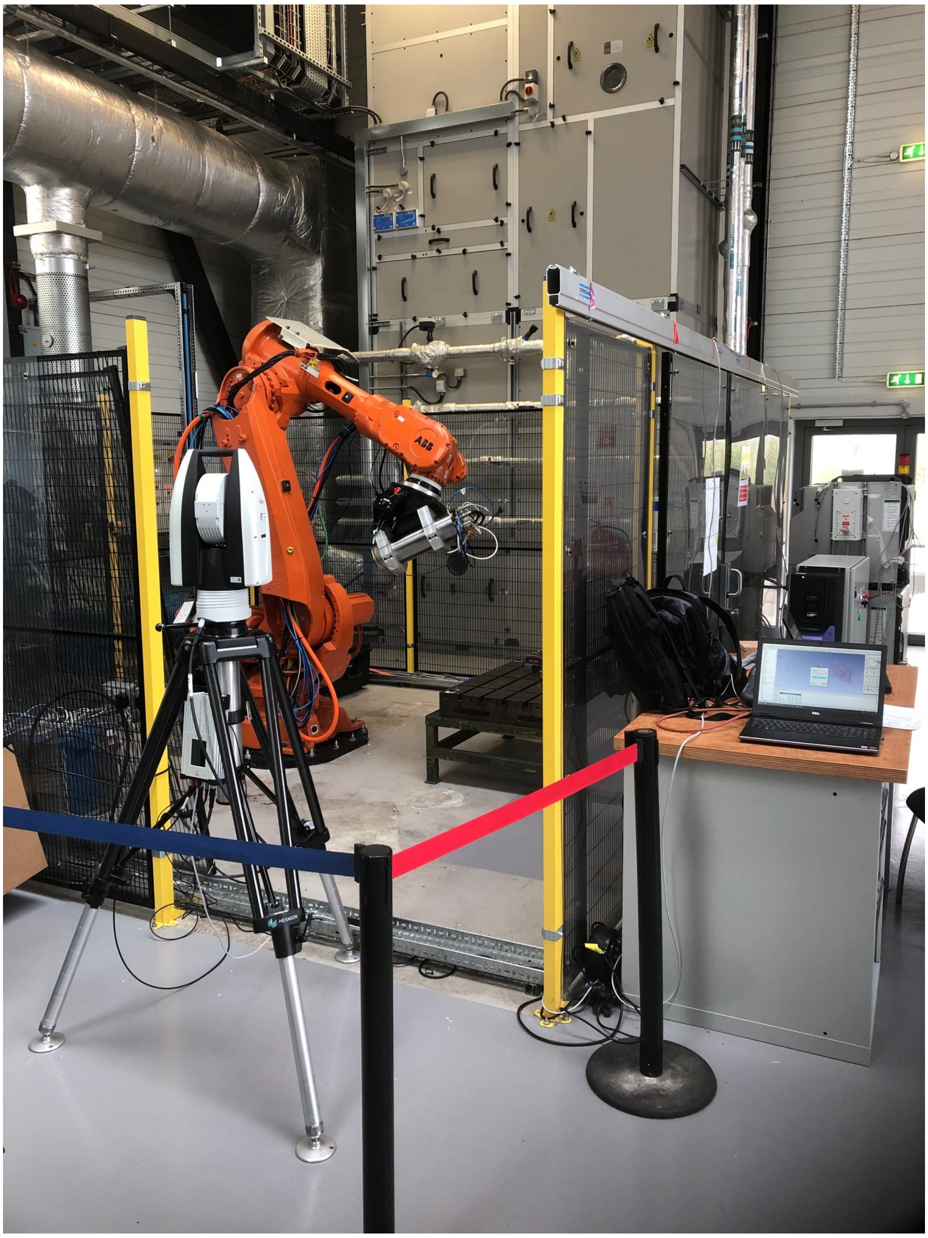

Figure 6.1: ABB IRB 6640 robot cell and laser tracker positioning.

- **Robot**: ABB IRB 6640, 6DOF articulated robot.
- **Measurement**: The AT-960 Leica laser tracker was located at the side of the cell. A side panel of the cell was removed for sensor visibility.
- **Sensor**: The T-mac sensor was mounted to the side of the spindle fixture.
- **Data capture and processing**: Measurements from the laser tracker were received and processed by Spatial Analyser (SA) software.

- **Base frame identification**: The base coordinate system was constructed using the CPA method.
- **Backlash**: The error due to backlash in the joint gearboxes was eliminated by approaching each pose from a nearby bump configuration.
- **Stability**: Transient vibration errors at the TCP when the robot came to an abrupt stop were minimised by approaching each configuration slowly, then waiting for a stable measurement.

6.1.1 Payload and TCP

The payload and centre-of-gravity (cog), relative to the end flange frame, was determined by an integrated robot procedure that uses joint torque data to estimate the payload details. The data is presented in Table 6.1 along with the T-mac transformation details relative to the joint 6 frame, which was used as the tool data.

Sensor position [mm]			T-mac frame orientation [deg]			Payload [kg]	Payload cog [mm]		
x	y	z	γ	β	α		x	y	z
58.553	-193.735	165.958	-179.703	-.0366	-0.481	94.5	-68.5	5.0	208.5

Table 6.1: Payload and TCP sensor location.

6.1.2 Training and validation target generation

The robot was directed to the training and validation poses from an input of joint vectors. The inputs were generated based on Latin hypercube sampling (LHS) between the joint limits presented in Table 6.2. Unlike the simulation study in Chapter 5, the input range was limited by workspace as well as joint space to avoid collision with the cell walls, floor and machining table. Workspace limits, shown in Figure 6.2, were applied by calculating the pose of the robot for each input and excluding those that exceeded the limits in Table 6.3.

Table 6.2: Experimental study joint angle limits by case study.

Joint	Calibration	1 dim	3 dim	6 dim (s)	6 dim (l)
q_1	$\pm 170^0$	5^0	$\pm 45^0$	$\pm 15^0$	$\pm 40^0$
q_2	$-65^0, 85^0$	0^0	$\pm 45^0$	$\pm 15^0$	$-15^0, 45^0$
q_3	$-180^0, 70^0$	$\pm 45^0$	$\pm 45^0$	$-15^0, 30^0$	$-15^0, 45^0$
q_4	$\pm 300^0$	0^0	0^0	$\pm 30^0$	$\pm 80^0$
q_5	$\pm 120^0$	0^0	0^0	$\pm 30^0$	$\pm 90^0$
q_6	$\pm 180^0$	0^0	0^0	$\pm 30^0$	$\pm 80^0$

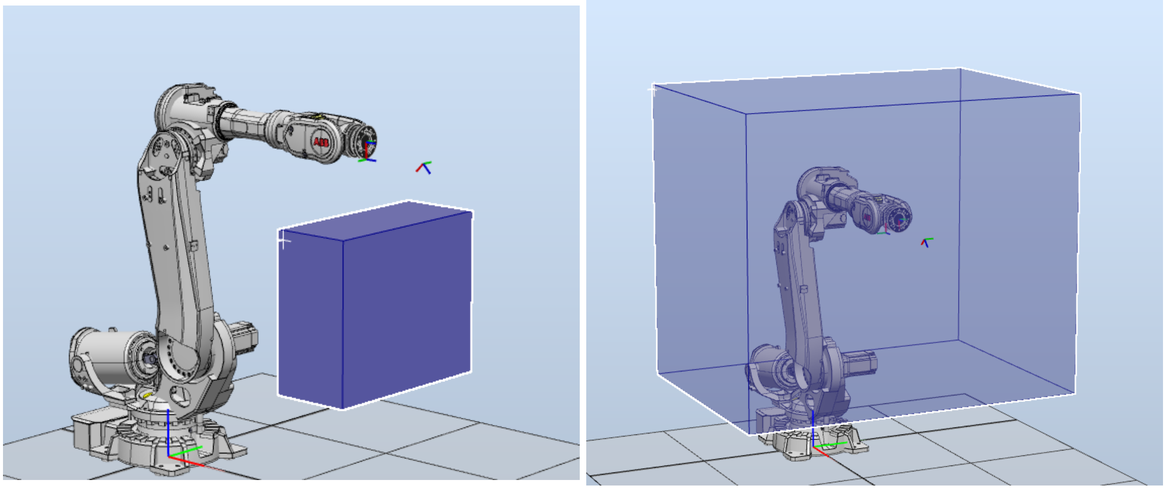

(a)

(b)

Figure 6.2: Diagram of robot workspace limits for (a) the 6 dim (s) and (b) the 6 dim (l) case studies.

Table 6.3: Case study workspace limits relative to robot base.

Test	x		y		z	
	max	min	max	min	max	min
6 dim (s) [mm]	1500	2000	-600	600	1000	2000
6 dim (l) [mm]	0	2000	-1400	1400	800	3200

Sensor visibility was also a design consideration when generating inputs. *Visibility* was determined for each pose by calculating the angle between T-mac normal axis and a line-of-sight vector calculated between laser tracker and T-mac reflector. Inputs with visibility angles that lay outside of $\pm\pi/6$rad T-mac aperture, were excluded.

By filtering out training and validation inputs that exceeded workspace and visibility limits, far fewer inputs were able to be used than generated. Figure 6.3 shows an example of the configuration and filtering process and the training data configuration quantities n at each stage of the process for the 6 dim (l) case study as an example. An initial quantity of 20,000 configurations were required to generate a 1200 sample size. It is acknowledged that the resulting experimental design will no longer be a true LHS, but was still deemed sufficient for the purposes of the study

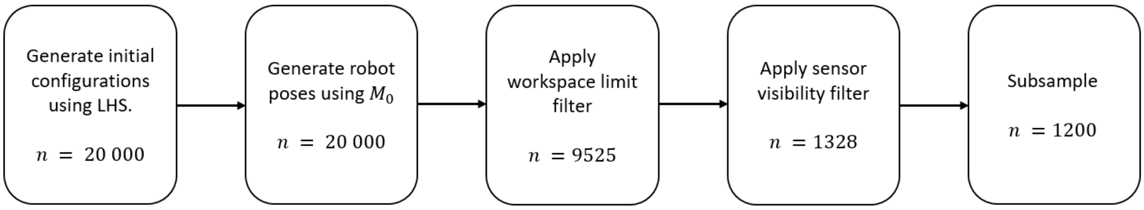

Figure 6.3: Experimental study, input generation flowchart

The training and validation data quantities for each case study and calibration phase, are shown in Table 6.4.

Table 6.4: Experimental study, case study training and validation data quantities.

Case study	Data quantity, n Training	Validation
Calibration	120	100
1 dim	80	20
3 dim	600	100
6 dim (s)	1200	100
6 dim (l)	1200	100

6.2 Calibration results

The aim of the study in this section is to use measured pose data to evaluate the accuracy of an industrial robot and create competing, calibrated models to which GPR based bias correction will be subsequently applied. The competing models were be used to generate bias data with a range of bias levels and form, which were then presented to the bias correction case studies. To remind the reader, the four competing models are: M_0: nominal model, M_1: base calibration, M_2: base and geometric parameter calibration, M_3: base, geometric parameter and joint compliance calibration.

6.2.1 Nominal model M_0accuracy

The pose errors generated by the nominal model M_0 were used to calibrate the competing models M_1, M_2 and M_3, and used a baseline data to be compared to the performance of the competing models. The distribution of positional errors by model M_0 is presented in Figure 6.4 for visual analysis. The summary of results for training and validation pose predictions by M_0 is presented in Table 6.5.

A flat distribution or possibly multi-mode distribution of the Δp_x data was observed in the numerical study in Chapter 5, however, the data was not problematic for calibration and the the competing models successfully reduced the level of bias. Also, the bias data was able to be modelled relatively accurately with by GPR. A similar distribution can be seen in the experimental data in this study, which suggests that the positional error is dominated by the base, geometric and compliance errors, modelled in the simulation study and that they are unlikely to be problematic for calibration or bias correction, and similar results to the numerical study may be achieved.

The distribution of Δp_y data is possibly bi-model. The reason is unclear and was not observed in the numerical study. Bi-modality indicates that the data can be separated into subsets which may be problematic for calibration, with two global minima when searching for hyperparameters, one for each subset of data. The ratio of peaks is high however, which may pull the calibration solution towards the solution that produces the more accurate position predictions.

The distribution of Δp_z is uni-modal with a mean of approximately -3mm, which is expected from payload deflections. With no payload compensation, it is reasonable to expect that a substantial deflection in Δp_z exists in all joint configurations.

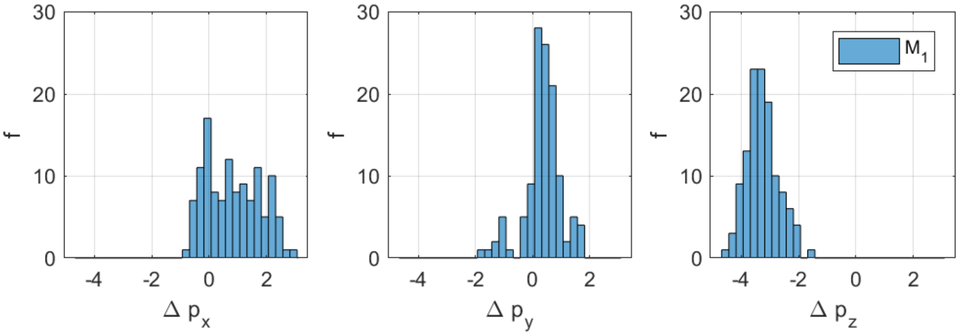

Figure 6.4: Experimental study, distribution of training bias data results for model M_1 in the calibration phase. f: frequency (number of measurements).

The majority of the positional error in rms $|\Delta p|$ terms can be attributed to a bias in Δp_z . The standard deviation in Δp_z is the smaller of distributions compared to Δp_x and Δp_y which is an indication that the payload produces a relatively consistent 3mm downward deflection. The similarity in the order of magnitude between training and validation data provides confidence that the calibrated models will result in an improved accuracy in the test space. Dissimilar results would mean that the model is calibrated and accuracy improved in a space that is not representative of the test space may will fail to provide a range of useful bias data.

Table 6.5: Experimental study, summary of training bias data results for model M_0.

	M_0 Training	M_0 Validation
$\bar{\Delta p}_x$ (std)[mm]	0.840 (0.956)	0.926 (0.934)
$\bar{\Delta p}_y$ (std)[mm]	0.360 (0.640)	0.392 (0.657)
$\bar{\Delta p}_z$ (std)[mm]	-3.265 (0.560)	-3.189 (0.608)
$\bar{\Delta \phi}_\alpha$ (std)[deg]	0.073 (0.230)	0.184 (0.566)
$\bar{\Delta \phi}_\beta$ (std)[deg]	0.045 (0.129)	0.044 (0.131)
$\bar{\Delta \phi}_\gamma$ (std)[deg]	-0.061 (0.252)	-0.168 (0.575)
rms $\lvert\Delta p\rvert$ (max)[mm]	3.622 (5.375)	3.583 (5.041)
rms $\lvert\Delta \phi\rvert$ (max)[mm]	0.186 (0.248)	0.181 (0.241)

6.2.2 Estimated Parameters

The estimated parameter errors from calibration of the competing models are presented in Table 6.6. The estimated parameters in model M_3 are of a similar order to those measured in Chapter 4 using the CPA method, which isolated the geometric errors from other error sources. The similar order is an indication that the calibration was successful in estimating physical parameters. While a comparison is not important in the continuation of this study, it is useful in determining whether the estimated parameters are still reasonable descriptions of the geometry of the system. The two problems are very different and the parameter estimation problem is one of finding parameters that best fit the data, without isolating the effects of each parameter and so the parameter values determined by the two methods should not be same.

The large base rotation parameter $\Delta\beta_0$ can be explained by a solution that models the large deflection observed in the z axis due to payload deflection. A rotation downwards in the y_0 by $\Delta\beta_0$ would be a simple solution to model the bias in Δp_z .

The joint compliance parameters were estimated to have negative values which are non-physical parameters. A negative joint compliance means that and downward payload would result in an upwards rotation by the joint, which is not a physical meaningful model. The non-physical estimation then suggest either that a local minima was found during the search or that the effect of compliance parameters on the data was not highly observable in a parameter search sense, after a simple bias correction by base rotation. The estimation may have returned parameters with a physical meaning if a parameter bounds or regularised least-squares algorithm had been used. In this thesis, the research focus is on providing bias correction with a range of bias data and so for the aim of this study, the calibrated models are sufficient.

Table 6.6: Experimental study, calibrated parameters for competing models.

$\Delta\theta$	M_1	M_2	M_3
$\Delta\gamma_0(10^{-4})$ [rad]	1.578	1.578	1.578
$\Delta\beta_0(10^{-4})$ [rad]	19.185	0.856	2.690
$\Delta\alpha_0(10^{-4})$ [rad]	2.102	0.556	0.184
Δx_0 [mm]	-2.605	-0.075	-0.332
Δy_0 [mm]	0.498	0.033	0.039
Δz_0 [mm]	-0.354	-0.354	-0.354
Δd_1 [mm]	-	-1.666	-1.109
Δd_2 [mm]	-	-	-
Δd_3 [mm]	-	0.166	-0.243
Δd_4 [mm]	-	0.297	0.141
Δd_5 [mm]	-	0.001	0.063
Δd_6 [mm]	-	0.429	0.347
Δa_1 [mm]	-	-0.795	0.120
Δa_2 [mm]	-	1.455	0.783
Δa_3 [mm]	-	-0.330	0.254
Δa_4 [mm]	-	-0.059	0.050
Δa_5 [mm]	-	-0.121	-0.310
Δa_6 [mm]	-	0.093	0.023
Δq_1 [rad]	-	-7.290	-5.391
Δq_2 [rad]	-	13.396	0.086
Δq_3 [rad]	-	-0.723	12.770
Δq_4 [rad]	-	6.884	6.722
Δq_5 [rad]	-	18.853	17.496
Δq_6 [rad]	-	-1.842	-1.310
$\Delta\alpha_1$ [rad]	-	3.440	2.232
$\Delta\alpha_2$ [rad]	-	7.631	5.484
$\Delta\alpha_3$ [rad]	-	4.140	5.084
$\Delta\alpha_4$ [rad]	-	0.979	0.594
$\Delta\alpha_5$ [rad]	-	2.658	2.501
$\Delta\alpha_6$ [rad]	-	3.155	2.534
$\Delta\beta_2$ [rad]	-	1.241	1.778
C_1 (10^{-9}) [rad/Nmm]	-	-	-0.887
C_2 (10^{-9}) [rad/Nmm]	-	-	0.499
C_3 (10^{-9}) [rad/Nmm]	-	-	-0.317
C_4 (10^{-9}) [rad/Nmm]	-	-	-0.877
C_5 (10^{-9}) [rad/Nmm]	-	-	-0.083
C_6 (10^{-9}) [rad/Nmm]	-	-	0.582

6.2.3 Results of calibrated model predictions

Figure 6.5 shows the distribution of the validation data, residual positional errors for the competing calibration models. The distribution errors by base calibration alone in M_1 has retained many of the features observed in the training data which is expected. The base calibration is a data transformation, or localisation, which can be seen as a bias correction of the distribution mean. The more complex errors and interactions between error sources will not be modelled. The distributions of M_2 and M_3 are uniformly Gaussian which indicates that the source of bi-modality in the training data distributions has been modelled by geometric parameters. Unlike the results in Chapter 5, models M_1 and M_2 will provide dissimilar bias data and different challenges for bias correction.

The similar means and distributions of M_2 and M_3 was expected by the analysis of the non-physical joint compliance values in M_3. The similarity indicates that it is unlikely that M_3 will provide sufficiently different challenge for bias correction and can be withdrawn from the remaining study.

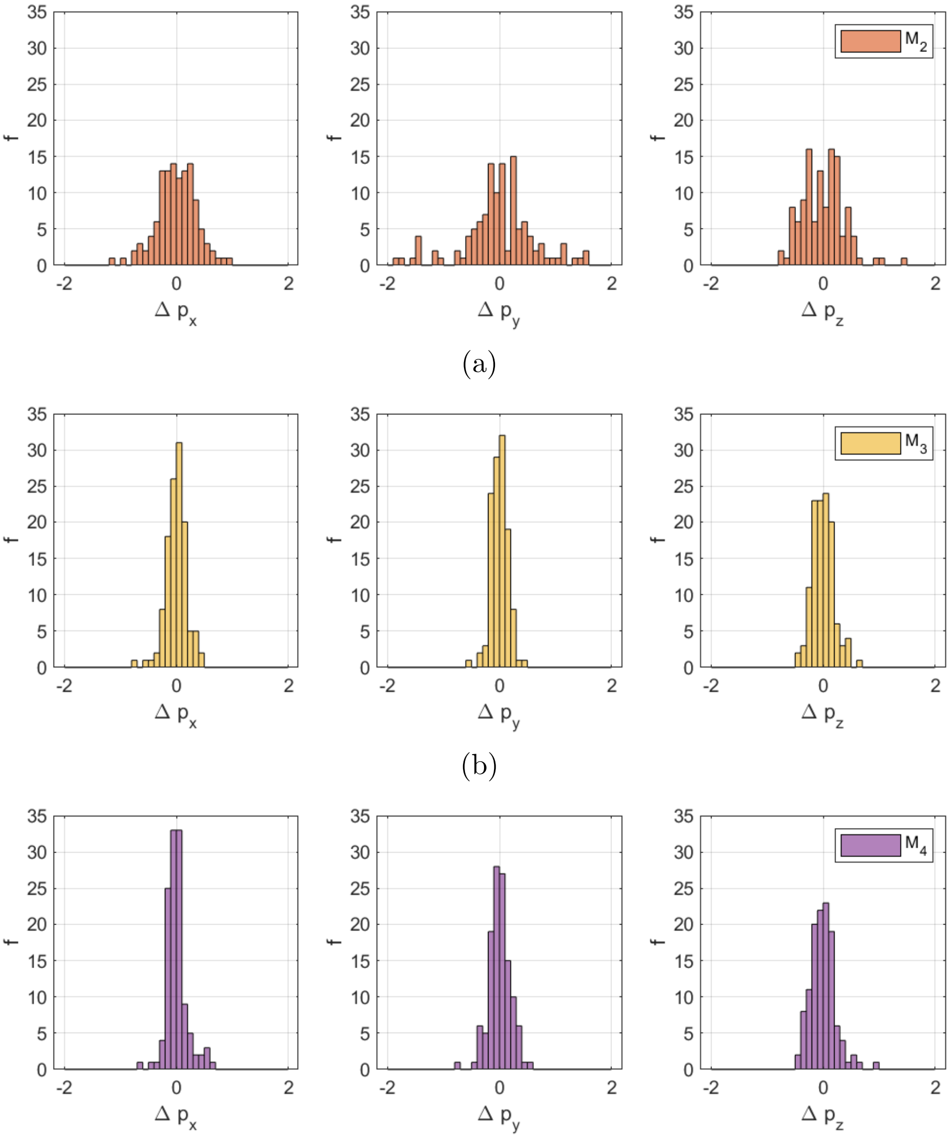

(a)

(b)

(c)

Figure 6.5: Experimental study, distribution of validation bias data results for competing models in the calibration phase. f: frequency (number of measurements).

A summary of bias correction results for training and validation bias data is presented in Tables 6.7 and 6.8. The positional error results after calibration matches the approximate 0.3mm error floor reported in the literature review, which increases confidence that the calibration has been successfully implemented. Calibration of the base alone has reduced the positional error, in rms Euclidian distance terms, by a factor for 3 from 3.6 to 0.8, whilst the additional geometric parameter calibration has reduced the positional error by a factor of 10. As expected, the error reduces with any level of model calibration but gains are reduced with increasing dimensionality.

The observations made by analysis of the error distributions is confirmed by the summary of results. Models M_0, M_1 and M_2 produce bias data that is sufficiently different in value and distribution to test whether bias reduction improves the performance of bias correction. The difference in bias data provided by M_2 and M_3 is not sufficiently different to provide value in the bias correction studies and can be withdrawn. In fact M_2 outperforms M_3 in the prediction of the training data which may be an indication that more parameters can result in a greater challenge in finding the global minima.

Table 6.7: Experimental study, summary of training bias data results for competing calibration models.

	M_0	M_1	M_2	M_3
$\bar{\Delta p}_x$ (std) [mm]	0.840 (0.956)	0.000 (0.356)	0.000 (0.183)	0.000 (0.185)
$\bar{\Delta p}_y$ (std) [mm]	0.360 (0.640)	0.000 (0.639)	0.000 (0.152)	0.003 (0.189)
$\bar{\Delta p}_z$ (std) [mm]	-3.265 (0.560)	0.000 (0.369)	0.000 (0.194)	-0.004 (0.225)
$\bar{\Delta \phi}_\alpha$ (std) [deg]	0.073 (0.230)	0.031 (0.124)	0.000 (0.028)	0.000 (0.025)
$\bar{\Delta \phi}_\beta$ (std) [deg]	0.045 (0.129)	0.016 (0.061)	-0.001 (0.041)	0.004 (0.040)
$\bar{\Delta \phi}_\gamma$ (std) [deg]	-0.061 (0.252)	-0.028 (0.141)	0.000 (0.036)	0.000 (0.030)
rms $\lvert\Delta p\rvert$ (max) [mm]	3.622 (5.375)	0.816 (1.960)	0.306 (1.051)	0.346 (1.145)
rms $\lvert\Delta \phi\rvert$ (max) [mm]	0.186 (0.248)	0.102 (0.213)	0.049 (0.149)	0.047 (0.138)

Table 6.8: Experimental study, summary of validation bias data results for competing calibration models.

	M_0	M_1	M_2	M_3
$\bar{\Delta p}_x$ (std) [mm]	0.926 (0.934)	-0.025 (0.395)	-0.021 (0.194)	0.003 (0.196)
$\bar{\Delta p}_y$ (std) [mm]	0.392 (0.657)	0.045 (0.654)	0.012 (0.177)	0.010 (0.208)
$\bar{\Delta p}_z$ (std) [mm]	-3.189 (0.608)	0.056 (0.388)	0.025 (0.205)	0.024 (0.232)
$\bar{\Delta \phi}_\alpha$ (std) [deg]	0.184 (0.565)	0.089 (0.293)	0.009 (0.087)	0.004 (0.088)
$\bar{\Delta \phi}_\beta$ (std) [deg]	0.044 (0.131)	0.016 (0.066)	-0.007 (0.043)	-0.001 (0.043)
$\bar{\Delta \phi}_\gamma$ (std) [deg]	-0.168 (0.575)	-0.078 (0.305)	-0.008 (0.086)	-0.004 (0.084)
rms $\lvert\Delta p\rvert$ (max) [mm]	3.583 (5.041)	0.856 (1.898)	0.334 (0.806)	0.367 (0.848)
rms $\lvert\Delta \phi\rvert$ (max) [mm]	0.181 (0.241)	0.101 (0.205)	0.055 (0.139)	0.052 (0.132)

6.2.4 Summary

The aim of the study in this section is to use measured pose data to evaluate the accuracy of an industrial robot and create competing, calibrated models to which GPR based bias correction will be subsequently applied.

The aim was successfully met with some useful observations. The positional error of the robot after calibration was substantially reduced by an order of magnitude to rms $|\Delta p| \approx 0.35$mm in this study. The positional error is also of the same order as the robot calibration results reported in research literature, and contributes to the hypothesis that there is a 0.3mm calibrated robot, error floor. The remaining positional error is assumed the be the result of unmodelled non-geometric errors.

Increasing the model *completeness*, by modelling joint compliance, did not result in an improvement in model accuracy. The results of model M_3 did not improve the accuracy over M_2 and resulted in non-physical parameters. However, it is desirable but not imperative that model parameters represent true physical properties. It may be that in other cases, and in future studies, particularly with higher payloads, or a range of payloads, the compliance parameters may be observable and offer a more complete and accurate model.

Moving forward, for the GP bias correction studies, models M_0, M_1 and M_2 will be used as testbeds to generate bias data to test the accuracy of bias correction on data with different bias level and form.

6.3 Bias correction of robot positional error with 1 joint angle input

The aim of the first case study is to test the proposed methodology in predicting robot positional error on an industrial robot by modelling bias data on a 1 dimensional problem, referred to as *1 dim*. In this study, only the angle of joint 3 (q_3) will be an input variable while other joints are fixed.

In the simulation study in Chapter 5, the bias form demonstrated a smooth curve as a function of joint angle. The GPR, which assumes a smooth function, modelled the data accurately as expected, limited only by the measurement variation. In the same study on the real robot, a periodic sinusoidal form on top of the expected smooth form was observed in the Δp_y data. The periodic form is explained in Section 2.2.1.3 as the consequence of gearbox transmission errors which may be modelled in a number ways. An analytical model of the gearbox is likely to be the most accurate approach and one which retains its accuracy in cases of higher input dimensions. However, extensive analytical modelling of the robot is out of the scope of the research presented in this thesis. Modelling the periodic form with GPR will be a test of the limitation of bias correction which is the aim of this chapter.

Periodic data can be modelled with GPR using a number of different kernels. The study in this chapter then is separated into two experiments to meet the following objectives:

I Compare the performance, in terms of bias prediction accuracy, of a squared-exponential kernel (SE) and squared-exponential with additional sinusoidal kernel (SES)

II Evaluate the performance of bias correction in bias prediction on a range of bias data from competing models.

An example of the bias data is presented in Figure 6.6. The Δp_x and Δp_z bias data demonstrate the 'smooth' forms also observed in the numerical model in Chapter 5. The expectation is that the accuracy of the predictions of Δp_x and Δp_z will be limited by the measurement variation. The bias data of Δp_y demonstrates the periodic form which is assumed to be sinusoidal with possible decaying amplitude, on top of a smooth curve. An amplitude of approximately 50μm in Δp_y of for a single joint rotation, could be an explanation for a 0.3mm error in a robot with 6 simultaneous joint rotations.

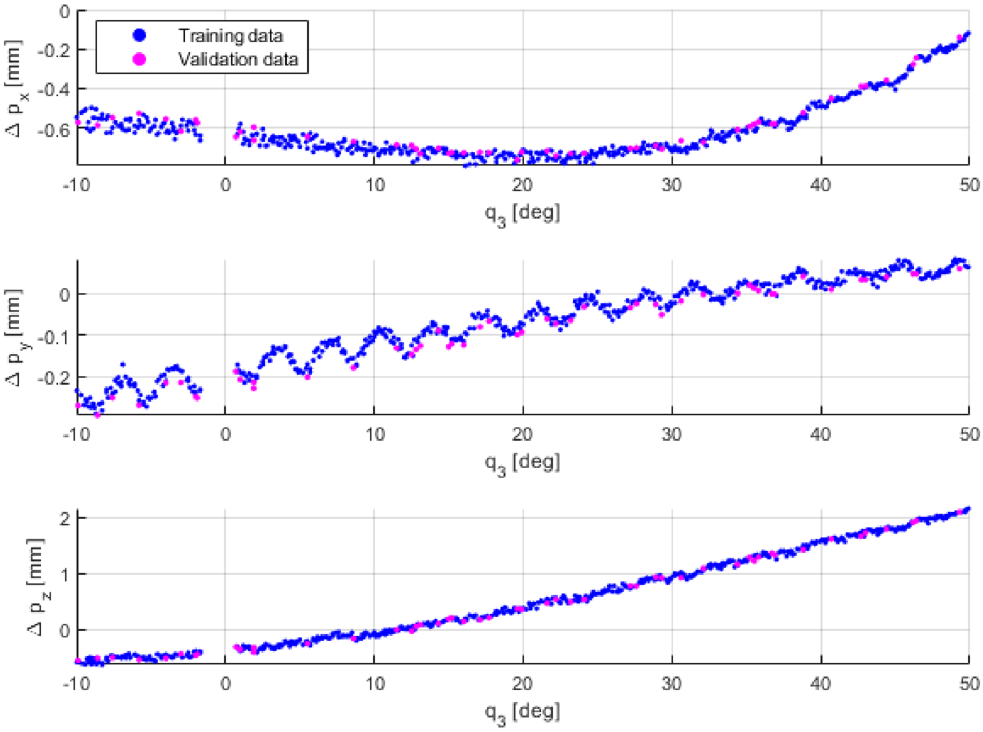

Figure 6.6: Experimental study, bias data plot for model M_1 in the 1 dim case study.

In the study in this chapter, research efforts will concentrate on the modelling of Δp_y bias data. Predictions of Δp_x and Δp_z bias data are expected to approach the limit of the measurement variation and are not considered a challenge for bias correction. The periodic oscillation in Δp_y is a more interesting challenge for bias correction and may indicate limitations in the proposed methodology.

6.3.1 Competing kernel comparison

In this study, bias correction using a GPR with an SE and SES kernel will be compared. Δp_y bias data is provided by model M_2 from measurements of the robot TCP from inputs of joint 1 angles. The experiment is conducted with 9.6 observations per degree of rotation [obs/deg] over a input range of -10^0 to 50^0 to evaluate the performance of the kernel in optimal, high resolution conditions. The data is separated into 500 training and 50 validation subsets.

To remind the reader, the SE and SES kernels are presented in Equations 6.1 and 6.2. σ_f, σ_n and l are hyperparameters, A is the covariance matrix and λ is the period of the oscillation which is known by simple analysis.

$$k(x,x') = \sigma_f^2 exp\left[-\left(\frac{|A|}{2l_1}\right)^2\right] \tag{6.1}$$

$$k(x,x') = \sigma_f^2 exp\left[-\left(\frac{|A|}{2l_1}\right)^2\right] + exp\left[-\lambda\left(\frac{sin|A|}{2l_2}\right)^2\right] \tag{6.2}$$

During the analysis it was noted that the results were sensitive to the initial estimate of the hyperparameters , h_0. The same approach used in Chapter 5 was used whereby 20 sets of randomly generated initial estimates were generated between 0.02 and 2.02. For each kernel, the default initial estimates of 1's were used for the first estimates as a reference.

The results for the competing kernels are presented separately (Figures 6.7 and 6.8) in order to make observations and present examples from the 20 initial hyperparameter estimates.

SE kernel results

The hyperparameter search was sensitive to the initial estimate, with all SE hyperparameter estimates converging to one of four solutions, producing three function forms. (a) The majority of SE functions were identical to Figure 6.7a which modelled the underlying smooth curve as expected. This is the result of a large length scale hyperparameter. This function is referred to as *smooth.* (b) Figure 6.7b shows the single case where the oscillation is partially modelled with a relatively small length scale hyperparameter, $l_1 = 0.299$ that allows the function to respond relatively rapidly with the data form. This function is referred to as *ripple.* (c) Figure 6.7c shows an example of two cases where the solution has a very small length scale hyperparameter, $l_1 = 0.090$ which allows the function to respond rapidly to changes in the data but does not overfit. Having modelled the oscillations, consequently the noise hyperparameter and variance were relatively small ($\sigma_n = 0.01$). This function is referred to as *oscillation.*

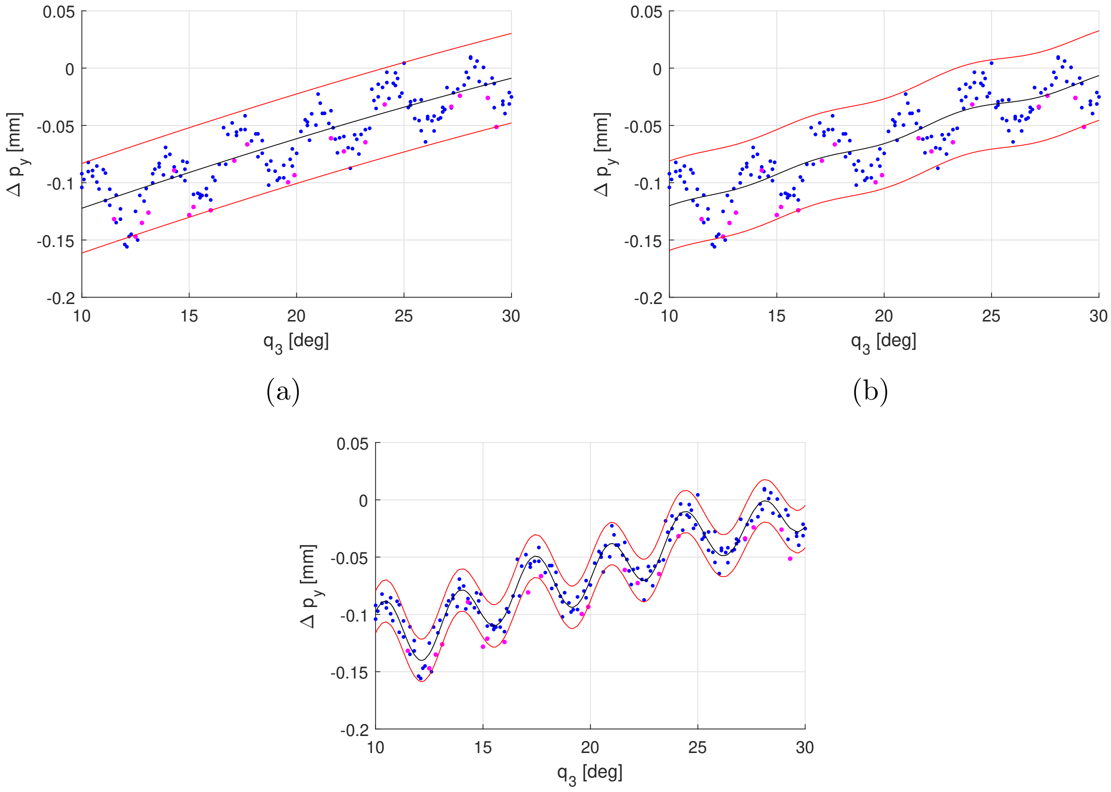

(a) (b)

(c)

Figure 6.7: SE kernel models of periodic oscillations in joint 3 in the 1 dim case study.

SES kernel results

The results for the SES kernel were not as accurate as the default SE kernel which was not expected. Unlike the SE function, there were no repetitions in the hyperparameter estimations, and therefore many local solutions. The optimal solution is therefore difficult to find, and likely to be even more so in higher dimensions. However, categorising by function output (*smooth*, *oscillation*) and variance (small, large), the functions can be described by one of four examples (Figures 6.8a to 6.8d).

The *smooth* functions (a) and (b) as expected, have relatively large length scales ($2.03 < l_1 < 0.450$) and either have a large variance and noise of $\sigma_n \approx 0.420$ or ≈ 0.150. The *oscillation* functions (c) and (d) have relatively small SE kernel length scales ($l_1 = 0.070$ and 0.100, respectively) which results in the SE kernel modelling the curve locally. The sine kernel is relatively ineffective in these solutions. Unexpectedly, the variance is relatively large, as indicated by a large σ_n (between 0.340mm and 0.080mm) when the oscillations are modelled, unlike the previous squared exponential only case.

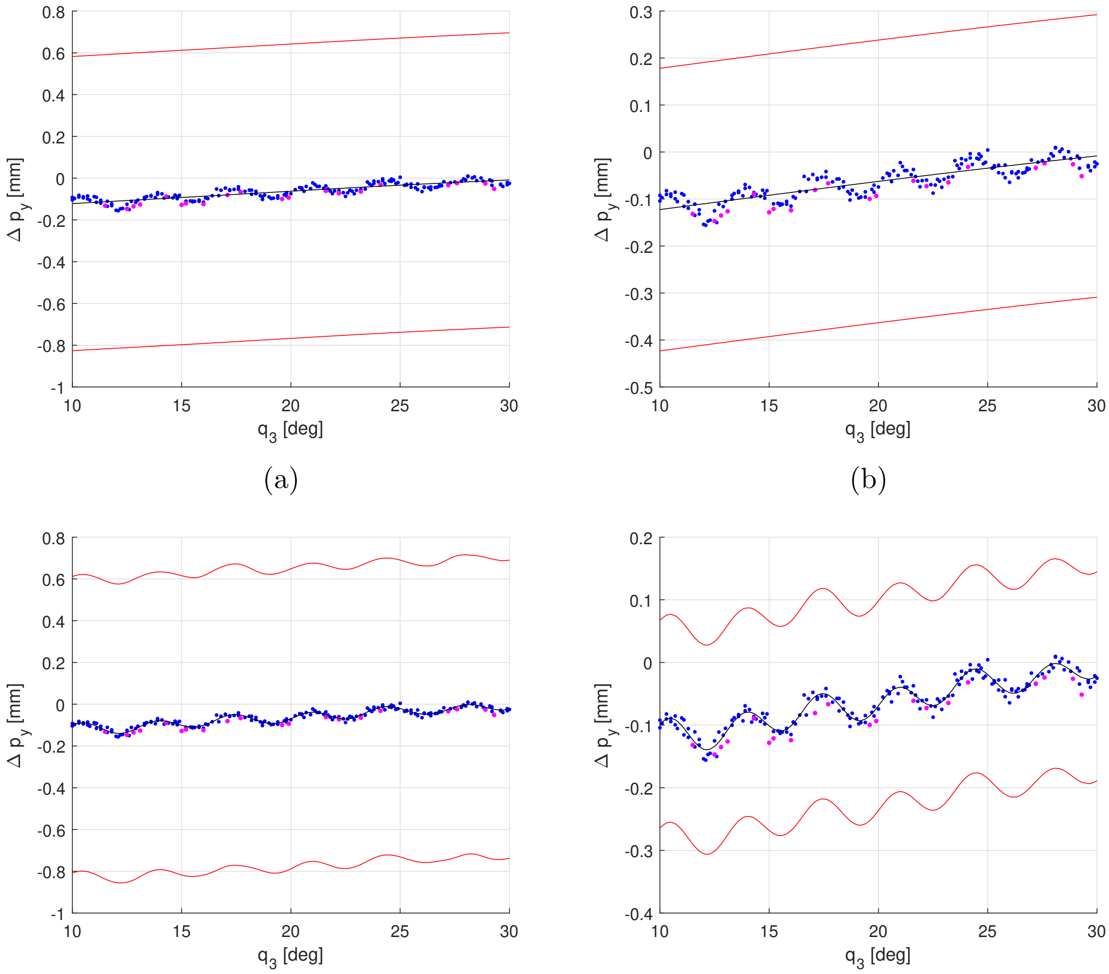

(a) (b)

(c) (d)

Figure 6.8: SES kernel models of periodic oscillations in joint 3 in the 1 dim case study.

In comparison to the SE kernel, the SES kernel produces similar 'smooth', 'ripple' and 'oscillation' models but with less confidence. Moving forward to the main 1 dim trial, it is likely that similar results will be found and that the SES kernel offers no additional advantage over the SE kernel in this case where the bias still has a relatively simple, and smooth form. There is value in exploring kernel selection in light of these results in future work, but it is beyond the scope of this trial. The SE kernel has demonstrated the ability to model both the underlying smooth function and oscillations given careful hyperparameter estimation. This approach can then be tested in the following main trial with confidence.

6.3.2 Bias correction results

In this subsection, the results for bias correction of competing calibration model Δp_y bias data is presented. Following the results in section 6.4, an SE kernel is used. To evaluate the bias correction predictions on less than ideal data quantities, the resolution of the training data was reduced to 4 observations per degree of rotation. 4 obs/^{0} was determined as the minimum required to avoid aliasing. The joint range was also reduced to $\pm 10^0$ as the bias form has been shown to continue outside of this range and has no additional value. 100 inputs were generated randomly using LHS and separated into 80 training inputs and 20 validation inputs.

The bias data in Δp_x and Δp_z for all models has been shown to be a simple, smooth form and is not presented. The bias data of the competing models for Δp_y is the more interesting study and is shown in Figure 6.9.

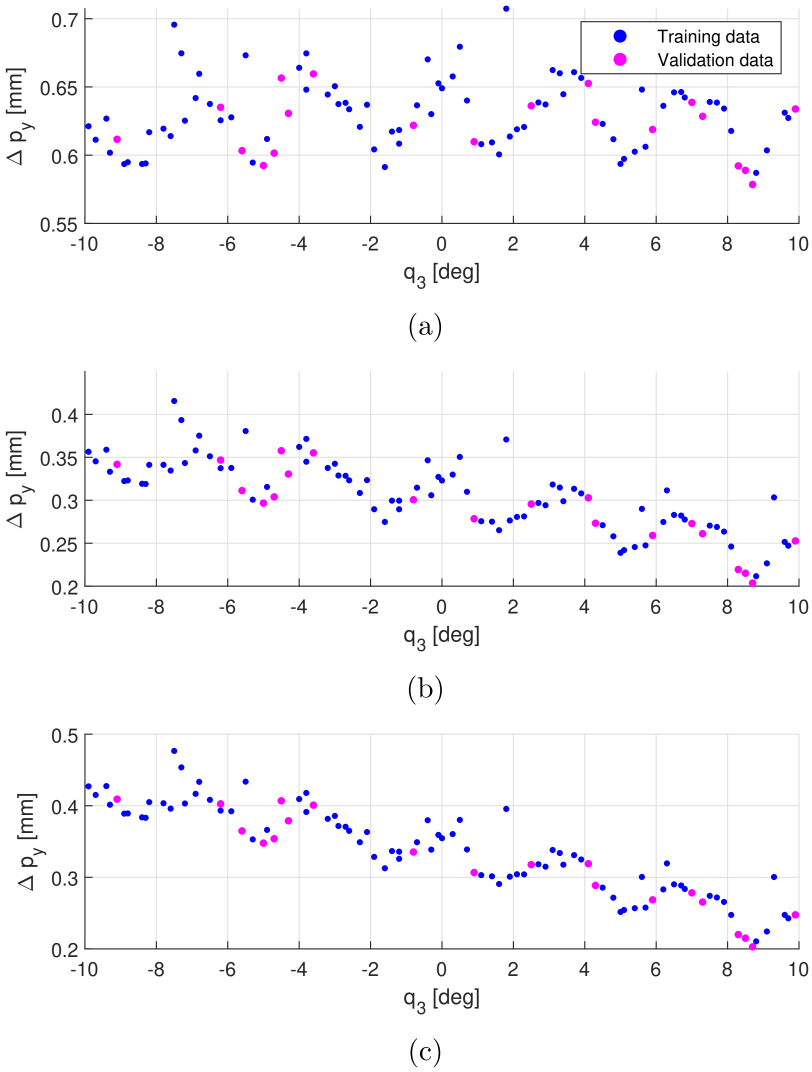

(a)

(b)

(c)

Figure 6.9: Experimental study, bias data plot for competing models (a) M_0, (b) M_1 and (c) M_2 for the 1 dim case study.

The results in predicting training and validation data by the competing models are summarised in Tables 6.9 and 6.10 respectively and provides an evaluation of the task provided to the GPR.

The mean positional error $\Delta\bar{p}_y$ is considerably higher than the zero mean presented in the calibration study in section 6.2. The high mean is the result of evaluating in a subspace of the input, but demonstrates that input spaces exist where positional errors are very high after calibration. The rms and maximum bias data values of M_0 are x2 that of M_1 which potentially presents a different change and will test the effect that bias reduction hs on bias correction accuracy. The bias data of M_2 does not present a significantly different problem and results are expected to be the same.

Table 6.9: Experimental study, training data bias correction results in the 1 dim case study.

Model	$\bar{\Delta p}_y$ (std) [mm]	rms Δp_y (max) [mm]
M_0	0.632 (0.026)	0.633 (0.707)
M_1	0.309 (0.041)	0.312 (0.416)
M_2	0.324 (0.059)	0.347 (0.477)

Table 6.10: Experimental study, validation data bias correction results in the 1 dim case study.

Model	$\bar{\Delta p}_y$ (std) [mm]	rms Δp_y (max) [mm]
M_0	0.621 (0.023)	0.621 (0.606)
M_1	0.289 (0.045)	0.292 (0.358)
M_2	0.317 (0.067)	0.323 (0.409)

Hyperparameter estimations and results

Kernel hyperparameters were estimated from 20 randomly generated initial estimates to find an optimal function in terms of prediction accuracy. The hyperparameters mostly converged to one of two solutions of each competing model bias data and are summarised in Table 6.11. The two solutions are described as *smooth* and *oscillation* functions. Figure 6.10 shows examples of the functions determined by the two solution for each of the calibrated model bias data.

Kernel hyperparameters were estimated from 20 randomly generated initial estimates to find an optimal function in terms of prediction accuracy. The hyperparameters mostly converged to one of two solutions for each of the competing model bias data, and are summarised in Table 6.11. The two solutions are described as *smooth* and *oscillation* functions. Figure 6.10 shows examples of the functions determined by the two solution for each of the calibrated model bias data.

The hyperparameters estimates tended to converge mainly to two solutions. One with a relatively large length scale, which results in a *smooth* curve function (left column) and one with small length scales which results in a function that models the curve locally and follows the *oscillation* (right column). The majority of functions for all of the competing model bias data, modelled the underlying smooth curve rather than the oscillation. The hyperparameters in M_0 vary considerably, however once σ_1 had converged to ≈ 0, the length scale became redundant and the function became linear and with all oscillations accounted for by σ_n.

It is likely that the oscillation in the bias is less able to be modelled with lower resolution data, which was not the case in the kernel comparison study. It can be assumed that as the input dimensions increase, and the input resolution decreases, the gearbox oscillations will not be modelled in favour of a smoother function. The challenge in identifying small changes in the data without over-fitting is an indication of the limitation of bias correction in this application.

Table 6.11: Optimised kernel hyperparameters.

Model	curve fit	σ_1	l_1	σ_n
M_0	smooth	10^{-7} to 10^{-5}	0.915 to 10.37	0.026
	oscillation	0.015	0.099	0.021
M_1	smooth	0.047	2.024	0.026
	oscillation	0.035	0.197	0.022
M_2	smooth	0.094	2.645	0.025
	oscillation	0.054	0.237	0.022

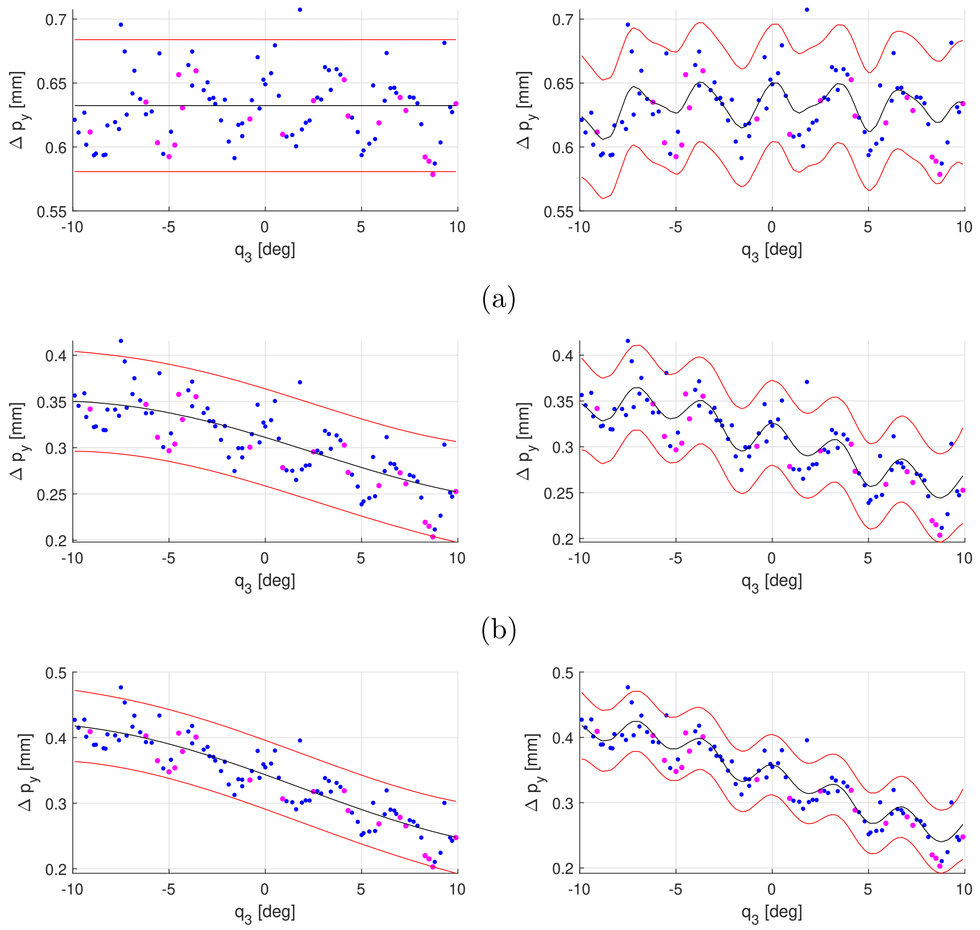

(a)

(b)

(c)

Figure 6.10: Experimental study, bias correction function and confidence ranges for models (a) $M_{0,GP}$, (b) $M_{1,GP}$ and (c) $M_{2,GP}$ in the 1 dim case study.

A summary of bias correction results for training and validation bias data is presented in Tables 6.12 and 6.13. The performance is summarised as above for two representative examples of the *smooth* and *oscillation* functions produced.

The residual error in the bias data has been substantially reduced using bias correction. The rms position error in Δp_y was reduced from approximately 600μm for model M_0, to 26μm by model $M_{0,GP}$. The residual error, however, exceeds the measurement variation in this study, unlike in the numerical study.

Bias reduction has a negligible effect on bias correction accuracy, as also seen in the numerical case study in Chapter 5. The accuracy of the competing model bias predictions is identical with a few microns. This is not unexpected as the competing model bias data sets were not substantially different from each other. Visually, the oscillation function could be considered to be a more accurate model, and as discussed, not modelling the oscillation in higher indention problems may be a limitation in using bias correction for this application. However, the *oscillation* function only is only approximately 5μm more accurate in this case and may not have a significant effect on accuracy in the higher dimension problems.

Table 6.12: Experimental study, summary of training bias correction results for competing models in the 1 dim case study.

Model	curve fit	$\overline{\Delta p_y}$ (std) [mm]	rms Δp_y (max) [mm]
$M_{0,GP}$	smooth	0.000 (0.027)	0.026 (0.075)
	oscillation	0.000 (0.019)	0.019 (0.077)
$M_{1,GP}$	smooth	0.000 (0.026)	0.026 (0.071)
	oscillation	0.000 (0.020)	0.020 (0.081)
$M_{2,GP}$	smooth	0.000 (0.026)	0.025 (0.072)
	oscillation	0.000 (0.020)	0.020 (0.081)

Table 6.13: Experimental study, summary of validation bias correction results for competing models in the 1 dim case study.

Model	curve fit	$\overline{\Delta p_y}$ (std) [mm]	rms Δp_y (max) [mm]
$M_{0,GP}$	smooth	-0.012 (0.023)	0.025 (0.054)
	oscillation	-0.011 (0.017)	0.020 (0.041)
$M_{1,GP}$	smooth	-0.013 (0.023)	0.026 (0.055)
	oscillation	-0.013 (0.017)	0.021 (0.041)
$M_{2,GP}$	smooth	-0.013 (0.023)	0.025 (0.054)
	oscillation	-0.013 (0.016)	0.021 (0.038)

6.3.3 Summary

The aim of the study in this section was to test the use of bias correction to reduce the positional error on an industrial robot in with 1 dimensional input. Bias data was determined as the difference between the measured TCP position and the predictions of the competing calibration models. The bias was predicted using Gaussian process regression. An oscillation in the position of Δp_y was observed, which is explained as a gearbox transmission error in literature, and became the research focus of the study. The oscillation was a more challenging case for bias correction and was used to inform limitations of bias correction for this application. The 0.3 mm positional error floor reached by the calibrated models may be partially explained by a gearbox oscillation in multiple joints and modelling the oscillation may significantly reduce the error further. In the first part of the study, the oscillation was modelled using a squared-exponential (SE) kernel and squared exponential with sinusoidal kernel (SES) and the results were compared. Both kernels returned functions that either modelled just the underlying smooth function that exists in data without gearbox errors, or modelled the oscillation as well as the smooth function. The function selection was sensitive to the initial hyperparameter estimate but the crude approach of testing multiple initial estimates was successful in identifying optimal solutions. Against expectation, the SE kernel provided a function with higher confidence than the SES kernel and was used in the second part of the study.

In the second part of the study, the accuracy of bias correction on bias data from the competing models was compared. Positional error was substantially reduced by bias correction, to the same level for all competing model bias data. The same observations were made in the numerical study in Chapter 5 and it was shown that bias reduction only improved bias correction accuracy in a high input dimension, low data resolution case.

It was shown that the oscillation was more difficult to model in the second study which had lower training data resolution. As the input dimensions or input range increases, the resolution will decrease and gearbox oscillations will be more challenging to identify.

Looking forward to the 3 dim study, the expectation is that positional error will be substantially improved but

6.4 Bias correction of robot positional error with a 3 joint angle input

The aim of this study is to explore the limitations of bias correction in predicting position error on an industrial robot, by increasing the complexity of the problem to 3 input variables, referred to as the *3 dim* case study. In the study in this section, joints 1, 2 and 3 will be rotated whilst all other joint angles are fixed. The results of bias correction predictions of competing model bias data will be compared to continue to explore the effect that bias reduction has on prediction accuracy.

The expectation is that the positional error of the robot will be substantially reduced using bias correction but will not achieve the level observed in the 1 dim case study. The bias form is expected to be more complex i.e. more highly non-linear, and the training data resolution will be lower. It is expected that the bias correction results for the competing model bias data will be very similar. In Chapter 5 it was reported that bias reduction had a negligible effect of bias correction accuracy in the 3 dim cases. The same observation was made in the 1 dim case study in section 6.2.

In the 3 dim study in this section, the GPR model will be trained with 600 measurements and validated with 100 measurements, generated separately using LHS.

The baseline data from the calibrated models is presented in Figure 6.11 and Tables 6.14 and 6.15

6.4.1 Baseline data

Figure 6.11 shows the distribution of training bias data generated by the competing models for a visual analysis. In Chapter 5, large validation data sets were exploited and the validation bias data was presented as a baseline. In the experimental studies in this chapter, due to practical constraints, the quantity of training data is greater than the quantity of validation data and so the training data is presented as a baseline.

Similar observations to those made in Chapter 5 can be made in the comparison of distributions. Firstly, the high bias mean but relatively narrow distribution in the nominal model Δp_z data is the result of a large deflection due to payload. Interestingly, the bias has not been corrected to a zero mean by calibration. Secondly, the nominal model Δp_x data has a relatively flat distribution which may be the result of bi-modality or multiple peaks. Unlike the results in Chapter 5, the calibrated results have a Gaussian distribution. The flatter distribution did not indicate an additionally challenging data set for bias correction and is not assumed to be an indication of bias correction performance.

The distributions of M_1 and M_2 are similar which is an indication that bias correction predictions will have very similar accuracy and the expectations will be confirmed.

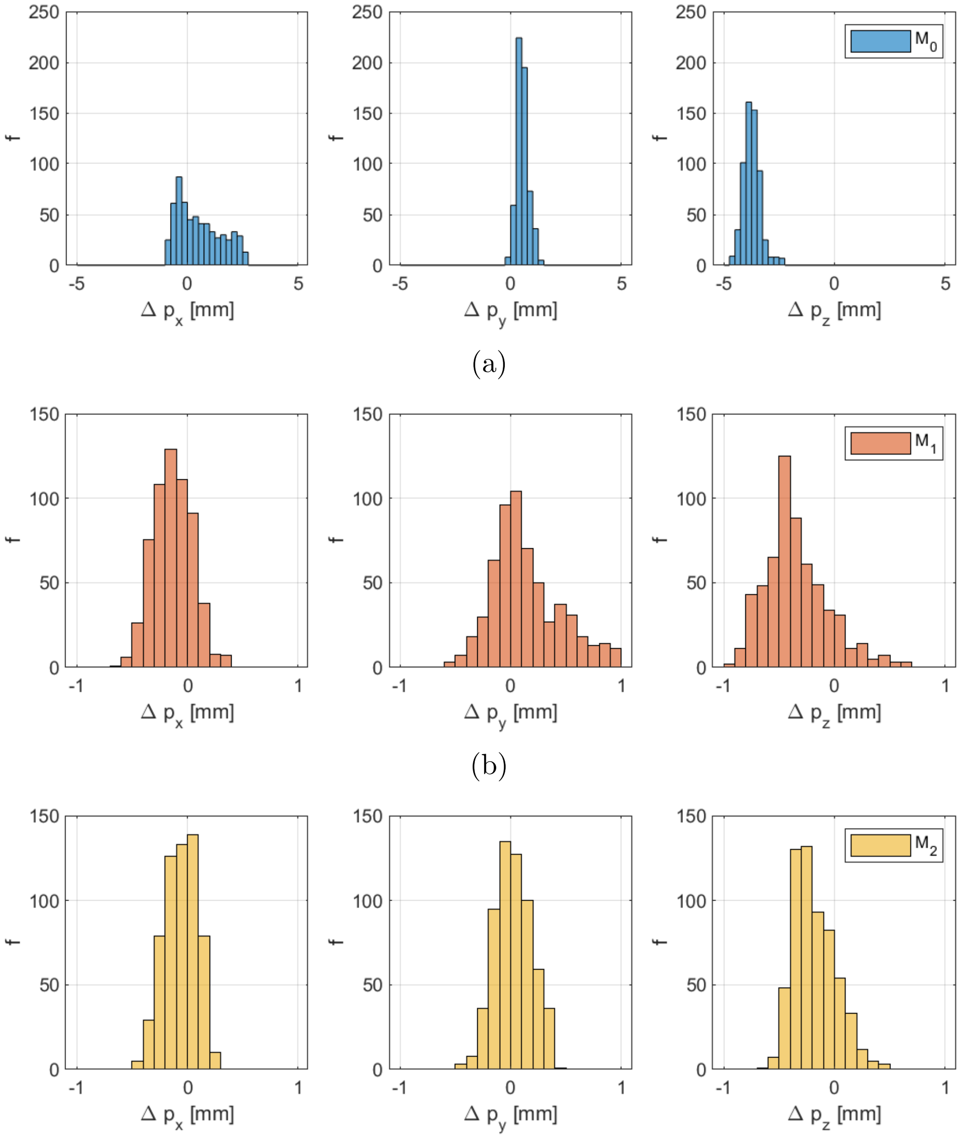

(a)

(b)

(c)

Figure 6.11: Experimental study, distribution of bias data for models (a) M_0, (b) M_1 and (c) M_2 in the 3 dim case study. f: frequency (number of measurements).

The training and validation bias data from the competing models are summarised in Tables 6.14 and 6.15, respectively. The bias data from the competing models will provide different challenges for bias correction, with rms $|\Delta p|$ of M_1 and M_2 being smaller by factors of x5 and x10 compared to M_0. The similar distributions however suggest that the bias data from the competing models will not be more or less challenging.

Table 6.14: Experimental study, summary of training bias data results for competing models in the 3 dim case study.

	M_0	M_1	M_2
$\bar{\Delta p}_x$ (std)[mm]	0.546 (0.993)	-0.131 (0.172)	-0.061 (0.147)
$\bar{\Delta p}_y$ (std)[mm]	0.539 (0.267)	0.150 (0.328)	0.024 (0.164)
$\bar{\Delta p}_z$ (std)[mm]	-3.739 (0.383)	-0.345 (0.287)	-0.181 (0.188)
rms $\lvert\Delta p\rvert$ (max)[mm]	3.971 (4.763)	0.615 (1.470)	0.347 (0.648)

Table 6.15: Experimental study, summary of validation bias data results for competing models in the 3 dim case study.

	M_0	M_1	M_2
$\bar{\Delta p}_x$ (std)[mm]	0.723 (1.043)	-0.139 (0.182)	-0.037 (0.145)
$\bar{\Delta p}_y$ (std)[mm]	0.561 (0.320)	0.197 (0.385)	0.045 (0.174)
$\bar{\Delta p}_z$ (std)[mm]	-3.662 (0.437)	-0.316 (0.314)	-0.168 (0.207)
rms $\lvert\Delta p\rvert$ (max)	3.951 (4.615)	0.659 (1.350)	0.353 (0.685)

6.4.2 Hyperparameter Search

For a visual comparison of solutions, Figure 6.12 shows the bias correction results of the competing models, in terms of rms Δp_x , Δp_y and Δp_z for all 20 hyperparameter estimates. The variation of results in the 20 solutions, for any single model data will be used as an indication of whether an local or global minima was found. A comparison of training and validation results will be used as an indication of overfitting. Examples of estimated hyperparameters are presented in Tables 6.16 and 6.17 for discussion.

A small variation of less than 10μm in the results of Δp_x and Δp_z for any model data is an indication that the global minim was found and thus the optimal function. Small variation can be attributed to early stopping criteria in the hyperparameter search function.

The majority of results for Δp_y also vary by a small amount, however the functions from estimates h_8 and h_{19} provide substantially more accurate results, confirmed by the training data. One explanation is the presence of a local minima relatively central to the searched error hyperspace, whilst the global minima is towards the edge and is found less often from initial searches. The search could be made more robust with an initial probing of the error hyperspace and then concentration of initial estimates.

Alternatively, a wider initial estimate range and more initial estimates could be used but would take considerably more time.

Model overfitting is demonstrated a zero error Δp_x for training data predictions but a very large error for validation data predictions by using h_{11} in the model of Δp_x for M_0.

There are examples of high performing models which can be selected automatically as optimum models. The estimates of h_{10} in x, h_8 in y and h_{12} in z represent the optimum performing models in terms of rms residual error. These will be used as the solutions in the GPR models.

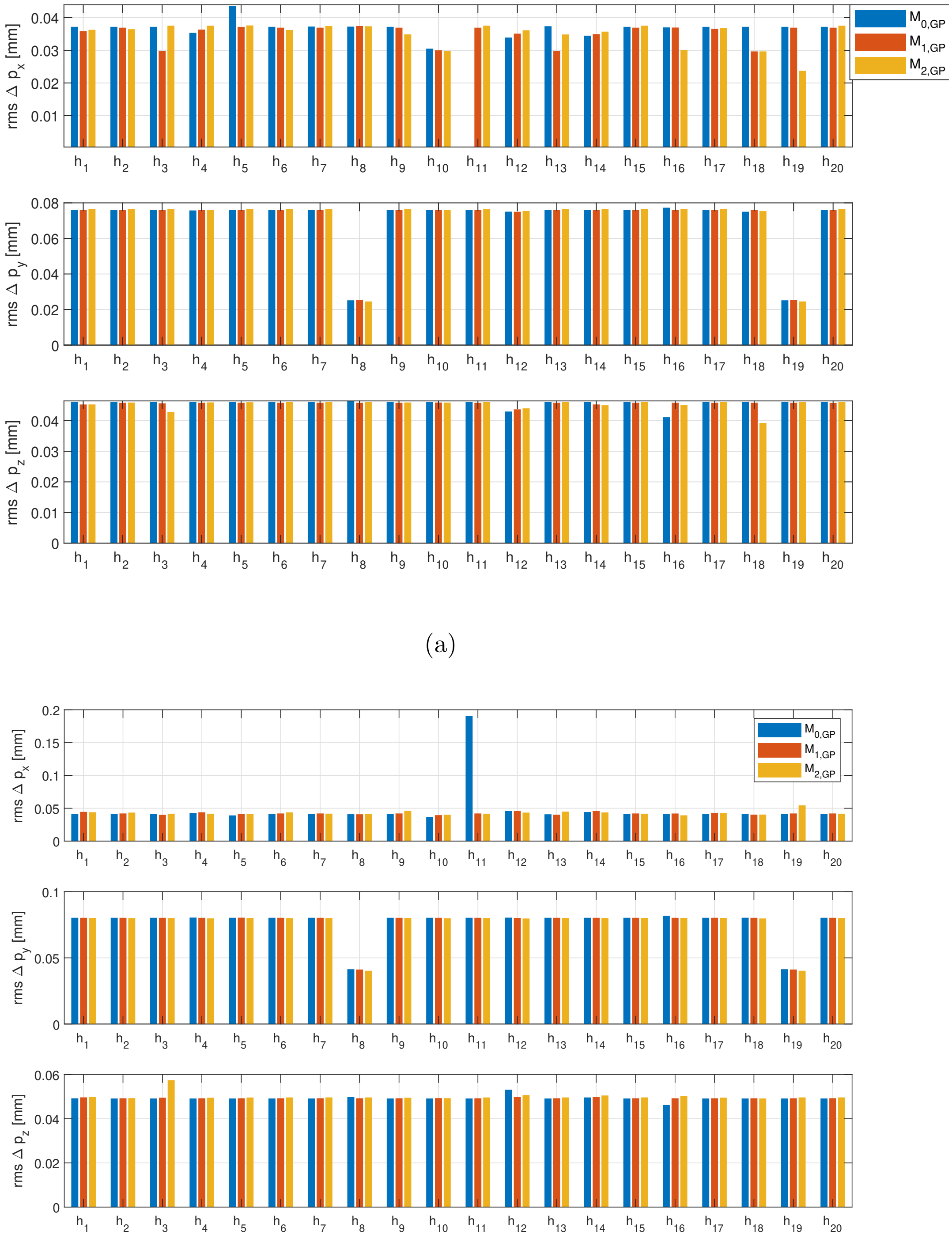

(a)

(b)

Figure 6.12: Experimental study, bias correction rms errors in Δp_x , Δp_y , Δp_z for hyperparameter search result for the 3 dim case study.

Table 6.16 shows the hyperparameters of h_2 as an example of the estimated hyperparameters that produced one of the majority results. These are referred to as the common results. Table 6.17 shows interesting hyperparameters for comparison.

The h_2 hyperparameter values are within reasonable expectations with the exception of $h_2(\Delta p_z\ )$ for model $M_{0,GP}$. The large length scale of $l_1 = 182$ means that the positional error in Δp_z is relatively insensitive to the joint 1 input. Intuitively this would be reasonable to assume. Joint 1 rotates the robot arm around a vertical axis and has the largest and most robust gearbox. It function can be seen as rotating the plane in which the robot operates and is unlikely to produce a complex bias form. However, the other models of Δp_z have much lower estimates which indicates that the function is relatively insensitive to the joint hyperparameter and not necessarily the joint input itself.

The noise hyperparameter σ_n values are considerably higher than the measurement variation of 13μm. An explanation would be that the measurement variation is higher than first measured, but hyperparameters estimates are higher than those estimated in the 1 dimension case study which does not confirm the explanation. The increase in σ_n means that more of the bias is explained by the function as noise which could be interpreted as an indication that the bias form is highly non-linear and cannot be fully modelled by a smooth function. It is possible that the global minim was not found in the hyperparameter search.

$h_8(\Delta p_y\ )$ is the solution with the lowest residual error, compared to the other hyperparameters. A small length scale of $l_1 = 0.1$ is the only significantly different feature which indicates that the bias changes quickly as a function of the joint 1 angle. An oscillation would occur in Δp_y if a gearbox error was present in joint 1 and would be more accurately modelled locally by a small length scale. $l_1 = 0.1$ is at the extreme edge of the search hyperplane set by the range of initial estimates which would explain why most solutions found a local minima.

Hyperparameter set $h_{11}(\Delta p_x)$ has a similarly small joint 2 length scale ($l_2 = 0.08$) however the result is overfitting, indicated by a zero σ_n and poor predictions of the validation data.

Hyperparameter set $h_5(\Delta p_x)$ is an example of the opposite case to the above, whereby l_1 is very large and the function is insensitive to the angle of joint 1 and does not model local changes well.

Table 6.16: Example of the estimated kernel hyperparameters, representative of the majority of estimations from 20 initial estimates.

Model		σ_f	l_1	l_2	l_3	σ_n
$M_{0,GP}$	$h_2(\Delta p_x)$	1.20	5.23	5.10	2.50	0.038
	$h_2(\Delta p_y)$	1.08	3.80	5.28	3.11	0.078
	$h_2(\Delta p_z)$	3.26	182.83	6.51	3.64	0.047
$M_{1,GP}$	$h_2(\Delta p_x)$	0.67	3.72	3.37	2.14	0.038
	$h_2(\Delta p_y)$	1.17	4.00	5.32	3.17	0.078
	$h_2(\Delta p_z)$	1.59	4.89	6.66	3.02	0.047
$M_{2,GP}$	$h_2(\Delta p_x)$	0.18	3.32	1.69	1.17	0.038
	$h_2(\Delta p_y)$	0.23	3.94	2.39	2.26	0.078
	$h_2(\Delta p_z)$	0.66	5.81	4.42	2.66	0.047

Table 6.17: Example of informative estimated GP SE kernel hyperparameters.

Model		σ_f	l_1	l_2	l_3	σ_n
$M_{0,GP}$	$h_8(\Delta p_y)$	0.55	0.10	6.23	3.31	0.031
	$h_{11}(\Delta p_x)$	0.62	0.456	0.08	1.09	0.00
	$h_5(\Delta p_x)$	29.96	597.19	7.70	5.13	0.04

6.4.3 Results of bias correction

Figure 6.13 shows the distribution of residual positional errors after bias correction of the competing model validation data for a visual analysis. The residual error in all competing model bias data has been reduced using bias correction, evidenced by a centralised mean and narrower distribution that observed in the bias data. The flatter distribution of Δp_z for $M_{1,GP}$ and $M_{2,GP}$ still demonstrate a second or possible multiple peaks observed in the competing model bias data which means that there are more input spaces where the positions errors remain relatively high. The bi-modal distribution of the bias data in Δp_x of M_0 is uniform after bias correction which now indicates that there as less input spaces where the positional error is high.

The distribution of bias correction results for the competing models is similar, which indicates that bias reduction is likely to have a marginal effect of bias correction accuracy.

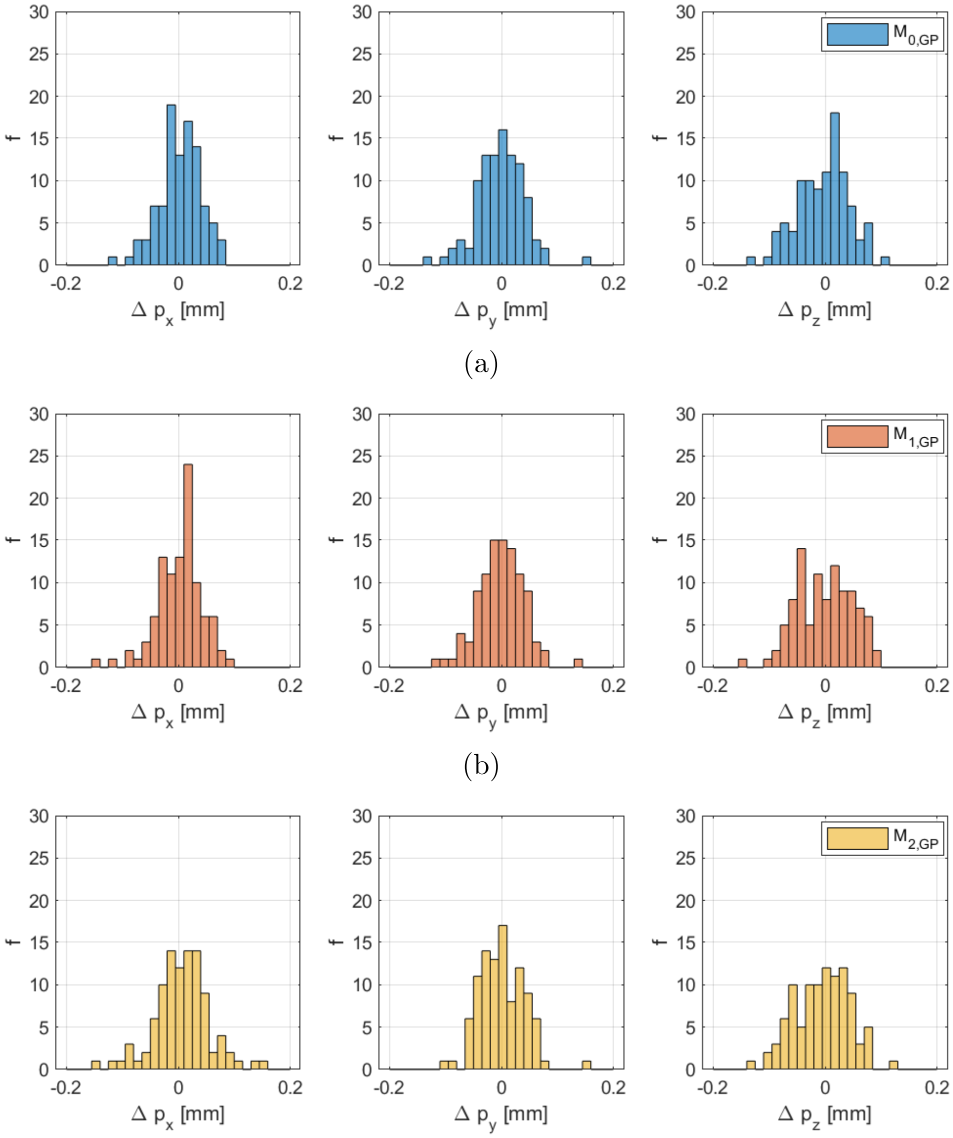

(a)

(b)

(c)

Figure 6.13: Experimental study, distribution of validation data bias correction results for models (a) $M_{0,GP}$, (b) $M_{1,GP}$ and (c) $M_{2,GP}$ for the 3 dim case study. f: frequency (number of measurements).

A summary of bias correction results for training and validation bias data is presented in Tables 6.18 and 6.19.

The residual error in the bias data has been substantially reduced using bias correction. Bias correction reduced the positional error of the robot for the most challenging data, that of M_0, from an rms $|\Delta p|$ of 3.9mm to 57μm for the training data and 72μm for validation data. The results are in fact similar to those in the numerical study in

Chapter 5 which provides confidence in the numerical study as a useful simulation.

Similar to the 1 dim case study, the accuracy of bias correction predictions is only marginally affected by the reduction of bias size and complexity. In fact, the rms and maximum $|\Delta p|$ values are the lowest for the $M_{0,GP}$ model, followed by the $M_{1,GP}$ model and $M_{2,GP}$ model which is against expectation. The range of rms $|\Delta p|$ distance results is only 8μm which is small, however the maximum positional error is 0.1mm higher for the $M_{2,GP}$ model.

Table 6.18: Experimental study, summary of training data bias correction results for competing models in the 3 dim case study.

	$M_{0,GP}$	$M_{1,GP}$	$M_{2,GP}$
$\bar{\Delta p}_x$ (std) [mm]	-0.000 (0.031)	-0.000 (0.029)	-0.000 (0.024)
$\bar{\Delta p}_y$ (std) [mm]	-0.000 (0.025)	-0.000 (0.025)	-0.000 (0.025)
$\bar{\Delta p}_z$ (std) [mm]	0.000 (0.041)	-0.000 (0.044)	0.000 (0.039)
rms $|\Delta p|$ (max) [mm]	0.057 (0.182)	0.059 (0.170)	0.052 (0.148)

Table 6.19: Experimental study, summary of validation data bias correction results for competing models in the 3 dim case study.

	$M_{0,GP}$	$M_{1,GP}$	$M_{2,GP}$
$\bar{\Delta p}_x$ (std) [mm]	0.003 (0.037)	0.003 (0.040)	0.003 (0.055)
$\bar{\Delta p}_y$ (std) [mm]	-0.001 (0.042)	-0.001 (0.041)	0.001 (0.040)
$\bar{\Delta p}_z$ (std) [mm]	-0.004 (0.046)	-0.001 (0.050)	-0.005 (0.049)
rms $|\Delta p|$ (max) [mm]	0.072 (0.163)	0.076 (0.186)	0.084 (0.265)

6.4.4 Summary

The aim of this study was to investigate the limitations of bias correction in predicting robot positional error from an input of 3 joint variables, with respect to bias reduction.

The positional error of the robot after bias correction was substantially reduced to sub 0.1mm levels which was expected. Bias reduction had a marginal effect of bias correction accuracy and against expectations, the bias correction predictions were more accurate for the nominal model bias data. The limitations of bias correction with respect to bias reduction will continue to be tested on higher dimensional problems.

The search for optimal hyperparameters has a significant influence on the accuracy of the GPR model.It was shown that global minima, can be easily missed if they exist at the outer edges of the search space if local minima exists. Search strategy involving careful section of initial search estimates will continue to be a design consideration but could be improved with further research.

6.5 Bias correction of robot positional error with a 6 joint angle input and small joint angle range

The aim of this study is to investigate the limitations of bias correction by increasing the complexity of the problem to 6 input variables, but with a relatively narrow input space, referred to as the 6 dim (s) case study. The input space is narrowed by reducing the joint angle range to take a small step towards a more complex problem and to reflect the challenge of milling which is often in a smaller workspace, compared to panel drilling. In this study joints 1 to 6 will all be rotated to configurations that provide TCP poses. The challenges of bias data prediction accuracy in relation to training data quantity and bias reduction from competing models are tested.

In Chapter 5, the study of bias correction on the numerical model in the same 6 dim (s) demonstrated that positional errors can be substantially reduced and that bias reduction has a negligible effect on bias correction accuracy. Similar observations were made in the study of an industrial robot in the 3 dim case study in section 6.4. The results in this case study are expected to confirm the same observations and will be compared to those in Chapter 5 and section 6.4.

In the 6 dim (s) study, the GPR model will be trained with 1200 measurements and validated with 100 measurements, generated separately using LHS. 1200 training data measurements is considerably higher than the 800 used in the similar case study in Chapter 5. In Chapter 5 it was suggested that substantially more training data measurements would be required to improve bias correction accuracy and test the limitations of bias correction in the 6 dim (l). In both the 6 dim case studies in this chapter, the larger 1200 training data quantity will be used so that the results can be compared.

The rotation of all six joints means that in some joint configurations, the T-mac sensor cannot be seen by the laser tracker. The input space is limited to a subspace where the sensor is visible. The process of generating joint angle input vectors, and selecting only those that meet the input space dimensions whilst remaining visible, was discussed in more detail in section 6.1. It was observed during the experiment that many of the training configurations were very similar to each other and were similar to the validation configurations as a result inputs being limited to a subspace. It can be assumed that the Latin hypercube used for input sampling, is not fully represented and the large training data set could be reduced and still maintain a relatively high resolution.

6.5.1 Baseline data

Figure 6.11 shows the distribution of validation bias data generated by the competing models for a visual analysis.

Similar observations to those made the 3 dim case study in section 6.4 can be made in the comparison of distributions. The high bias mean but relatively narrow distribution in the nominal model Δp_z data is the result of a large deflection due to payload. Also, the bias has not been corrected to a zero mean by calibration. In Chapter 5 the same case study presented a flat or multi-modal bias distribution in Δp_x and a skewed symmetric bias distribution in Δp_z . The reason was not investigated but the same distributions are not evident in the bias data in this study in this section. The different distributions between the numerical and experimental data could be the contribution of unmodelled errors, such as gearbox errors in the real robot, the more extensive analysis provided by more data in the experimental study or the limitation of the input to a subspace due to sensor visibility. The Uniform distribution in this case study does not indicate any concerns for bias correction.

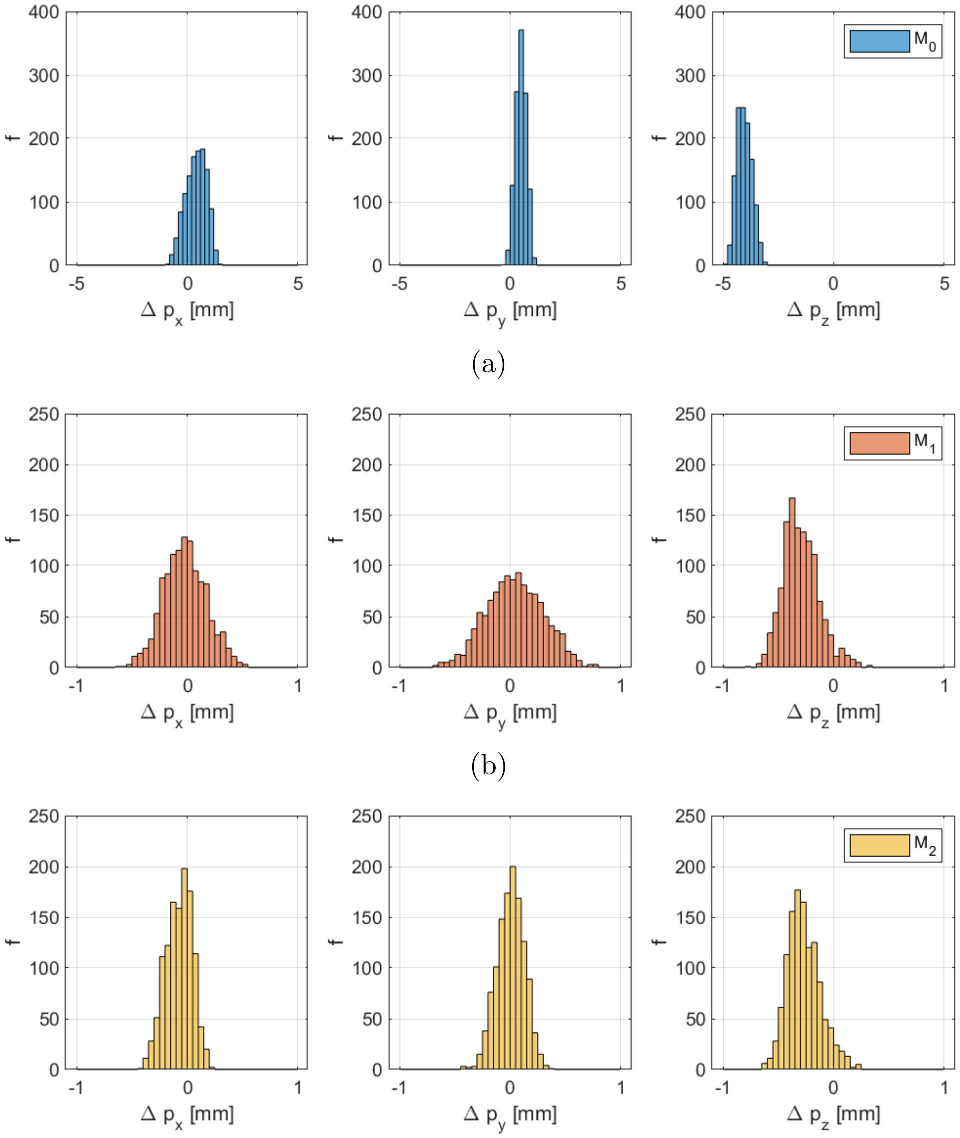

(a)

(b)

(c)

Figure 6.14: Experimental study, distribution of validation bias data for models (a)M_0, (b)M_1 and (c) M_2 in the 6 dim (s) case study. f: frequency (number of measurements).

The training and validation bias data from the competing models is summarised in Tables 6.20 and 6.21 respectively. The bias data from the competing models will provide different challenges for bias correction, with two orders of magnitude, 4mm and 0.4mm in terms of rms $|\Delta p|$.

The higher input dimensions, but smaller input range in this study compared the 3 dim study produce positional errors with a similar magnitude for each competing model: 4, 0.65 0.35mm for the 3 dim case study and 4.1, 0.45 ad 0.35 in the 6 dim (s) case study. In Chapter 5, the same observation was made and the results showed that the accuracy of the bias correction predictions of the 6 dim (s) case was only marginally less accurate than the 3 dim case. The assumption was that the 6 dim case retained a similar training data resolution by reducing the input range. It can be assumed that similar observations will be made in the case study in this section.

However, the bias data of models M_1 and M_2 are only different by approximately 0.1mm in rms $|\Delta p|$ and bias correction of the two sets of data are likely to result in predictions with negligible difference.

Table 6.20: Experimental study, summary of training bias data results for competing models in the 6 dim (s) case study.

	M_0	M_1	M_2
$\overline{\Delta p}_x$ (std) [mm]	0.400 (0.464)	-0.021 (0.193)	-0.074 (0.118)
$\overline{\Delta p}_y$ (std) [mm]	0.490 (0.244)	0.045 (0.258)	0.004 (0.123)
$\overline{\Delta p}_z$ (std) [mm]	-4.036 (0.334)	-0.295 (0.163)	-0.268 (0.148)
rms $\lvert\Delta p\rvert$ (max) [mm]	4.132 (4.974)	0.469 (0.940)	0.358 (0.697)

Table 6.21: Experimental study, summary of validation bias data results for competing models in the 6 dim (s) case study.

	M_0	M_1	M_2
$\overline{\Delta p}_x$ (std) [mm]	0.410 (0.510)	-0.005 (0.194)	-0.064 (0.127)
$\overline{\Delta p}_y$ (std) [mm]	0.496 (0.242)	0.050 (0.255)	-0.015 (0.130)
$\overline{\Delta p}_z$ (std) [mm]	-4.011 (0.327)	-0.267 (0.177)	-0.238 (0.162)
rms $\lvert\Delta p\rvert$ (max) [mm]	4.114 (5.027)	0.454 (0.867)	0.346 (0.638)

6.5.2 Hyperparameter search

An initial investigation showed that the hyperparameter search did not converge to one of a few solutions and that the results when modelling the bias data using the different hyperparameter solutions were wide ranging. For a visual comparison of solutions, the bias correction results for training and validation data predictions from the competing models, in terms of rms Δp_x , Δp_y and Δp_z , for all 20 hyperparameter estimates is presented in Figure 6.12. A comparison of the accuracy of training data predictions for the estimated hyperparameter from the 20 initial estimates will be used to indicate the number of solutions and local minima. A comparison of the accuracy of training and validation results is used as an indication of sensitivity to hyperparameter selection and to identify overfitting.

The wide range in the accuracy of training data predictions is an indication that there are many local minima when searching for optimum hyperparameter solutions. Also, accuracy of training data predictions is sensitive to the hyperparameters used by the GPR model, evidenced by a range of 0.1mm in rms Δp_y and Δp_z . It can be assumed that the higher dimensions compared to the 3 dim case study, results in a search space with many more solutions. It was discussed in the 3 dim case study in section 6.4 that the hyperparameter search strategy is an important design consideration. In this study, the approach of comparing results for 20 random initial estimates is used but it is recognised that a more reliable strategy should form part of future work.

As a likely result of over-fitting, there are exceptions of poor performing models, which predict the training data with near zero rms Δp, then predict the validation data with a large rms Δp, $M_{0,GP}$ $h_{16}(\Delta p_x)$ and $h_{19}(\Delta p_x)$ being good examples.

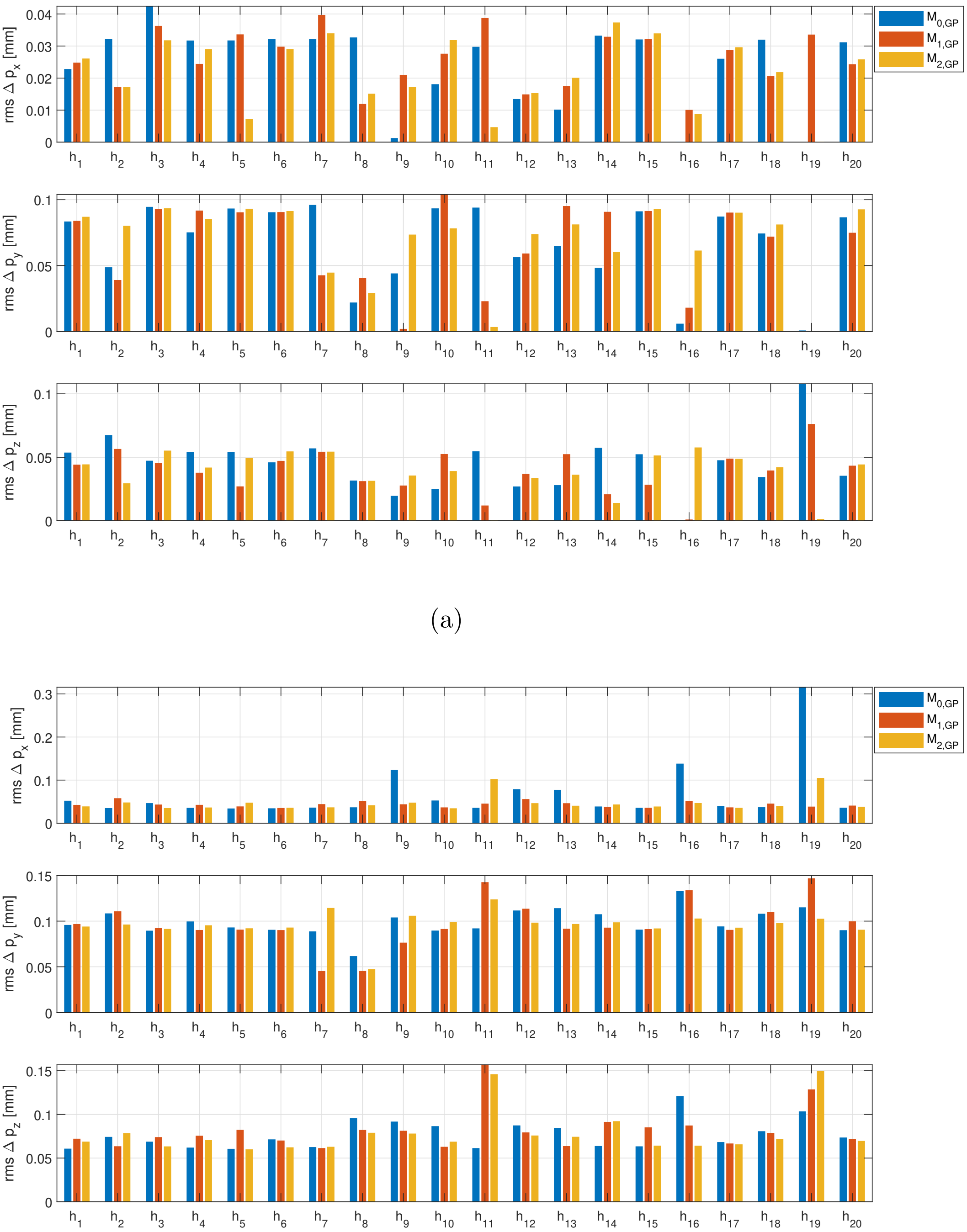

(a)

(b)

Figure 6.15: Experimental study, bias correction rms errors in Δp_x , Δp_y , Δp_z for hyperparameter search result for the 6 dim (s) case study.

Table 6.22 shows examples of interesting hyperparameters that are worth further discussion.

The first set of hyperparameters ($M_{0,GP}$: $h_9(\Delta p_x)$,$h_{16}(\Delta p_x)$,$h_{19}(\Delta p_x)$) are examples where the bias correction, validation data has high residual errors. The relatively small σ_n, is evidence that using these hyperparameters in the GPR model, results in training data overfitting and a poor prediction of the validation data. The result is a large uncertainty and the measurement variation in the validation observations can no longer be explained. Hyperparameter estimates with $\sigma_n << \sigma_{epsilon}$ will produce GPR models that predict test data with relatively low accuracy. It can be assumed that σ_n can be used as a simple filter to remove model solutions when searching for optimal hyperparameters.

The second set ($M_{2,GP}$: $h_{19}(\Delta p_y)$) is another example where the bias correction, validation data has high residual errors, which is partially explained by very small l_1 and l_4 length scales. Models with small length scales change rapidly to local changes in data but fail to model medium or longer term data trends and therefore may not predict test data if it isn't sufficiently local to the training data.

The third set ($M_{2,GP}$: $h_3(\Delta p_y)$) is an example of a model with very large length scales but the bias correction, validation data has residual errors that are of a similar order to others. Models with large length scales are insensitive to the inputs that are associated with those large length scales, in this case, the angles of joints 5 and 6. It would be expected that the model would not able model highly non-linear data accurately, but that is not confirmed by the results in this study.

It is a difficult task to assume the relative accuracy of a GPR from the hyperparameter length scales in a 9 parameter hyper-space and would require extensive investigation to be able to use length scale as a filter for model selection. This is beyond the scope of this study.

Table 6.22: Example of the estimated GP SE kernel hyperparameters, representative of the majority of estimations from 20 initial estimates.

Model		σ_f	l_1	l_2	l_3	l_4	l_5	l_6	σ_n
$M_{0,GP}$	$h_9(\Delta p_x)$	0.23	0.58	0.85	1.13	1.28	1.26	0.54	**-0.011**
	$h_{16}(\Delta p_x)$	0.25	0.84	0.24	0.36	2.21	0.99	0.86	**-0.006**
	$h_{19}(\Delta p_x)$	0.38	0.10	0.95	1.00	0.20	1.15	13.12	**-0.002**
$M_{2,GP}$	$h_{11}(\Delta p_z)$	0.14	0.32	**0.05**	1.09	0.28	0.67	2.01	**-0.006**
	$h_{19}(\Delta p_z)$	0.15	**0.07**	2.19	0.62	**0.05**	0.90	2.12	0.014
$M_{2,GP}$	$h_3(\Delta p_y)$	3.48	22.76	15.33	66.97	**4889.20**	**752.49**	21.02	0.092

6.5.3 Bias correction results

Figures 6.16 and 6.17 show the distribution of residual positional errors after bias correction of the competing model training and validation data respectively, for visual analysis.

The distribution of training data bias in section 6.2.1, which is referred to as baseline data, was broadly described as uniform with a non-zero mean. The distribution of residual error data after bias correction is compared to the baseline data as an indication that the training data has been modelled with some success. The distribution of bias correction, residual error data has an approximately zero mean and a narrower distribution i.e. expected lower standard deviation, compared to the training data bias which is a positive indication that the training data was modelled with some success and positional errors have been reduced.

A comparison of distribution mean, standard deviations and profile (e.g. uniform, bi-modal) between competing models is used to indicate whether bias reduction has increased the accuracy of bias correction predictions. The residual error distributions for the competing models are very similar in terms of means and distribution width and profile with the small exception of the distribution of Δp_y . The prediction of the Δp_y bias data for model M_0 is more accurate than the M_1 and M_2 bias data which is against expectation, evidenced by a narrower distribution. It is reasonable to assume the range is small enough to be explained by hyperparameter estimates that maybe sub-optimal, possibly only through early stopping criteria.

Some distributions of the residual errors in the validation data show evidence of multiple peaks. For example, there is a small second peak in the residual error data in Δp_z from model $M_{2,GP}$ which means that there are approximately 10 robot configurations where the positional error Δp_z is greater than 0.1mm.

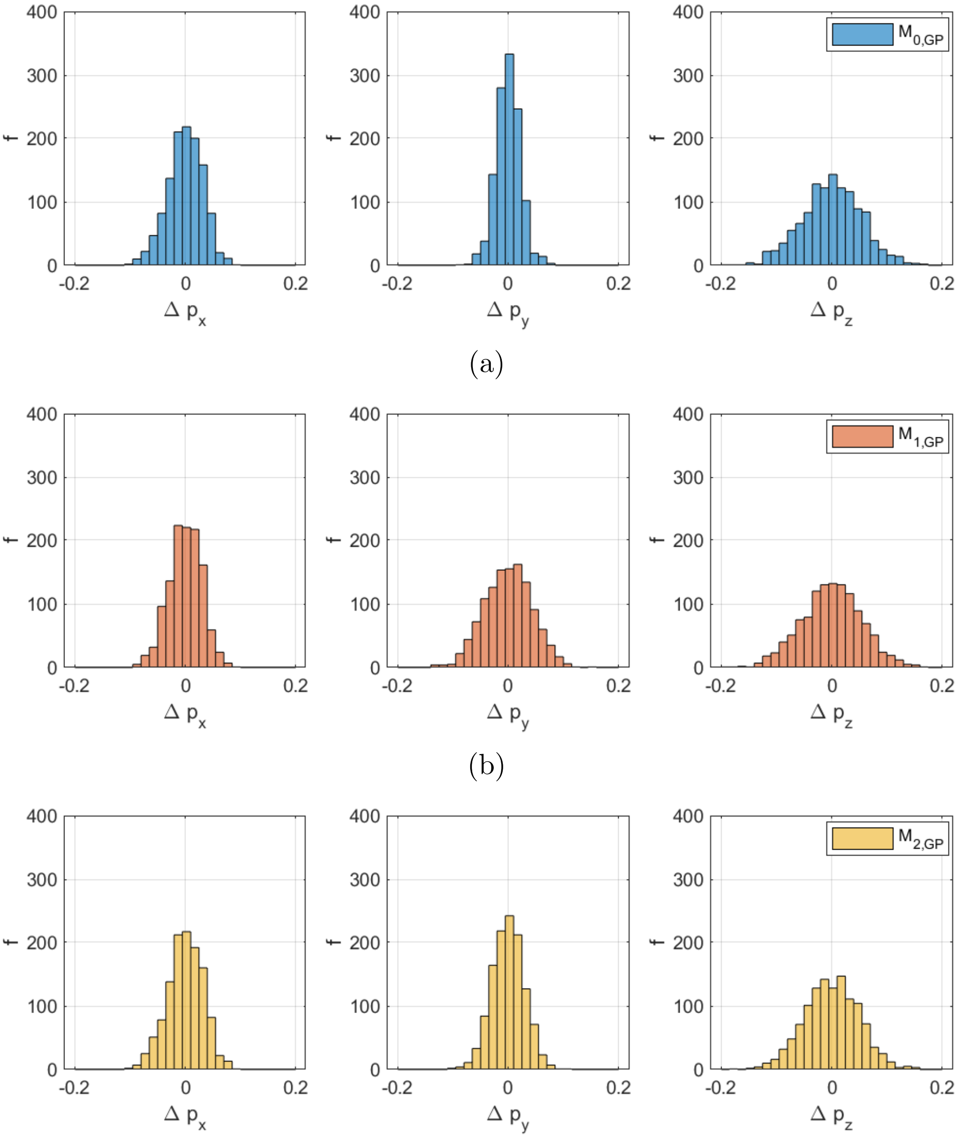

(a)

(b)

(c)

Figure 6.16: Experimental study, distribution of training data bias correction results for models (a) $M_{0,GP}$, (b) $M_{1,GP}$ and (c) $M_{2,GP}$ in the 6 dim (s) case study. f: frequency (number of measurements).

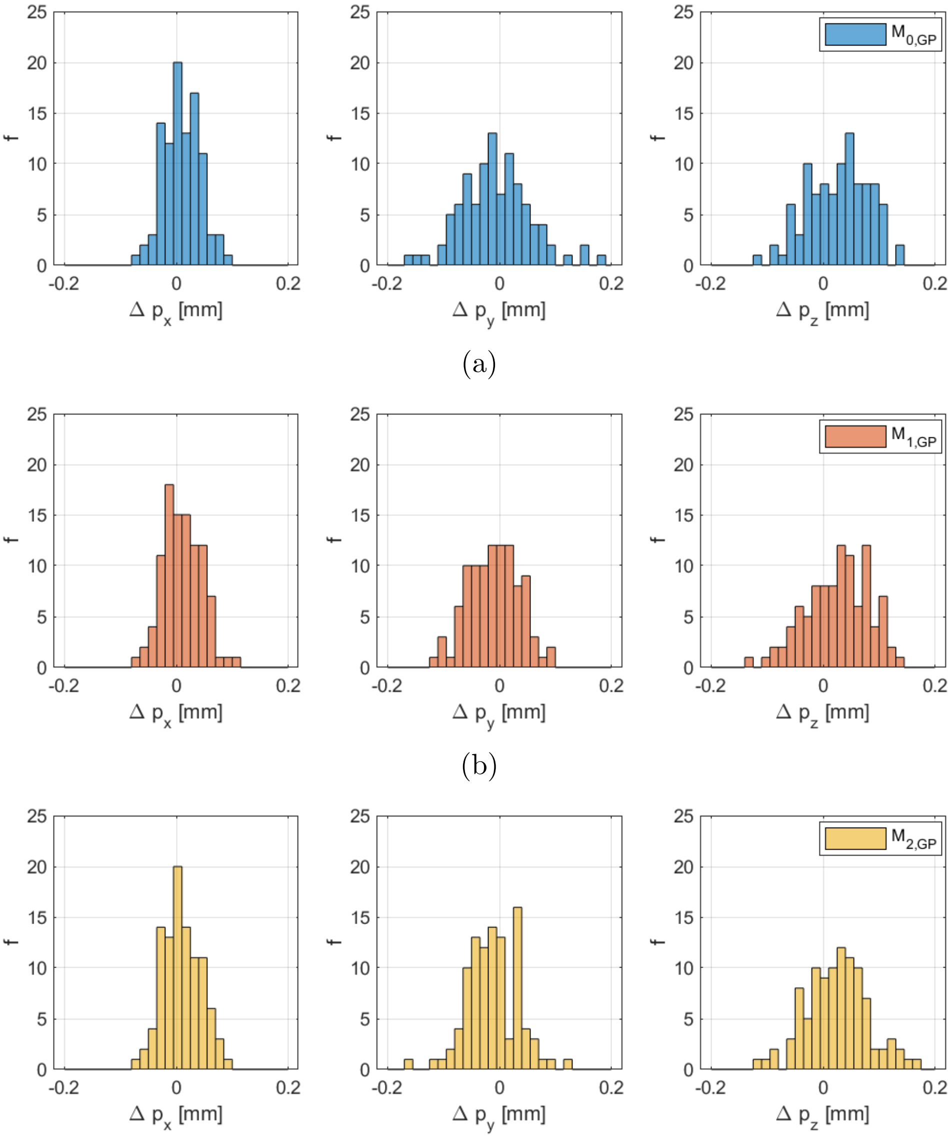

(a)

(b)

(c)

Figure 6.17: Experimental study, distribution of validation data bias correction results for models (a) $M_{0,GP}$, (b) $M_{1,GP}$ and (c) $M_{2,GP}$ in the 6 dim (s) case study. f: frequency (number of measurements).

A summary of bias correction results for training and validation bias data is presented in Tables 6.23 and 6.24. The residual error in the bias data has been substantially reduced using bias correction as expected. Bias correction reduced the positional error of the robot for the most challenging data, that of M_0, from an rms $|\Delta p|$ of 4mm to 66μm for the training data and 93μm for validation data.

Bias reduction has had only a small contribution to the accuracy of bias correction predictions. The range of results can be considered as small, 9μm in comparison to the measurement variation of 13μm. The range of results is almost entirely from the models of Δp_y . It is unclear why bias correction of the uncalibrated bias data M_0 would be more accurate than calibrated model data with a lower and less complex bias form. However, as the range is small, no conclusions can be drawn with confidence.

In comparison to the results from the 3 dim case study in section 6.4.3, the bias correction residual errors are not significantly higher for all models as a result of increasing the number of input dimensions from 3 to 6 in this case study. The rms $|\Delta p|$ are 20μm higher in this study for $M_{0,GP}$ and less for $M_{1,GP}$ and $M_{2,GP}$. The same observations were made in Chapter 5. It was concluded that a reduction in training data resolution will result in a reduction in the prediction accuracy of test data. In this case study, the increase in input dimensions reduced the resolution of training data substantially but an increase in training data quantity and a smaller input range will have increased the resolution, but not to the same resolution as the 3 dim case study.

Table 6.23: Experimental study, summary of training data bias correction results for competing models in the 6 dim (s) case study.

	M_0	M_1	M_2
$\Delta \bar{p}_x$ (std) [mm]	0.000 (0.032)	0.000 (0.030)	0.000 (0.032)
$\Delta \bar{p}_y$ (std) [mm]	0.000 (0.022)	0.000 (0.043)	0.000 (0.029)
$\Delta \bar{p}_z$ (std) [mm]	0.000 (0.054)	0.000 (0.054)	0.000 (0.049)
rms $\lvert\Delta p\rvert$ (max) [mm]	0.066 (0.195)	0.075 (0.187)	0.066 (0.174)

Table 6.24: Experimental study, summary of validation data bias correction results for competing models in the 6 dim (s) case study.

	M_0	M_1	M_2
$\Delta \bar{p}_x$ (std) [mm]	0.010 (0.033)	0.010 (0.034)	0.010 (0.033)
$\Delta \bar{p}_y$ (std) [mm]	-0.007 (0.062)	-0.010 (0.045)	-0.012 (0.046)
$\Delta \bar{p}_z$ (std) [mm]	0.026 (0.055)	0.026 (0.056)	0.025 (0.055)
rms $\lvert\Delta p\rvert$ (max) [mm]	0.093 (0.185)	0.084 (0.155)	0.084 (0.197)

6.5.4 Summary

The aim of this study was to investigate the limitations of bias correction in predicting robot positional error from an input of 6 joint variables with a small joint range, with respect to bias reduction.

Observations made in the numerical study were confirmed by comparing the bias correction results in this study to the previous 3 dim case study in section 6.3. Namely, bias correction using GPR reduced the rms $|\Delta p|$ to sub 0.1mm. The accuracy of bias correction predictions is not necessarily increased by an initial bias reduction achieved by model calibration. The accuracy of bias correction predictions is expected to be lower as the number of input dimensions increases. For a non-linear bias form, the GPR model may be less able to accurately predict the data between training data points if the resolution is lower.

The search for kernel hyperparameters identified many solutions and the GPR model accuracy is sensitive to the hyperparameters used. Many more solutions were found in the 6 dim case compared to the 3 dim case study which is expected when searching in a higher dimensional space. The search strategy of probing with 20 initial estimates was adequate but takes a long time to run with high training data quantities. Hyperparameter search strategies to improve efficiency and accuracy, is a topic that would add value in future work.

The practical limitations of sensor visibility resulted in the pose of the robot only being modelled in a subspace of joint configurations.

There were a number of observations that were not investigated in the study and a number of questions remain. The first is the explanation of multiple peaks in the bias correction, residual error data distributions. The second is the relationship between hyperparameter length scale values and model accuracy which could be used to as a crude filter to identify models that will perform poorly, in terms of predicting test data accurately.

Looking forward, the methodology used in this case study will be used again in the 6 dim (l) case study and the results will be directly compared.

6.6 Bias correction of robot positional error with a 6 joint angle input and large joint angle range

The aim of this study is to investigate the limitations of bias correction by increasing the complexity of the problem to 6 input variables, but with a relatively wide input space (referred to as 6 dim (l)). In this study joints 1 to 6 will all be rotated to configurations that provide TCP poses. The challenges of bias data prediction in relation to training data quantity and bias reduction from competing models are tested.

In Chapter 5, the 6 dim (l) case study conducted on the numerical model demonstrated that positional errors can be reduced by using bias correction. The hypothesis that bias reduction by model calibration has a negligible effect on bias correction accuracy, was not conclusively proven. The the 6 dim (l) case study was the only study to show that bias reduction reduced the bias correction residuals error, but only by 20μm which is too small in relation to measurement variation to be conclusive. In the 3 dim and 6 dim (s) case studies on the real robot in this Chapter, a narrow range of bias correction results between competing model data was reported and in fact, the uncalibrated model bias data was predicted with the lowest residual errors, which is against expectation. However, the range was again too small to be conclusive. A comparison of bias correction results for the competing models in this study will be used to test the hypothesis.

In the 6 dim (l) input space study in this section, the GPR model will be trained with 1160 measurements and validated with 100 measurements, generated separately using LHS. It is acknowledged that the test is conducted in a subspace of the joint inputs due to sensor visibility and the results cannot be generalised to the entire joint-space or Cartesian workspace.

6.6.1 Baseline data

Again, some familiar observations, also observed in the 3 dim and 6 dim – small case studies, can be made: (1) The high bias mean of the nominal model, M_0 Δp_z bias data is the result of a large deflection due to payload; (2) the errors of Δp_z are substantially reduced by correcting the distribution to a zero mean with a simple base localisation; (3) the bias data from model M_0 will provide a different challenge to that of M_1 and M_2. In this case study, the bias data of M_1 may provide a different challenge for bias correction than that of M_2. The wider distribution of M_1 indicates that the unmodelled errors from the geometric parameter errors produces a more complex bias form to model.

The distribution of M_0 Δp_z bias data is bi-modal which was also partially evident in both the numerical and experimental the 3 dim studies, and the 6 dim (l) in Chapter 5. The two peaks were explained by the deflection due to payload causing being in the positive of negative p_x direction depending on if the angle of the arm was above or below the horizontal. It was not investigated further as having two peaks was not problematic for bias correction.

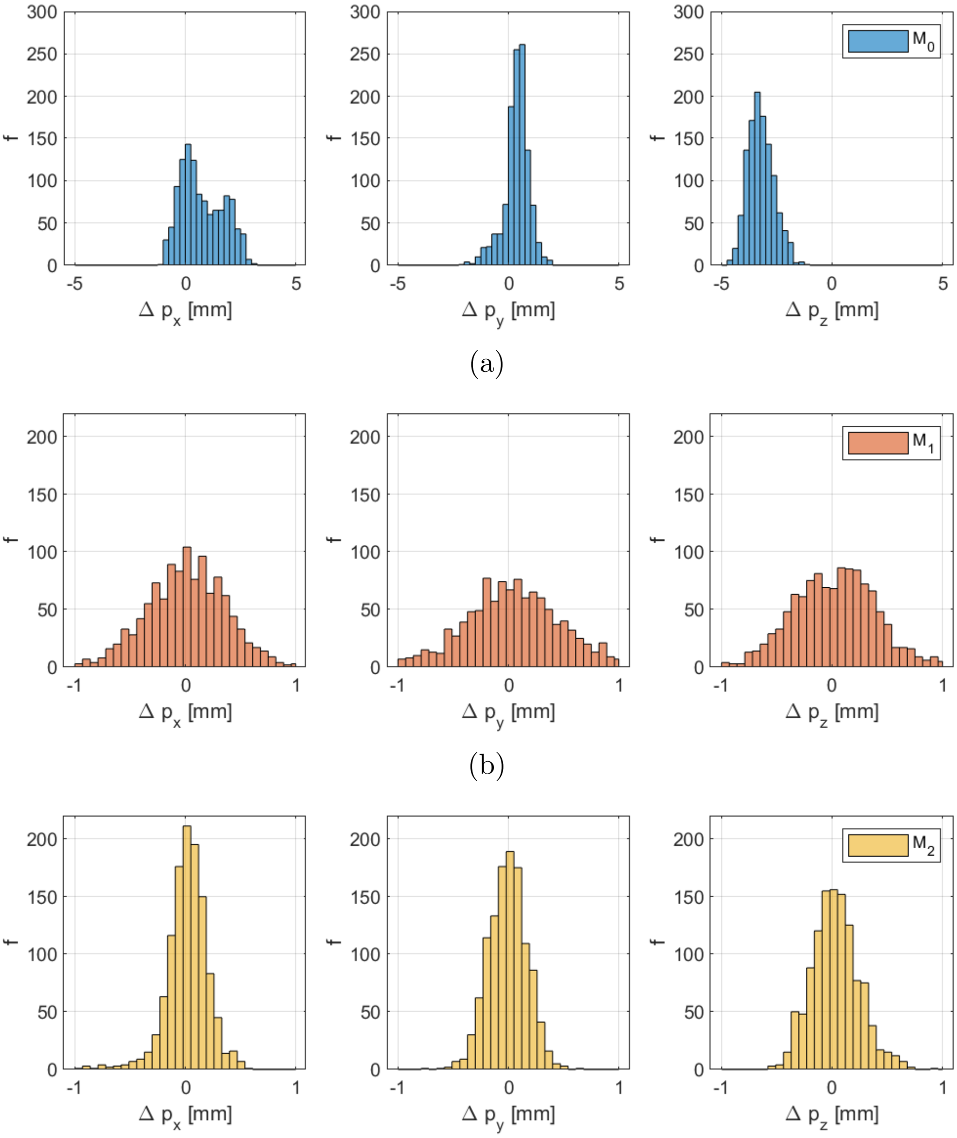

(a)

(b)

(c)

Figure 6.18: Experimental study, distribution of bias data for models (a)M_0, (b)M_1 and (c) M_2 in the 6 dim (l) case study. f: frequency (number of measurements).

The training and validation bias data from the competing models is summarised in Tables 6.28 and 6.29, respectively.

In the 6 dim (s) case study in section 6.5 there were many solutions to the hyper-parameter search as a result of the high number of input dimensions. The accuracy of the GPR models, in terms of rms Δp, was sensitive to the hyperparameter choice. The same observations are made with respect to the hyperparameters estimated in this study.

There are notable examples, such as $h_{14}(\Delta p_x)$, where model overfitting has occurred, indicated by a lower error in the training data and higher error in the validation data. The residual error in the validation data models are less sensitive to hyperparameter choice than training data models. Once hyperparameters that results in models with very high or very low residual errors, in rms Δp are withdrawn, the residual errors in the validation data have a range of approximately 20μm. This observation suggests that it may be possible to provide upper and lower limits for hyperparameters or training data error limits to able to identify optimal or near optimal solutions.

Table 6.25: Experimental study, summary of training bias data results for competing models in the 6 dim (l) case study.

	M_0	M_1	M_2
$\bar{\Delta p}_x$ (std) [mm]	0.764 (0.959)	0.001 (0.368)	0.014 (0.201)
$\bar{\Delta p}_y$ (std) [mm]	0.371 (0.568)	0.003 (0.565)	-0.007 (0.173)
$\bar{\Delta p}_z$ (std) [mm]	-3.220 (0.586)	0.037 (0.389)	0.032 (0.214)
rms $\|\Delta p\|$ (max) [mm]	3.560 (5.077)	0.779 (2.379)	0.342 (1.413)

Table 6.26: Experimental study, summary of validation bias data results for competing models in the 6 dim (l) case study.

	M_0	M_1	M_2
$\bar{\Delta p}_x$ (std) [mm]	0.831 (0.955)	-0.029 (0.309)	0.042 (0.207)
$\bar{\Delta p}_y$ (std) [mm]	0.340 (0.632)	-0.012 (0.634)	-0.042 (0.159)
$\bar{\Delta p}_z$ (std) [mm]	-3.123 (0.626)	0.070 (0.413)	0.071 (0.242)
rms $\|\Delta p\|$ (max) [mm]	3.499 (5.024)	0.817 (1.896)	0.366 (0.966)

6.6.2 Hyperparameter search

For a visual comparison of solutions, Figure 6.19 shows the bias correction results for training and validation data predictions from the competing models, in terms of rms Δp_x , Δp_y and Δp_z , for all 20 hyperparameter estimates.

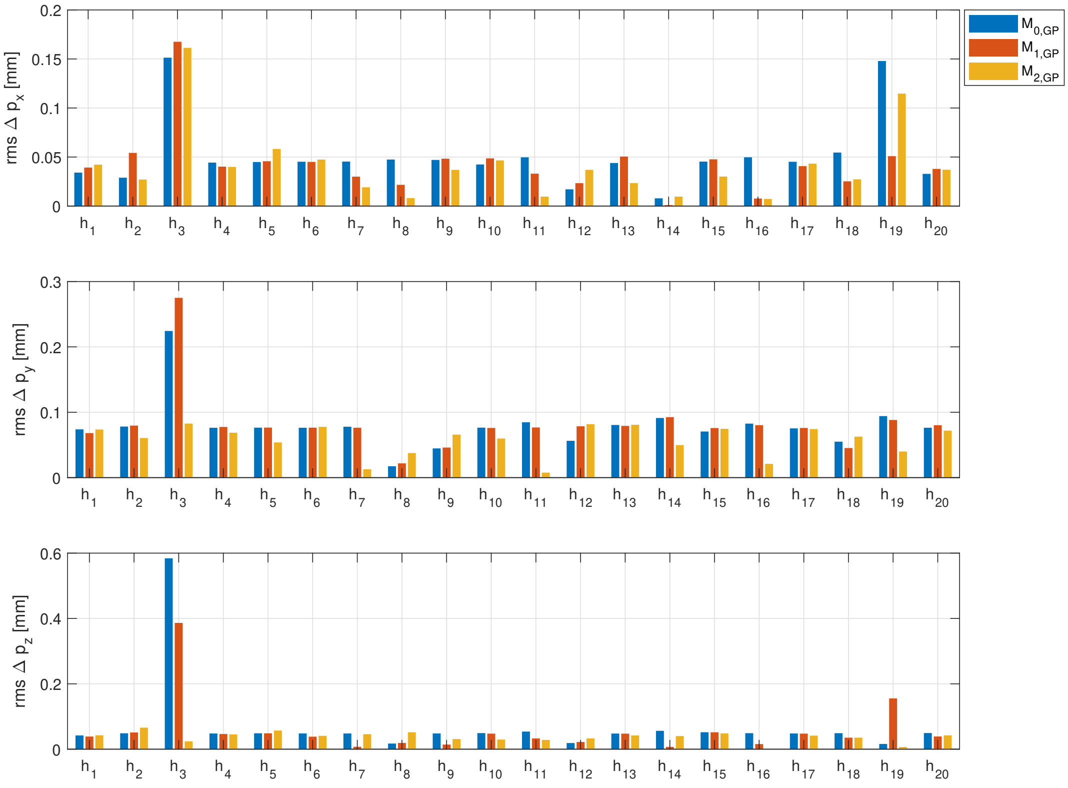

rms Δ p_x [mm]
rms Δ p_y [mm]
rms Δ p_z [mm]
0
0.05
0.1
0.15
0.2
0.3
0.4
0.6
h_1 h_2 h_3 h_4 h_5 h_6 h_7 h_8 h_9 h_10 h_11 h_12 h_13 h_14 h_15 h_16 h_17 h_18 h_19 h_20
M_0,GP
M_1,GP
M_2,GP

(a)

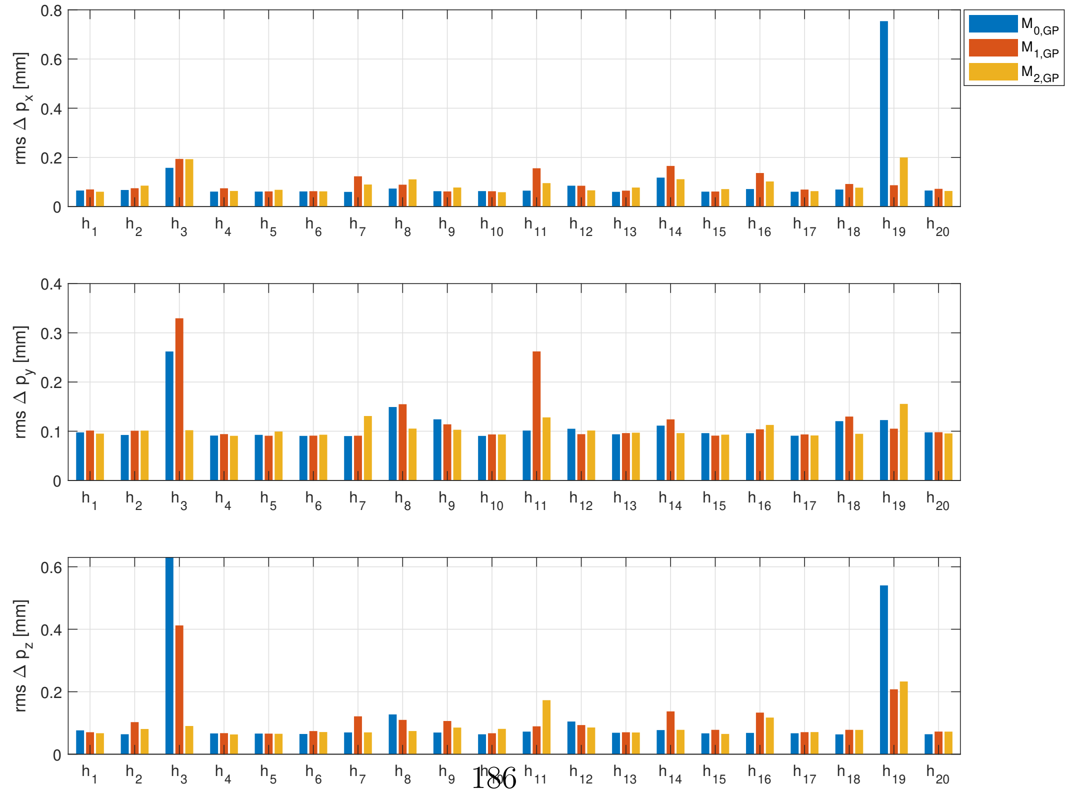

rms Δ p_x [mm]
rms Δ p_y [mm]
rms Δ p_z [mm]
0
0.1
0.2
0.3
0.4
0.6
0.8
h_1 h_2 h_3 h_4 h_5 h_6 h_7 h_8 h_9 h_10 h_11 h_12 h_13 h_14 h_15 h_16 h_17 h_18 h_19 h_20
M_0,GP
M_1,GP
M_2,GP

(b)

Table 6.27 shows examples of the hyperparameters from the poor performing models, in relative terms, along with typical models from the same initial estimates for comparison. The h_3 hyperparameters are examples where the residual errors are either high for both training and validation data predictions or low for both. Models $M_{0,GP}$ and $M_{1,GP}$ that use $h_3(\Delta p_x)$, $h_3(\Delta p_y)$ and $h_3(\Delta p_z)$ hyperparameters and $M_{2,GP}$ that uses $h_3(\Delta p_x)$ are examples where residual error are very high and are referred to as set 1. Model $M_{2,GP}$ that uses $h_3(\Delta p_y)$ and $h_3(\Delta p_z)$ are examples where the residual errors are typical of other models and is referred to as set 2. In set 1 there are examples of very small length scales in the order of 0.02, and very large length scales in the order of 280 but which are not indications of model accuracy. A common feature of hyperparameters in set 1 is a very large σ_n compared to the approximate 13μm measurement variation. The large noise hyperparameter results in a model that is relatively flat and describes 'wiggles' in the bias form as noise and so predictions of both training and validation data have high residual errors. In comparison, set 2 has σ_n hyperparameters that are of the same order as the measurement variation and residual errors are within expectation. This observation confirms that without further investigation, the length scales cannot be used as an indication of model accuracy but model accuracy is sensitive to σ_n. Investigation of this topic is beyond the scope of this research but would benefit future work.

Table 6.27: Example of the estimated kernel hyperparameters, representative of poor performing estimations from 20 initial estimates.

Model		σ_f	l_1	l_2	l_3	l_4	l_5	l_6	σ_n
$M_{0,GP}$	$h_3(\Delta p_x)$	0.40	1.64	4.56	1.39	32.27	2.55	0.67	**0.160**
	$h_3(\Delta p_y)$	0.42	1.54	3.81	4.26	12.43	27.73	3.86	**0.250**
	$h_3(\Delta p_z)$	**0.03**	0.37	0.90	0.84	1.62	0.55	0.03	**0.580**
$M_{1,GP}$	$h_3(\Delta p_x)$	0.71	46.45	3.66	103.99	1.48	0.87	8.44	**0.176**
	$h_3(\Delta p_y)$	1.24	1.63	36.37	-280.19	-2.80	109.81	-2.23	**0.273**
	$h_3(\Delta p_z)$	**0.02**	0.29	0.41	0.56	1.03	1.47	0.08	**0.387**
$M_{2,GP}$	$h_3(\Delta p_x)$	**0.07**	0.55	0.53	0.61	0.84	0.35	0.12	**0.166**
	$h_3(\Delta p_y)$	0.24	5.38	2.62	2.22	1.54	1.08	1.98	0.094
	$h_3(\Delta p_z)$	0.22	0.97	0.82	1.25	1.28	0.90	0.48	-0.045

6.6.3 Bias correction results

Figures 6.16 and 6.17 show the distribution of residual positional errors after bias correction of the competing model training and validation data respectively, for visual analysis.

The distribution of training data bias is referred to as baseline data, was broadly described as uniform with a non-zero mean, with the exception of the Δp_x bias data for model M_0. The movement of the distribution mean and the narrower distribution width, in standard deviation terms, of the bias correction training data compared to the bias data is a positive indication that the training data was modelled successfully.

It was suggested that the bi-modal distribution in the Δp_x bias data for model M_0 had two subsets of data separated in to payload deflections in arm raised or lowered configurations relative to the horizontal. As a function of joint angle it was not expected to be challenging to model. The bias correction data distribution of Δp_x for $M_{0,GP}$ is uniform which could be interpreted as confirmation of the assumption made.

The distribution of bias correction validation bias data has multiple peaks in all data sets which means that the positional errors are not concentrated near to the mean and that there are significantly large numbers of configurations where the positions error is higher than 0.1mm in any direction. However it is possible that there is not enough validation data to confirm the presence of significantly large peaks to indicate subsets of data rather than instances. The second largest peaks are rarely larger than at five configurations which is not a significant portion of the joint-space. Higher quantities of validation data would be required to investigate the presence of significant peaks and possible 'high-error' subspaces.

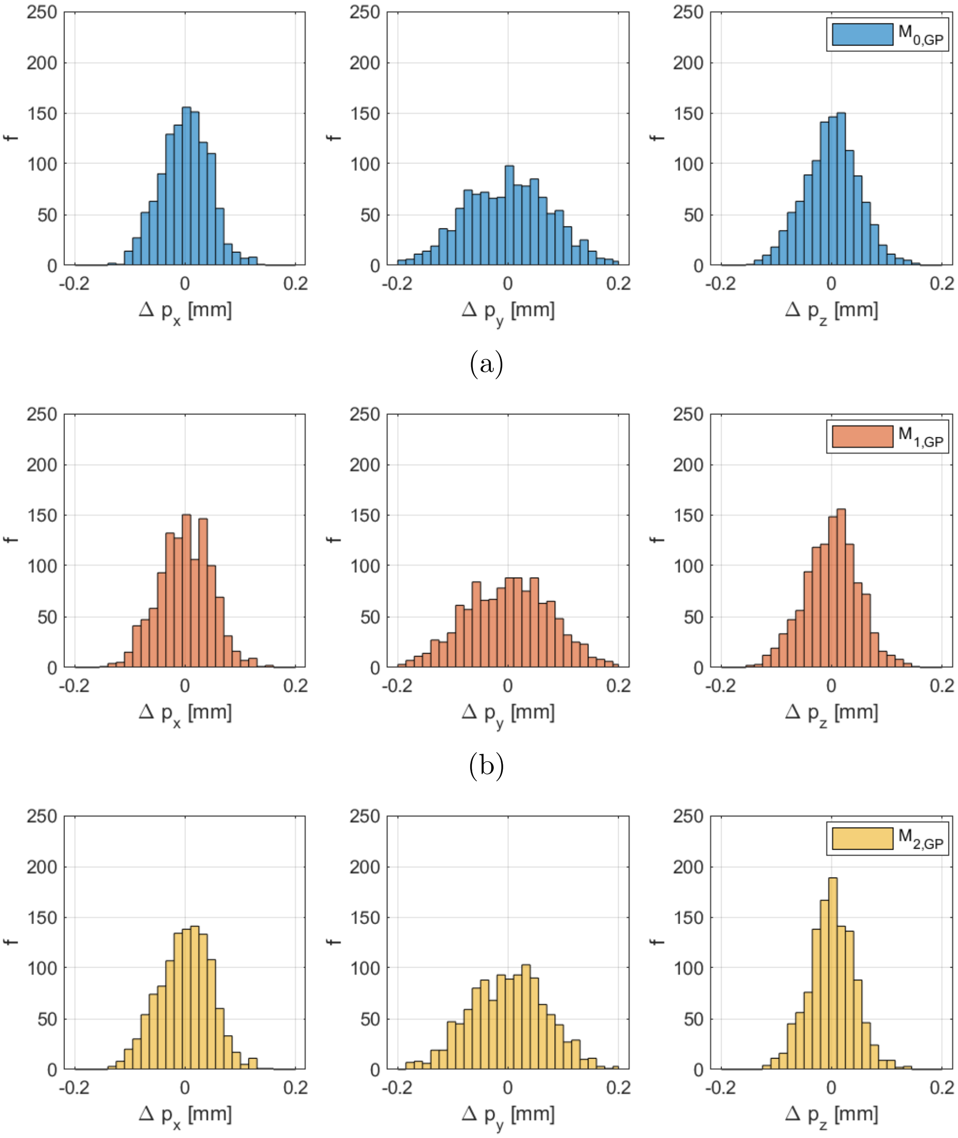

(a)

(b)

(c)

Figure 6.20: Experimental study, distribution of training data bias correction results for models (a) $M_{0,GP}$, (b) $M_{1,GP}$ and (c) $M_{2,GP}$ in the 6 dim (l) case study. f: frequency (number of measurements).

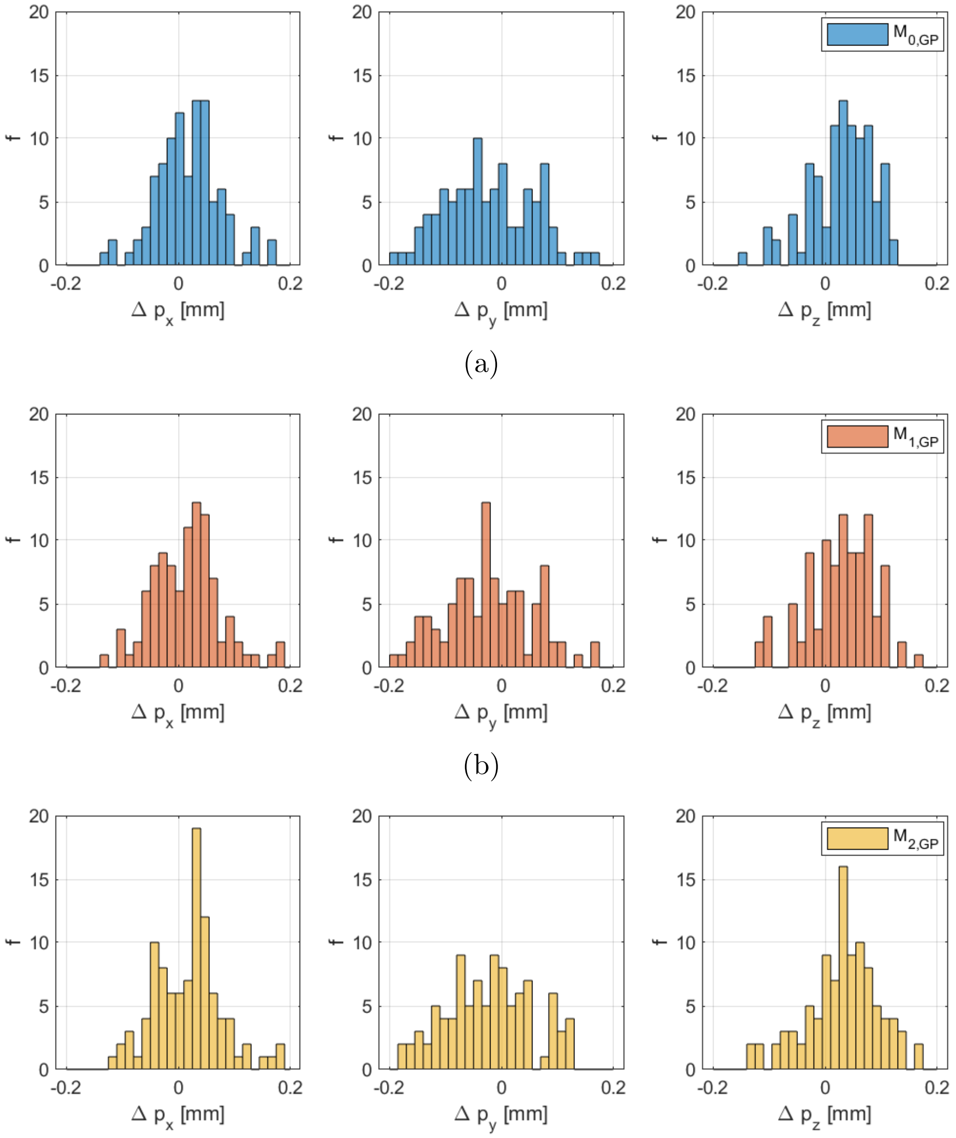

(a)

(b)

(c)

Figure 6.21: Experimental study, distribution of validation data bias correction results for models (a) $M_{0,GP}$, (b) $M_{1,GP}$ and (c) $M_{2,GP}$ in the 6 dim (l) case study. f: frequency (number of measurements).

A summary of bias correction results for training and validation bias data is presented in Tables 6.28 and 6.29. The residual error in the bias data has been substantially reduced using bias correction as expected. Bias correction reduced the positional error of the robot for the most challenging data, that of M_0, from an rms $|\Delta p|$ of 3.5mm to 0.102mm for the training data and 0.126mm for validation data. A more interesting comparison is the bias correction residual error of 0.128mm and the positional error of 0.366mm from M_2, the kinematic model with a geometric parameter calibration. The positional error can be substantially reduced below the 0.3mm error floor observed in literature.

The residual errors of the bias correction training data, rms $|\Delta p|$ terms can be interpreted as the limitation of the proposed methodology, on the assumption of confidence in the GPR model. An approximate 0.1mm positional accuracy was achieved by bias correction using GPR, which is in the order of the desired accuracy for robot drilling tasks in aerospace. The maximum positional error of 0.27mm exceeds this specific application target but equally there are many configurations with a smaller positional error.

To achieve positional accuracy results close to the bias correction training data results, a perceived limit, the resolution of the training data must be sufficiently high. The resolution of the training data is accepted as a satisfactory quantity for this case study with the validation data residual errors, in rms $|\Delta p|$ terms, being only 20 to 30μm higher than the training data residual errors. Considerably larger training data quantities would be required to achieve results in test data that are significantly closer to the training data results.

For comparison to literature, experimental results of EFK calibration of geometric parameters followed by ANN bias correction were presented by Nguyen et al. [44]. The author reported results of $|\Delta p|$ as 0.424mm (mean), 0.201mm (standard deviation) and 0.922mm (max). The equivalent results in this study are 0.118mm, 0.056mm and 0.214mm which are significantly lower by a factor of x4. The ANN was trained with 200 data points whilst in this study, 1160 data points were used to test the limitations of bias correction for this application.

Table 6.28: Experimental study, summary of training data bias correction results for competing models in the 6 dim (l) case study.

	$M_{0,GP}$	$M_{1,GP}$	$M_{2,GP}$
$\bar{\Delta p}_x$ (std)[mm]	0.000 (0.044)	0.000 (0.048)	0.000 (0.047)
$\bar{\Delta p}_y$ (std)[mm]	0.000 (0.078)	0.000 (0.077)	0.000 (0.069)
$\bar{\Delta p}_z$ (std)[mm]	0.000 (0.049)	0.000 (0.049)	0.000 (0.041)
rms $|\Delta p|$ (max)[mm]	0.102 (0.267)	0.102 (0.254)	0.093 (0.214)

Table 6.29: Experimental study, summary of validation data bias correction results for competing models in the 6 dim (l) case study.

	$M_{0,GP}$	$M_{1,GP}$	$M_{2,GP}$
$\bar{\Delta p}_x$ (std)[mm]	0.019 (0.057)	0.015 (0.060)	0.018 (0.060)
$\bar{\Delta p}_y$ (std)[mm]	-0.028 (0.086)	-0.027 (0.087)	-0.025 (0.087)
$\bar{\Delta p}_z$ (std)[mm]	0.030 (0.056)	0.028 (0.060)	0.031 (0.064)
rms $\lvert\Delta p\rvert$ (max)[mm]	0.126 (0.311)	0.128 (0.332)	0.131 (0.326)

Whilst the rms $|\Delta p|$ is a typical reference metric for machine tools and some robotics research, in the most comparable, related research literature by Nguyen et al. [44], Tao and Yang [86] and Jing et al. [45], the $|\bar{\Delta p}|$ is used. Table 6.30 shows the same results presented in this case study, as $|\bar{\Delta p}|$ for comparison. The referenced research literature are comparable because the authors use a similar 6-DOF articulated robot, measured with a laser tracker and use a combined calibration and bias correction approach to improve positional accuracy. Training and validation data quantities refer to the data used for bias correction. There are notable similarities and differences in the problems presented in the research. The first is that after calibration, the mean error ($M_2|\bar{\Delta p}|$) data presented in the 6 dim (l) case study is already lower than that achieved by the bias correction methods used in the related research literature, thus seemingly having an advantage. However, if the conclusion is drawn in this chapter, that calibration has no significant effect on the accuracy after bias correction, then the data presented by all four studies can be considered as comparably similar. The nominal robot error M_0 6 dim (l) and Nguyen et al. [44] study are within 0.13mm, whilst the base calibrated model (M_1) data by Tao and Yang [86] and Jing et al. [45] are approximately within a much larger 0.4mm of the 6 dim (l) data. The results can be compared but with these notable differences. The relatively low $|\bar{\Delta p}|$, is a substantial reduction in positional error compared to related research literature, which is expected to mainly be the result of a training data quantity that is four to five times higher.

Table 6.30: Experimental study, comparison of validation data bias correction results, $M_{2,GP}$ in the 6 dim (l) case study, to related research literature.

	6 dim (l)	Nguyen et al. [44]	Tao and Yang [86]	Jing et al. [45]
Training data quantity	1160	200	150	300
Validation data quantity	100	100	150	100
$M_0\lvert\bar{\Delta p}\rvert$[mm]	3.452	3.587	-	-
$M_1\lvert\bar{\Delta p}\rvert$[mm]	0.717	-	0.96 to 1.03	1.17 to 1.76
$M_2\lvert\bar{\Delta p}\rvert$[mm]	0.325	0.908	0.46 to 0.52	0.83 to 1.30
Bias correction $\lvert\bar{\Delta p}\rvert$[mm]	0.118	0.424	0.35 to 0.42	0.43 to 0.57

6.6.4 Summary

The case study in this section was presented as the most challenging case study in terms of high number of input dimensions (all 6 joints) and a wide input range (joint angles). The expectations were that the bias correction results would demonstrate a substantial reduction in positional error to a value approaching 0.1mm in rms $|\Delta p|$ terms, and that the range of results for the competing models would be small, in the same order of the measurement variation.

The observations made in the numerical study in Chapter 5 and in the previous case studies in this chapter were also made in this study in this section. Bias correction, using GPR, substantially reduced the positional error of the robot to approximately 0.1mm for the training data and 0.12mm for the validation data which is in the order expected and lower than in similar studies in literature. The results contribute to the analysis of the limitations of bias correction for this application. The accuracy of the bias correction predictions will be compared to the results from the other case studies in this chapter in section 6.7 to analyse the limitations of bias correction in this application.

A comparison of bias correction results of the competing models was used to test the bias reduction hypothesis presented in Chapter 5. The accuracy of bias correction predictions was not improved significantly by an initial bias reduction. The same observation was not conclusively made in the numerical study of the 6 dim (l) case or the 3 dim case study in this chapter, as the range of results was in the same order as the measurement variation. A further analysis will be made in section 6.7.

In the 6 dim (s) study in this chapter, it was stated that a near zero σ_n hyperparameter would be an indication of overfitting and would produce large errors in predicting test data. The suggestion was made that an analysis of the estimated σ_n could be used as a filter to exclude models from the hyperparameter search. The same observation was made in the study in this section. It was also observed in the 6 dim (l) study that high σ_n produced large errors in the predictions of both training and validation data. In future work, the analysis of σ_n could be a useful tool to improve the efficiency and accuracy of hyperparameter searching.

The possible presence of multiple peaks in the results of the bias correction validation data was not explored. Multiple peaks could be interpreted as regions of configurations where the positional error is high relative to the mean which would be a useful outcome. The small quantity of validation data was not enough for significant multiple peaks to be confirmed.

The practical limitation of sensor visibility meant that only a subspace of configurations was tested and the results cannot be generalised to the whole space. In future work, multiple laser trackers or measurements taken from multiple locations would provide more conclusive evidence. This has also not been explored in literature and would contribute to the analysis of robot accuracy limitations in future work.

The aim of this study was to investigate the limitations of bias correction in predicting robot positional error from an input of 6 joint variables with a large joint range, with respect to bias reduction.

6.7 Synthesis of case study results

The aim of the studies in this chapter was to explore the limitations of bias correction to improve the accuracy of an industrial robot. The limitation of prediction accuracy was tested with respect to the number of input dimensions (number of joints rotating) and input range (joint angle range). The higher dimension case studies were expected to provide a more challenging bias form to model as a result of the interaction of error sources, and a reduction in training data resolution. In each case study, the limitation of prediction accuracy was tested with respect to bias reduction. A hypothesis was presented in Chapter 5 that bias reduction by initially calibrating the robot model had an insignificant effect of bias correction prediction accuracy. The results from the case studies in this chapter are summarised in this section and the two limitations are analysed separately.

6.7.1 Input dimension and input range analysis

In the numerical and experimental studies, the application of GPR as a bias correction tool was tested in case studies that increased sequentially in complexity through increased input dimensions or input range. The results of bias correction accuracy, presented as rms errors for the validation data in Δp_x , Δp_y , Δp_z and $|\Delta p|$ are presented in Figure 6.22. The same conclusions can be drawn from the data of each of the competing models.

The higher dimensional case study of 6 dim (s) did not pose a significantly greater challenge for bias correction than the 3 dim case which had a wider input range. The difference in accuracy between the two cases has a maximum range of only 20μm in any direction and while the accuracy in rms Δp_x is lower in the 3 dim case that the 6 dim (s) case study, the reverse is true in rms Δp_y and Δp_z resulting in up to 20μm accuracy difference in rms $|\Delta p|$ in the $M_{0,GP}$ residual error data and negligible difference in $M_{2,GP}$ residual error data.

A comparison of the 3 dim and 6 dim (l) results can be used to analyse the increase in errors as a result of additional rotations of joints 4 to 6. The robot accuracy, in rms $|\Delta p|$ terms is significantly lower in the 6 dim (l) case compared to the 3 dim case, by approximately 50μm. The majority of the additional error is evident in a large difference in Δp_y , whilst Δp_z results remain within 10μm. This can be explained by the fact that joints 2 and 3 move to robot in a plane and joint 1 simply rotates that plane, whilst joints 4 to 6 rotate the robot into configurations that twist the structure and so some of the errors will be evident in Δp_y .

A comparison of 6 dim (s) and 6 dim large results can be used to analyse the reduction in errors by reducing the joint range. The 6 dim (s) case study had a reduced joint range and a relatively small Cartesian workspace to represent a milling application. The robot accuracy was significantly higher in the small case study, compared to the large, with a reduction in rms $|\Delta p|$ of 40 to 50μm.

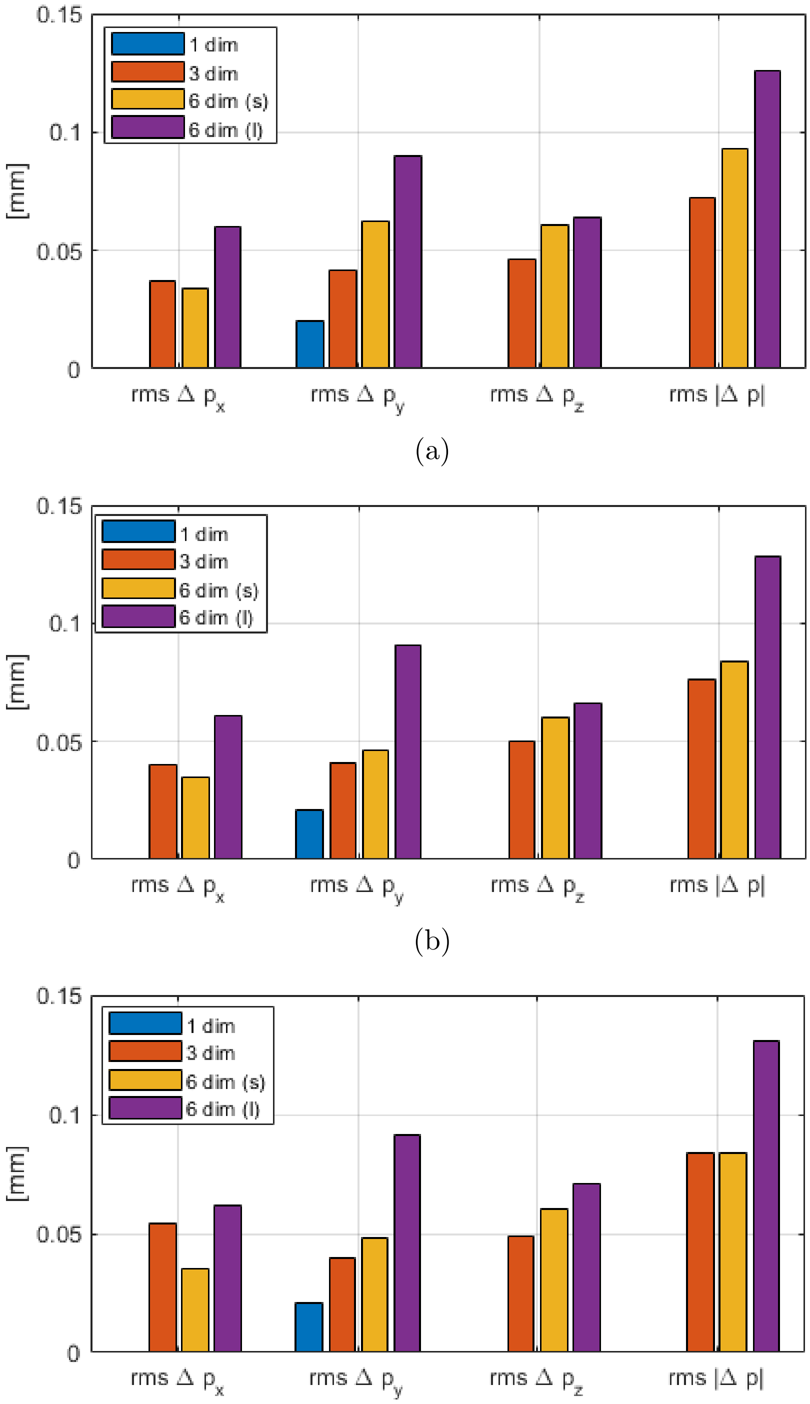

(a)

(b)

(c)

Figure 6.22: Experimental study, comparison of case study validation data bias correction results for model (a) $M_{0,GP}$, (b) $M_{2,GP}$ and (c) $M_{2,GP}$.

6.7.2 Bias reduction analysis

In the three case studies presented, the accuracy of the bias correction predictions is not increased by an initial calibration of the kinematic model. In two of the case studies, the reverse appears to be true with lowest errors presented in the order of $M_{0,GP}$ to $M_{2,GP}$ which was against expectation. However, the range of results between models is approximately 10μm which is lower than the measurement variation and so the range can be considered as non-substantial and the order inconclusive. The bias reduction hypothesis presented in Chapter 5 can be considered to have been proven in these case studies.

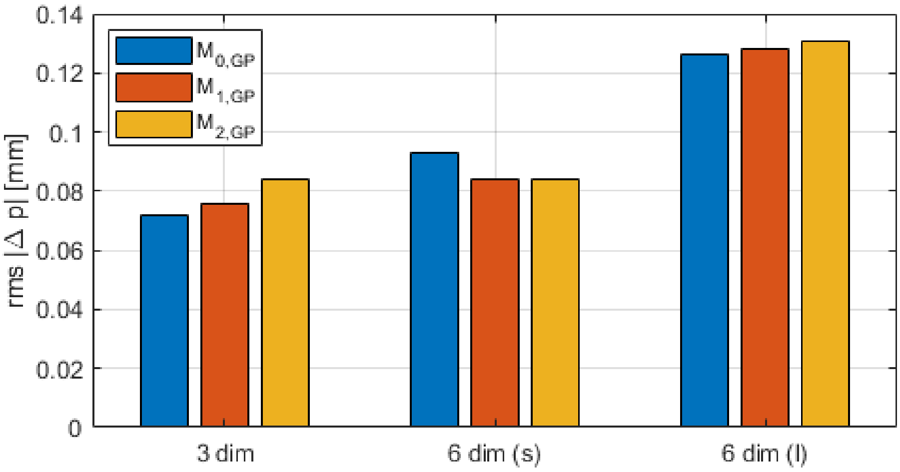

Figure 6.23: Experimental study, comparison of validation data bias correction results for competing models.

6.8 Chapter summary

The aim of this chapter was to explore the limitations of bias correction, using Gaussian Process Regression, to reduce the positional errors on an industrial robot. The research focus was to evaluate bias correction accuracy with respect to training data resolution and bias reduction by calibration. The results in this chapter are used to validate the observations and conclusions made in Chapter 5, which are numbered in this section, and present new findings.

In Chapter 5 it was concluded that (1) base calibration provides the largest gain in model accuracy, and that further gains are made by calibrating the geometric parameters, but with diminishing returns as the number of calibration parameters increased.

The same observation was made in section 6.2 with the notable exception that calibration of the most complete model, M_3, which also had joint compliance parameters, was marginally less accurate than M_2 and resulted in non-physical parameter values. It was assumed that this was the result of finding sub-optimal solutions when estimating higher numbers of parameters which creates more local minima i.e. 'the curse of dimensionality'.

In Chapter 5, it was observed that (2) bias correction substantially reduced the residual errors compared to the calibrated model positional errors, in all case studies. The same observations were made in this chapter. The results presented in the 6 dim (l) case study in section 6.6 are also significantly lower than the results reported in related works in literature. Related works by Nguyen et al. [44] and Tao and Yang [86] used a calibration method followed by an ANN to reduce the mean positional error to 0.33mm (using 200 training data values) and 0.36mm (using 150 training data values), respectively. Jing et al. [45] achieved a similar mean error of 0.4mm using a calibration method and GP bias correction (cross-validated with 300 data values). Increasing the training data quantity to four or five times higher than those used in related works enable the results to approach the limits of bias correction accuracy whilst maintaining a pragmatic amount of measurement and processing time. It was also concluded that (3) bias correction accuracy reduces substantially as the number of input dimensions (number of actuated joints) increases. However, if the joint angle ranges are reduced, the accuracy can be also substantially increased. The results can be interpreted as an observation that bias correction accuracy increases with training data resolution, which is expected. In terms of machining applications, if the robot is limited to a small workspace for milling applications for example, an rms $|\Delta p|$ of less that 0.1mm can be achieved compared to the 0.13mm accuracy in the larger workspace.

In Chapter 5, a bias reduction hypothesis was presented that stated that (4) calibrating the robot kinematic model to reduce the bias level, did not increase the accuracy of bias correction predictions. The hypothesis was proven in this chapter by an analysis of competing model data in section 6.7.2. However, GPR does not extrapolate well to regions of the input space (i.e. joint configurations) which are far from the training inputs, and the test was limited by sensor visibility to a subspace. Consequently, it is reasonable to assume that whilst a calibrated model will retain a similar accuracy throughout the workspace compared to the training configurations, if trained in the workspace, the bias correction model may not.

In Chapter 5, (5) GPR was used successfully as a relatively novel machine learning tool in this application and is a viable option for future related works. (6) The model accuracy is sensitive to hyperparameter estimates and it is computationally time-consuming. In addition, it may not necessarily return the optimal solution (to search for hyperparameters from multiple initial estimates) with large training data quantities.

In addition to the observations made in Chapter 5, other observations of the experimental results in this chapter were made. The maximum accuracy of the robot (after calibration) was 0.365mm. This is of a similar order to values reported in related works and contributes to the hypothesis that an approximate 0.3mm error floor exists when calibrating large, articulated, industrial robots.

In section 6.3, the bias data in the 1 dim case study confirmed that a significantly large periodic oscillation was present in Δp_y . The oscillation has not been modelled parametrically in most research literature, and not with a data-based model. This partially explains the presence of an error floor. In literature it was stated that a joint oscillation is the result of gearbox transmission errors. A comparison of the bias correction accuracy between GPR models using an SE and SES kernel, showed that both were equally capable of modelling the data. However, the SE kernel predictions were more confident. In addition, both kernels produced multiple solutions, which modelled the data as either a smooth or oscillating function (depending on hyperparameter solutions). With multiple input dimensions and lower training data resolution, it is expected to become very challenging for the more accurate, oscillation function to be determined. The oscillation was modelled analytically by Nubiola et al. [51], which could be argued, is a more reliable solution when the bias is modelled with multiple joint angle inputs.

To conclude, thesis objective 3 was met and Gaussian Process Regression was used to successfully reduce the positional error of a robot in a range of case studies, validating the conclusions made in Chapter 5. The calibration and bias correction results can be compared to related works in literature, which will be discussed further in Chapter 8. The proposed calibration and bias correction method, has demonstrated that is has the potential to increase the positional accuracy of an industrial robot sufficiently, for some machining applications. The methodology will be validated in a robot machining application in Chapter 7 by utilising the GPR model created in the 6 dim (l) case study, and testing the model accuracy in a panel drilling task.

Chapter 7

Case Study: Application to Robot Drilling

The aim of this chapter is to meet thesis objective 4 by validating the proposed bias correction methodology for an industrial robotic machining application. Here, the robot was programmed to simulate a panel drilling task by moving a machining spindle TCP to hole positions on a plane, and a GPR model was used to predict the positional error. The results are compared to the desired accuracy of 0.2mm maximum $|\Delta p|$ error stated in Chapter 1 (to achieve the positional tolerance required in an aerospace robotic drilling task).

There are notable comparisons between the problem presented in this chapter and those presented in Chapters 5 and 6. Firstly, while the hole positions are located in the p_y, p_z plane, to maintain the tool axis normal to the plane, all six joints may rotate and the problem remains a 6 dimensional input study. However, it is expected that some joints will have a small range which means that results similar to those achieved in the 6 dim (s) study in Chapter 6 may be achieved. Secondly, the validation poses are Cartesian positions and not randomly generated joint configurations which were used in Chapter 5 and 6. The input to the GPR model remains as a vector of joint angles in this study but the inverse kinematic (IK) model was used to convert poses to joint angles. This process was discussed in section 3.3.1 and has implications which are discussed in this section.

During the analysis of the drilling study results, it became evident that the experiment could not be conducted as intended and that changes were necessary. The intention was to use model $M_{0,GP}$, trained using in the 6 dim (l) study in Chapter 6, and to test the model accuracy at predicting the TCP positional errors at the drilling hole locations. However, this approach was not possible for two reasons.

I The desired validation poses, along with the tool data, were programmed into the robot and also into the Robot Studio software. Robot Studio IK model was used to calculate the same set of joint vectors used by the robot to achieve the poses, and which were then used as an input to the GPR model. Unfortunately, there was a discrepancy between the tool data provided to the robot and the Robot Studio. This resulted in the GPR model receiving marginally incorrect input data. It was expected, given the simplicity of the drilling case and the small input deviation, that the GPR model would still learn the bias as a function of the approximate joint angles.

II The joint configurations calculated by the IK model, which enabled the robot to achieve the desired pose, were far outside of the input ranges used to train model $M_{0,GP}$. It is known that GPR models do not extrapolate well to regions of input space far from the training data. With a zero mean model, as used in the GPR models in this thesis, the bias correction was predicted as zero and no reduction in positional error was made. Consequently, model $M_{0,GP}$ is not used in here. Instead, the bias correction accuracy is evaluated with a k-fold cross-validation of the positional errors, and approximate joint configurations at the hole positions.

7.1 Experimental design

The robot testbed, measurement equipment and data processing used in the study in this chapter were the same as those used in the studies in Chapter 6. To summarise, an AT-960 Leica laser tracker was used to measure to pose of a T-Mac sensor mounted onto a spindle fixture on the end of an ABB IRB 6640 industrial robot and data was processed in the Spatial Analyzer software. The CPA method described in Chapter 3 was used to determine a base coordinate system as a measurement reference.

To simulate a panel drilling task, the robot was programmed to move the spindle TCP to 35 hole positions on a 1.2m high 0.5m wide panel. The hole positions were spaced equally apart on a 5 by 7 grid, on a vertical p_y, p_z plane in front of the robot. It is typical for robot drilling applications to use a drilling machining spindle that is actuated independently to the robot. By this, it means that the task of the robot is to move the drilling spindle to the correct pose in front of the panel and then the drilling spindle drives the drill into the panel as a separate operation. The accuracy of the drilled hole is therefore dependent only on the start position of the TCP which is the focus of this study. An example of the robot TCP at one of the hole positions is shown in Figure 7.1.

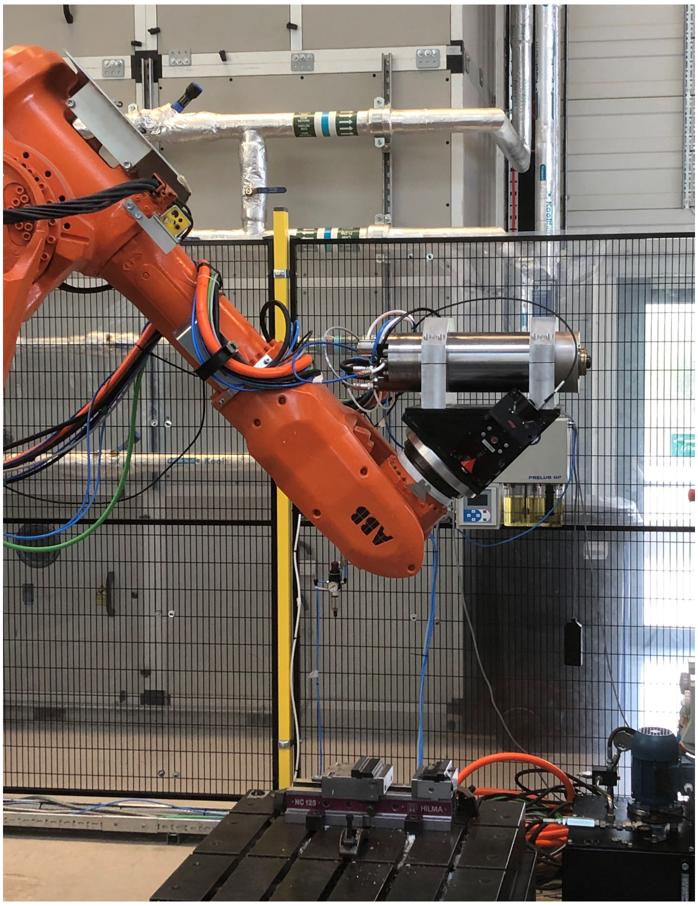

Figure 7.1: ABB IRB 6640 robot in an example vertical panel drilling configuration.

7.1.1 Bias data generation and model predictions

The process of generating joint angle inputs using and predicting positional errors is shown in Figure 7.2. The GPR model, as in previous chapters predicts the positional error Δp between the desired hole position p_d and measured position p, from a joint vector input q. Unlike in previous chapters, p_d was first converted to q by the IK model $M_0^{-1}(p)$. By using different tool data $H_6^{t(1)}$ and $H_6^{t(2)}$ the Robot and Robot Studio IK models output joint vectors $q^{(1)}$ and $q^{(2)}$ respectively. Model $\zeta(.) + \epsilon$ represents the true kinematic model plus measurement variation, and p the measured position.

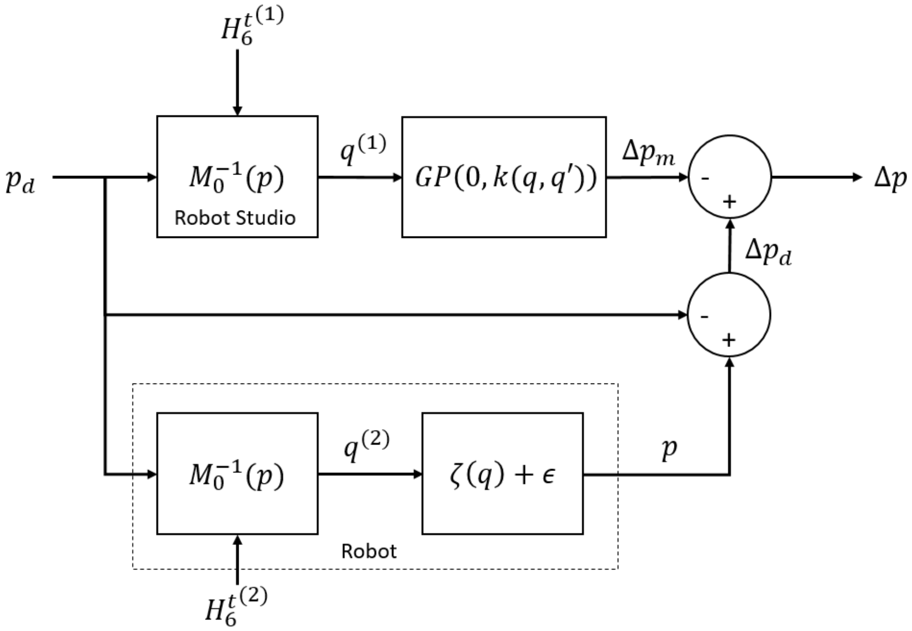

Figure 7.2: Input generation and bias correction process flow chart for machining tasks.

7.1.2 Training and cross-validation

The bias correction accuracy was validated using a 7-fold cross-validation. The position measurements of the 35 holes were separated into seven sets of 30 training data points and 5 validation points with each hole position being used once for validation with no replacement to ensure that all hole positions were used for validation.

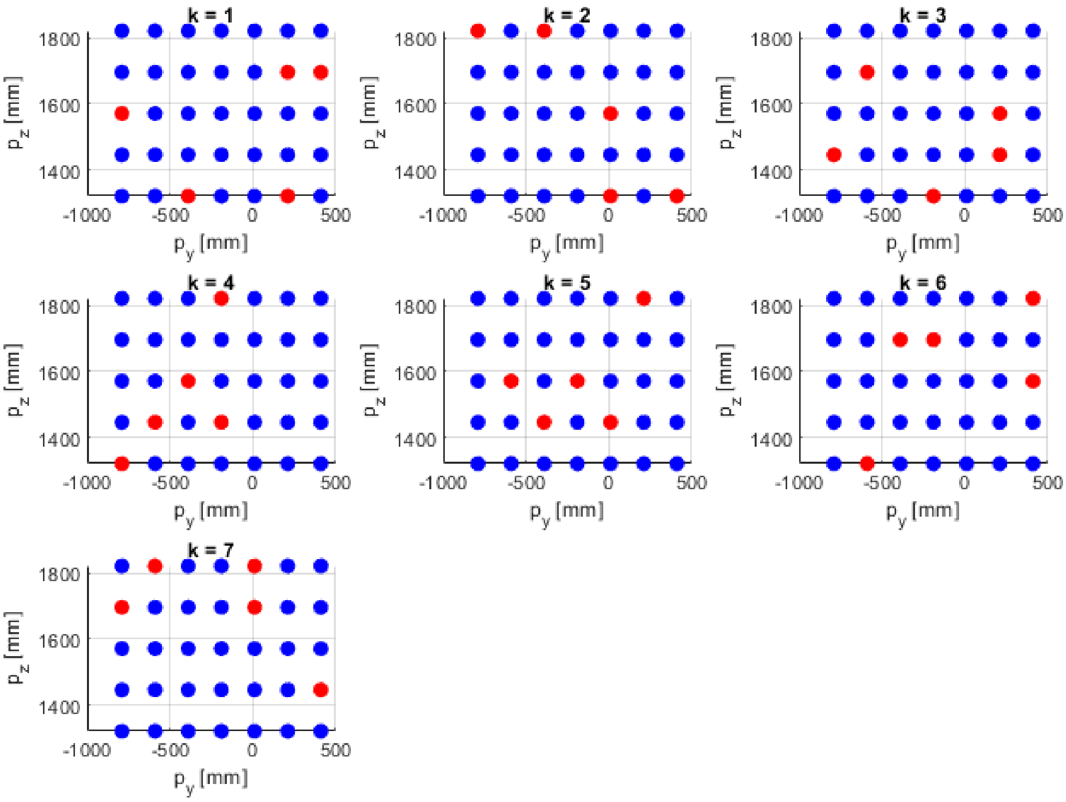

Figure 7.3: Robot drilling case study, 7-fold cross-validation positions.

7.2 Results

7.2.1 Nominal model bias data

The positional error data at each hole location in the drilling surface plane is presented as an error surface in Δp_x , Δp_y , and Δp_z in Figure 7.4. As a cautionary note, the GPR model is a function of joint angles and not Cartesian position and the error surface does not necessarily provide a measure of how challenging the bias form will be in joint-space, it can be assumed to partially infer the complexity of the problem. The error Δp_x decreases linearly i.e. the TCP moves closer to the plane, with the exception of a spike, as the robot TCP moves across the drilling surface plane in the positive p_y direction (sideways relative to the robot). The spike occurs at a hole location referred to as p28 (position 28 out of 35). The cause of the spike is unknown and may be considered to be an outlier. Without further investigation to prove that the measurement of p_x at p28 is an outlier, the value will remain. Error Δp_y decreases and increases again by approximately 0.5mm which is a large range with respect to the desired maximum error, however the surface is relatively smooth and could be interpreted with more data as a polynomial or sinusoidal function. This means that the bias form may also be smooth in joint-space, which is a positive indication that the GPR will be able to model the data with some success.

The error surface in Δp_z is less intuitive but could be interpreted as linear, or simple decreasing *smooth* form in Δp_z as the robot moves the TCP downwards in the negative p_z direction with an additional sinusoidal *oscillation* in both the p_y and p_z directions. Both could be the result of gearbox transmission errors that were observed in Chapter 6.

If the error surfaces are in fact used to infer a smooth and continuous bias form in joint-space, it is expected that the bias correction may pose no greater challenge than the case studies in Chapter 6.

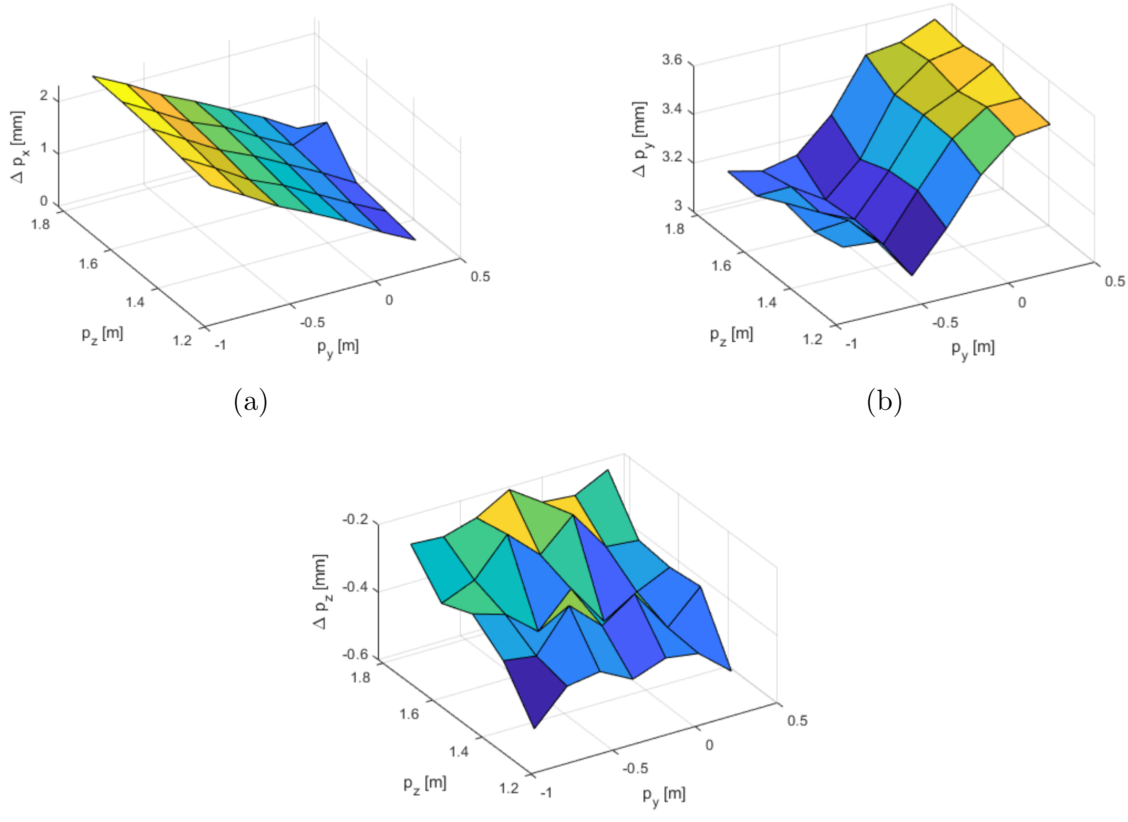

(a)

(b)

(c)

Figure 7.4: Positional error surface plots of Δp_x (a), Δp_y (b) and Δp_z (c) by drilling hole location.

7.2.2 Bias correction results

The bias correction residual errors in Δp_x , Δp_y , Δp_z and $|\Delta p|$ are presented for each cross-validation set for comparison in Figure 7.5. There are two notable spikes in the rms Δp_x results in sets $k = 1$ and 6 which contribute to a high $|\Delta p|$ error which in the order of 0.125mm and 0.200mm respectively. The spikes can be explained by analysing the training and validation role of p28 and the data at positions nearby to it. In the data set of $k = 1$, the GPR model is trained on bias data directly above and below p28, which is used as a validation value. We can assume that the GPR function modelled the training data as a simple, almost linear surface and did predict a rapid change in bias at p28. The result was a poor prediction $\Delta p28$. In the data set of $k = 6$, the GPR model was trained using p28, rather than validated with it, and therefore did not extrapolate well to predicting a rapid decrease in error at locations nearby. If it is assumed that p28 is an outlier, then the results for $k = 1$ and 6 can be withdrawn. It is assumed in the remaining cross-validation sets that although p28 was used as a training data value in these sets also, the accuracy of the bias correction predictions will not have been compromised because the nearby locations were also training values which it was assumed, were modelled accurately.

With the exception of $k = 1$ and 6, the results can be analysed with confidence that the bias correction accuracy was not sensitive to the training data and that the results are consistent for the remaining data sets ($k = 2, 3, 4, 5$ and 7). The bias correction residual errors in have a range of less than 20μm Δp_x and Δp_y , and approximately 40μm in Δp_z which is small in the context of drilling tolerances. Also with the exception of $k = 1$ and 6, the rms $|\Delta p|$ error has a range of 55μm to 85μm which is more accurate than the desired 0.1mm to 0.3mm range. It should be noted that the model created from the $k = 1$ data set was not corrupted by the outlier and the positional errors $|\Delta p|$, of the validation data other than in the outlier positions, range between 0.039mm and 0.136mm.

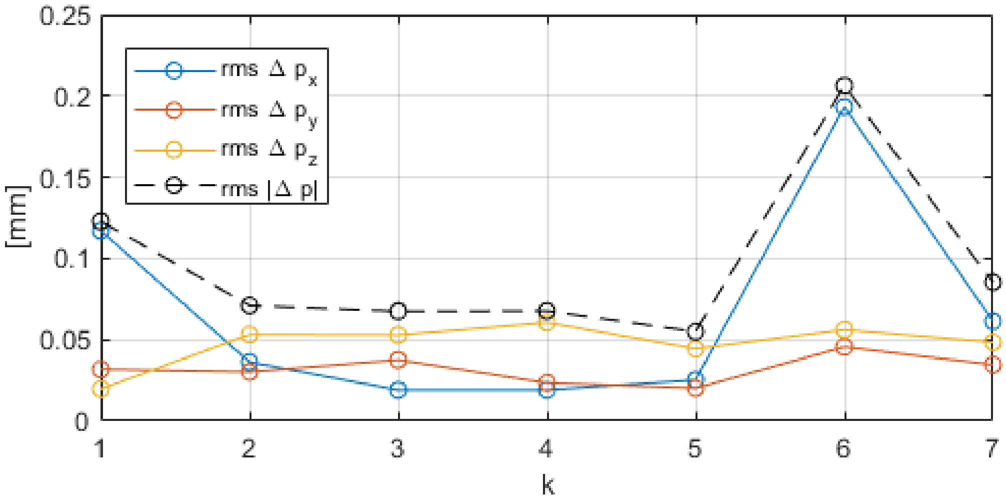

Figure 7.5: Robot drilling case study, cross-validation residual error results.

In Table 7.1 the training and validation results, which include the results from sets $k = 1$ to 7, are summarised. In Table 7.2 the results, which include the results from sets $k = 2, 3, 4, 5, 7$, are summarised for comparison of bias correction accuracy without the inclusion of the data from p28.

In both cases, the residual error in the bias data has been substantially reduced using bias correction as expected. In an analysis of the complete data set ($k = 1$ to 7), bias correction reduced the positional error of the robot from an rms $|\Delta p|$ of 3.584mm to 0.056mm for the training data and 0.108mm for the validation data. The results are within the desired 0.1mm to 0.3mm general accuracy range. There are still holes that would be drilled in a position with a positional error of up to 0.5mm which is considerably higher than the desired 0.2mm maximum error. Further scrutiny determines that the location of the 0.501mm error was at p28 again which demonstrates that the GPR did not model that particular data value accurately. It was expected that with sufficient distance (in covariance terms) between training data points, in Cartesian terms, the spike in bias value at p28 would be modelled. It is known that GPR, particularly with an SE kernel, is not able to model a discontinuous function because of a pre-disposal to smooth functions.

In comparison, the maximum positional error once the data from $k = 1$ and 6 has been removed, is just 0.115mm which is substantially lower than the desired accuracy.

Table 7.1: Robot drilling study, summary of training and validation data bias, and bias correction results for combined data sets $k = 1$ to 7.

	Training data		Validation data	
	M_0	$M_{0,GP}$	M_0	$M_{0,GP}$
$\bar{\Delta p}_x$ (std)[mm]	1.174 (0.663)	0.000 (0.046)	1.185 (0.685)	-0.017 (0.090)
$\bar{\Delta p}_y$ (std)[mm]	3.280 (0.180)	0.000 (0.017)	3.286 (0.180)	0.000 (0.033)
$\bar{\Delta p}_z$ (std)[mm]	-0.390 (0.092)	0.000 (0.027)	-0.379 (0.092)	0.005 (0.050)
rms $\lvert\Delta p\rvert$ (max)[mm]	3.584 (3.910)	0.056 (0.501)	3.584 (3.910)	0.108 (0.339)

Table 7.2: Robot drilling study, summary of training and validation data bias, and bias correction results for combined data sets $k = 2, 3, 4, 5, 7$.

	Training data		Validation data	
	M_0	$M_{0,GP}$	M_0	$M_{0,GP}$
$\bar{\Delta p}_x$ (std)[mm]	1.175 (0.678)	0.000 (0.090)	1.249 (0.682)	-0.010 (0.035)
$\bar{\Delta p}_y$ (std)[mm]	3.288 (0.180)	0.000 (0.033)	3.271 (0.163)	0.003 (0.030)
$\bar{\Delta p}_z$ (std)[mm]	-0.379 (0.090)	0.000 (0.050)	-0.384 (0.097)	0.002 (0.053)
rms $\lvert\Delta p\rvert$ (max)[mm]	3.582 (3.910)	0.063 (0.501)	3.590 (3.906)	0.070 (0.115)

7.3 Chapter summary

The aim of this chapter was to evaluate the proposed bias correction methodology in a robot machining application as an industry focussed, validation case study. The robot was programmed to move the TCP to positions that simulated a panel drilling task and the positional error data between the desired hole position and measured position was used to train and validate the GPR model. The results are not directly comparable to the results in Chapter 6 or to related works, due to differences in tool, data and experimental design. However, the study contributes to the body of knowledge on robotic machining by presenting bias correction results using a 'task-focussed' model (i.e. trained and tested locally). In fact, it can be argued that if an industrial robot will perform the same task for a long period of time, then a local model is a logical approach. The results in this study contribute to evaluating an industrial robot for such an application. This topic is discussed further in Chapter 8.

As expected, bias correction substantially reduced the positional error of the robot. With an outlier removed, the maximum error was considerably lower than the desired 0.2mm accuracy. However, an assumption was made that the spike in error surface was the result of an outlier. A higher resolution of data (or repetition) would identify if the spike was an outlier, which could be filtered out, or was the result of a configuration that was prone to high errors. In either case, higher resolution of data would enable the data to be cleaned or for the spike to be modelled.

To conclude, thesis objective 4 was met and the case study successfully evaluated the use of bias correction on an industrially focussed, machining application. The results were evaluated against a desirable maximum error which demonstrated that bias correction, using GPR, may be used to achieve a positional accuracy required for wider machining applications. The contribution of this case study, to the thesis aims and the existing body of knowledge, is discussed in Chapter 8.

Chapter 8

Conclusions and Future Work

The aim of the research presented in this thesis is to explore the use of bias correction to improve the positional accuracy of an industrial robot for machining applications. The poor positional accuracy of industrial robots limits their use to a small number of machining applications, and it is the intention that the research presented in this thesis will contribute to their wider use in higher accuracy machining applications.

The limit of positional accuracy was defined in Chapter 5 as 'an achievable positional accuracy for which considerably larger training data quantities are required to achieve marginal gains'. A desirable positional accuracy, quantified as the accuracy in a volume by an rms $|\Delta p|$, was determined as a region between 0.1mm and 0.3mm. The region represented a bounds that were currently unachievable by robot calibration, and the lower accuracy of conventional CNC machine tools. In addition, a maximum positional error of 0.2mm was set as a target for drilling tasks. The research in this thesis was focussed on determining if the limit of accuracy, using ML-based bias correction, would achieve either of the targets. Two research questions were formulated to meet the aims of this thesis.

- Research question 1: What are the limitations of the positional accuracy of an industrial robot, given sufficient training data quantities, when using bias correction to reduce positional errors?
- Research question 2: To what extent does bias reduction, by robot model calibration prior to bias correction, increase the positional accuracy of an industrial robot?

The experiments presented in each of Chapters 4 to 7 were conducted to meet a single objective in turn. The objectives of this thesis were to:

I Investigate the error sources on a conventional industrial robot and develop a numerical model to simulate robot positional errors.

II Test the proposed bias correction method on simulated models with increasing complexity.

III Validate the results of the bias correction method with an empirical study of an industrial robot

IV Validate the bias correction method for a robotic machining task.

This chapter is organised into two sections. In section 8.1, conclusions relating to the research questions are stated, followed by additional observations made during the process of this research. In section 8.2, recommendations for future work are presented.

8.1 Conclusions

It can be concluded that the application of ML-based bias correction can be successful in improving an industrial robot's positional accuracy to such an extent that may enable it to be used in wider machining applications. An accuracy approaching 0.1mm may be achieved using ML-based bias correction through more extensive error mapping and training than in related research literature. In the related literature, a mean error range of 0.3mm to 0.4mm is achieved by Tao and Yang [86], Jing et al. [45] and Yuan et al. [108] who used ANN, GPR and an extreme learner machine respectively. This also leads to the conclusion that the level of accuracy demonstrated in this thesis is not exclusive to GPR, but that a wider range of ML tools may be used to achieve similar results. Further conclusions, relating to each of the research questions, can be made on how the accuracy gains may be achieved.

In relation to research question 1, it can be concluded that the positional accuracy of an industrial robot may be improved by a significant amount by increasing the bias correction training data resolution. This meets general subject expectations. The accuracy achievable is a step towards that required for wider machining tasks. Increased training data resolution may be achieved through increased training data quantity, reduction in the number of input dimensions (i.e. joint variables) and reduction the input space (i.e. joint angle range). It can also be concluded that the greatest model accuracy gains occur in the 100 to 400 training data quantity range. This may infer why training data quantities within this range are used in related research to demonstrate the potential of ML-based bias correction to improve industrial robot accuracy, using ANN [44][86][91] and GPR [45] but without fully establishing their limits. The major contribution of this research is the demonstration that by using training data quantities of four to five times higher than presented in the related literature, further significant increases in accuracy can achieve the desired accuracy for wider machining applications. In a manufacturing context, this means that higher accuracies could be achieved by extensively mapping positional errors and/or by limiting the model to a local task space. Extensively mapping the joint-space errors with high training data quantities comes with additional measurement and computational time. It can further be concluded that the desirable levels of accuracy can still be achieved with relatively low measurement and computational cost by training locally to the intended task. This was demonstrated in Chapter 7, in which a drilling task was conducted and the 0.2mm accuracy was achieved. The case study further confirms the conclusion of Summers [37] that typical industrial robots were not capable of achieving at desired 0.2mm accuracy in a similar drilling task, but allows the conclusion that it may be achieved with the same robots and ML-based bias correction.

In relation to research question 2, it can be concluded that the level of calibration is not a determining factor in the level of accuracy achievable when bias correction is used post-calibration (or with no calibration) in this application. This is assuming that the task space is within the training space. Consequently, an argument can be made for not calibrating the kinematic model, and instead the data may be better utilised in training the bias correction model. In practical terms, this means that time can be saved by not measuring positions of the robot for calibration and that an arbitrary base frame can be used as a coordinate reference system. Whilst this conclusion does not contradict the combined calibration and bias correction approach in related research literature [44][45][86][91][117][119], it infers that the model accuracies achieved were the result of bias correction alone, in which case, more reliable comparisons between research results can be made. The proposal to remove the calibration procedure, in favour of bias correction alone is not necessarily straightforward, however. The desired configuration is not easy to predict using the inverse kinematic model, and the result may be joint angle inputs that are far from the training data input values, as demonstrated in the intended machining case study in Chapter 7. It transpired that GPR had a negligible effect on positional accuracy in this case, which is to be expected from a GPR with a zero mean. If some relatively low accuracy tasks are required outside of the training input space, calibration may still be required and bias correction can be focused on a small task space that requires higher accuracy.

It can be concluded that GPR-based bias correction is able to model the robot error data flexibly without being tailored to each case study, and therefore can be used as a general bias correction tool for a wide range of industrial robot types. By 'flexibly' it is meant that GPR was able to model the data for the different case studies, which presented problems of different complexity and input dimensions, without the author's influence (e.g. kernel selection). For an industrial solution to be applied generally to other industrial robotic machining systems, it is preferable that extensive analysis of the kinematic structure and bias correction expertise are not required to tailor the solution to the problem. GPR-based bias correct can be confirmed as an appropriate solution for robot surgical assistants, which have different non-geometric errors from due to cable driven actuators, as used by Mahler et al. [117] and Fan Zhang et al. [119]. The author's research can be extended to improve model accuracy further, without requiring extensive robot kinematics knowledge or GPR expertise.

8.1.1 Additional observations and recommendations

The focus of this thesis was the use of bias correction for industrial robot machining applications. However, numerous robot error and calibration observations were made in the process that may be useful to know in future, related research. Some of these observations and recommendations are briefly discussed in this subsection.

It can be concluded that non-geometric errors, such as those from joint compliance and gearbox transmission errors, may equal those from geometric parameters, but their relative contribution to the positional errors are expected to be unique to each application and robot. This agrees with a similar statement by Whitney [49] which was in contradiction to earlier research literature. In Chapter 6, it was shown that the positional errors resulting from the machining spindle payload and gearbox oscillations were considerably large and would be limitations to a geometric model calibration. It can further be concluded that ML-based bias correction models are also limited by these gearbox errors unless high-resolution training data is available. For a 6-DOF robot, the resolution is unlikely to be achievable within practical considerations. A parametric model of the gear transmission errors in each joint would contribute to a more accurate, numerical model for simulated studies which was a solution proposed by Nubiola et al. [51].

8.2 Future work

The research presented in this thesis has demonstrated that ML-based bias correction, using GPR, can be used to improve the accuracy of industrial robots beyond the level achieved by calibration alone. There are numerous avenues that can be followed to continue this research and some of these are discussed in this section.

There are very few ML tools that have been applied to industrial robot accuracy in literature. It would be beneficial to explore the use of other ML tools with a focus of either increasing prediction accuracy or computational efficiency.

At the core of GPR is the choice of kernel and its associated hyperparameters. An early decision was made to use an SE kernel that, without evidence to the contrary, was based on similar works in literature and an assumption that the bias data could be modelled with a smooth function. This was a logical decision that has worked with some success. The addition of a periodic kernel was explored temporarily to model a gearbox oscillation, but alternative kernels and combinations were not explored beyond this. Future work may benefit in a comparison of kernels or automatic kernel selection. In recent research Abdessalem et al. [122] discussed the issue of kernel selection and proposed a method to automatically select a kernel and optimal hyperparameters.

The GPR model accuracy was sensitive to the choice of hyperparameter in the higher input dimension case studies. Randomly seeding of initial estimates was used with relative success but was extremely time consuming and did not necessarily return the globally optimal solution. Future work should utilise one of the many methods proposed in the current and active field of research referred to as hyperparameter optimisation (HPO). The reader is directed to Kang et al. [123] who used a particle swarm variant to for HPO, and to Klein et al. [124] for a useful discussion on HPO and comparison of current HPO methods on the proposed meta-surrogate model.

In Chapter 7, the results of the drilling application case study demonstrated that high levels of accuracy can be achieved with small training data quantities. This is considered to be ‘task-based’ training. Task-based training can be extended to create multiple, independent local GP models, which are more accurate than a global model and quick to run. Treed GPs partition the input space into regions, in a process taken from decision-trees, and apply separate GP models [125], [126] that are better suited to the local data. Treed GP research is an active field of research with existing tools that could be applied to this problem.

Bibliography

[1] Paul Shore and Paul Morantz. Ultra-precision: Enabling our future. *Philosophical Transactions of the Royal Society A: Mathematical, Physical and Engineering Sciences*, 370(1973):3993–4014, 2012.

[2] Alexander Verl, Anna Valente, Shreyes Melkote, Christian Brecher, E. Ozturk, and Lutfi Taner Tunc. Robots in machining. *CIRP Annals*, 68(2):799–822, 2019.

[3] Francesco Leali, Alberto Vergnano, Fabio Pini, Marcello Pellicciari, and Giovanni Berselli. A workcell calibration method for enhancing accuracy in robot machining of aerospace parts. *International Journal of Advanced Manufacturing Technology*, 85(1-4):47–55, 2016.

[4] Nirosh Jayaweera and Phil Webb. Robotic edge profiling of complex components. *Industrial Robot: An International Journal*, 38(1):38–47, 2011.

[5] Hui Zhang, Heping Chen, Xi Ning, George Zhang, and Jianmin He. On-Line Path Generation for Robotic Deburring of Cast Aluminum Wheels. In *IEEE/RSJ International conference on Intelligent Robots and Systems*, pages 2400–2405, Bejing, 2006. IEEE.

[6] Berend Denkena, Benjamin Bergmann, and Thomas Lepper. Design and optimization of a machining robot. *Procedia Manufacturing*, 14:89–96, 2017.

[7] L F F Furtado, E Villani, L G Trabasso, and R Sutério. A method to improve the use of 6-dof robots as machine tools. *International Journal of Advanced Manufacturing Technology*, (92):2487–2502, 2017.

[8] E Ozturk, A Barrios, C Sun, S Rajabi, and J Munoa. CIRP Annals - Manufacturing Technology Robotic assisted milling for increased productivity. *CIRP Annals - Manufacturing Technology*, 67(1):427–430, 2018.

[9] Michael F Zaeh and Oliver Roesch. Improvement of the machining accuracy of milling robots. *Prod. Eng. Res. Devel.*, 2(8):737–744, 2014.

[10] Jie Liang and Shusheng Bi. Design and experimental study of an end effector for robotic drilling. *International Journal of Advanced Manufacturing Technology*, 2010.

[11] Tomas Olsson, Mathias Haage, Henrik Kihlman, Rolf Johansson, Klas Nilsson, Anders Robertsson, Mats Björkman, Robert Isaksson, Gilbert Ossbahr, and Torgny Brogårdh. Cost-efficient drilling using industrial robots with high-bandwidth force feedback. *Robotics and Computer-Integrated Manufacturing*, 26(1):24–38, 2010.

[12] S. Van Duin, P. J. Crothers, P. Steele, and J. Newberry. A comparison between indoor GPS versus laser tracking metrology for robotic drilling. *SAE Technical Papers*, (724), 2006.

[13] Robert Bogue. Finishing robots: a review of technologies and applications. *Industrial Robot: An International Journal*, 36(1):6–12, 2009.

[14] M Sabourin, F Paquet, B Hazel, J Côté, and P Mongenot. Robotic Approach to Improve Turbine Surface Finish. In *1st International Conference on Applied Robotics for the Power Industry*, pages 1–6, Montreal, 2010.

[15] Fan Chen, Huan Zhao, Dingwei Li, Lin Chen, Chao Tan, and Han Ding. Contact force control and vibration suppression in robotic polishing with a smart end effector. *Robotics and Computer Integrated Manufacturing*, 57:391–403, 2019.

[16] M J Ã Tsai, J F Huang, and W L Kao. Robotic polishing of precision molds with uniform material removal control. *International Journal of Machine Tools and Manufacture*, 49(11):885–895, 2009.

[17] A. Karim and A. Verl. Challenges and obstacles in robot-machining. In *44th International Symposium on Robotics*, 2013.

[18] John Pandremenos, Christos Doukas, Panagiotis Stavropoulos, and George Chryssolouris. Machining with robots: A critical review. In *7th International Conference on Digital Enterprise Technology*, Athens, 2011.

[19] I. Iglesias, M. A. Sebastián, and J. E. Ares. Overview of the State of Robotic Machining: Current Situation and Future Potential. *Procedia Engineering*, 132:911–917, 2015.

[20] Christian Möller, Hans Christian Schmidt, Philip Koch, Christian Böhlmann, Simon Markus Kothe, Jörg Wollnack, and Wolfgang Hintze. Machining of large scaled CFRP-Parts with mobile CNC-based robotic system in aerospace industry. *Procedia Manufacturing*, 14:17–29, 2017.

[21] Yonghua Chen and Fenghua Dong. Robot machining : recent development and future research issues. *International Journal of Advanced Manufacturing Technology*, (66):1489–1497, 2013.

[22] J Belchior, M Guillo, E Courteille, P Maurine, L Leotoing, and D Guines. Robotics and Computer-Integrated Manufacturing Off-line compensation of the tool path deviations on robotic machining : Application to incremental sheet forming $. *Robotics and Computer Integrated Manufacturing*, 29(4):58–69, 2013.

[23] Gang Xiong, Ye Ding, and Li Min Zhu. Stiffness-based pose optimization of an industrial robot for five-axis milling. *Robotics and Computer-Integrated Manufacturing*, 55:19–28, 2019.

[24] Yin Bu, Wenhe Liao, Wei Tian, Jin Zhang, and Lin Zhang. Stiffness analysis and optimization in robotic drilling application. *Precision Engineering*, 49:388–400, 2017.

[25] Hui Zhang, Jianjun Wang, G. Zhang, Zhongxue Zhongxue Gan, Zengxi Pan, Hongliang Cui, and Zhenqi Zhu. Machining with flexible manipulator: toward improving robotic machining performance. *IEEE/ASME International Conference on Advanced Intelligent Mechatronics.*, pages 24–28, 2005.

[26] Christian Lehmann, Marcel Halbauer, Dirk Euhus, Daniel Overbeck, and Sellhorner Weg. Milling with industrial robots : Strategies to reduce and compensate process force induced accuracy influences Chair of Automation Technology. *17th IEEE International Conference on Emerging Technologies and Factory Automation.*

[27] Julian Ricardo, Diaz Posada, Shivaram Kumar, Alexander Kuss, Ulrich Schneider, Manuel Drust, Thomas Dietz, and Alexander Verl. Automatic Programming and Control for Robotic Deburring Description of the Robot Debur- ring System. 2016:688–695, 2016.

[28] Yingjie Guo, Huiyue Dong, and Yinglin Ke. Stiffness-oriented posture optimization in robotic machining applications. *Robotics and Computer-Integrated Manufacturing*, 35:69–76, 2015.

[29] L. T. Tunc and Dave Stoddart. Tool path pattern and feed direction selection in robotic milling for increased chatter-free material removal rate. *International Journal of Advanced Manufacturing Technology*, 89(9-12):2907–2918, 2017.

[30] Zengxi Pan and Hui Zhang. Robotic machining from programming to process control. *Industrial Robot: An International Journal*, pages 499–503, 2008.

[31] H. W. Park, H. S. Yang, Y. P. Park, and S. H. Kim. Position and vibration control of a flexible robot manipulator using hybrid controller. *Robotics and Autonomous Systems*, 28(1):31–41, 1999.

[32] Hamza Alzarok, Simon Fletcher, Andrew P. Longstaff, and Alan Myers. Assessment of the positioning accuracy of a small articulated robot during machining operations. In *Computing and Engineering Annual Researchers' Conference*, Huddersfield, 2013.

[33] C. Wang. Current issues on 3D volumetric positioning accuracy: measurement, compensation, and definition. In *Seventh International Symposium on Instrumentation and Control Technology: Measurement Theory and Systems and Aeronautical Equipment*, volume 7128, Beijing, 2008.

[34] Soichi Ibaraki, Masahiro Sawada, Atsushi Matsubara, and Tetsuya Matsushita. Machining tests to identify kinematic errors on five-axis machine tools. *Precision Engineering*, 34(3):387–398, 2010.

[35] Ondrej Svoboda, Pavel Bach, Gianmarco Liotto, and Charles Wang. Definitions and correlations of 3D volumetric positioning errors of CNC machining centers. *The IMTS 2004 . . .*, pages 1–8, 2004.

[36] Ulrich Schneider, Manuel Drust, Matteo Ansaloni, Christian Lehmann, Marcello Pellicciari, Francesco Leali, Jan Willem Gunnink, and Alexander Verl. Improving robotic machining accuracy through experimental error investigation and modular compensation. *The International Journal of Advanced Manufacturing Technology*, 2014.

[37] Mark Summers. Robot capability test and development of industrial robot positioning system for the aerospace industry. *SAE Technical Papers*, (724), 2005.

[38] A.Y. Elatta, Li Pei Gen, Fan Liang Zhi, Yu Daoyuan, and Luo Fei. An overview of robot calibration. *Information Technology Journal*, 3(1):74–78, 2004.

[39] Z. Roth, B. Mooring, and B. Ravani. An overview of robot calibration. *IEEE Journal on Robotics and Automation*, 3(5), 1987.

[40] Benjamin Mooring, Driels Morris, and Roth Zvi. *Fundamentals of manipulator calibration*, volume 29. 1993.

[41] Kevin P. Murphy. *Machine Learning: A Probabilstic Perspective.* The MIT Press, 2012.

[42] Jonathan Schmidt, Mário R.G. Marques, Silvana Botti, and Miguel A.L. Marques. Recent advances and applications of machine learning in solid-state materials science. *npj Computational Materials*, 5(1), 2019.

[43] Jay H. Lee, Joohyun Shin, and Matthew J. Realff. Machine learning: Overview of the recent progresses and implications for the process systems engineering field. *Computers and Chemical Engineering*, 114:111–121, 2018.

[44] Hoai-Nhan Nguyen, Jian Zhou, and Hee-Jun Kang. A calibration method for enhancing robot accuracy through integration of an extended Kalman filter algorithm and an artificial neural network. *Neurocomputing*, 151:996–1005, 2015.

[45] Wei Jing, Pey Yuen Tao, Guilin Yang, and Kenji Shimada. Calibration of industry robots with consideration of loading effects using Product-Of-Exponential (POE) and Gaussian Process (GP). In *IEEE International Conference on Robotics and Automation*, pages 4380–4385, Stockholm, 2016.

[46] C.E. Rasmussen and C.K.I. Williams. *Gaussian Processes for Machine Learning.* The MIT Press, 2006.

[47] J M Renders, J M Renders, E Rossignol, E Rossignol, M Becquet, M Becquet, R Hanus, and R Hanus. Kinematic Calibration and Geometrical Parameter-Identification For Robots. *IEEE Transactions on Robotics and Automation*, 7(6):721–732, 1991.

[48] R P Judd and a B Knasinski. A Technique to Calibrate an Industrial Robot with Experimental Verification. *IEEE Transactions on Robotics and Automation*, 6(1):20–30, 1990.

[49] D E Whitney, C A Lozinski, and J M Rourke. Industrial Robot Forward Calibration Method and Results. *Journal of Dynamic Systems, Measurement, and Control*, 108:1–8, 1986.

[50] Ken Young and Craig G. Pickin. Accuracy assessment of the modern industrial robot. *Industrial Robot: An International Journal*, 27(6):427–436, 2000.

[51] Albert Nubiola and Ilian a. Bonev. Absolute calibration of an ABB IRB 1600 robot using a laser tracker. *Robotics and Computer-Integrated Manufacturing*, 29(1):236–245, 2013.

[52] S. Hayati, K. Tso, and G. Roston. Robot geometry calibration. In *IEEE International Conference on Robotics and Automation*, pages 947–951, 1988.

[53] Henry W Stone, Arthur C Sanderson, and Charles P Neuman. Arm Signature Identification. In *IEEE International Conference on Robotics and Automation*, pages 41–48, 1986.

[54] M. Abderrahim and A. R. Whittaker. Kinematic model identification of industrial manipulators. *Robotics and Computer-Integrated Manufacturing*, 16(1):1–8, 2000.

[55] I. Ming Chen and Guilin Yang. Kinematic calibration of modular reconfigurable robots using product-of-exponentials formula. *Journal of Robotic Systems*, 14(11):807–821, 1997.

[56] Koichiro Okamura and F. C. Park. Kinematic calibration using the product of exponentials formula. *Robotica*, 14(4):415–421, 1996.

[57] P. Y. Tao, G. Yang, Y. C. Sun, M. Tomizuka, and C. Y. Lai. Product-of-exponential (POE) model for kinematic calibration of robots with joint compliance. *IEEE/ASME International Conference on Advanced Intelligent Mechatronics, AIM*, pages 496–501, 2012.

[58] Guozhi Li, Fuhai Zhang, Yili Fu, and Shuguo Wang. Kinematic calibration of serial robot using dual quaternions. *Industrial Robot*, 46(2):247–258, 2019.

[59] Claire Dumas, Stéphane Caro, Sébastien Garnier, and Benoît Furet. Joint stiffness identification of six-revolute industrial serial robots. *Robotics and Computer-Integrated Manufacturing*, 27(4):881–888, 2011.

[60] J. Salisbury. Active stiffness control of a manipulator in cartesian coordinates. In *IEEE Conf. on Decision and Control (CDC)*, volume 19, pages 95–100, 1980.

[61] E. Abele, M. Weigold, and S. Rothenbücher. Modeling and identification of an industrial robot for machining applications. *CIRP Annals - Manufacturing Technology*, 56(1):387–390, 2007.

[62] Shih Feng Chen and Imin Kao. Conservative congruence transformation for joint and Cartesian stiffness matrices of robotic hands and fingers. *International Journal of Robotics Research*, 19(9):835–847, 2000.

[63] Shih-feng Chen and Imin Kao. Simulation of Conservative Congruence Transformation - Conservative Properties in the Joint and Cartesian Spaces. In *IEEE International Conference on Robotics and Automation*, number April, San Fransisco, 2000.

[64] A. Klimchik, Y. Wu, C. Dumas, S. Caro, B. Furet, and A. Pashkevich. Identification of geometrical and elastostatic parameters of heavy industrial robots. In *EEE International Conference on Robotics and Automation*, pages 3707–3714, 2013.

[65] Anatol Pashkevich, Alexandr Klimchik, and Damien Chablat. Enhanced stiffness modeling of manipulators with passive joints. *Mechanism and Machine Theory*, 46(5):662–679, 2011.

[66] Le Ma, Patrick Bazzoli, Patrick M. Sammons, Robert G. Landers, and Douglas A. Bristow. Modeling and calibration of high-order joint-dependent kinematic errors for industrial robots. *Robotics and Computer-Integrated Manufacturing*, 50:153–167, 2018.

[67] John Hollerbach, Wisama Khalil, and Maxime Gautier. Model Identification. *Springer Handbook of Robotics*, pages 321–344, 2008.

[68] John M. Hollerbach and Charles W. Wampler. The calibration index and taxonomy for robot kinematic calibration methods. *International Journal of Robotics Research*, 15(6):573–591, 1996.

[69] Wyatt S. Newman, Craig E. Birkhimer, Robert J. Horning, and Ann T. Wilkey. Calibration of a Motoman P8 robot based on laser tracking. In *IEEE International Conference on Robotics and Automation*, volume 4, pages 3597–3602, San Fransisco, 2000.

[70] Jorge Santolaria, Javier Conte, and Manuel Ginés. Laser tracker-based kinematic parameter calibration of industrial robots by improved CPA method and active retroreflector. *International Journal of Advanced Manufacturing Technology*, 66(9-12):2087–2106, 2013.

[71] Abdullah Aamir Hayat, Riby Abraham Boby, and Subir Kumar Saha. A geometric approach for kinematic identification of an industrial robot using a monocular camera. *Robotics and Computer-Integrated Manufacturing*, 57:329–346, 2019.

[72] W Gao, H Wang, and Y Jiang. Kinematic calibration method of robots based on distance error. *Robot*, 35:600–606, 2003.

[73] T Zhang, X Dai, and L Du. Robot error calibration based on distance measurement with parameter selection. *Journal of Beijing University fo Aeronautics and Astronautics*, 40:585–590, 2014.

[74] Shiwei Wang, Qingxuan Jia, Gang Chen, and Dan Liu. Complete relative pose error model for robot calibration. *Industrial Robot*, 46(5):622–630, 2019.

[75] Zhenhua Wang, Hui Xu, Guodong Chen, Rongchuan Sun, and Lining Sun. A distance error based industrial robot kinematic calibration method. *Industrial Robot*, 41(5):439–446, 2014.

[76] Shi Yun, Fang Jie, and Weng Zhiyuan. Research on kinematic parameter calibration of handling robot. In *IEEE 13th International Conference on Electronic Measurement and Instruments*, pages 224–228, 2017.

[77] In Chul Ha. Kinematic parameter calibration method for industrial robot manipulator using the relative position. *Journal of Mechanical Science and Technology*, 22(6):1084–1090, 2008.

[78] Shanshan He, Lei Ma, Changya Yan, Chen Han Lee, and Pengcheng Hu. Multiple location constraints based industrial robot kinematic parameter calibration and accuracy assessment. *International Journal of Advanced Manufacturing Technology*, 102(5-8):1037–1050, 2019.

[79] Heping Chen, Thomas Fuhlbrigge, Sang Choi, Jianjun Wang, and Xiongzi Li. Practical industrial robot zero offset calibration. In *4th IEEE Conference on Automation Science and Engineering*, pages 516–521, 2008.

[80] Ahmed Joubair and Ilian A. Bonev. Kinematic calibration of a six-axis serial robot using distance and sphere constraints. *International Journal of Advanced Manufacturing Technology*, 77(1-4):515–523, 2015.

[81] Zexiao Xie, Pengfei Zong, Peng Yao, and Ping Ren. Calibration of 6-DOF industrial robots based on line structured light. *International Journal for Light and Electron Optics*, 183:1166–1178, 2019.

[82] M. R. Driels. Using passive end-point motion constraints to calibrate robot manipulators. *Journal of Dynamic Systems, Measurement and Control, Transactions of the ASME*, 115(3):560–566, 1993.

[83] Albert Nubiola and Ilian A. Bonev. Absolute robot calibration with a single telescoping ballbar. *Precision Engineering*, 38(3):472–480, 2014.

[84] Mohamed Slamani, Ahmed Joubair, and Ilian A. Bonev. A comparative evaluation of three industrial robots using three reference measuring techniques. *Industrial Robot*, 42(6):572–585, 2015.

[85] Albert Nubiola, Mohamed Slamani, Ahmed Joubair, and Ilian a. Bonev. Comparison of two calibration methods for a small industrial robot based on an optical CMM and a laser tracker. *Robotica*, 32(03):447–466, 2013.

[86] P. Y. Tao and G. Yang. Calibration of industrial robots with product-of-exponential (POE) model and adaptive Neural Networks. In *EEE International Conference on Robotics and Automation*, pages 1448–1454, 2015.

[87] Ahmed Joubair, Mohamed Slamani, and Ilian a. Bonev. Kinematic calibration of a five-bar planar parallel robot using all working modes. *Robotics and Computer-Integrated Manufacturing*, 29(4):15–25, 2013.

[88] D Stanton and J R R Mayer. *Robot Calibration within CIM_SEARCH.* Chapman & Hall, 1993.

[89] G. Alici and B. Shirinzadeh. Kinematic identification of a closed-chain manipulator using a laser interferometry based sensing technique. In *IEEE/ASME International Conference on Advanced Intelligent Mechatronics*, volume 1, pages 332–337, 2003.

[90] Joon Hyun Jang, Soo Hyun Kim, and Keun Kwak Yoon. Calibration of geometric and non-geometric errors of an industrial robot. *Robotica*, 19:311–321, 2001.

[91] S. Aoyagi, A. Kohama, Y. Nakata, Y. Hayano, and M. Suzuki. Improvement of robot accuracy by calibrating kinematic model using a laser tracking system-compensation of non-geometric errors using neural networks and selection of

optimal measuring points using genetic algorithm-. In *IEEE/RSJ International Conference on Intelligent Robots and Systems*, pages 5660–5665, Taipei, 2010.

[92] Jin Hwan Borm and Chia Hsiang Menq. Determination of Optical Measurement Configurations for Robot Calibration Based on Observability Measure. *International Journal of Robotics Research*, 10(1), 1991.

[93] Hanqi Zhuang, Kuanchih Wang, and Z.S. Roth. Optimal selection of measurement configurations for robot calibration using simulated annealing. In *IEEE International Conference on Robotics and Automation*, pages 393–398, 1994.

[94] Yu Sun and John M. Hollerbach. Observability index selection for robot calibration. In *EEE International Conference on Robotics and Automation*, pages 831–836, 2008.

[95] A. Nahvi and J.M. Hollerbach. The noise amplification index for optimal pose selection in robot calibration. In *IEEE International Conference on Robotics and Automation*, volume 1, pages 647–654, 1996.

[96] Xiaoyan Chen, Qiuju Zhang, and Yilin Sun. Non-kinematic calibration of industrial robots using a rigid–flexible coupling error model and a full pose measurement method. *Robotics and Computer-Integrated Manufacturing*, 57:46–58, 2019.

[97] British Standard. BS EN ISO 9283:1998.pdf, 1998.

[98] Zhihong Jiang, Weigang Zhou, Hui Li, Yang Mo, Wencheng Ni, and Qiang Huang. A New Kind of Accurate Calibration Method for Robotic Kinematic Parameters Based on the Extended Kalman and Particle Filter Algorithm. *IEEE Transactions on Industrial Electronics*, 65(4):3337–3345, 2018.

[99] Shida Liu, Run Zhang, Yizhou Jiang, and Liandong Yu. The calibration method for robotic kinematic parameters based on articulated coordinate measuring machine. In *International Symposium on Precision Mechanical Measurements*, page 16, 2019.

[100] Alberto Omodei, Giovanni Legnani, and Riccardo Adamini. Three methodologies for the calibration of industrial manipulators: Experimental results on a SCARA robot. *Journal of Robotic Systems*, 17(6):291–307, 2000.

[101] Temesguen Messay, Raúl Ordóñez, and Eric Marcil. Computationally efficient and robust kinematic calibration methodologies and their application to industrial robots. *Robotics and Computer-Integrated Manufacturing*, 37:33–48, 2016.

[102] Gürsel Alici and Bijan Shirinzadeh. A systematic technique to estimate positioning errors for robot accuracy improvement using laser interferometry based sensing. *Mechanism and Machine Theory*, 40(8):879–906, 2005.

[103] Ying Bai and Hanqi Zhuang. On the comparison of bilinear, cubic spline, and fuzzy interpolation techniques for robotic position measurements. *IEEE Transactions on Instrumentation and Measurement*, 54(6):2281–2288, 2005.

[104] Ying Bai. On the comparison of model-based and modeless robotic calibration based on a fuzzy interpolation method. *International Journal of Advanced Manufacturing Technology*, 31(11-12):1243–1250, 2007.

[105] Yuanfan Zeng, Wei Tian, and Wenhe Liao. Positional error similarity analysis for error compensation of industrial robots. *Robotics and Computer-Integrated Manufacturing*, 42:113–120, 2016.

[106] Tian Wei, Zeng Yuanfan, Zhou Wei, and Liao Wenhe. Calibration of robotic drilling systems with a moving rail. *Chinese Journal of Aeronautics*, 27(6):1598–1604, 2014.

[107] Nobuaki Takanashi. 6 D.O.F. Manipulators absolutepositioning accuracy improvement using a neaural-network. *IEEE Int. Workshop on Intelligent Robotics and Systems*, pages 635–640, 1990.

[108] Peijiang Yuan, Dongdong Chen, Tianmiao Wang, Shuangqian Cao, Ying Cai, and Lei Xue. A compensation method based on extreme learning machine to enhance absolute position accuracy for aviation drilling robot. *Advances in Mechanical Engineering*, 10(3):1–11, 2018.

[109] Dali Wang, Ying Bai, and Jiying Zhao. Robot Manipulator Calibration Using Neural Network and a Camera-Based Measurement System. *Transactions of the Institute of Measurement and Control*, 34(1):105–121, 2012.

[110] Juš Kocijan, Agathe Girard, Blaž Banko, and Roderick Murray-Smith. Dynamic systems identification with Gaussian processes. *Mathematical and Computer Modelling of Dynamical Systems*, 11(4):411–424, 2005.

[111] Duy Nguyen-Tuong and Jan Peters. Learning robot dynamics for computed torque control using local Gaussian processes regression. In *ECSIS Symposium on Learning and Adaptive Behaviors for Robotic Systems,*, pages 59–64, 2008.

[112] Krzysztof Chalupka, Christopher K.I. Williams, and Iain Murray. A framework for evaluating approximation methods for Gaussian process regression. *Journal of Machine Learning Research*, 14(1):333–350, 2013.

[113] C E Rasmussen and C K I Williams. Regression. In *Gaussian Processes for Machine Learning*, page Chapter 2. M.I.T. Press, 2006.

[114] Yali Wang and Brahim Chaib-draa. KNN-based Kalman filter: An efficient and non-stationary method for Gaussian process regression. *Knowledge-Based Systems*, 114:148–155, 2016.

[115] Matthias Seeger, Christopher K. I. Williams, and Neil D. Lawrence. Fast Forward Selection to Speed Up Sparse Gaussian process regression. *Artif. Intell. Stat.9*, 2003.

[116] Edward Snelson and Zoubin Ghahramani. Sparse Gaussian processes using pseudo-inputs. *Advances in Neural Information Processing Systems*, pages 1257–1264, 2005.

[117] Jeffrey Mahler, Sanjay Krishnan, Michael Laskey, Siddarth Sen, Adithyavairavan Murali, Ben Kehoe, Sachin Patil, Jiannan Wang, Mike Franklin, Pieter Abbeel, and Ken Goldberg. Learning accurate kinematic control of cable-driven surgical robots using data cleaning and Gaussian Process Regression. In *IEEE International Conference on Automation Science and Engineering*, pages 532–539. IEEE, 2014.

[118] Peter Pastor, Mrinal Kalakrishnan, Jonathan Binney, Jonathan Kelly, Ludovic Righetti, Gaurav Sukhatme, and Stefan Schaal. Learning task error models for manipulation. In *EEE International Conference on Robotics and Automation*, pages 2612–2618. IEEE, 2013.

[119] Fan Zhang, Zhiyuan Yan, and Zhijang Du. Preoperative setup planning for robotic surgery based on a simulation platform and Gaussian process. In *IEEE International Conference on Mechatronics and Automation*, pages 902–907. IEEE, 2016.

[120] H Zhuang and Z.S. Roth. *Camera-Aided Robot Calibration.* CRC Press, Inc, 1996.

[121] Mark Ebden. Gaussian Processes: A Quick Introduction, 2008.

[122] Anis Ben Abdessalem, Nikolaos Dervilis, David J. Wagg, and Keith Worden. Automatic kernel selection for gaussian processes regression with approximate bayesian computation and sequential Monte Carlo. *Frontiers in Built Environment*, 3(May 2018), 2017.

[123] Lanlan Kang, Ruey Shun Chen, Naixue Xiong, Yeh Cheng Chen, Yu Xi Hu, and Chien Ming Chen. Selecting Hyper-Parameters of Gaussian Process Regression Based on Non-Inertial Particle Swarm Optimization in Internet of Things. *IEEE Access*, 7:59504–59513, 2019.

[124] Aaron Klein, Zhenwen Dai, Frank Hutter, Neil Lawrence, and Javier Gonzalez. Meta-Surrogate Benchmarking for Hyperparameter Optimization. (NeurIPS):1–11, 2019.

[125] Robert B. Gramacy and Herbert K.H. Lee. Bayesian treed Gaussian process models with an application to computer modeling. *Journal of the American Statistical Association*, 103(483):1119–1130, 2008.

[126] T. Zhang, R. J. Barthorpe, and K. Worden. On Treed Gaussian Processes and piecewise-linear NARX modelling. *Mechanical Systems and Signal Processing*, 144:106877, 2020.